AWARD NUMBER: W81XWH-15-1-0060

TITLE: Development of Novel Drugs for High Risk Triple Negative Breast Cancer Treatment

PRINCIPAL INVESTIGATOR: Lester R. Drewes

CONTRACTING ORGANIZATION:

Regents of the University of Minnesota

Minneapolis, MN 55455-2009

REPORT DATE: Nov 2019

TYPE OF REPORT: Final Report

PREPARED FOR: U.S. Army Medical Research and Development Command

Fort Detrick, Maryland 21702-5012

REPORT DOCUMENTATION PAGE

Form Approved
OMB No. 0704-0188

1. REPORT DATE	2. REPORT TYPE	3. DATES COVERED
Nov 2019	Final Report	03/15/2015 - 08/31/2019

4. TITLE AND SUBTITLE

Development of Novel Drugs for High-Risk Triple-Negative Breast Cancer Treatment

5a. CONTRACT NUMBER

5b. GRANT NUMBER
W81XWH-15-1-0060

5c. PROGRAM ELEMENT NUMBER

6. AUTHOR(S)
Initiating PI Venkatram R. Mereddy and Partnering PI: Lester Drewes

E-Mail: vmereddy@d.umn.edu ldrewes@d.umn.edu

5d. PROJECT NUMBER

5e. TASK NUMBER

5f. WORK UNIT NUMBER

7. PERFORMING ORGANIZATION NAME(S) AND ADDRESS(ES)

1039 University Dr, CHEM 138
Department of Chemistry and Biochemistry,
University of Minnesota Duluth

1035 University Dr, SMed 251,
Department of Biomedical Sciences,
School of Medicine,
University of Minnesota Duluth

8. PERFORMING ORGANIZATION REPORT NUMBER

9. SPONSORING / MONITORING AGENCY NAME(S) AND ADDRESS(ES)

U.S. Army Medical Research and Development Command
Fort Detrick, Maryland 21702-5012

10. SPONSOR/MONITOR'S ACRONYM(S)

11. SPONSOR/MONITOR'S REPORT NUMBER(S)

12. DISTRIBUTION / AVAILABILITY STATEMENT

Approved for Public Release; Distribution Unlimited

13. SUPPLEMENTARY NOTES

14. ABSTRACT

Triple negative breast cancer (TNBC) constitutes 10–20% of all breast cancers and is associated with aggressive tumor growth, metastasis and poor patient outcome. The standard treatment involves surgery, radiation and chemotherapy. Many of these chemotherapeutics are hampered by their lack of cancer cell selectivity and significant serious side effects. Most patients initially respond to the chemotherapy but a majority relapses and become drug resistant. Hence, novel therapeutics that are selectively toxic to cancer cells are urgently needed. Vigorous glycolysis is the hallmark of all advanced stage tumors. The end products of glycolysis are metabolites such as pyruvate and lactate. These are transported in and out of the cells by monocarboxylate transporters 1 & 4 (MCT1/4) and serve as nutrients for further energy production. We have developed small molecule based MCT1/4 inhibitors that exhibit an efficient tumor growth inhibition in MCT1 and MCT4 expressing tumor xenograft models. The purpose of this project is to explore the potential of these inhibitors as anticancer agents.

15. SUBJECT TERMS
triple negative breast cancer, MDA-MB-231, HCC1395, tumor glycolysis, cytotoxicity, Warburg effect, reverse Warburg effect

16. SECURITY CLASSIFICATION OF:			17. LIMITATION OF ABSTRACT	18. NUMBER OF PAGES	19a. NAME OF RESPONSIBLE PERSON
a. REPORT	b. ABSTRACT	c. THIS PAGE			USAMRMC
Unclassified	Unclassified	Unclassified	Unclassified		19b. TELEPHONE NUMBER *(include area code)*

TABLE OF CONTENTS

	Page
1. Introduction	1
2. Keywords	1
3. Accomplishments	1
4. Impact	67
5. Changes/Problems	68
6. Products	69
7. Participants & Other Collaborating Organizations	70
8. Special Reporting Requirements	71
9. Appendices	71

Introduction

Triple negative breast cancer (TNBC) constitutes 10–20% of all breast cancers and is associated with aggressive tumor growth, recurrence, metastasis and poor patient outcome. The absence of well-defined molecular targets such as estrogen/progesterone receptors or HER2 receptor makes TNBC treatment very challenging. The standard treatment involves surgery, radiation and chemotherapy with anthracyclins and taxane based drugs. The mechanism of these drugs involves either cellular DNA damage or inhibition of DNA synthesis. Many of these drugs are hampered by their lack of cancer cell selectivity and significant serious side effects that include permanent damage to the immune system, thereby, limiting the treatment efficacy. Most patients initially respond to the chemotherapy but a majority relapses and become drug resistant. Hence, novel and inexpensive therapeutics that are selectively toxic to cancer cells and, also preferably that work on drug resistant cells, are urgently needed. Vigorous glycolysis is the hallmark of all advanced stage tumors. The end products of glycolysis are metabolites such as pyruvate and lactate. These products are transported in and out of the cells by monocarboxylate transporters-1 and 4 (MCT1/4) and serve as nutrients for further energy production. We hypothesize that the inhibition of these transporters leads to glycolytic arrest, metabolic dysfunction and cancer cell death. Furthermore, aerobic glycolysis reportedly also takes place in neighboring cancer-associated stromal fibroblasts rather than in epithelial cancer cells. These fibroblasts also produce lactate and pyruvate that are then taken up by the adjacent cancer cells via MCT1/4 for ATP production and proliferation. Recently, we discovered very potent MCT1/4 inhibitors and anticancer studies in mice using a colon cancer model and toxicology studies proved that these new molecules efficiently reduce the tumor growth without causing any systemic toxicity. In this proposed research, we carried out a detailed *in vivo* preclinical evaluation of these novel molecules and their efficacy for treating TNBC.

Key Words: Triple negative breast cancer, glycolysis, mitochondrial respiration, OxPhos, monocarboxylate transporter, Warburg effect, reverse Warburg effect, MDA-MB-231, 4T1

Accomplishments

- **What were the major goals of the project?**
  Major Task 1: Identification of lead inhibitor
  Major Task 2: Efficacy of lead inhibitor in orthotopic models
  Major Task 3: *In vivo* efficacy in metastatic, PDTX, drug resistant and transgenic models
- **What was accomplished under these goals?**

Working hypothesis: Cancer cells have been shown to exhibit altered metabolic phenotypes when compared to normal cells; and the characterization of this phenomenon is being actively pursued in the literature for a better understanding of disease progression toward the development of cancer therapeutics. In solid tumors, including those of breast cancer origin, malignant transformation leads to high rates of proliferation

with increased metabolic needs, wherein numerous heterogeneous tissue types cooperate in tumor progression. Heightened metabolism in breast and other solid tumors has historically been described as being highly glycolytic in nature, and were uniformly characterized by increased glucose uptake and lactate production to meet energetic and biosynthetic needs. However, recent literature reports have indicated that oxygen and nutrient gradients along with heterogeneous tumor tissue dictate a new energetic/synthetic phenomena called metabolic plasticity where small metabolites are shuttled between anabolic and catabolic tumor compartments, and mitochondrial respiratory processes play a critical role in aggressive and proliferative subtypes. To facilitate this metabolic plasticity, numerous breast and other tumors overexpress MCTs to distribute lactate, pyruvate, and other energy rich metabolites throughout the tumor and hence, we hypothesize that the pharmacological targeting of MCTs with small molecules has potential in disrupting metabolic plasticity and ultimately cancer cell death.

Results

Synthesis and evaluation of first generation MCT inhibitors: α – cyanohydroxycinnamic acid (CHC), and MCT1 inhibitor, has long been used as a biochemical tool in studying lactate and pyruvate shuttling. However, low potency has limited its use as a potential therapeutic agent. In this regard, we undertook the project of synthesizing and evaluating new-generation MCT1 inhibitors based on the CHC template (Figure 1).

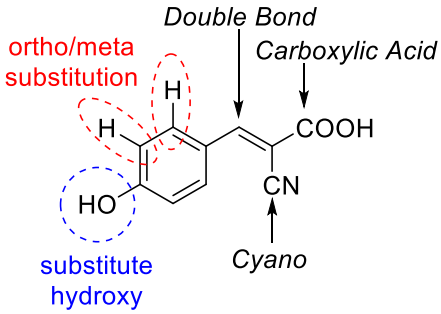

Figure 1. Structure of CHC with potential sites of synthetic modification. Pharmacophore is the cyanocinnamic acid template, where the cinnamic double bond, cyano group, and carboxylic acid are required for activity.

In this regard, we have carried out an extensive structure activity relationship (SAR) study on the CHC template which has led to the discovery of numerous potent MCT1 and MCT4 inhibitors at low nanomolar concentrations. The most potent derivatives were synthesized based on an *p*-N,N-dialkyl/aryl-*o*-methoxy cyanocinnamic acid template and were found to inhibit MCT1 and MCT4 function in the single digit nanomolar range (Figure 2, Scheme 1-2).

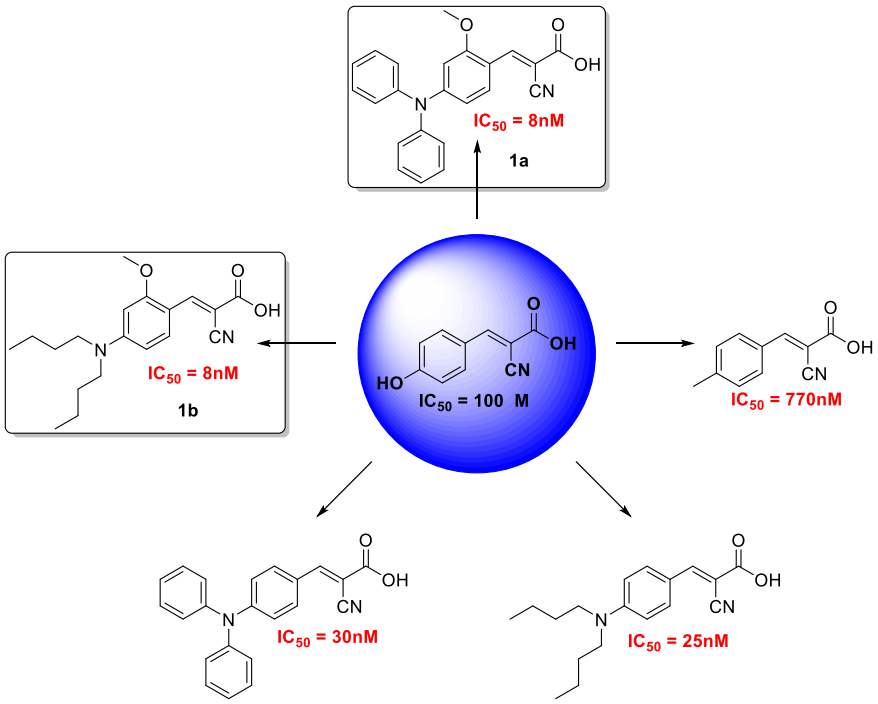

Figure 2. Structure activity relationship study revealed that *p*-N,N-dialkyl/aryl-*o*-methoxy CHC template exhibits highest inhibitory concentration (IC_{50}) of MCT1 mediated lactate uptake. Lead candidate inhibitors **1a** and **1b** exhibit 8nM IC_{50}, compared to ~100,000nM IC_{50} of parent CHC; qualifying these candidates for further pre-clinical development.

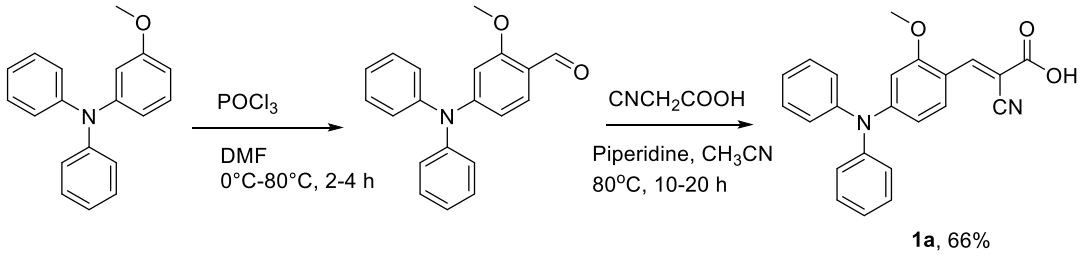

Scheme 1. Synthetic scheme of lead candidate compound **1a**.

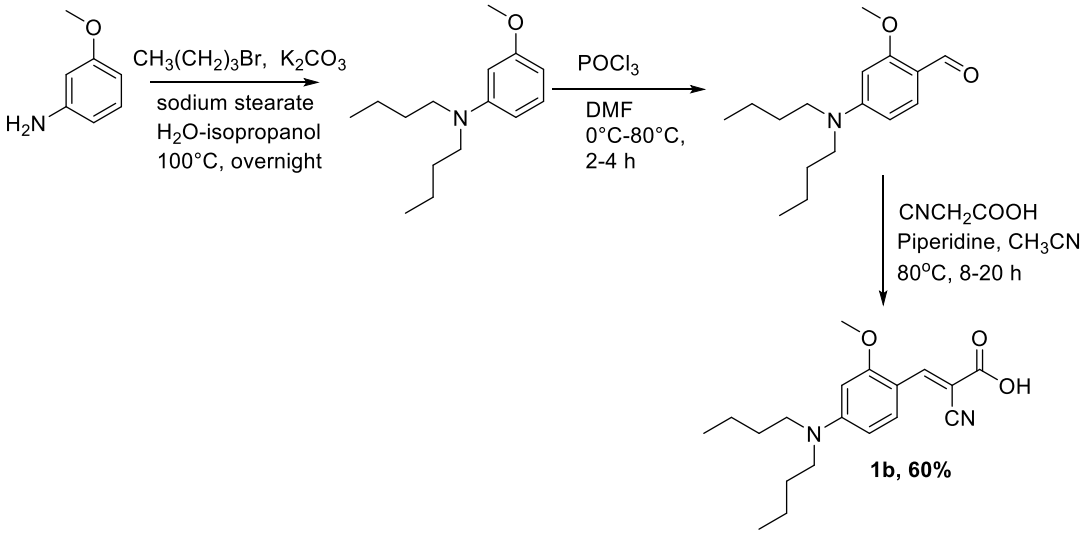

Scheme 2. Synthetic scheme of lead candidate compound **1b**.

MCT1 inhibitory properties of candidate compounds was evaluated using 14C-lactate uptake studies in MCT1 expressing rat brain endothelial (RBE4 cell line).

Table 1. MCT1 IC_{50} (nM)* of *N,N*-dialkyl/diaryl *o*-substituted CHC derivatives **1a-1b** in RBE4 cell line

Sl. No.	Compound	MCT1 IC_{50}
1a	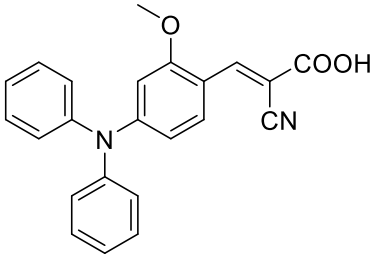	8±1
1b	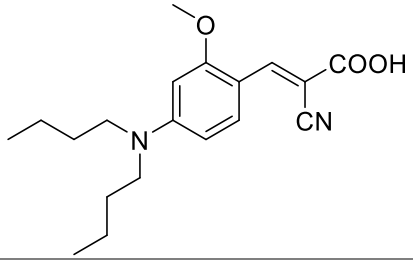	8±1

* IC_{50} values reported in nM, average ± SEM of minimum three separate experimental values

To further investigate the utility of candidate inhibitors as anticancer agents, we carried out *in vitro* cell proliferation inhibition properties of **1a** and **1b** along with parent compound CHC in several breast and other cancer cell lines using both MTT (Table 2) and SRB (Table 3) based cell proliferation assays. MTT reports on the activity of mitochondrial reductase activity as a function of cell proliferation. Inhibition of metabolite flux of

candidate compounds may result in mitochondrial dysfunction and hence, we confirmed the cell proliferation inhibition results obtained from the MTT assay using the SRB assay which reports on total cell protein; independent of respiratory or metabolic processes. Cell lines tested included aggressive and difficult to treat MCT4 expressing triple-negative breast cancer MDA-MB-231, MCT1 expressing stage IV metastatic breast cancer 4T1-luc2, and other MCT1 expressing cancer cell lines WiDr, and GL261. Gratifyingly, the candidate compounds exhibited several fold enhanced cell proliferation inhibition properties when compared to parent compound CHC in all of the cell lines tested, with compound **1a** exhibiting increased potency over **1b** in breast cancer cell lines MDA-MB-231 and 4T1-luc2 (Tables 2 & 3).

Table 2: MTT assay IC_{50}^{*} values of *N,N*-dialkyl *o*-methoxy CHC derivatives **1a** and **1b** in MDA-MB-231, WiDr, 4T1-luc2 and GL261-luc2 cell lines

Sl. No	MDA-MB-231	WiDr	4T1-luc2	GL261-luc2
CHC	5.71±0.44	>0.5	5.35±1.35	5.27±0.33
1a	0.08±0.01	0.0077±0.000	0.05±0.01	0.09±0.00
1b	0.13±0.01	0.0056±0.001	0.05±0.01	0.16±0.01

* IC_{50} values reported in mM, average ± SEM of minimum three separate experimental values

Table 3: SRB assay IC_{50}* values of *N,N*-dialkyl *o*-methoxy CHC derivatives in MDA-MB-231, WiDr, 4T1-luc2 and GL261-luc2 cell lines

Sl. No.	MDA-MB-231	WiDr	4T1-luc2	GL261-luc2
CHC	5.57±0.99	2.16±0.52	4.66±0.43	6.49±1.41
1a	0.08±0.01	0.0042±0.000	0.08±0.01	0.11±0.00
1b	0.12±0.02	>0.025	0.11±0.02	0.08±0.04

* IC_{50} values reported in mM, average ± SEM of minimum three separate experimental values

Encouraged by enhanced MCT1 and cell proliferation inhibition properties, compound **1a** was further advanced to *in vivo* pharmacokinetic analysis in mice to evaluate its potential for translation to *in vivo* efficacy studies. The concentration-time profile was plotted for both ip and oral administration of **1a** where it was found that the $t_{1/2}$ of **1a** was found to be 15 minutes for ip and 30 minutes for oral gavage routes of administration (Figure 3A & B). Short half-life as indicated by time-plasma profile of compound **1a** in mice revealed a potential metabolic vulnerability of the unsubstituted N-phenyl groups that are readily

oxidized by CYP450 enzymes during first-pass metabolism which may result in the rapid elimination rates of compound **1a** *in vivo* (Figure 3).

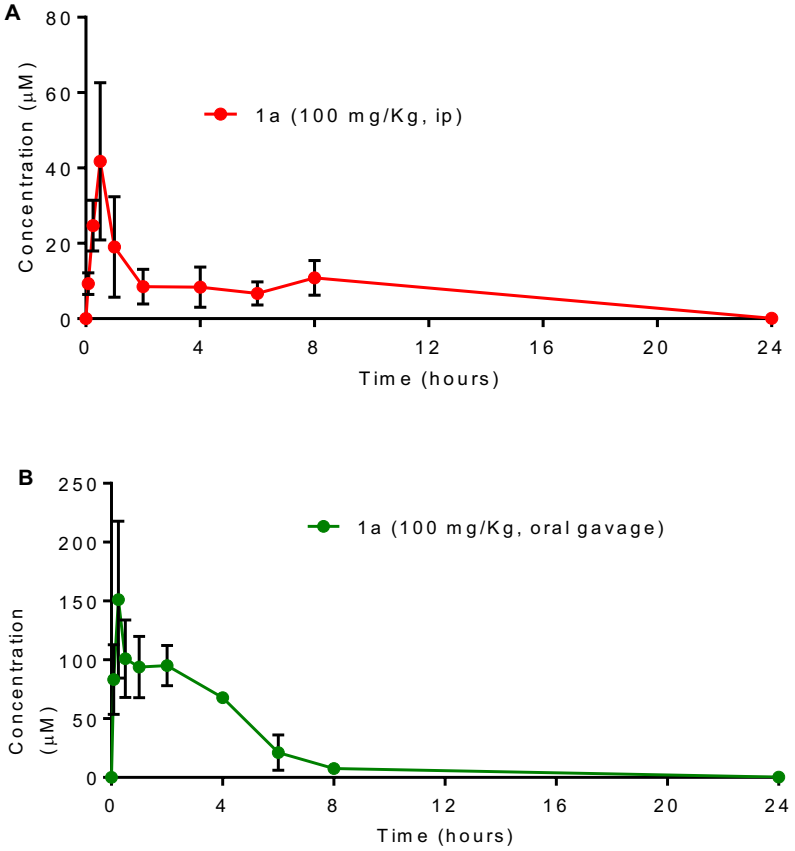

Figure 3. *In vivo* pharmacokinetic analysis of compound **1a** administered (**A**) intraperitoneal and (**B**) oral gavage.

Nonetheless, we sought to investigate the systemic toxicity and efficacy of candidate **1a** *in vivo* as a proof of concept. In this regard, healthy CD-1 mice were administered compound **1a** at 50mg/kg, once daily intraperitoneal over the course of 15 days. Gratifyingly, mice exhibited no body weight loss when compared to control (vehicle treated) mice (Figure 4). The blood counts of treated mice were also not found to be effected when compared to the untreated control group (data not shown).

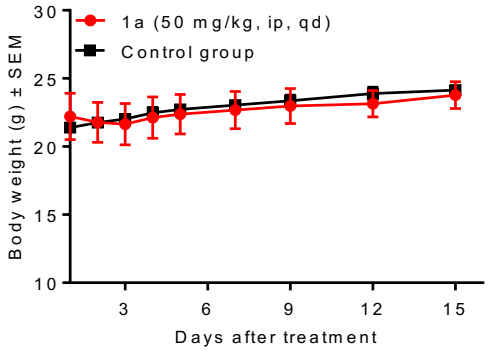

Figure 4. Systemic toxicity study of compound **1a** in healthy CD-1 mice.

To investigate the *in vivo* efficacy of compound **1a,** we utilized an aggressive and difficult to treat stage IV breast cancer model 4T1-luc2 that expresses MCT1. Female BALB/c mice (4 weeks old) were injected with 1 × 10^5 4T1-luc2 cells. Mice were randomized in to 3 groups (n = 6 mice per group) after 48 hours of tumor inoculation. Mice in groups 1 and 2 were administered with lead molecule **1a** at a dosage of 25 mg/Kg, ip, qd and doxorubicin was administered at 0.5 mg/Kg, i.p. five days a week as a positive control in group. Mice in group 3 were used as a control group and were administered with vehicle (10% DMSO in saline). Tumors were measured every 3-4 days. At the end of the study (day-21), mice were euthanized, and tumor samples were retrieved and weighed. From this study, **1a** and doxorubicin exhibited 38, and 36% tumor growth inhibition, respectively, based on tumor volume, and 20 and 39% tumor growth inhibition based on weights from the resected tumors (Figure 5A & B).

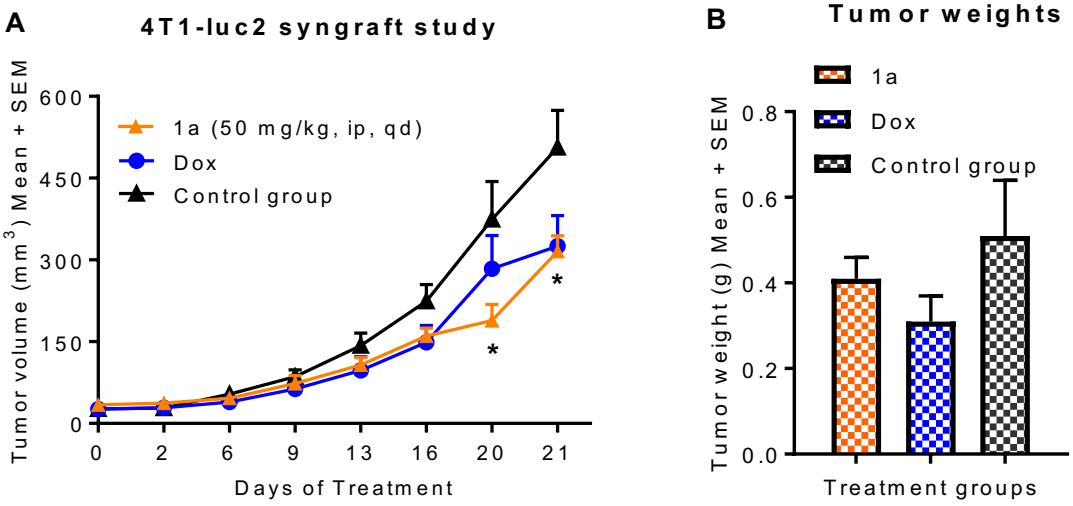

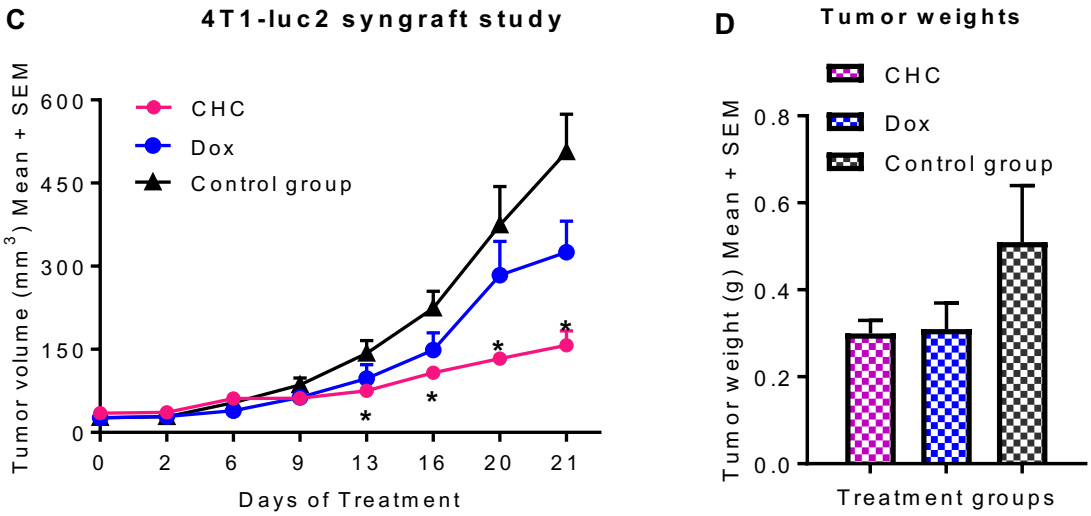

Figure 5. In vivo efficacy study of candidate **1a** (25mg/kg) in a stage IV breast cancer model 4T1-luc2. (**A**) Tumor volumes and (**B**) weights were recorded to evaluate efficacy over a 21-day treatment period. (**C-D**) Parent compound **CHC** (100mg/kg) was also tested in the same fashion.

In this regard, we have also tested the parent CHC derivative at very high concentrations, where we observed a significant tumor growth inhibition in this aggressive stage IV breast cancer tumor model – further illustrating the potential of targeting MCT1 for breast cancer treatment.

Moderate but statistically significant tumor growth reduction of compound **1a** as a single agent in an aggressive and difficult to treat 4T1 breast cancer model illustrated the potential of targeting MCT1 for cancer treatment. However, metabolic vulnerabilities and rapid elimination half-life of this compound led us to expand the structural diversity of our library toward the development of MCT1 inhibitors on a structurally and pharmacologically privileged coumarin template.

Synthesis and evaluation of second-generation MCT1 inhibitors:

Our first generation SAR studies revealed the importance of N,N-dialkyl/aryl cyanocinnamic acid template in providing biological activity. To further investigate the structure activity relationship of these compounds, we sought to utilize a pharmacologically privileged and structurally similar N,N-dialkyl coumarin carboxylic acid template (Figure 3).

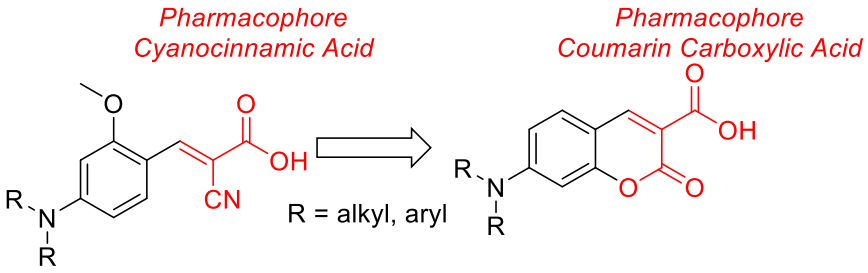

Figure 6. First generation p-N,N-dialkyl/aryl-o-methoxy cyanocinnamic acid based MCT inhibitors share numerous structural characteristics with coumarin carboxylic acids.

Literature reports and our SAR studies revealed the importance of a doubly activated 1,4 acceptor for pharmacological activity for our first generation MCT1 inhibitors. Interestingly, coumarin carboxylic acid also exhibits a doubly activated 1,4 acceptor, with a cyclic ester in place of the cyano group of our first generation inhibitors, where *p*-N,N-dialkyl/aryl substation may similarly result in MCT1 inhibition. In this regard, we synthesized a structurally diverse library of N,N-dialkyl coumarin carboxylic acids and evaluated them for their MCT1 inhibition properties.

We first synthesized *N,N*-dimethyl and *N,N*-diethyl carboxy coumarins **2a** and **2b** starting from commercially available aldehydes 4-(dimethylamino)-2-hydroxybenzaldehyde and 4-(diethylamino)-2-hydroxybenzaldehyde. The aldehydes were condensed with diethyl malonate, and the resulting diesters were hydrolyzed with NaOH and acidified to pH 7 to obtain the corresponding products **2a** and **2b** (Scheme 3).

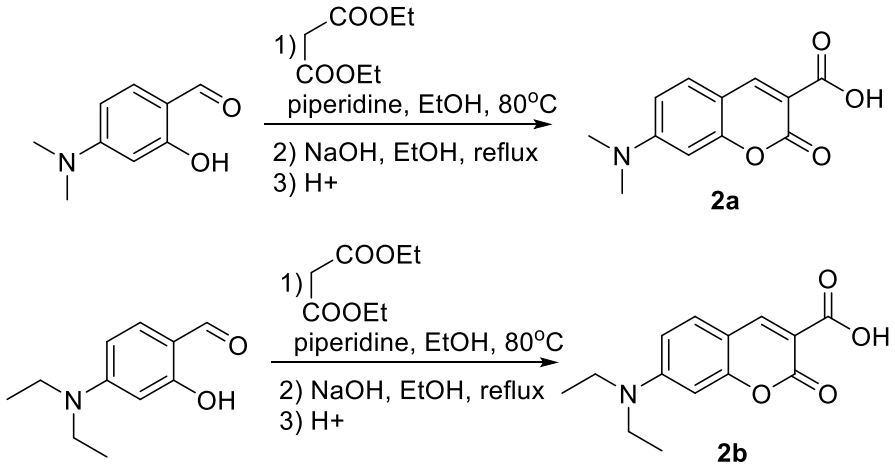

Scheme 3: Synthesis of 7-(dimethylamino)-2-oxo-2H-chromene-3-carboxylic acid **2a** and 7-(diethylamino)-2-oxo-2H-chromene-3-carboxylic acid **2b.**

We then synthesized various *N,N*-dialkyl substituted carboxy coumarins via alkylating *o*-aminophenol in the presence of K_2CO_3 in DMSO or ethanol. For this purpose, we used propyl bromide, butyl bromide, allyl bromide, propargyl bromide and benzyl bromides. The alkylated aminophenols were then formylated using $POCl_3$ in DMF to obtain corresponding aldehydes. These aldehydes were condensed with diethyl malonate and

hydrolyzed as mentioned in scheme 3 to obtain corresponding coumarin carboxylic acids **2c-2g** (Scheme 4).

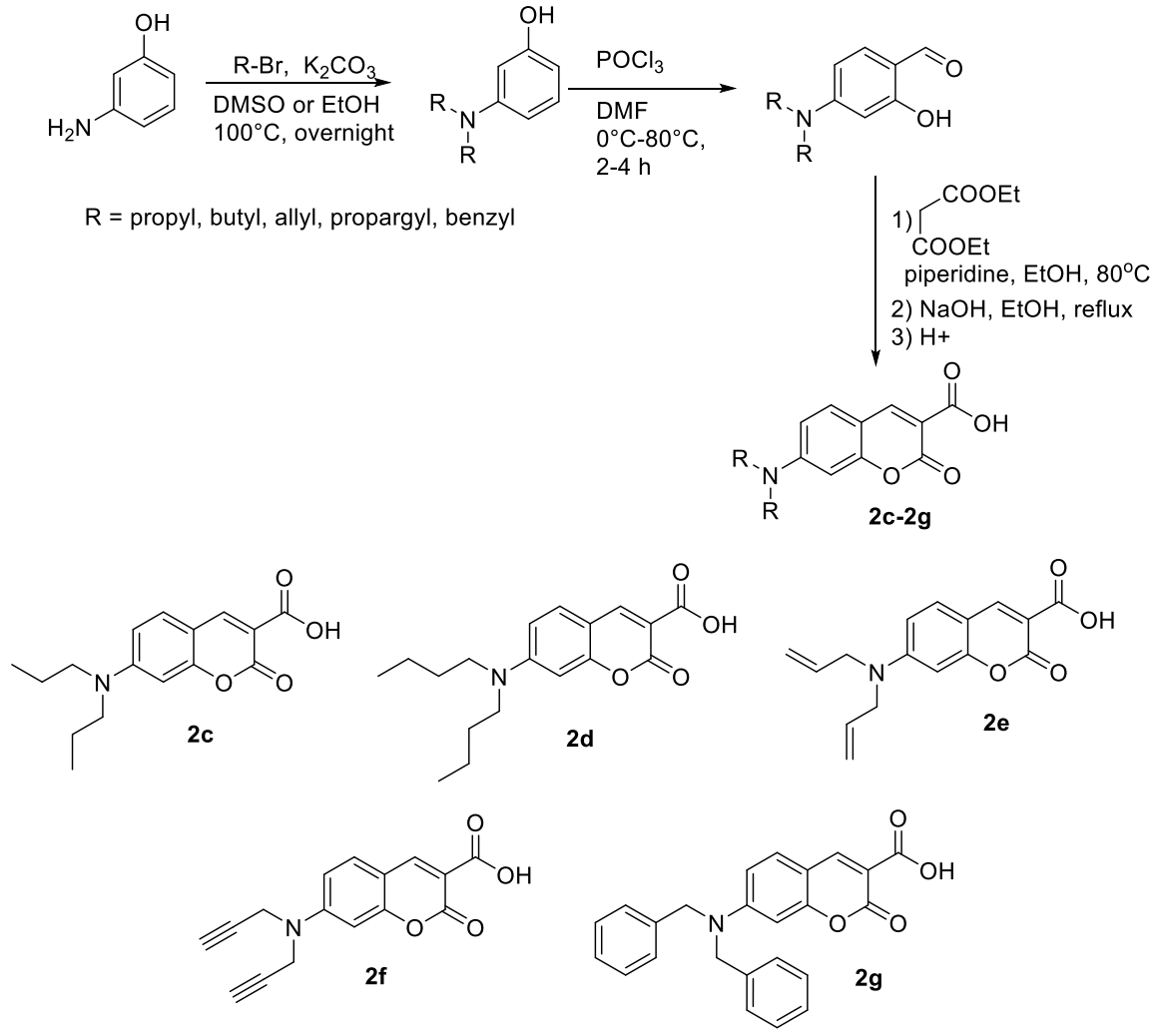

Scheme 4: Synthesis of coumarin carboxylic acids **2c-2g**

We also synthesized cyclic pyrrolidinyl carboxy coumarin **2h** via dialkylation of *o*-aminophenol with 1,4-dibromobutane (Scheme 5).

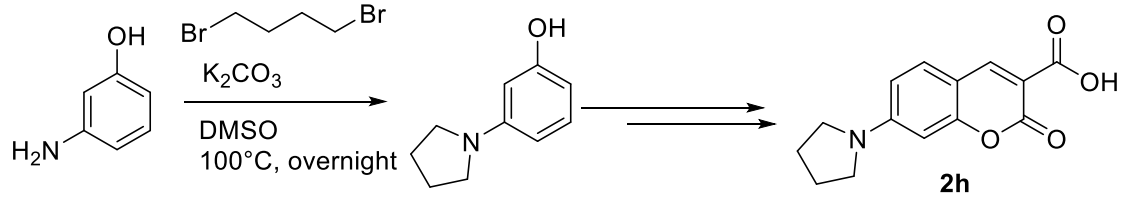

Scheme 5: Synthesis of 2-oxo-7-(pyrrolidin-1-yl)-2H-chromene-3-carboxylic acid **2h**

Diphenyl carboxy coumarin **2i** was also synthesized starting from aminophenol. In this case, 3-methoxy-N,N-diphenylaniline was hydrolyzed using BBr_3, followed by formylation

via Villsmeier-Haack conditions and subsequent treatment with diethyl malonate and hydrolysis to obtain **2i** (Scheme 4d).

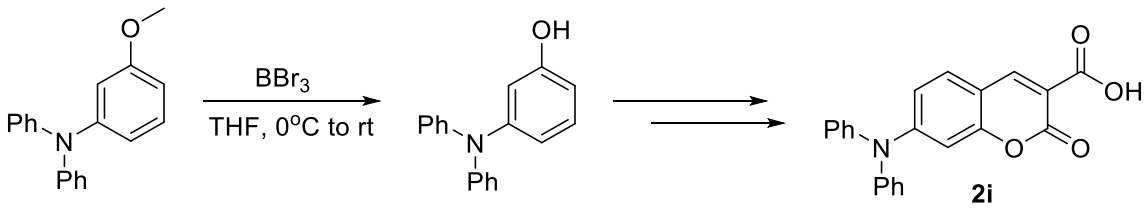

Scheme 6: Synthesis of coumarin carboxylic acid **2i**

The MCT1 inhibitory properties of candidate compounds were again evaluated using ^{14}C-lactate uptake studies in MCT1 expressing RBE4 cell line (Table 4).

Table 4. MCT1 IC_{50} (nM)* of *N,N*-dialkyl/diaryl carboxy coumarin derivatives **2a-2b** in RBE4 cell line

Sl. No.	Compound	MCT1 IC_{50}
2a	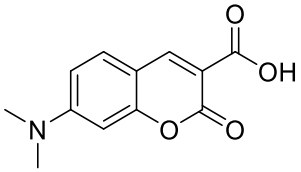	72±22
2b	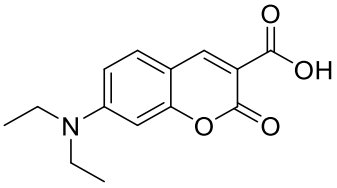	97±14
2c	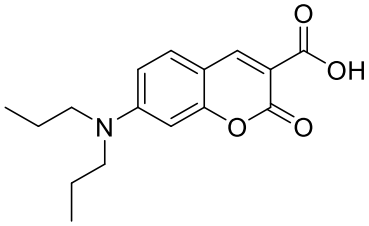	299±43
2d	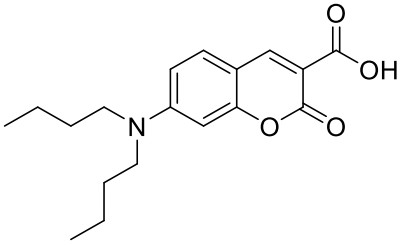	333±19

2e	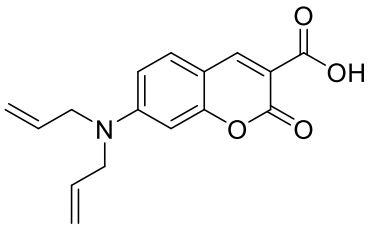	254±71
2f	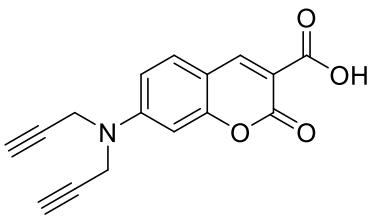	151±14
2g	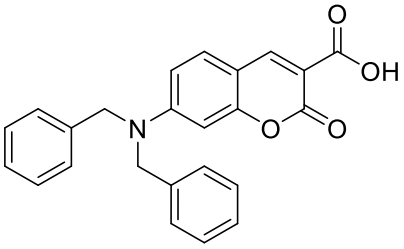	57±6
2h	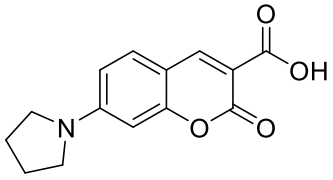	229±13
2i	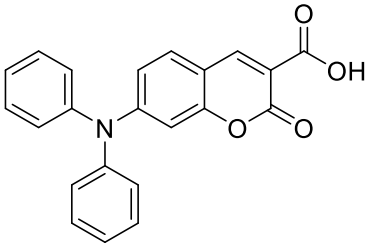	131±11

* average±sem of three independent experiments

MCT1 lactate uptake studies revealed that candidate compound **2g** exhibited the most potent inhibition - qualifying this derivative for further *in vitro* pharmacokinetic studies. To evaluate oral bioavailability of candidate compounds *in vitro*, Caco-2 permeability assays were employed. Caco-2 permeability assays for compounds **1a** and **2g** in both apical to basolateral (A-B, Table 5) and basolateral to apical (B-A, Table 6) were employed to illustrate oral bioavailability. Caco-2 is a human epithelial colorectal cancer cell line that simulates the human enterocytic intestinal layer. This cell line is widely used to estimate human intestinal permeability and drug efflux of candidate compounds to predict oral

bioavailability. Compound **1a** and **2g** had efflux ratios of 0.9 and 0.2, respectively, indicating that they are not substrates for efflux pumps, will absorbed through the intestine, and will be available for anticancer efficacy. Control compounds included highly permeable propranolol, moderately permeable labetalol, poorly permeable ranitidine, and colchicine, a P-glycoprotein substrate, were used for comparison.

Table 5: A-B Caco-2 permeability studies of compounds **1a** and **2g**:

A-B permeability (Caco-2, pH 6.5/7.4)							
Compound	Test Concentration	Permeability (10^{-6} cm/s)			Percent Recovery (%)		
		1st	2nd	Mean	1st	2nd	Mean
1a	1.0E-05 M	5.96	6.15	6.1	28	28	28
2g	1.0E-05 M	30.32	33.73	32	33	35	34
colchicine	1.0E-05 M	0.36	0.32	0.3	75	75	75
labetalol	1.0E-05 M	8.68	8.31	8.5	61	71	66
propranolol	1.0E-05 M	41.45	40.34	40.9	67	66	67

Table 6: B-A Caco-2 permeability studies of compounds **1a** and **2g**:

B-A permeability (Caco-2, pH 6.5/7.4)							
Compound	Test Concentration	Permeability (10^{-6} cm/s)			Percent Recovery (%)		
		1st	2nd	Mean	1st	2nd	Mean
3j	1.0E-05 M	5.28	5.78	5.5	31	29	30
4g	1.0E-05 M	6.32	6.54	6.4	53	58	55
colchicine	1.0E-05 M	15.25	15.39	15.3	81	82	81
labetalol	1.0E-05 M	34.59	38.49	36.5	72	73	72
propranolol	1.0E-05 M	38.02	44.94	41.5	80	80	80

ranitidine	1.0E-05 M	3.59	3.85	3.7	88	82	85

Encouraged by the *in vitro* bio-availability of candidate compounds **1a** and **2g**, we further investigated the metabolic stability of these compounds in human liver microsomes (Table 7). To illustrate high, medium and low metabolic stabilities, propranolol, imipramine, verapamil and terfenadine were used as respective controls. It was not surprising that compound **1a** exhibited very low metabolic stability in line with our previous *in vivo* pharmacokinetic results and metabolically vulnerable unsubstituted N,N-diphenyl system. Gratifyingly, compound **2g** exhibited enhanced metabolic stability, similar or greater than that of highly stable controls imipramine and propranolol (Table 7).

Table 7: Metabolic stability in human liver microsomes for compounds **1a** and **2g**:

Intrinsic clearance (liver microsomes, human)					
Compound	**Test Concentration**	**Half-Life (minute)**			**Clint**
		1st	**2nd**	**Mean**	
1a	1.0E-07 M	12.9	11.5	12	571.1
2g	1.0E-07 M	922.2	>60	>60	<115.5
imipramine	1.0E-07 M	213.9	194.4	>60	<115.5
propranolol	1.0E-07 M	334.4	373	>60	<115.5
terfenadine	1.0E-07 M	9.8	9.1	9	736.8
verapamil	1.0E-07 M	21.1	21.5	21	324.8

To further investigate the translational potential of the second generation carboxy coumarin compounds, we advanced the lead candidate **2g** to *in vivo* systemic toxicity studies in healthy mice (Figure 7). As anticipated and in line with toxicity profile of first generation MCT1 inhibitors, compound **2g** was well tolerated at high doses of 20mg/kg (i.p.) and 100mg/kg (oral gavage) over the course of a 14-day treatment period.

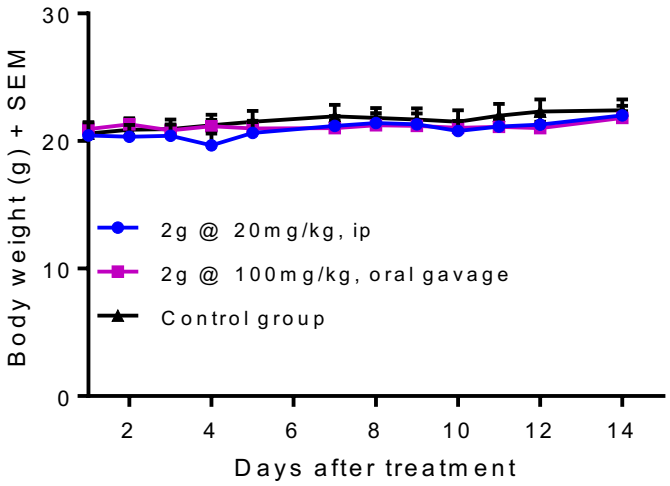

Figure 7. *In vivo* systemic toxicity study of lead carboxy coumarin derivative **2g**.

In conclusion, we have designed, synthesized, and evaluated novel carboxy coumarin derivatives that have retained MCT1 inhibition properties and enhanced metabolic stability. Metabolic stability and safety profile qualified candidate **2g** for further pre-clinical evaluation as potential anticancer agents.

Evaluation of first generation *p*-N,N-dialkyl/aryl-*o*-methoxy cyanocinnamic acid candidates for MCT4 inhibition:

Following the extensive SAR studies toward MCT1 inhibition via ^{14}C-lactate uptake in MCT1 expressing RBE4 cells, we sought to investigate the ability of candidate compounds on MCT4. Using a modified ^{14}C-lactate uptake experiment in MCT4 expressing triple negative breast cancer cell line MDA-MB-231, we found that our lead candidate compounds **1a** and **1b** exhibited potent MCT4 inhibition properties (**Table 8**).

Table 8: MCT4 IC_{50} (nM)* of *N,N*-dialkyl/diaryl *o*-methoxy CHC derivatives **1a** and **1b** in MDA-MB-231 cell line

Sl. No.	Compound	MCT4 IC_{50}
1a	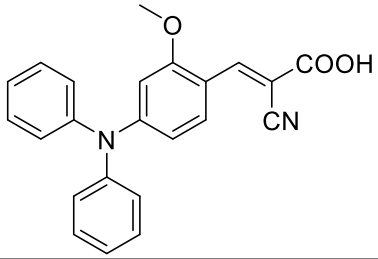	23±4

1b	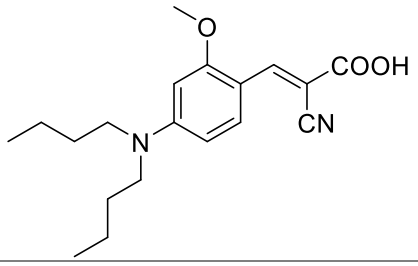	14±2

* average±sem of three independent experiments

We also screened the second generation carboxy coumarin derivatives for MCT4 inhibition, finding that none of the derivatives exhibited MCT4 inhibition properties below 1000nM other than the **2g** which modestly inhibited MCT4 at 200nM (data not shown). These results indicated that the carboxy coumarin derivatives were more selective toward MCT1. In fact, we carried out an *in vivo* efficacy study utilizing MCT4 expressing MDA-MB-231 and found that there was no tumor growth inhibition, indicating that these compounds are not active in MCT4 expressing tumors (data not shown).

In line with our hypothesis and to expand on our understanding of the effects of candidate compounds on cellular metabolism, we carried out Seahorse XFe96 based glycolysis and mitochondrial stress tests. As a control, we employed both parent compound CHC along with known MCT1 inhibitor AZD3965 (AZD). AZD exhibits no inhibition properties on MCT4 mediated lactate transport, and is structurally distinct from our cyanocinnamic acid and carboxy coumarin based inhibitors (Figure 8).

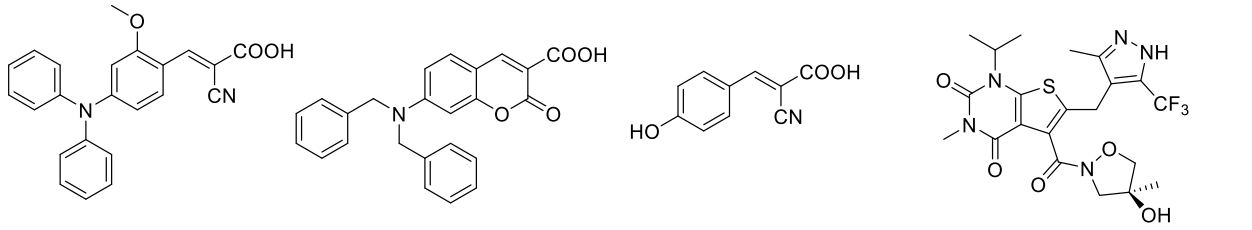

1a	**2g**	**CHC**	**AZD3965 (AZD)**
MCT1 IC_{50} = 6 nM	MCT1 IC_{50} = 57 nM	MCT1 IC_{50} = >100 μM	MCT1 IC_{50} = 5-10 nM
MCT4 IC_{50} = 23 nM	MCT4 IC_{50} = ~200 nM	MCT4 IC_{50} = >100 μM	MCT4 IC_{50} = no activity

Figure 8. Compounds used for metabolic assays.

The cell lines utilized in these studies included MDA-MB-231 (MCT1-, MCT4+) and WiDr (MCT1+, MCT4-). Differential MCT1 and 4 expressions in these two cell lines allow for interpretation of dual MCT1/4 and MCT1 inhibition and their effects on both glycolysis and mitochondrial respiration. We first evaluated the effects of candidate compounds on glycolysis, glycolytic capacity, and glycolytic reserve in both cell lines (Figure 8). It was found that compounds **1a** and **2g** inhibited all glycolytic parameters in MCT4 expressing cell line MDA-MB-231, whereas AZD only inhibited glycolysis in MCT1 expressing WiDr cell line, with no appreciable effects in MDA-MB-231. These results indicate that effects on glycolysis are dependent on MCT expression and isoform selectivity (Figure 8).

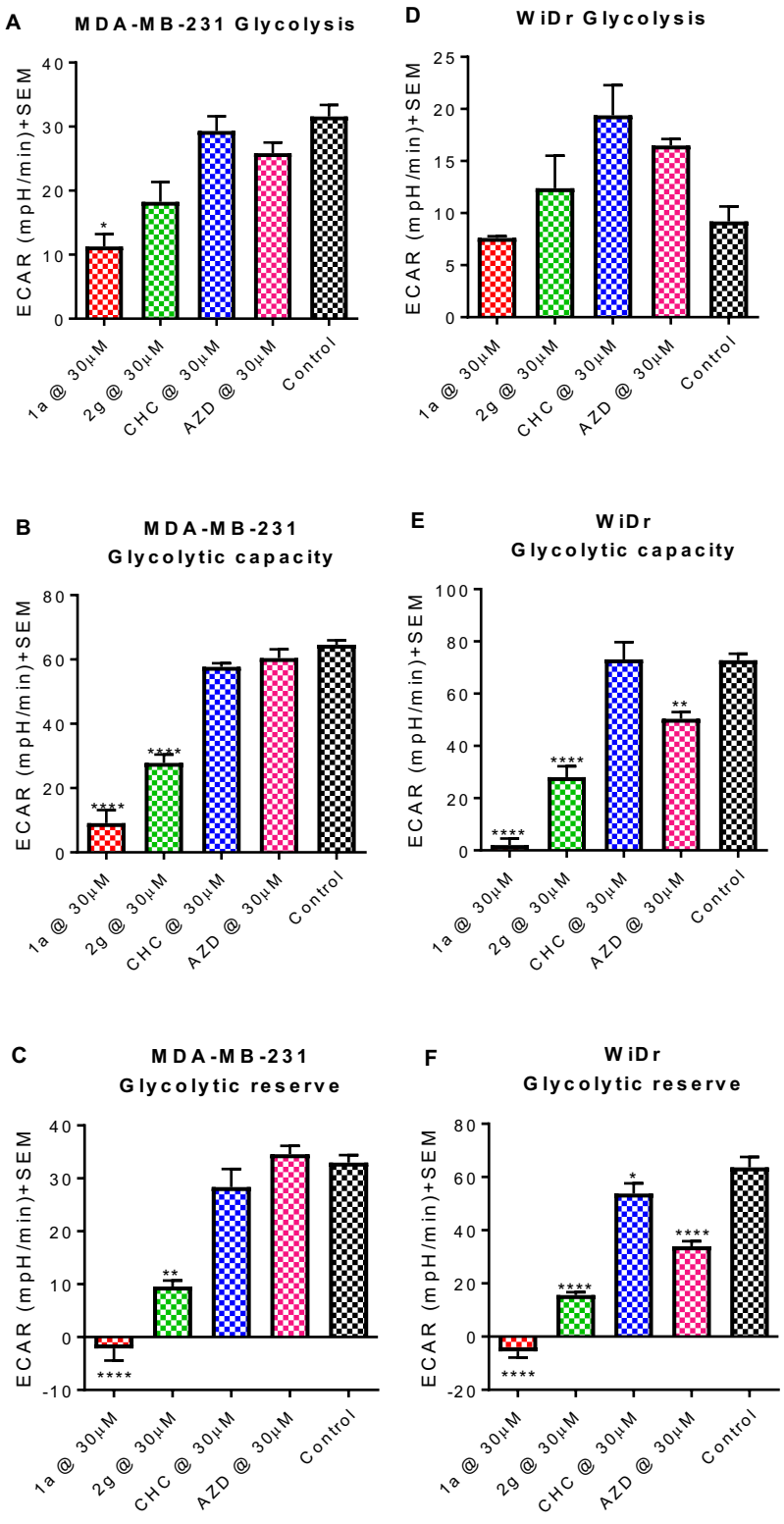
A
MDA-MB-231 Glycolysis
ECAR (mpH/min)+SEM
1a @ 30μM
2g @ 30μM
CHC @ 30μM
AZD @ 30μM
Control
D
WiDr Glycolysis
B
MDA-MB-231
Glycolytic capacity
E
WiDr
Glycolytic capacity
C
MDA-MB-231
Glycolytic reserve
F
WiDr
Glycolytic reserve

Figure 8. Effects of compound treatment (**A, D**) glycolysis, (**B,E**) glycolytic capacity, and (**C,F**) glycolytic reserve in (**A-C**) MCT4 expressing MDA-MB-231 and (**D-F**) MCT1 expressing WiDr cell lines.

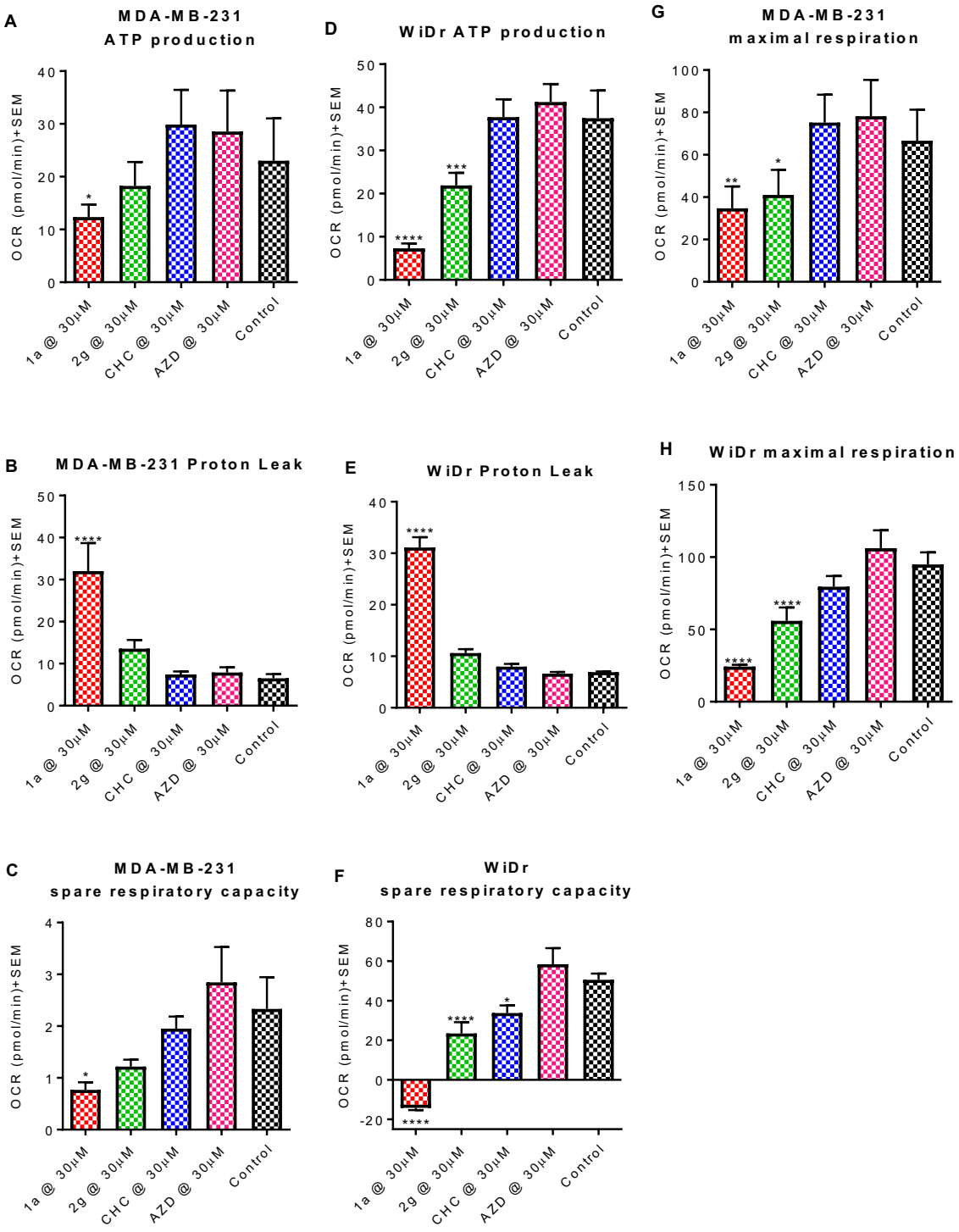

Figure 9. Effects of compound treatment on mitochondrial respiratory parameters (**A, D**) ATP production, (**B, E**) proton leak, (**C, F**) spare respiratory capacity and (**G, H**) maximal

respiration in (**A-C, G**) MCT4 expressing MDA-MB-231 and (**D-F, H**) MCT1 expressing WiDr cell lines.

Next, due to the potential effects of inhibition of MCT1/4 on mitochondrial respiration, we carried out extensive analysis on mitochondrial stress using widely employed mitochondrial stress tests. Interestingly, candidate compound **1a** strongly inhibited all tested parameters of mitochondrial respiration in both MCT1 and MCT4 expressing cell lines (Figure 9A-H). In contrast, MCT1 inhibitor AZD did not exhibit appreciable effects on mitochondrial parameters, except modest inhibition of spare respiratory capacity in MCT1 expressing WiDr (Figure 9F).

Intrigued by the substantial effects of compound **1a** on mitochondrial respiration in both MDA-MB-231 and WiDr cell lines, we sought to investigate the cellular localization of **1a** using epifluorescent microscopy. Gratifyingly, **1a** exhibits fluorescent characteristics when exposed to GFP wavelengths and hence, co-localization of **1a** with mitochondrial fluorescent probe MitotrackerRed CMXROS enabled interpretation of mitochondrial targeting. These experiments revealed that **1a** was readily internalized in both MDA-MB-231 and WiDr cells and was concentrated in regions near mitochondria (Figure 10).

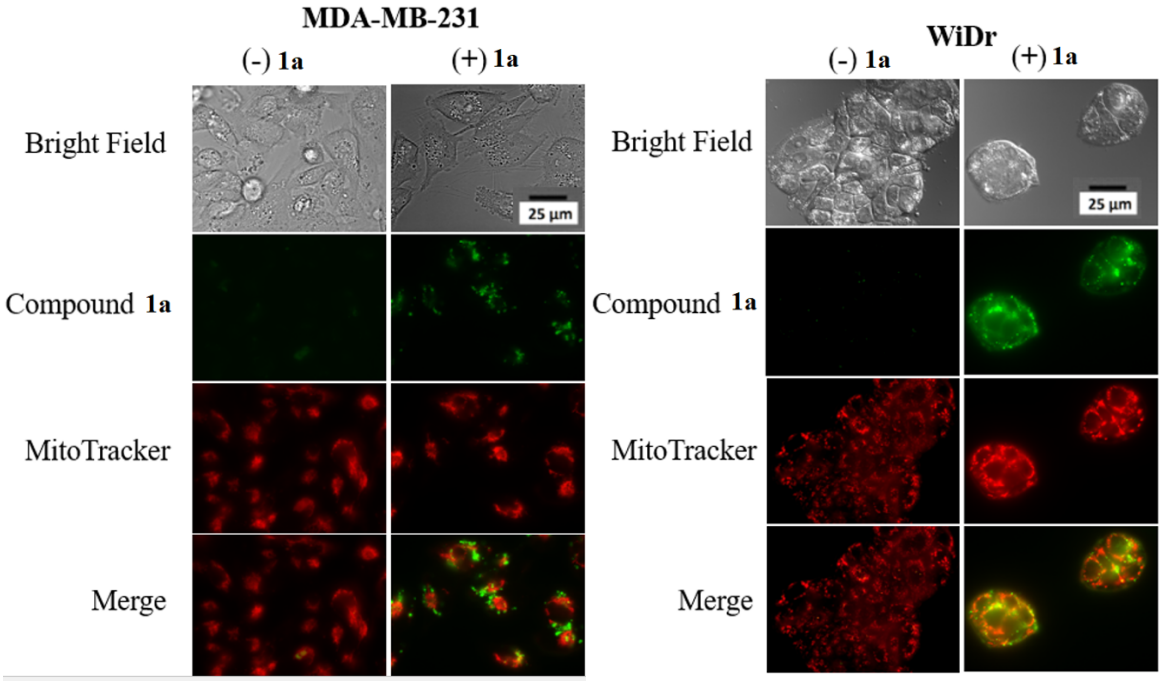

Figure 10. Epifluorescent microscopy of candidate **1a** and Mitotracker red in MDA-MB-231 and WiDr cells. All images were captured at the same magnification (see scale bar).

With new found knowledge that candidate compound **1a** exhibits MCT4 inhibition, we sought to further investigate the translational potential of **1a** *in vivo* in an MDA-MB-231 xenograft model (Figure 11). Gratifyingly, **1a** exhibited significant tumor growth inhibition

properties in a dose dependent fashion (Figure 11 A-D). Further, compound **1a** at 70mg/kg exhibited similar tumor growth inhibition properties similar to that of doxorubicin, and exhibited synergy when given in combination (Figure 11C & D).

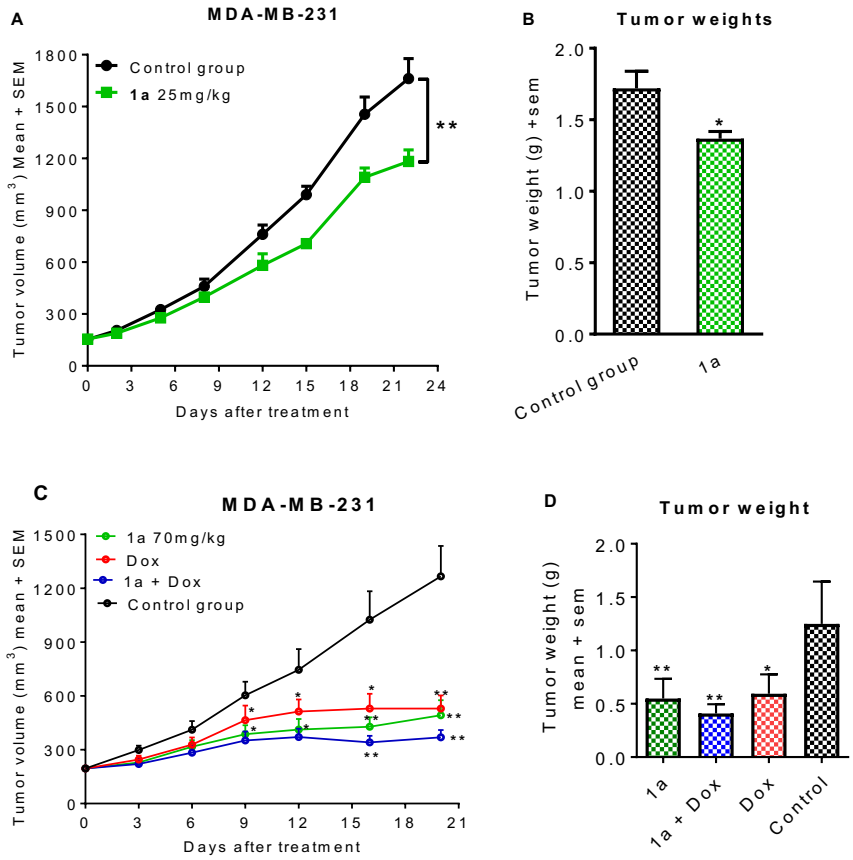

Figure 11. *In vivo* efficacy study of candidate **1a** in an MDA-MB-231 flank xenograft model at increasing doses of (A,B) 25mg/kg and (C,D) 70mg/kg. Doxorubicin was given at 1mg/kg once daily, five days a week over the course of the study.

In conclusion, we further characterized the MCT inhibition properties of our lead candidate inhibitors and have found that they also exhibit potent inhibition of MCT4. Further, *in vitro* treatment with lead **1a** potently inhibited numerous characteristics of glycolysis and mitochondrial respiratory processes. Epifluorescent studies revealed that candidate **1a** was internalized and localized to regions near mitochondria. Finally, candidate **1a** led to significant tumor growth inhibition properties in an MCT4 expressing triple negative breast cancer tumor model MDA-MB-231.

To further investigate the reverse Warburg hypothesis wherein fibroblasts play a role in the metabolic symbiosis of cancer cells, we carried out co-culture studies using MCT4 expressing epithelial cancer cell line MDA-MB-231 and mouse fibroblasts 3T3-MEF. Acute loss of stromal caveolin-1 leads to oxidative stress, mitochondrial dysfunction and aerobic glycolysis in cancer related fibroblasts – driving proliferation. Hence, we included Cav-1 WT and KO cell lines for co-culture studies to evaluate this phenomenon. In this

regard, we first evaluated the seeding density for optimal growth curves of the 3T3-MEFs in culture, and in co-culture with MDA-MB-231 (Figure 11.1).

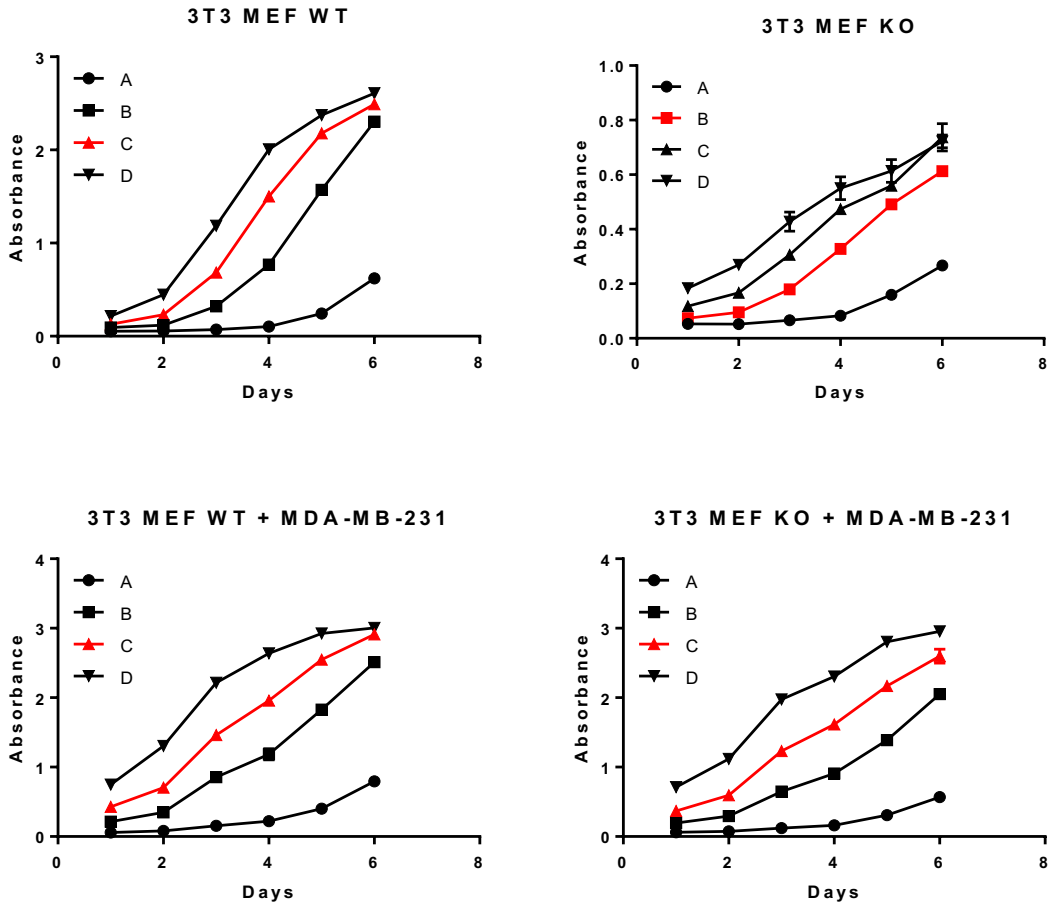

Figure 11.1. Optimal seeding concentration of 3T3 MEFs cells. Growth curve of 3T3 MEF WT cells: A) $5x10^4$ cells/mL, B) $2x10^4$ cells/mL, C) $1x10^4$ cells/mL and D) $0.5x10^4$ cells/mL (cells in 400µL of growth media); (ii) Growth curve of 3T3 MEF KO cells: A) $1x10^4$ cells/mL, B) $0.5x10^4$ cells/mL, C) $0.25x10^4$ cells/mL and D) $0.1x10^4$ cells/mL (cells in 400µL of growth media).

Next, we evaluated the *in vitro* cell proliferation inhibition properties of compound **1a** under co-culture conditions in normoxic (Table 8.1) and hypoxic (Table 8.2) conditions. These studies revealed that the inhibition properties of **1a** were consistent with the results obtained in MDA-MB-231 as a monoculture, and the presence of fibroblasts – nor oxygen gradients- dictated the antiproliferative effects of 1a.

Table 8.1: MTT assay IC_{50}^{*} values of compounds **1a** in MDA-MB-231, and co-cultures with 3T3 MEF WT and 3T3 MEF KO under normoxic conditions

Compound	MDA-MB-231	MDA-MB-231 + 3T3 MEF WT	MDA-MB-231 + 3T3 MEF KO
1a	0.08±0.01	0.08±0.01	0.06±0.01

* IC_{50} values reported in mM, average ± SEM of minimum three separate experimental values

Table 5c: MTT assay IC_{50}^{*} values of compounds **1a** in MDA-MB-231, and co-cultures with 3T3 MEF WT and 3T3 MEF KO under hypoxic conditions

Compound	MDA-MB-231	MDA-MB-231 + 3T3 MEF WT	MDA-MB-231 + 3T3 MEF KO
1a	0.09±0.00	0.13±0.00	0.14±0.00

*IC_{50} values reported in mM, average ± SEM of minimum three separate experimental values

To investigate the ability of candidate compounds to inhibit co-culture tumor growth *in vivo*, we carried out two – *in vivo* tumor growth inhibition studies in both Cav-1 WT and KO 3T3-MEF co-cultured with MDA-MB-231 cells. These studies indicated that candidate **1a** exhibited enhanced tumor growth inhibition properties in co-injected MDA-MB-231 + 3T3-MEF Cav1 KO cell lines when compared to co-injected MDA-MB-231 + 3T3-MEF Cav1 WT (Figures 11.2 and 11.3). Interestingly, it was observed that MDA-MB-231 tumors co-injected with 3T3 – MEF Cav1 KO cells had substantially increased tumor volume at the end of the treatment period, substantiating the role of the reverse Warburg effect and Cav-1 expression levels in cancer associated stromal fibroblasts (Figure 11.4).

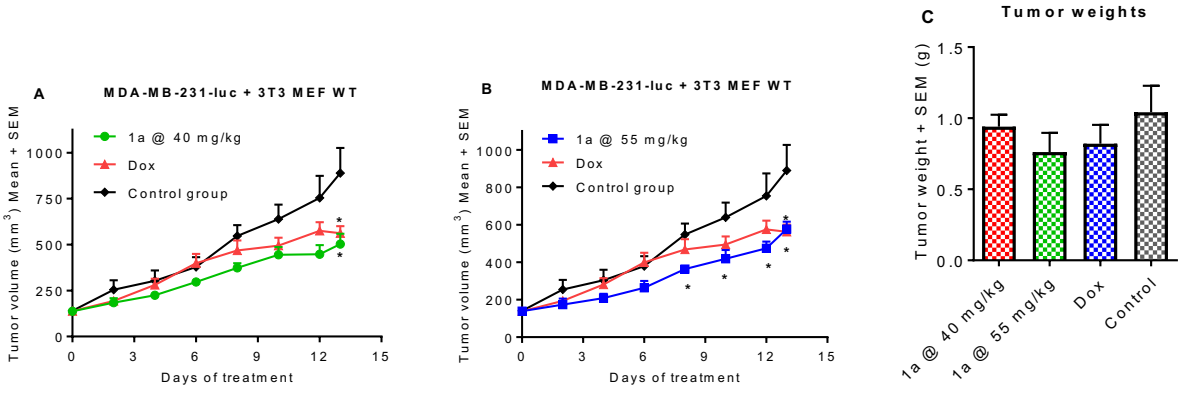

Figure 11.2. In vivo efficacy of candidate compound **1a** at (**A**) 40mg/kg and (**B**) 55mg/kg in MDA-MB-231 – 3T3-MEF Cav1 WT co-injected xenograft model. (**C**) Resected tumor mass at the end of the study.

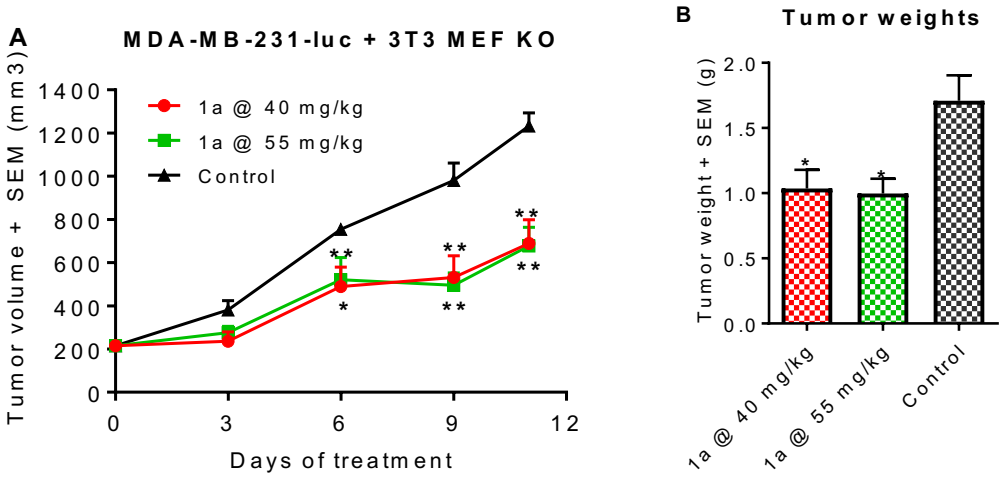

Figure 11.3. *In vivo* efficacy of candidate compound **1a** in MDA-MB-231 – 3T3-MEF Cav1 KO co-injected xenograft model with observed tumor (**A**) volumes. (**B**) Resected tumor mass at the end of the study.

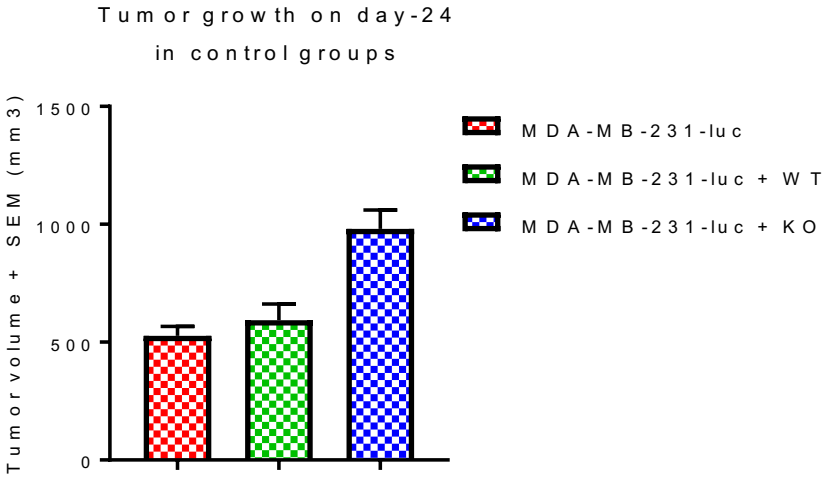

Figure 11.4. Comparative tumor volumes of MDA-MB-231 cells co cultured with either Cav1 WT or KO 3T3-MEFs indicate enhanced tumor growth with Cav1 KO.

These first generation candidate compounds, although potent, are burdened with low metabolic stability, and tumor growth inhibition properties *in vivo* required very high doses. Further, these candidate compounds do not exhibit substantial cancer cell cytotoxicity, which may limit the translational potential. Hence, we designed several new generation compounds with the goal of improving pharmaceutical and cancer cell proliferation inhibition properties while retaining pharmacological potency.

Synthesis and evaluation of novel silylated CHC derivatives as anticancer agents

To address the metabolic and anticancer shortcomings of the first generation MCT1 inhibitors, we sought to design novel CHC derivatives based on a structurally and metabolically stable silyl-ether template. Silyl ethers are widely used in organic synthesis as alcohol protecting groups, but have largely been underutilized in pharmacological and therapeutic agents. Recently, silicon has been used as a bioisostere for carbon in numerous medicinal applications to improve metabolic stability – as silicon is not a metabolic substrate for enzymatic processing and elimination. Further, silicon is highly lipophilic, and synthetic silyl ether derivatives of drug templates have the potential to increase cell permeability and cancer cell cytotoxicity. Hence, we envisioned that CHC based silyl ethers would have increased metabolic stability and improved cytotoxicity while retaining pharmacological inhibition of MCTs. In this regard we generated a library of first generation silylated CHC compounds (Figure 12).

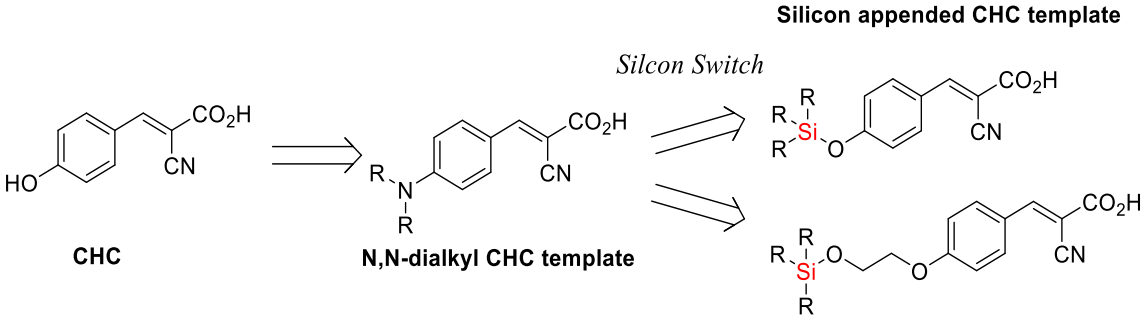

Figure 12. Design of silicon appended CHC derivitives as MCT inhibitors.

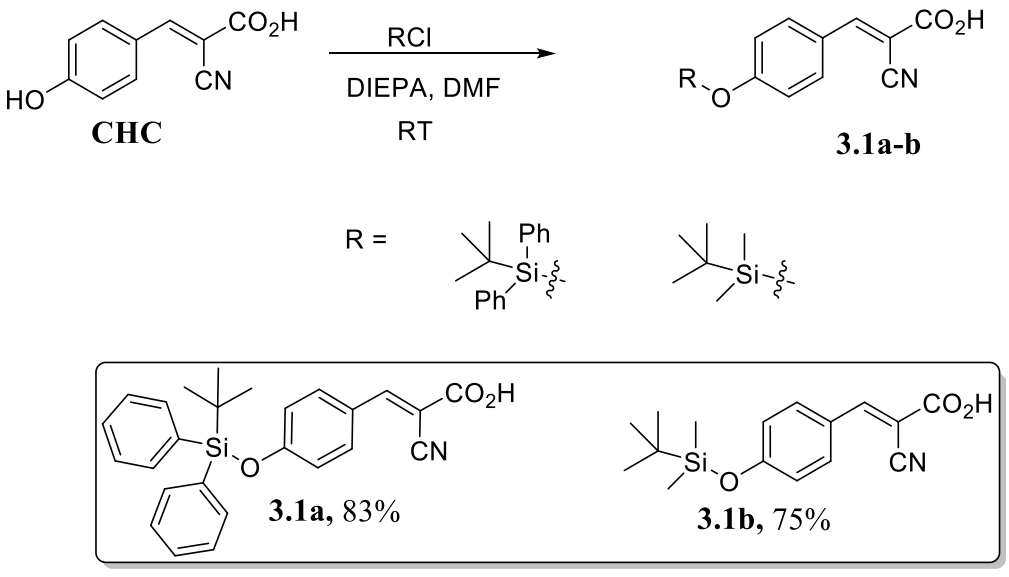

Scheme 7. Synthesis of candidate silyl CHC derivatives **3.1a** and **3.1b**.

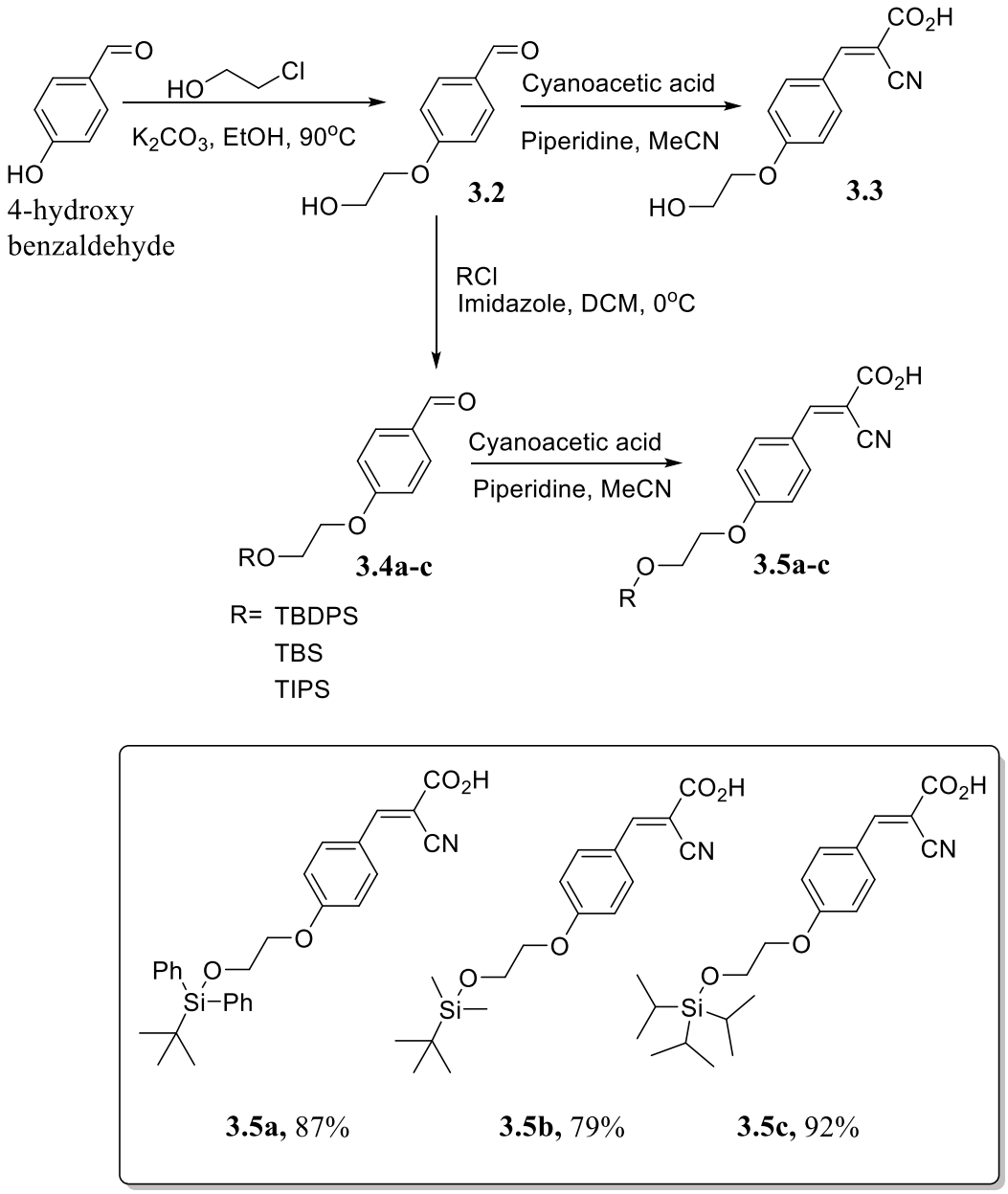

Scheme 8. Synthesis of candidate silyl ether CHC derivatives **3.5a**, **3.5b**, and **3.5c**.

To evaluate the anticancer potential of candidate silylated CHC derivatives, *in vitro* cell proliferation inhibition properties of candidate compounds were carried out in various solid tumor cell lines. Cell lines included TNBC cell line MDA-MB-231, stage IV breast cancer cell line 4T1, and MCT1 expressing cancer cell line WiDr (Table 9). The directly attached silylated CHC derivative **3.1a** with the t-butyl silyl diphenyl (TBDPS) exhibited substantially enhanced cell proliferation inhibition properties when compared to the t-butyl dimethyl (TBS) derivative **3.1b**. Further, extended silyl-CHC derivatives **3.5a** and tri-isopropyl silyl (TIPS) **3.5c** exhibited similar potency against the cell lines tested, with **3.5b** exhibiting slightly lower potency (Table 9). It is interesting to note that non-silylated analog

3.3, along with parent compound **CHC** exhibit several fold decreased potency, illustrating the importance of the silyl ether in providing biological activity (Table 9).

Table 9. Cell proliferation inhibition IC_{50}*(μM) properties of compounds **3.1a-b**, **3.5a-c**, and **3.3**.

	MDA-MB-231	**4T1**	**WiDr**
3.1a	93±0	56±1	41±2
3.1b	>500	>500	>500
3.5a	71±1	22±1	6 ± 1
3.5b	>500	82 ± 1	123±4
3.5c	134±5	41 ± 6	5 ± 1
3.3	>500	>500	>500
CHC	5300±130	3600±300	1100±96

***** Values represent the average IC_{50} ± SEM (μM) of at least three independent experiments.

The TBS silyl ether exhibits significantly less chemical stability and thus, may be cleaved *in vitro* resulting in decreased relative cell proliferation inhibition properties when compared the TBDPS and TIPS analogs. These results indicate that candidate silyl CHC derivatives did not result in enhanced cell proliferation inhibition properties when compared to first generation N,N-dialkyl CHC analogs, but still hold the potential to exhibit enhanced metabolic stability, qualifying them for further pre-clinical investigation as anticancer agents.

To validate that candidate silyl CHC derivatives retain MCT1 inhibitory properties, ^{14}C-lactate uptake studies were again employed. For this purpose, we selected structurally diverse silyl ethers from both directly attached and extended series **3.1a**-**b** and **3.5a**-**b** respectively. These studies indicated that candidate compounds retained MCT1 inhibition properties (Table 10).

Table 10. MCT1 IC_{50} values of compounds **3.1a-b** and **3.5a-b**.

Compound	**MCT1 IC_{50} (μM)**
3.1a	0.408±0.005
3.1b	0.095±0.007
3.5a	0.097±0.007
3.5b	0.010±0.0003

*Values represent the average IC_{50} ± SEM (**μM**) of at least three independent experiments.

As the candidate compounds are based on the CHC template and have retained MCT1 inhibitory characteristics, we sought to investigate the effects of candidate compounds on metabolic pathways in MCT1 expressing cancer cell line WiDr and MCT4 expressing TNBC cell line MDA-MB-231. In this regard, SeahorseXFe96 based glycolysis and mitochondrial stress tests were employed on candidates **3.1a-b** and **3.5a-c** in a similar fashion as the first generation MCT inhibitors. These experiments revealed that candidate compounds led to significant effects on both glycolytic and mitochondrial respiratory processes (Figure 12 & 13). Again, non-silylated analog **3.3** did not affect either glycolysis or mitochondrial metabolism at the concentrations tested.

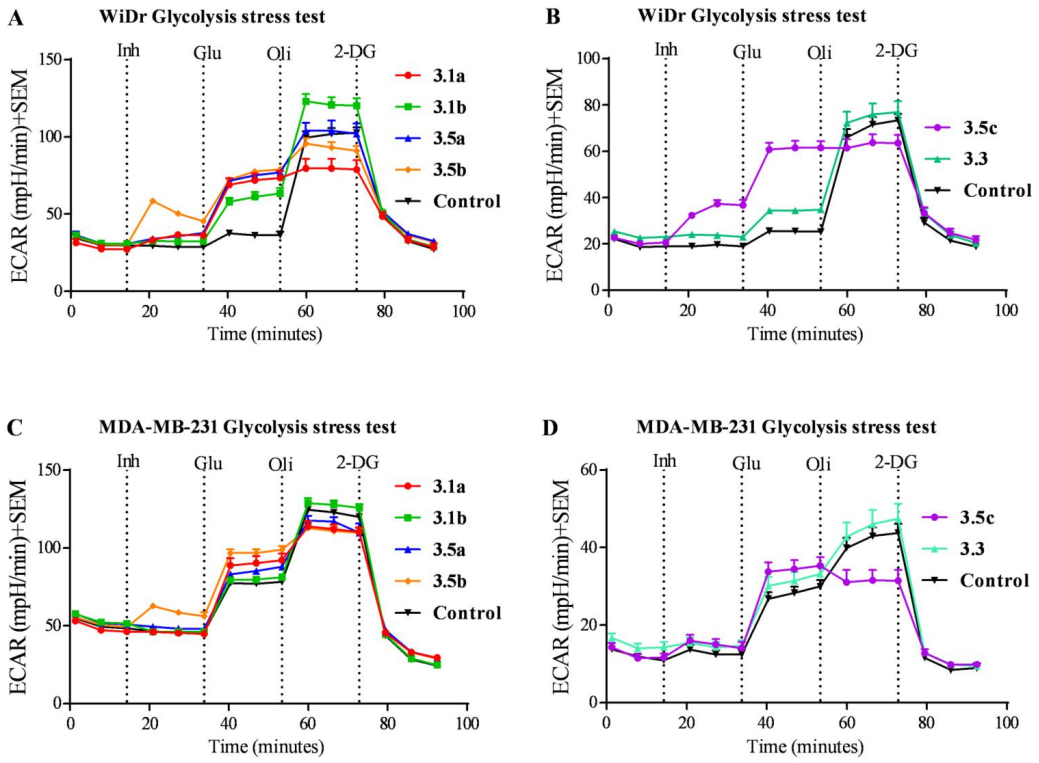

Figure 12. Glycolytic stress test evaluating candidate compounds **3.1a-b** and **3.5a-c** in (**A-B**) WiDr and (**C-D**) MDA-MB-231 cell lines revealed perturbations in glycolytic metabolism.

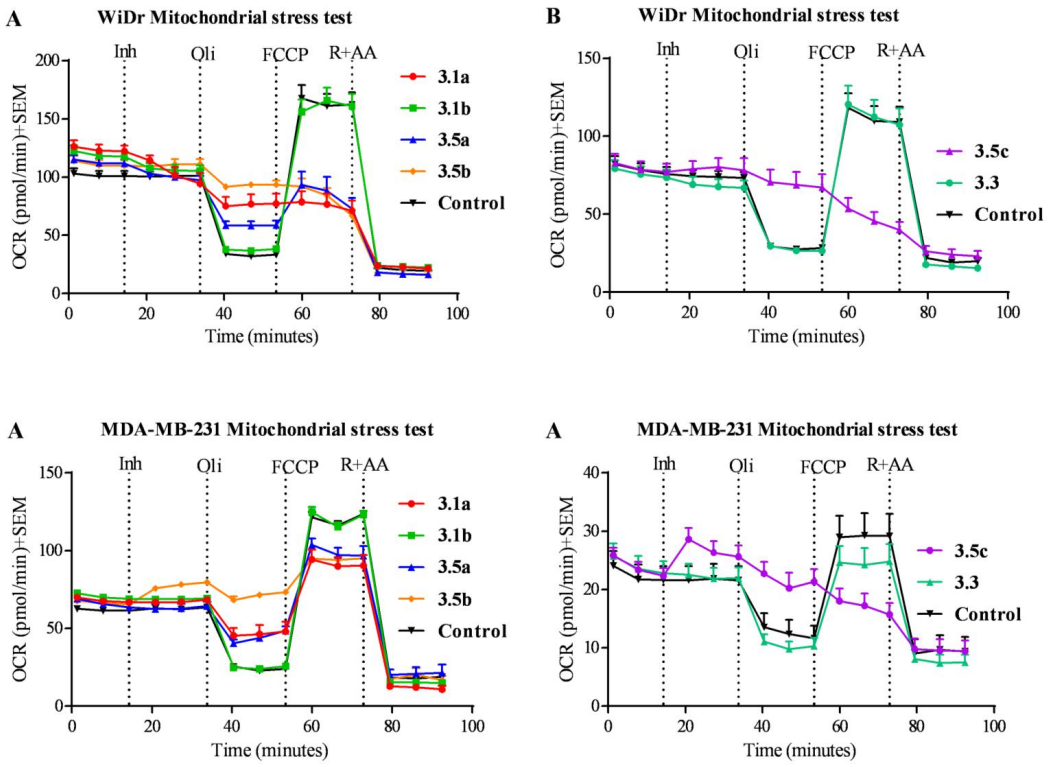

Figure 13. Mitochondrial stress test evaluating candidate compounds **3.1a-b** and **3.5a-c** in (**A-B**) WiDr and (**C-D**) MDA-MB-231 cell lines revealed perturbations in mitochondrial metabolism.

Due to the enhanced lipophilic characteristics of candidate silyl CHC derivatives, we envisioned that these compounds exhibit enhanced membrane permeable characteristics and lead to mitochondrial dysfunction – as illustrated in mitochondrial stress tests (Figure 13). In this regard, we sought to investigate the effects of candidate **3.1a** and **3.5a** on mitochondrial morphology using epifluorescent microscopy techniques with mitochondrial labeling agent MitotrackerRed CMXROS (MTR). These experiments revealed that **3.1a** and **3.5a** led to substantial redistribution of MTR indicative of treatment-induced mitochondrial dysfunction (Figure 14).

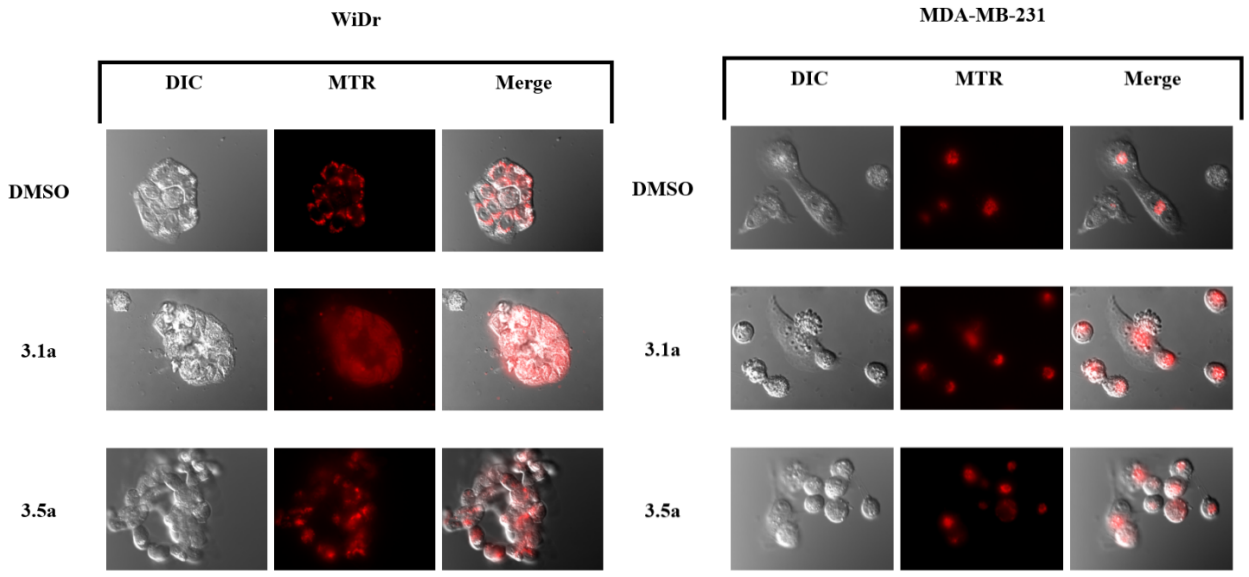

Figure 14. Epifluorescent microscopic evaluation of candidate 3.1a and 3.5a in WiDr and MDA-MB-231 cell lines using MTR.

To further investigate the cellular mechanisms of silyl ethers in inducing cancer cell death, western blotting methods were employed to examine important molecular players in cell death processes. These studies indicated that candidate **3.1a** induced DNA damage and apoptotic cell death processes as evidenced by phosphorylation of histone 2AX (H2AX) and caspase mediated PARP1 cleavage in both WiDr and MDA-MB-231 cell lines (Figure 15). It was interesting to note that mutant p53 expression was increased in a **3.1a** dose dependent fashion. In combination with PARP1 cleavage and H2AX phosphorylation, results with p53 may indicate a regained pro-apoptotic function of mut p53 in MDA-MB-231 cells (Figure 15).

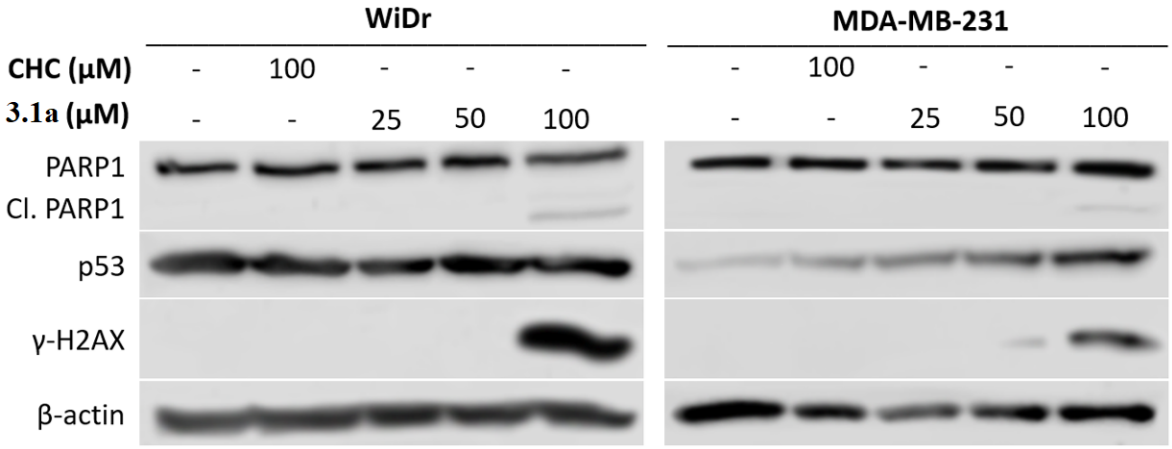

Figure 15. Western blot analysis of DNA damage and apoptotic response of WiDr and MDA-MB-231 cells as evidenced by PARP1, H2AX, and p53.

Intrigued by substantial DNA damage induced by **3.1a**, we sought to investigate the mechanism. Since these compounds were not expected to directly cause DNA damage,

we envisioned that the DNA damage observed in treated cultures was a result of mitochondrial dysfunction and increased reactive oxygen species. In this regard, we treated WiDr and MDA-MB-231 cells with **3.1a** in the presence and absence of reactive oxygen sequestering agent N-acetyl cysteine (NAC). These experiments revealed that co-treatment of **3.1a** treated cells with NAC reversed H2AX phosphorylation and hence, DNA damage (Figure 16). As an extension, we investigated the ability of NAC to reverse PARP1 cleavage and found that **3.1a** treated cultures still exhibited PARP1 cleavage in the presence of NAC, indicating cell death pathways are independent of ROS in **3.1a** treated cells (Figure 16).

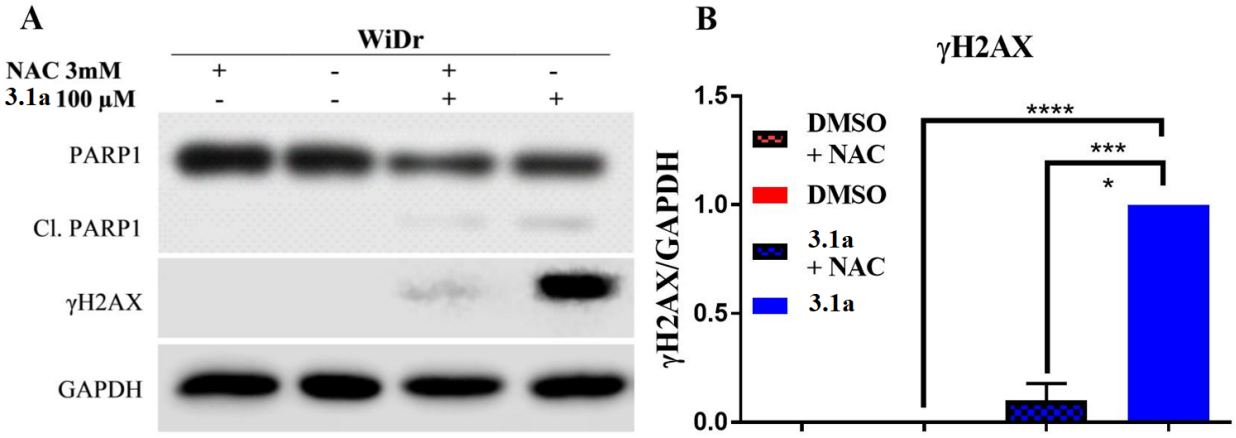

Figure 16. Western blot evaluation of ability of NAC to reverse **3.1a** induced DNA damage in WiDr cells.

To further understand the translational potential of candidate compounds, we investigated the *in vivo* systemic toxicity of lead candidates **3.1a** and **3.5a** in healthy CD-1 mice. These studies revealed that treated mice gained healthy weight when compared to untreated mice over a 14-day treatment period (Figure 17A-B).

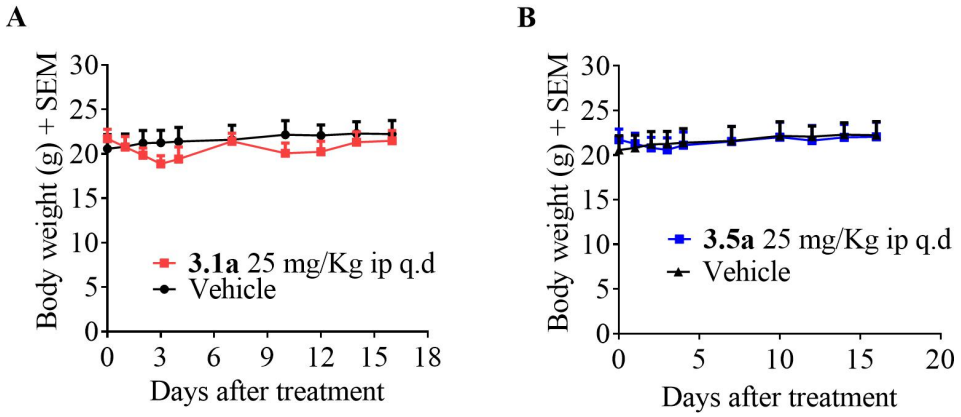

Figure 17. Systemic toxicity study of candidate (A) **3.1a** and (B) **3.5a** in healthy CD-1 mice.

Intrigued by the utilization of silicon, we further expanded our library by synthesizing *p*-N,N-dialkyl/aryl-*o*-alkoxy silyl ether CHC compounds as analogs of our first generation compounds (Figure 18, Scheme 9).

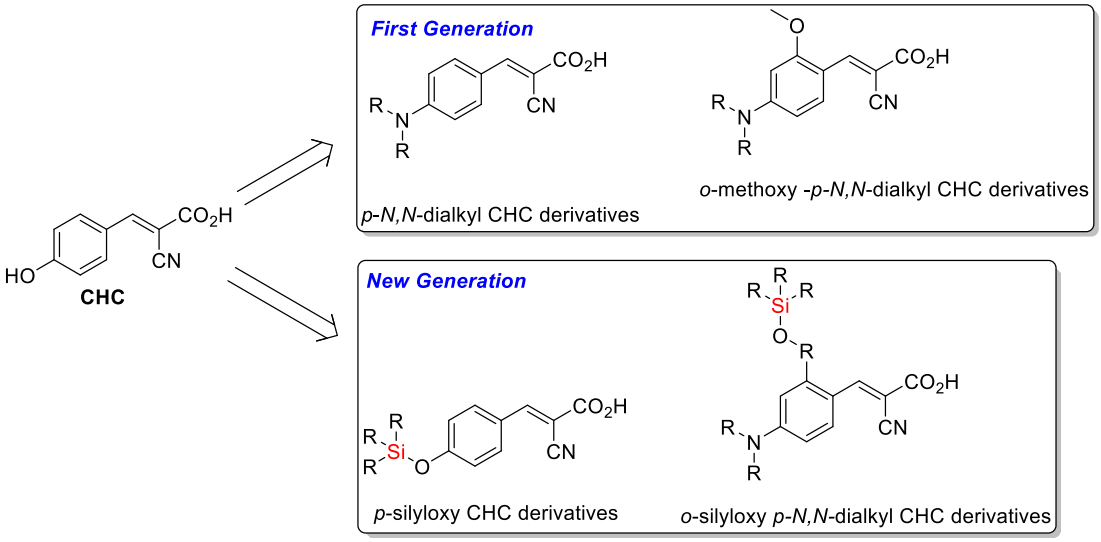

Figure 18. Design aspects and structural comparison of new generation silylated CHC derivatives.

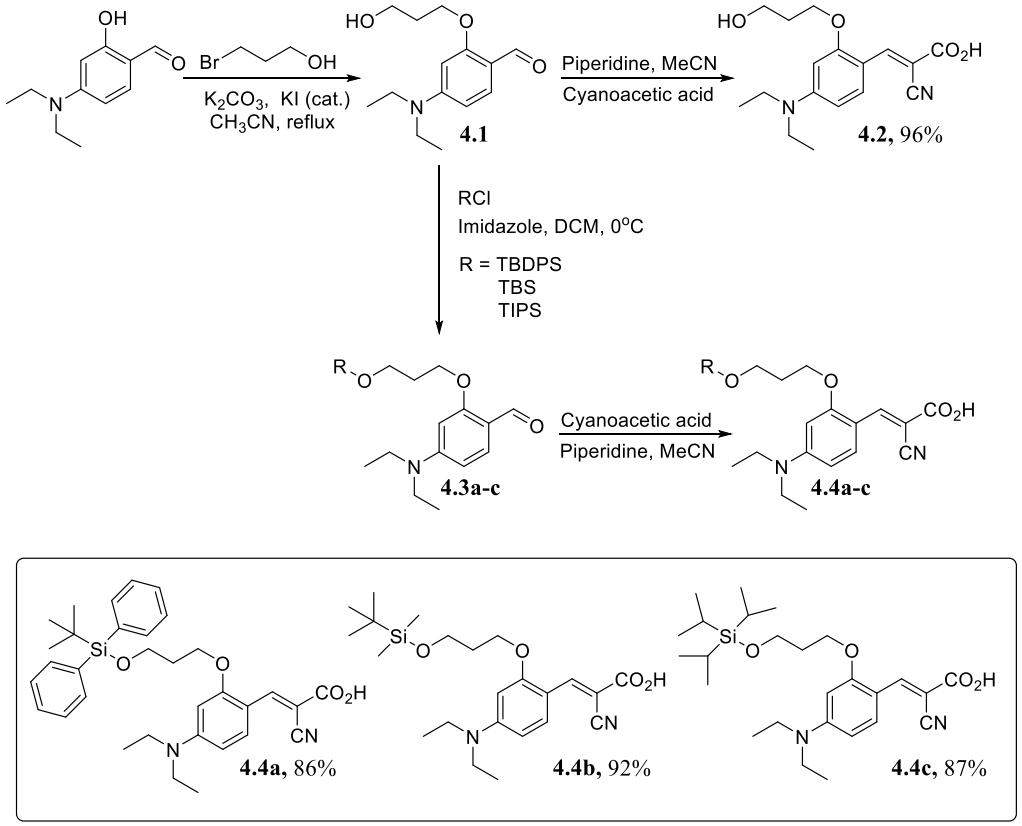

Scheme 9. Synthesis of *p*-N,N-dialkyl/aryl-*o*-alkoxy silyl ether CHC compounds **4.4a-c**.

To investigate the potential of new generation *p*-N,N-dialkyl/aryl-*o*-alkoxy silyl ether CHC candidates as anticancer agents, we first evaluated the *in vitro* anti-proliferative properties of **4.4a-c**, revealing that these compounds exhibit enhanced cell proliferation inhibition properties when compared to *p*-silyloxy CHC derivatives **3.1a-b** and **3.5a-c** (Table 11). As illustrated previously, non-silylated derivative **4.2** did not exhibit cell proliferation inhibition properties below 1,000μM concentration, again illustrating the importance of the silyl ether in providing biological activty (Table 11).

Table 11. Cell proliferation inhibition (IC_{50})* properties of compounds **4.2** and **4.4a-c** against MDA-MB-231, 4T1, and WiDr.

	MDA-MB-231	**4T1**	**WiDr**
4.4a	26 ± 6.1	13 ± 0.75	21 ± 1.7
4.4b	128 ± 10	16 ± 1.4	15 ± 0.69
4.4c	15 ± 0.02	5.7 ± 0.83	13 ± 0.59
4.2	>1000	>1000	>1000

***** Values represent the average IC_{50} ± SEM (μM) of at least three independent experiments.

We next evaluated the ability of **4.2** and **4.4a-c** to influence glycolysis and mitochondrial respiration using SeahorseXFe96 based stress tests in a similar fashion as previously described. These studies revealed that candidate compounds **4.4a-c** led to substantial increases in glycolysis and decreases in mitochondrial respiration in both MCT1 expressing WiDr and MCT4 expressing MDA-MB-231 cell lines (Figures 19-20). These results indicate that the compound induced mitochondrial dysfunction is substantial and specific enough to result in cellular compensatory glycolysis to account for drastic decreases in mitochondrial respiration. This may be due to greater lipophillic characteristics of **4.4a-c** over o-silyloxy CHC derivatives **3.1a-b** and **3.5a-c**. Non-silyated **4.2** did not exhibit effects on either glycolysis or mitochondrial respiration – further substantiating the requirement of lipophoilic silyl ether template in providing biological activity (Figures 19-20).

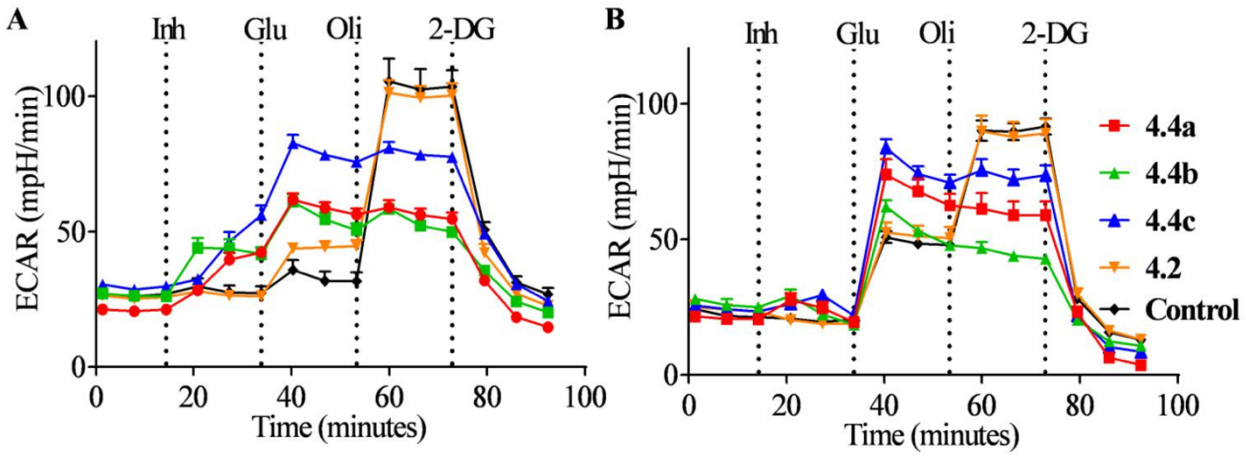

Figure 19. Mitochondrial stress test of candidates **4.2** and **4.4a-c** in (A) WiDr and (B) MDA-MB-231 cell lines.

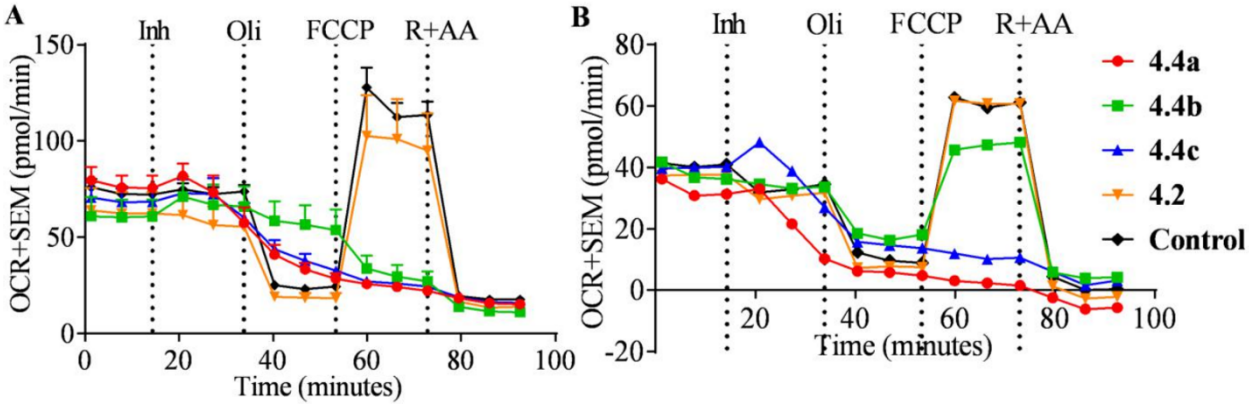

Figure 20. Mitochondrial stress test of candidates **4.2** and **4.4a-c** in (**A**) WiDr and (**B**) MDA-MB-231 cell lines.

Enhanced cell proliferation inhibition properties, along with comparatively enhanced effects on mitochondrial respiratory processses in cancer cells have qualified the *p*-N,N-dialkyl/aryl-*o*-alkoxy silyl ether CHC candidates **4.4a-c** for further preclinical investigation. In particular, we plan to investigate the *in vitro* and *in vivo* pharmacokinetic properties of these compounds to evaluate the predicted increased oral bioavailability, along with increased metabolic stability to finally advance these agents for *in vivo* efficacy studies in pre-clinical mouse models of breast cancer.

Synthesis and evaluation of hybrid nitric oxide (NO)-donor containing *p*-N,N-dialkyl CHC MCT1/4 inhibitors as potential anticancer agents

To further diversify our library of MCT1/4 inhibitors, we explored the utility of synthetically hybridizing NO-donor furoxan to our first generation *p*-N,N-dialkyl CHC derivatives (Figure 21, Scheme 10-12). Furoxan is a chemically stable NO-donor that reacts intracellularly with glutathione and glutathione-s-transferase resulting in release of NO. High intracellular levels of NO have been shown to result in cancer cell toxicity and hence, we designed this series of MCT inhibitors to have enhanced cancer cell proliferation inhibition properties over the first generation *p*-N,N-dialkyl CHC derivatives.

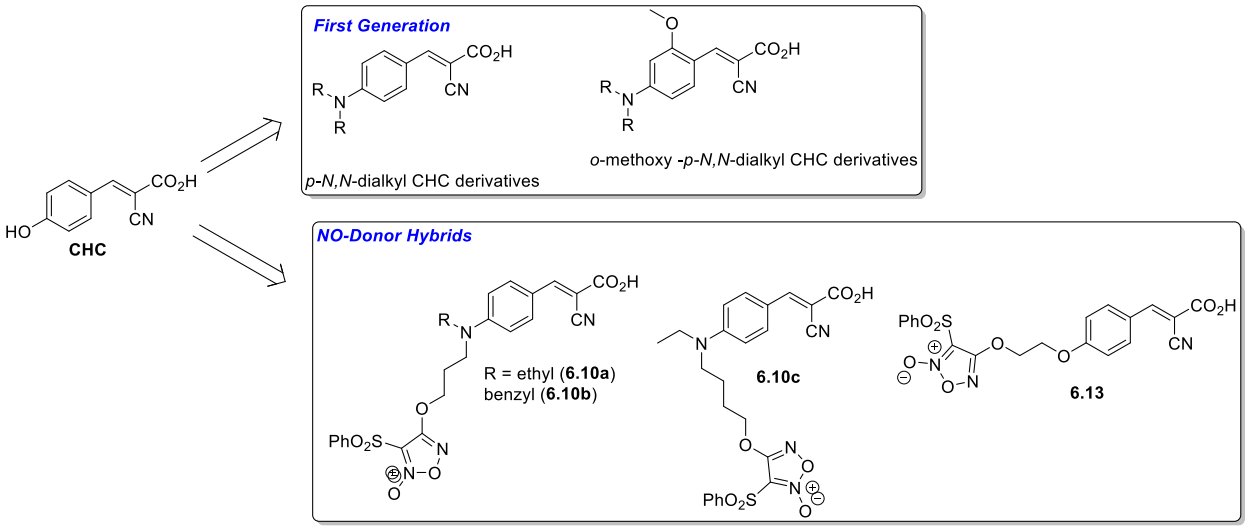

Figure 21. Design of new generation NO-donor hybrids of first generation *p*-N,N-dialkyl CHC derivatives.

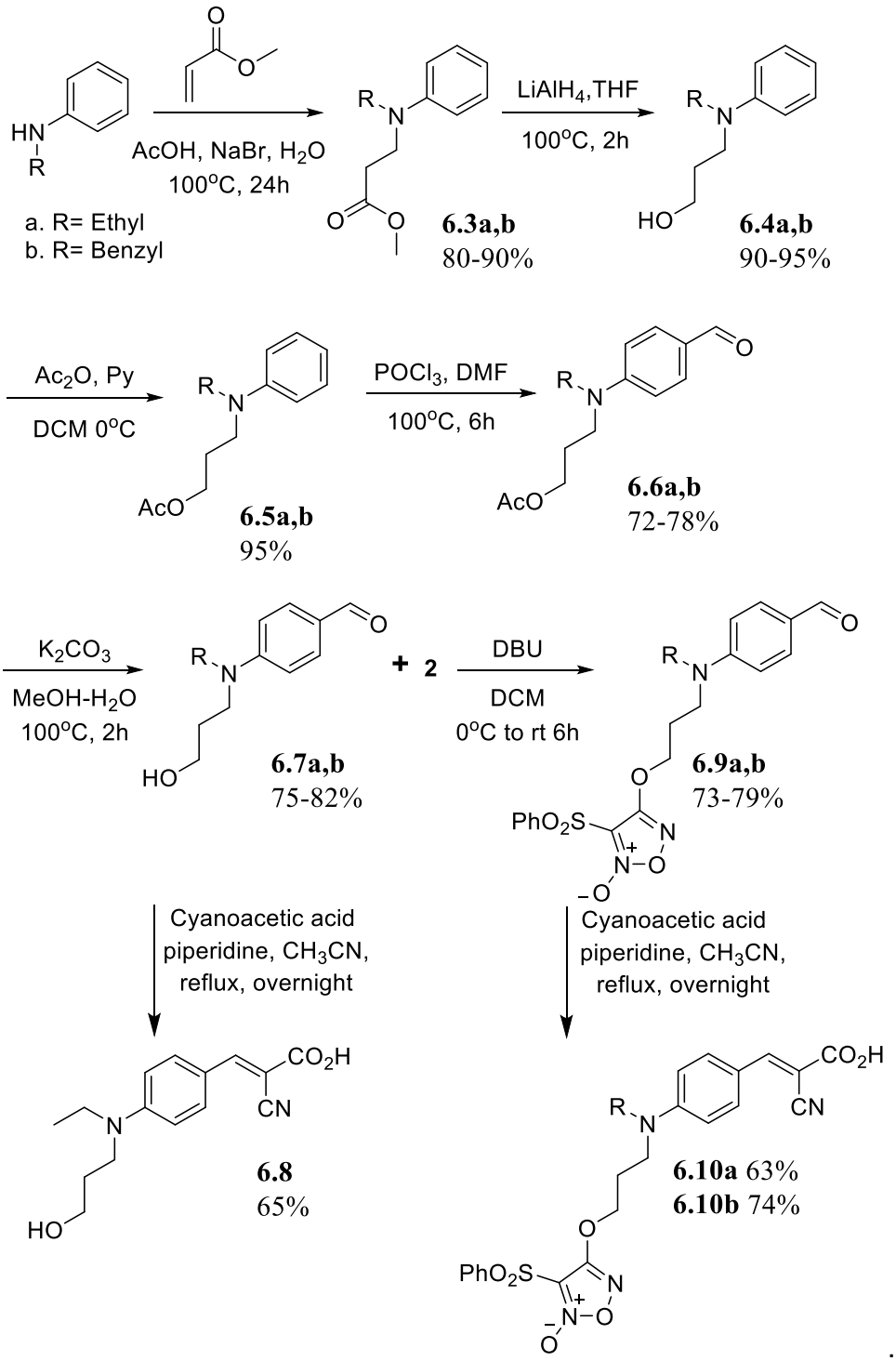

Scheme 10. Synthesis of NO-donor hybrid candidates **6.10a** and **6.10b**.

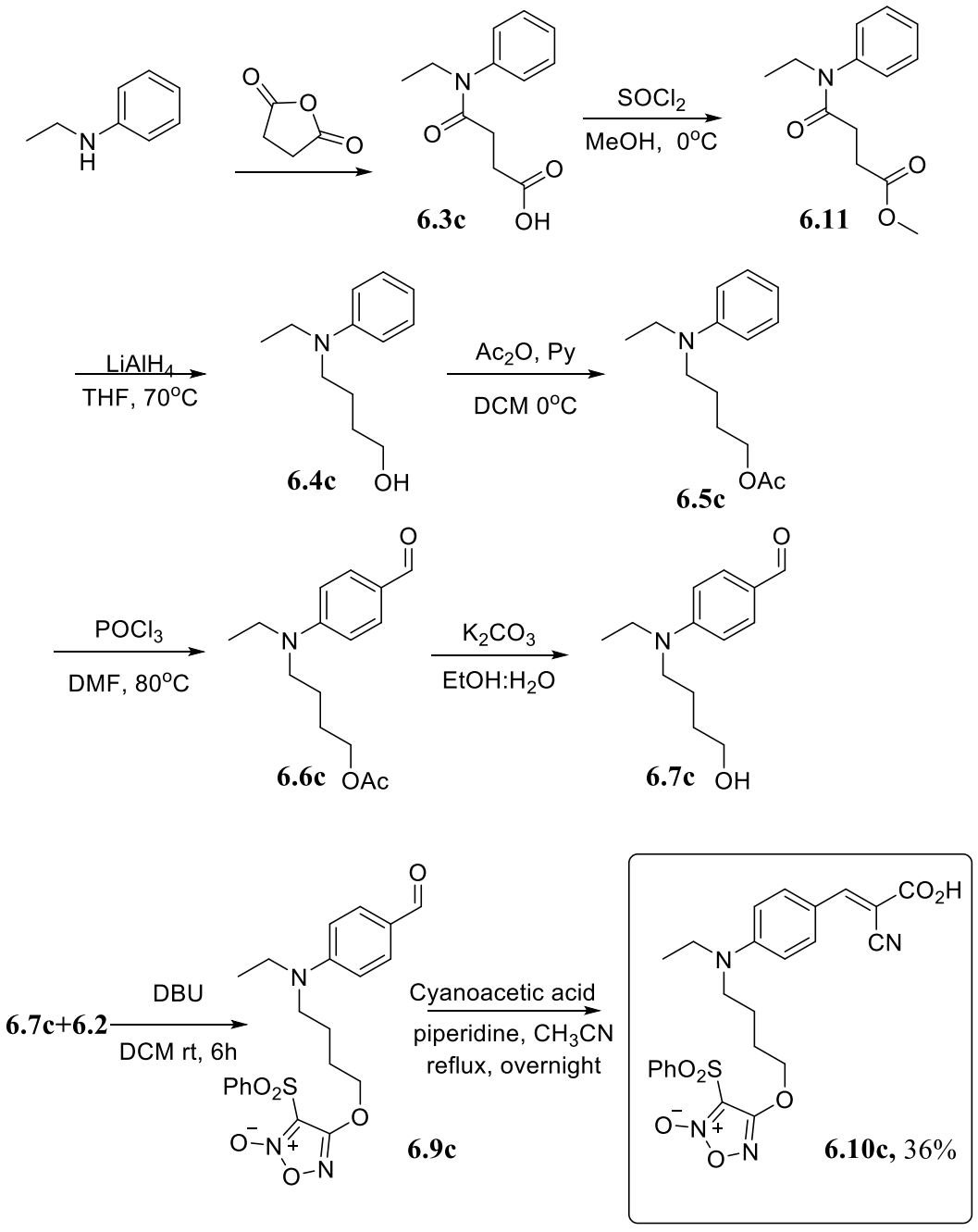

Scheme 11. Synthesis of NO-donor hybrid candidate **6.10c**.

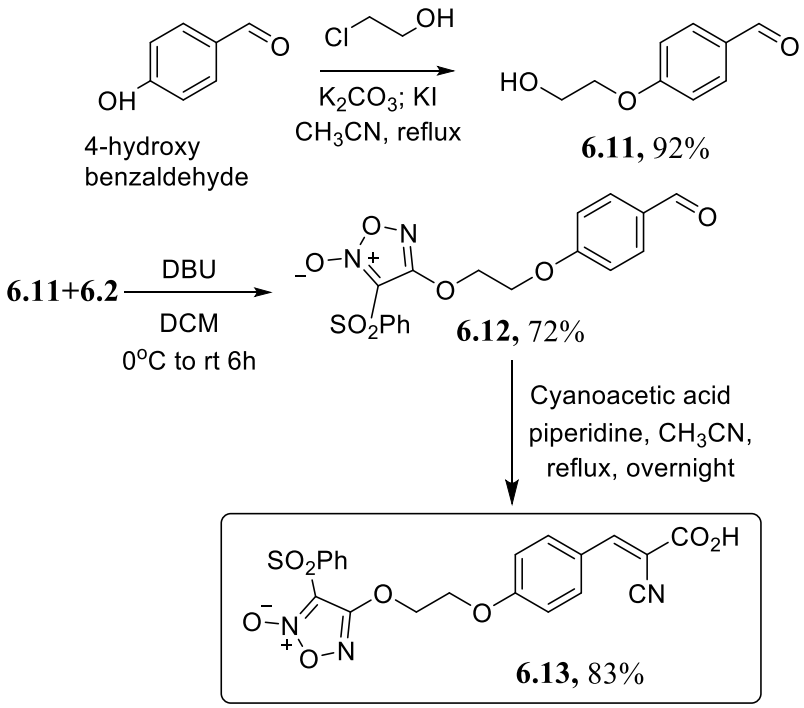

Scheme 12. Synthesis of NO-donor hybrid candidate **6.13.**

To investigate the potential utility of candidate NO-donors as anticancer agents, we first evaluated their cell proliferation inhibition properties in breast cancer cell lines MDA-MB-231 and 4T1, along with another MCT1 expressing cancer cell line WiDr. These studies revealed that compounds **6.10a-c** exhibited potent cancer cell proliferation inhibition properties in single digit micromolar concentration in the cell lines tested (Table 12). Interestingly, o-substituted compound **6.13** had a substantial decrease in potency against the breast cancer cell lines tested, disqualifying this candidate from further development (Table 12). Further, non-furoxan based homolog **6.8** did not exhibit antiproliferative properties at the concentrations tested, providing evidence toward the furoxan NO-donor providing biological activity (Table 12).

Table 12: Cell proliferation inhibition (IC_{50}) properties of compounds **6.10a-c**, **6.13**, and **6.8**.

	MDA-MB-231	**4T1**	**WiDr**
6.10a	3.2±0.58	8.3±0.7	5.16±1.71
6.10b	2.9±0.63	6.1±1.5	31.1±3.6
6.10c	2.0±0.63	8.2± 0.4	9.3± 2.0
6.13	168.0±7.2	131.2±13.2	8.3±0.7
6.8	>250	>250	>250

***** Values represent the average IC_{50} ± SEM (μM) of at least three independent experiments.

To validate if the MCT inhibition properties were retained following hybridization with furoxan NO-donors on the *p*-N,N-dialkyl CHC template, we evaluated the ^{14}C-lactate uptake studies as carried out in previous generation MCT inhibitors in both MCT1 expressing RBE4 cell line, and MCT4 expressing MDA-MB-231. These studies illustrated retained MCT1 and MCT4 inhibition properties of NO-donor hybrid derivatives **6.10a-c** (Table 13, Figure 22). Interestingly, non-furoxan homolog **6.8** did not exhibit MCT inhibition properties in either cell line tested, suggesting a potential role of lipophilic furoxan in inhibiting lactate uptake.

Table 13: MCT1 and MCT4 IC_{50} values of compounds **6.10a-c**, **6.13,** and **6.8**.

Compound	**MCT1 IC_{50} (μM)**	**MCT4 IC_{50} (μM)**
6.10a	0.057±0.016	0.116±0.002
6.10b	0.114±0.014	0.161±0.019
6.10c	0.229	0.106±0.005
6.13	0.099±0.004	TBD
6.8	>10	>10

*Values represent the average IC_{50} ± SEM (μM) of at least three independent experiments.

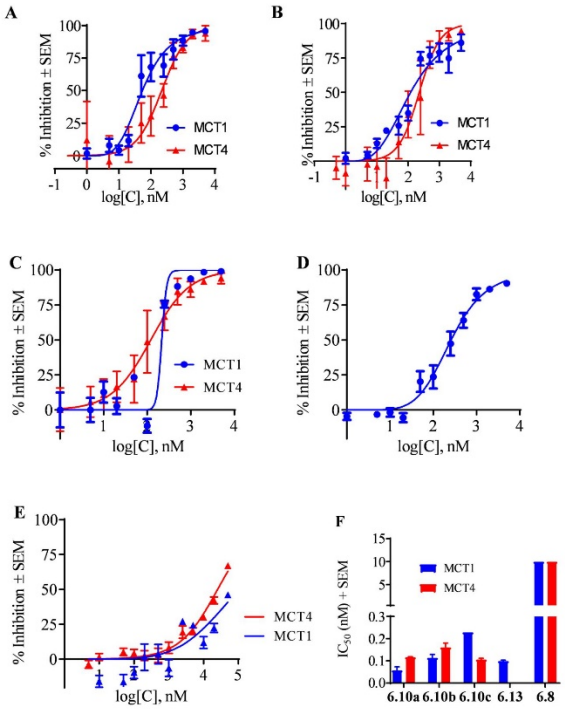

Figure 22. Dose response curves of ^{14}C-lactate uptake indicate equipotent MCT1 and MCT4 inhibition with candidate compounds.

With retained MCT inhibition characteristics and enhanced cancer cell proliferation inhibition properties, we next evaluated the effects of test compounds on cellular metabolism using glycolysis and mitochondrial stress tests as described previously in both WiDr and MDA-MB-231 cell lines. These studies indicated that *p*-N,N-dialkyl CHC NO-donor hybrids **6.10a-c** exhibited potent effects on both metabolic processes in the cell lines tested (Figures 23-26). As expected, the o-furoxan NO donor CHC hybrid **6.13** exhibited comparatively modest effects on metabolism, and treatment with non-NO-donor homolog **6.8** led to metabolic profiles similar to that of control cultures – indicating the importance of both the *p*-N,N-dialkyl CHC furoxan template in offering metabolic inhibition properties (Figures 23-26). These results are substantiated by the similar lack of potency of **6.8** and **6.13** toward MCT inhibition and cell proliferation inhibition.

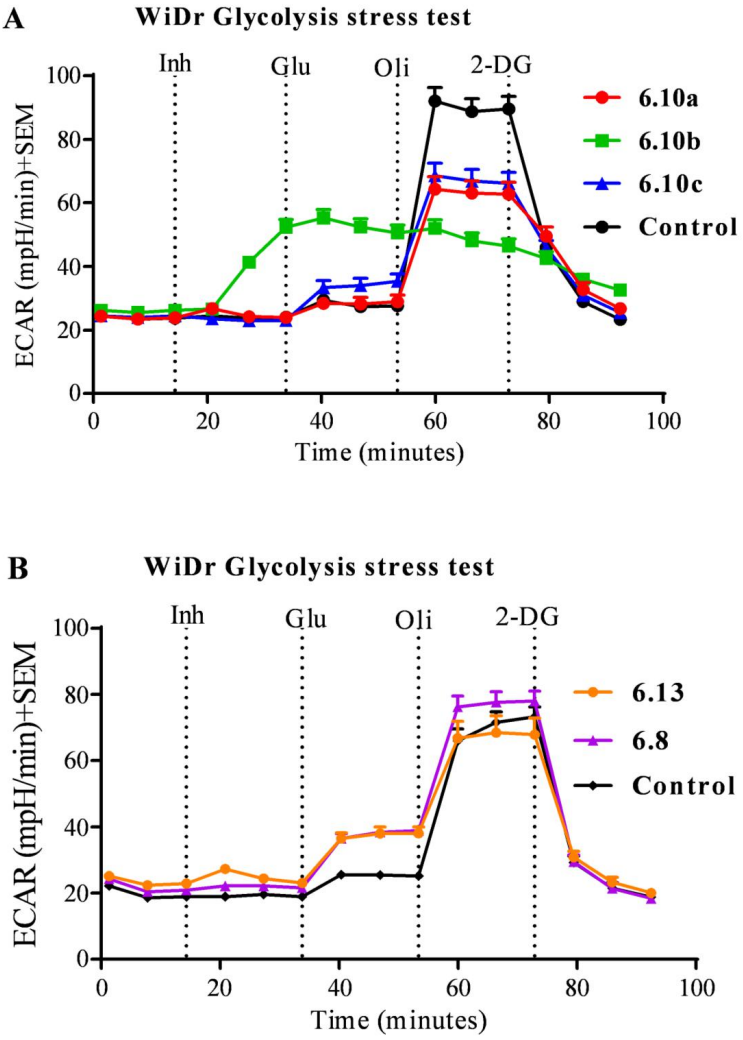

Figure 23: Glycolysis stress test profile in WiDr cell line for compounds (**A**) **6.10a-c** and (**B**) **6.13** and **6.8**.

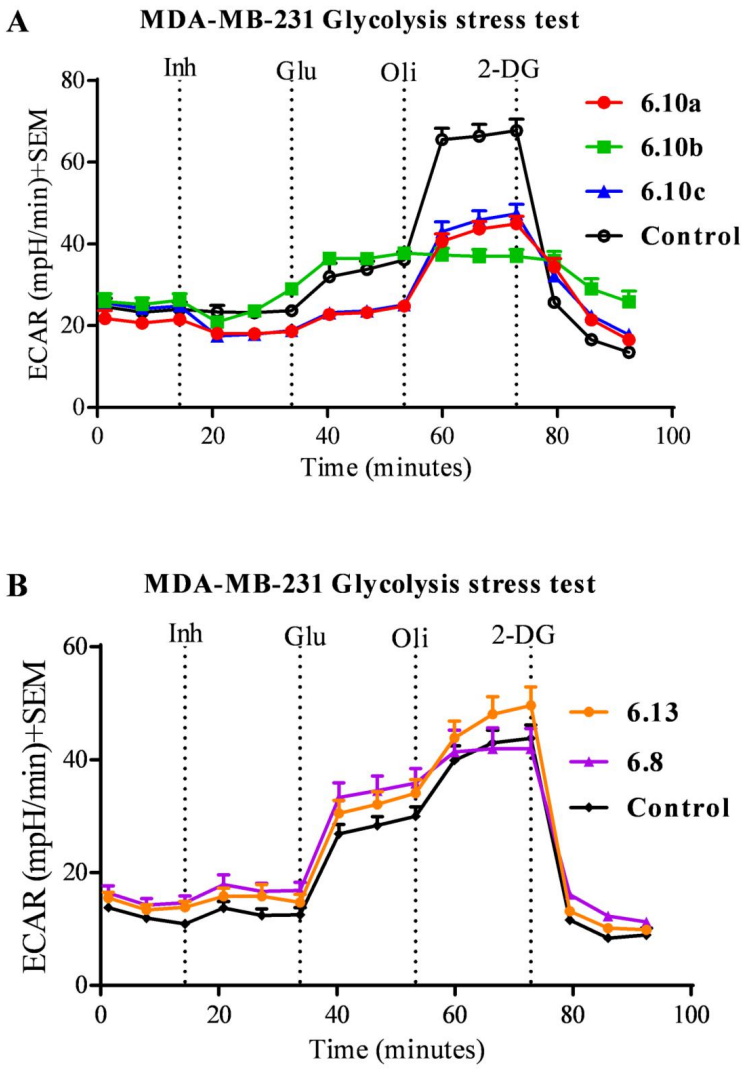

Figure 24: Glycolysis stress test profile in MDA-MB-231 cell line for compounds (**A**) **6.10a-c** and (**B**) **6.13** and **6.8**.

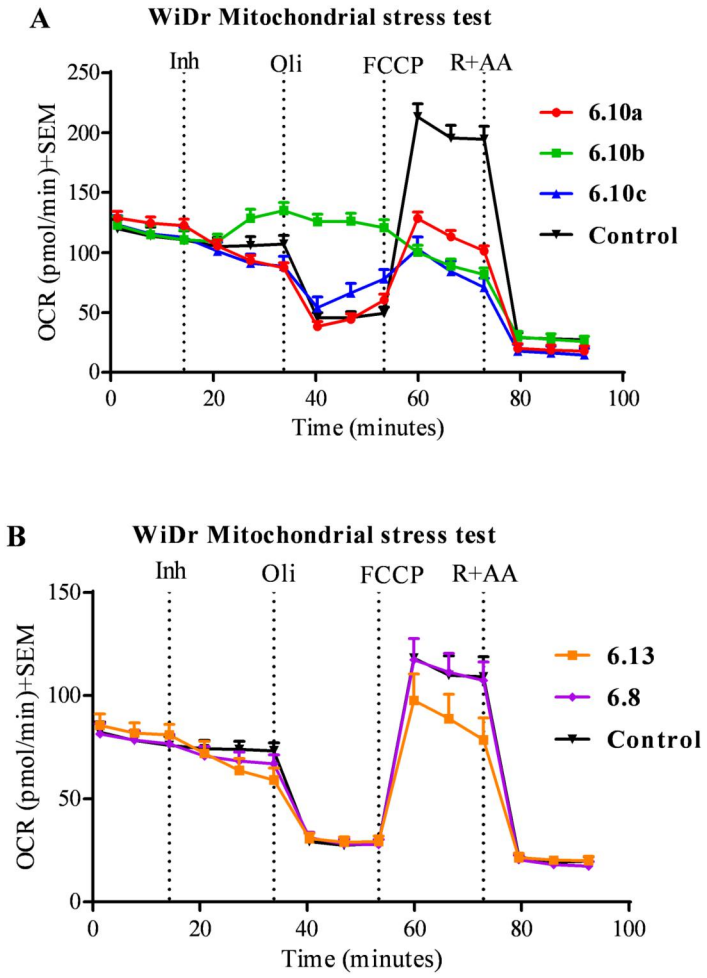

Figure 25: Mitochondrial stress test profile in WiDr cell line for compounds (**A**) **6.10a-c** and (**B**) **6.13** and **6.8**.

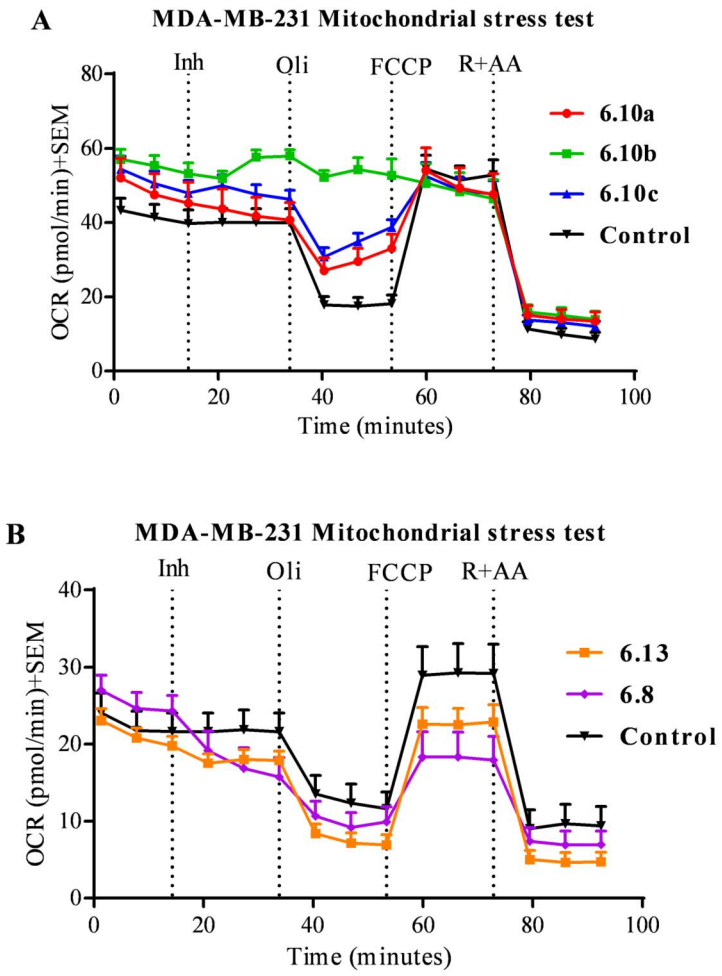

Figure 26: Mitochondrial stress test profile in MDA-MB-231 cell line for compounds (**A**) **6.10a-c** and (**B**) **6.13** and **6.8**.

Encouraged by potent cell proliferation inhibition, dual MCT1/4 inhibition, and potent effects on glycolysis and mitochondrial respiratory processes, we sought to translate lead candidate NO-donors **6.10a-c** to *in vivo* systemic toxicity and efficacy studies. Gratifyingly, these candidates were well tolerated at clinically relevant doses in healthy CD-1 mice as indicated by normal weight gains when compared to untreated mice over a 14-day treatment period (Figure 27).

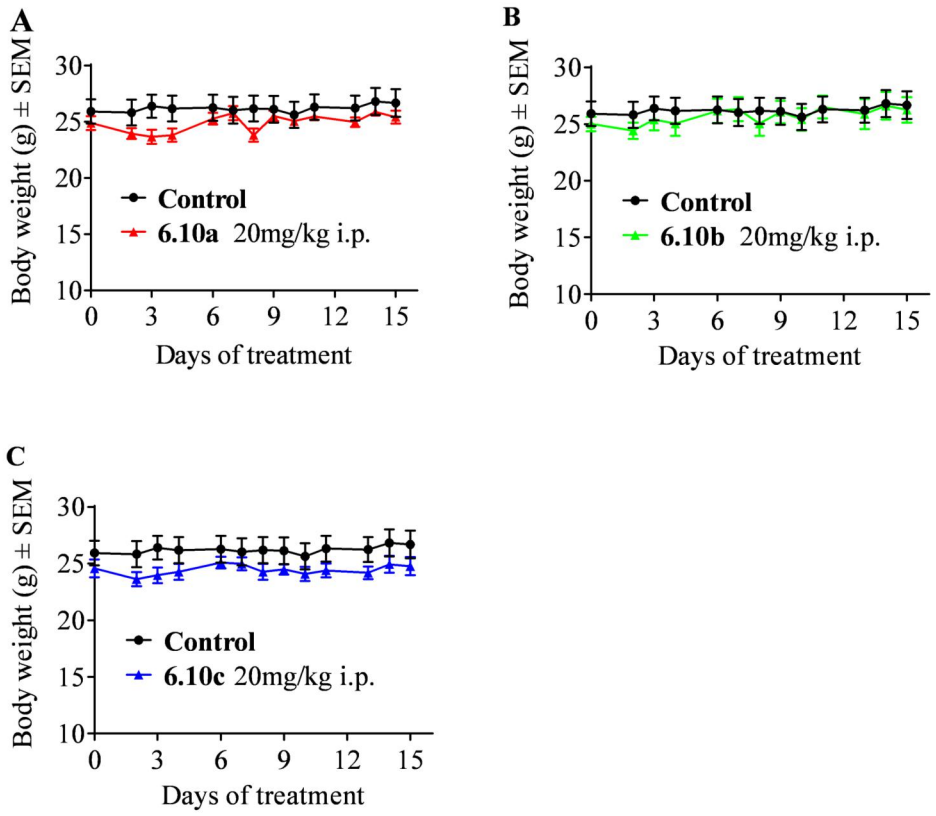

Figure 27. Systemic toxicity study of candidate NO-donor CHC hybrids (**A**) **6.10a**, (**B**) **6.10b**, and (**C**) **6.10c** in healthy CD-1 mice.

Systemic toxicity study indicated that lead candidate compound **6.10a** was well tolerated at 20mg/kg intraperitoneal once daily dosage and hence, we carried out an *in vivo* xenograft efficacy study in an aggressive human triple negative breast cancer model of MDA-MB-231. Gratifyingly, compound **6.10a** exhibited significant tumor growth reduction as a single agent (Figure 28).

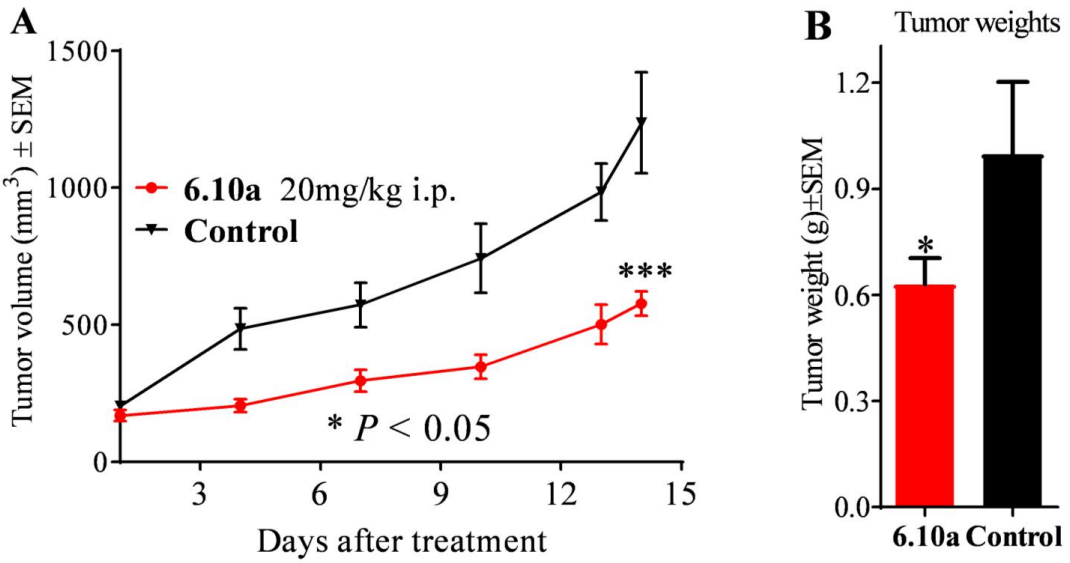

Figure 28. *In vivo* efficacy of candidate compound **6.10a** in a TNBC xenograft MDA-MB-231 indicated significant single agent tumor growth inhibition properties as indicated by (**A**) tumor volume and (**B**) tumor weight.

In conclusion, we have synthesized and evaluated novel furoxan based *p*-N,N-dialkyl CHC NO-donor hybrids that exhibit potent cell proliferation inhibition properties in several aggressive breast and other cancer cell lines. Further, these candidate compounds exhibit potent MCT1 and MCT4 inhibition properties and also significantly inhibit metabolic pathways in cancer cells. Finally, candidates are well tolerated in healthy mice, and exhibit significant tumor growth inhibition properties in an MDA-MB-231 xenograft model.

Synthesis and evaluation of pharmacologically privileged MCT1 inhibitors for cancer treatment

We have demonstrated that utilizing pharmacologically privileged templates, namely the bicyclic coumarin carboxylic acid template, has led to enhanced pharmaceutical properties including bioavailability and metabolic stability. In line with these observations, we have designed, synthesized and evaluated a series of candidate MCT1 inhibitors based on pharmacologically privileged tricyclic phenothiazine and iminodibenzyl templates (Figure 29, Scheme 13-14).

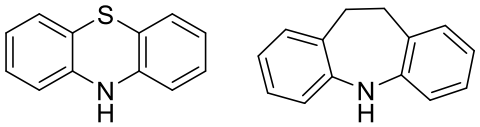

Figure 29. Structures of pharmacologically privileged tricyclic phenothiazine and iminodibenzyl.

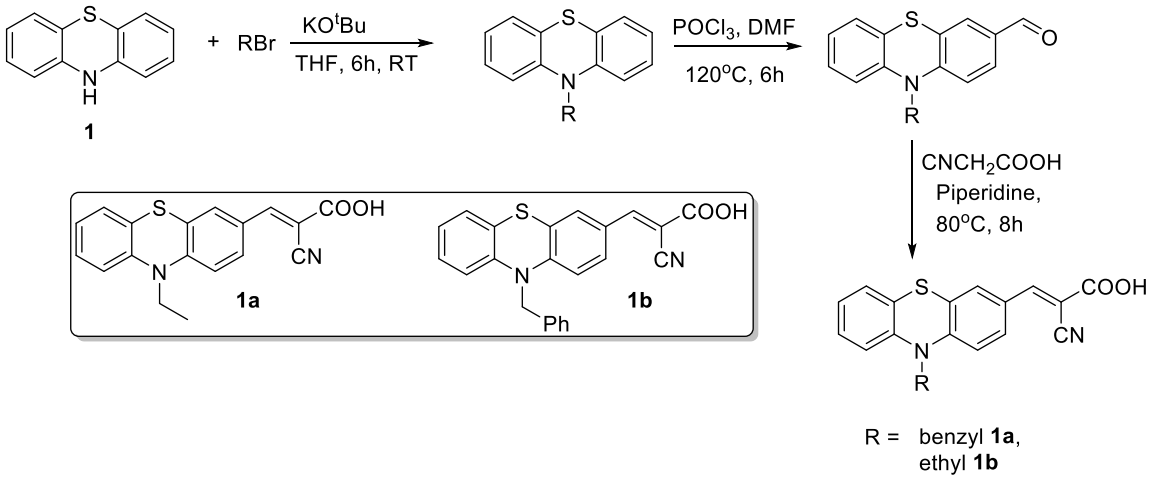

Scheme 13. Synthesis of tricylic phenothiazine candidates **1a** and **1b**.

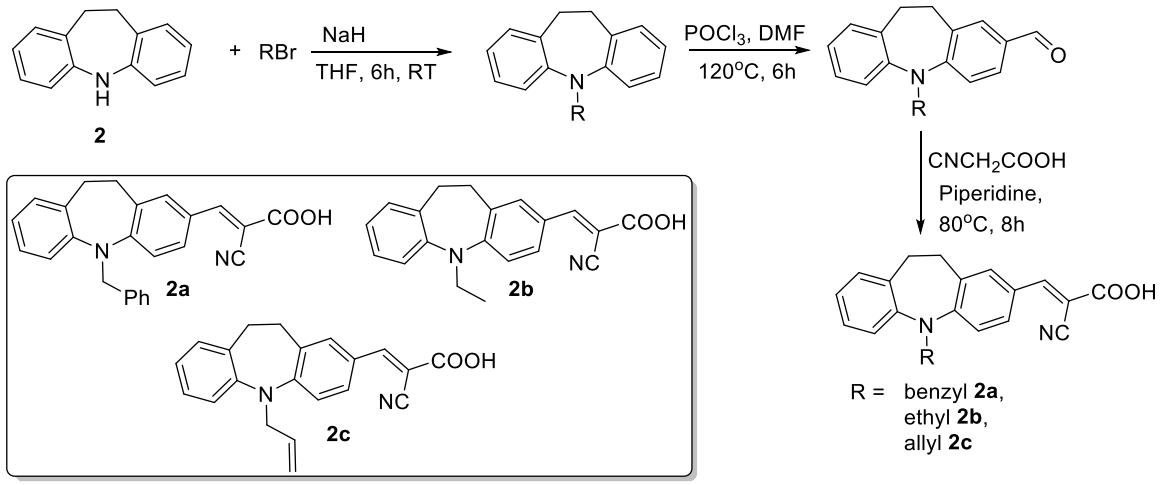

Scheme 14. Synthesis of tricylic iminodibenzyl candidates **2a**-c.

Candidate compounds were synthesized with MCT inhibiting pharmacophore cyanocinnamic acid template and hence, the MCT1 inhibition properties of **1a-b** and **2a-c** were evaluated using our standard ^{14}C-lactate uptake in RBE4 cells as previously described. Gratifyingly, all candidate compounds exhibited potent nanomolar MCT1 inhibition properties (Table 14).

Table 14: MCT1 IC_{50}^{*} (μM) of N-substituted iminodibenzyl (**2a-c**) and phenothiazine (**1a-b**) based cyanocinnamic acids

Compound	MCT1 IC_{50}
1a	0.007±0.00
1b	0.012±0.00
2a	0.11±0.02
2b	0.08±0.01
2c	0.05±0.01

*IC_{50} values reported in μM, average ± SEM of minimum three separate experimental values

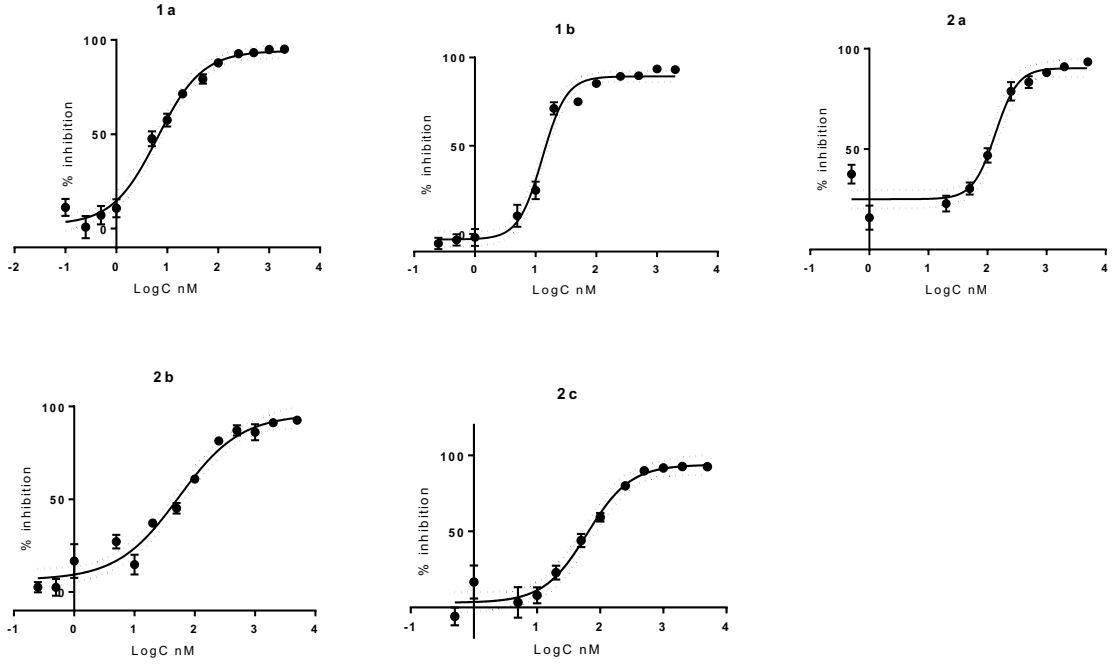

Figure 30. Graphical representation of MCT1 inhibition properties of candidate compounds **1a-b** and **2a-c**.

In line with the development of previously described MCT1/4 inhibitors, **1a-b** and **2a-c** were next evaluated for *in vitro* cancer cell proliferation inhibition properties in breast cancer cell lines MDA-MB-231 and MCF7, along with other MCT1 expressing cancer cell line WiDr. Interestingly, candidate compounds exhibited potency against WiDr cell line at micromolar concentrations, but did not exhibit cell proliferation inhibition properties against MDA-MB-231 or MCF7 at the concentrations tested (Table 15).

Table 15: MTT IC_{50}*(μM) values of N-substituted iminodibenzyl and phenothiazine based cyanocinnamic acids

Compound	WiDr	MDA-MB-231	MCF7
1a	26.2±2.1	>100	>100
1b	36.4±4.5	>100	>100
2a	38.5±7.3	>100	>100
2b	46.6±8.4	>100	>100
2c	40.4±3.4	75.1±7.5	>100

* Average±SEM of minimum three separate experimental values

Interestingly, we found that when compared to MDA-MB-231 and MCF7, WiDr cells exhibit a higher basal level of mitochondrial respiration – indicating that the potency of candidates **1a-b** and **2a-c** may depend on basal metabolic phenotypes and are more selective to cancer cells that predominately pursue mitochondrial respiration for energy (data not shown). In this regard, we carried out Seahorse based glycolysis and mitochondrial stress tests as previously described in the WiDr cell line. These studies indicated that **1a** and **2a** lead to dysfunction of both glycolysis and mitochondrial respiration, with a substantial decrease in mitochondrial derived ATP production and other respiratory processes (Figures 31 & 32).

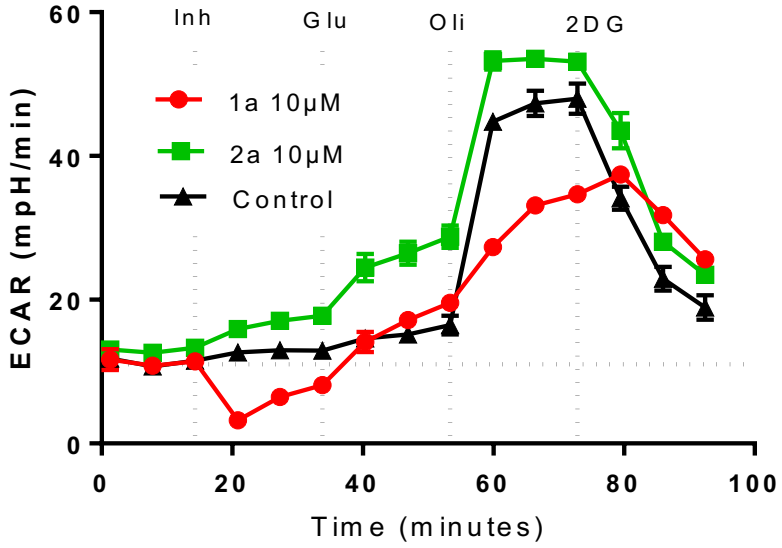

Figure 31. Glycolysis stress test of candidate **1a** and **2a** in WiDr cell line.

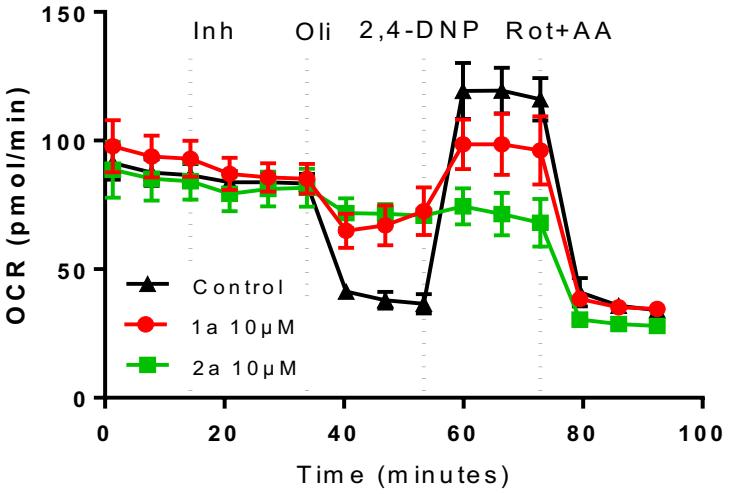

Figure 32. Mitochondrial stress test of candidate **1a** and **2a** in WiDr cell line.

The design of tricyclic candidate compounds **1a-b** and **2a-c** was in part to investigate if pharmacologically privileged phenothiazine and iminodibenzyl templates provided enhanced pharmaceutical properties. In this regard, *in vitro* bio-availability and metabolic stability experiments were employed using **1a** and **2a** as previously carried out using coumarin based MCT1 inhibitors. The efflux ratio was calculated between B-A and A-B permeability and a ratio > 2 signifies drug efflux. For compound **2a**, this ratio was found to be 1.6 implying that this molecule has low efflux ratio indicating this compound has acceptable bioavailability (Table 16). Further, *in vitro* metabolic stability of candidate compounds was evaluated in both mouse and human liver microsomes. These studies

indicated that both phenothiazine **1a** has improved metabolic stability (half-life >60 min) over first generation MCT inhibitors (Table 17 & 18). Finally, plasma protein binding studies were carried out and indicated that **1a** exhibits low protein binding rates (Table 19). These studies indicate that candidate **1a** exhibits superior pharmaceutical properties over other candidate inhibitors.

Table 16: A-B and B-A Caco-2 permeability of N-substituted iminodibenzyl and phenothiazine based cyanocinnamic acids

A-B permeability (Caco-2, pH 6.5/7.4)		
Compound	Permeability (10^{-6} cm/s)	Percent Recovery (%)
	Mean*	Mean*
1a	0.03	11
2a	1.4	15
colchicine	0.3	75
labetalol	8.5	66
propranolol	40.9	67
B-A permeability (Caco-2, pH 6.5/7.4)		
1a	1.3	16
2a	2.2	29
colchicine	15.3	81
labetalol	36.5	72
propranolol	41.5	80
ranitidine	3.7	85

* Mean of two experiments

Table 17: Metabolic stability of iminodibenzyl and phenothiazine based cyanocinnamic acids in mouse liver microsomes

Intrinsic clearance (liver microsomes, mouse)				
Compound	Half-Life (minute)			Cl_{int}
	1st	2nd	Mean	
1a	>60	>60	>60	<115.5
2a	>60	>60	>60	<115.5
Propranolol	9.1	9.5	9	744.5
Imipramine	15.7	15.4	16	446.2
Verapamil	17.6	17.5	18	394.6
Terfenadine	7.5	6.1	7	1027.4

* $T_{1/2}$ is reported in minutes, mean value of two experiments

Table 18: Metabolic stability of iminodibenzyl and phenothiazine based cyanocinnamic acids in human liver microsomes

Intrinsic clearance (liver microsomes, human)				
Compound	Half-Life (minute)			Cl_{int}
	1st	2nd	Mean	
1a	>60	>60	>60	<115.5
2a	28.2	31.2	30	234
Propranolol	334.4	373	>60	<115.5
Imipramine	213.9	194.4	>60	<115.5
Verapamil	21.1	21.5	21	324.8
Terfenadine	9.8	9.1	9	736.8

* $T_{1/2}$ is reported in minutes, mean value of two experiments

Table 19: Protein binding capability of iminodibenzyl and phenothiazine based cyanocinnamic acids in human plasma

Compound	% Protein bound	% Recovery
	Mean*	Mean*
1a	77	121
2a	>99	94
Acebutolol	26	111
Quinidine	68	97
Warfarin	97	95

* mean value of two experiments

To evaluate the *in vivo* translational potential of candidate compounds, systemic toxicity studies in healthy CD-1 mice were employed. These studies indicated that candidate compounds were well tolerated at clinically relevant doses over the indicated treatment period as evidenced by healthy body weight gains when compared to untreated mice (Figure 33).

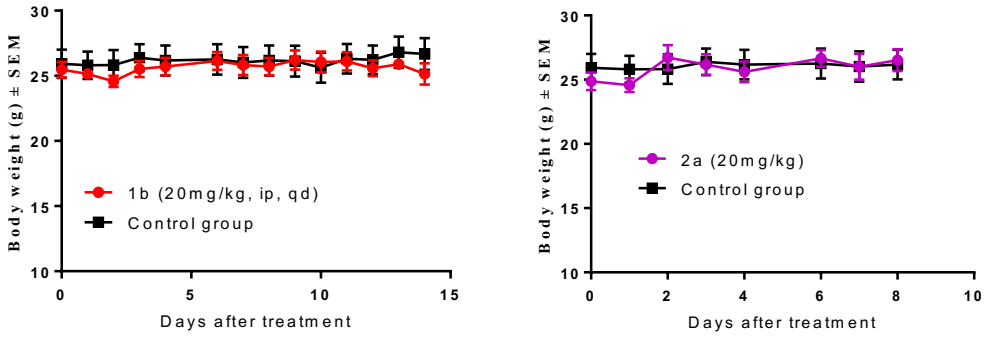

Figure 33. *In vivo* systemic toxicity study of candidate tricyclic MCT inhibitors 1b and 2a in healthy CD-1 mice.

In conclusion, we have designed, synthesized, and evaluated novel MCT1 inhibitors based on pharmacologically privileged tricyclic phenothiazine and iminodibenzyl synthetic templates. 14C-lactate uptake studies in RBE4 cells indicated potent inhibition of MCT1 mediated lactate uptake. Metabolic assays also revealed that candidate compounds led to both glycolytic and mitochondrial dysfunctions in MDA-MB-231 and WiDr cells. ADME studies indicated that tricyclic candidate **1a** exhibited marked increases in bioavailabilty, metabolic stability, and a substantial decrease in plasma protein binding. Finally, candidate compounds were evaluated for their *in vivo* systemic toxicity in healthy CD-1 mice and were found to be well tolerated at clinically relevant doses. These compounds need to be evaluated for *in vivo* efficacy properties in breast cancer tumor models to realize their anticancer potential.

Synthesis and evaluation of potent inhibitors of mitochondrial pyruvate respiration

As mentioned in the hypothesis, cancer cells exhibit the ability to alter energetic pathways in response to cellular micro-environmental conditions. This metabolic plasticity has been identified in a variety of solid tumors and is largely responsible for aggressive and resistant phenotypes. In this regard, targeting glycolysis and mitochondrial respiration has the potential to inhibit metabolic plasticity and eradicate the tumor. Our previous generations of MCT1 and MCT4 inhibitors has indicated that enhanced lipophilic characteristics have increased the ability of candidate compounds to alter mitochondrial energetics and have increased cell proliferation inhibition properties. Further, it has recently been illustrated by others that N,N-dialkyl coumarin carboxylic acids initially developed by us as MCT1 inhibitors (**7ACC1** and **7ACC2,** Figure 34) lead to potent inhibition of mitochondrial pyruvate uptake in cancer cells. Further, it has recently been proposed that these compounds inhibit the mitochondrial pyruvate carrier (MPC), similar to that of known cyanocinnamate based MPC inhibitor **UK5099** (Figure 34), and inhibit MCT mediated lactate flux via indirect feedback mechanisms. In this regard, we have designed and synthesized a series of novel pharmacologically privileged and lipophilic cyanocinnamate candidate compounds toward the inhibition of MPC mediated pyruvate driven mitochondrial respiration (**CMPD1-4**, Figure 34). Additionally, as a proof of concept, we synthesized a metabolically stable lipophilic fluorine substituted homolog of our first generation lead derivative **1a** in hopes to block CYP450 mediated enzymatic oxidation (**F-1a**, Figure 34).

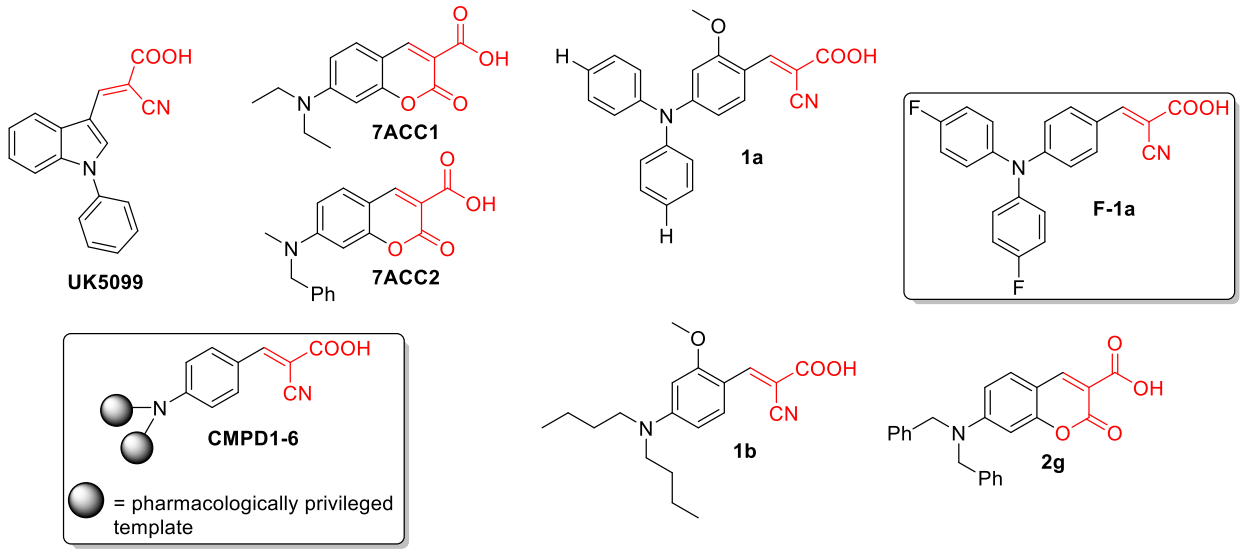

Figure 34. Inhibition of mitochondrial pyruvate driven respiration by compounds based on our previously developed and known cyanocinnamate and coumarin carboxylic acid templates.

After synthesizing a structurally diverse series of pharmacologically privileged and lipophilic candidate compounds **CMPD1-6**, we first evaluated their ability to inhibit cancer cell proliferation *in vitro*. For these studies, we employed solid tumor cell lines including

breast cancer cell lines MDA-MB-231, 4T1, 67nr, and MCF7, colorectal cancer cell line WiDr, and pancreatic cancer cell line MIAPaCa-2. These studies indicated that candidates **CMPD1-6** exhibited cancer cell proliferation properties in the micromolar range, with the most potent derivative **CMPD4** exhibiting single digit micromolar potency on aggressive stage IV breast cancer cell line 4T1 (Table 20).

Table 20: MTT IC_{50}* values of **CMPD1-6** in various cancer cell lines

Sl. No	MDA-MB-231	WiDr	4T1	67NR	MIAPaCa2	MCF7
CMPD-1	>100	20±7	37±11	45±12	98±2	>100
CMPD -2	89±4	14±3	20±6	21±1	80±12	36±3
CMPD -3	85±7	10±3	18±6	22±2	77±14	31±3
CMPD -4	91±6	8±4	7±2	13±3	84±7	35±6
CMPD -5	58±11	32±4	30±2	32±3	73±11	26±6
CMPD -6	73±11	5±1	19±5	25±3	79±14	49±12

* Average±SEM of minimum three independent experiments

Encouraged by potent cancer cell proliferation inhibition, we sought to validate our hypothesis by investigating the effects of candidate **CMPD1-6** mitochondrial respiration utilizing standard Seahorse based mitochondrial stress tests as previously described. Gratifyingly, these studies revealed potent and acute effects on mitochondrial respiratory processes (Figure 35).

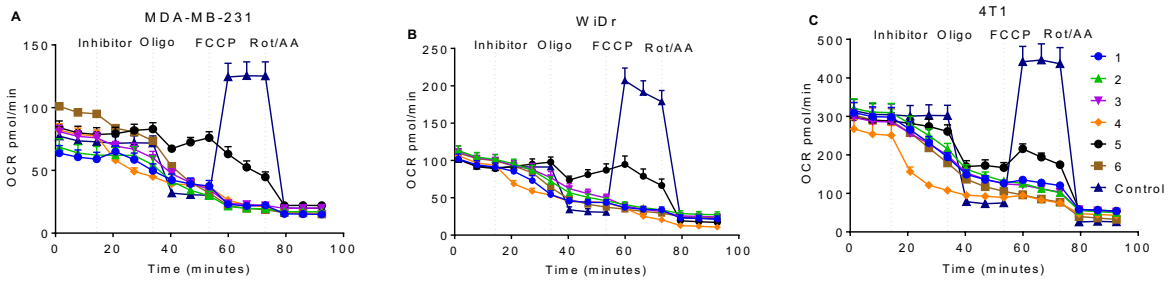

Figure 35. Mitochondrial stress tests reveal **CMPD1-6** potently inhibit mitochondrial respiratory processes in (**A**) MDA-MB-231, (**B**) WiDr, and (**C**) 4T1 cell lines.

Intrigued by potent inhibition of mitochondrial respiration by candidate compounds, we sought to investigate the ability of candidate compounds to inhibit mitochondrial respiration driven by specific mitochondrial tri-carboxylic acid cycle (TCA) substrates. To perform these assays, 4T1 cells were permeabilized using cell membrane specific permeabilizing agent rPFO, and specific substrates were delivered to the mitochondria. Resulting oxygen consumption rates in the presence of these substrates indicate the magnitude of substrate-linked mitochondrial respiration. These studies indicated that

candidate compounds specifically inhibited ETC complex-I mediated pyruvate driven respiration, and did not affect glutamate or complex-II mediated succinate driven respiratory processes (Figure 36).

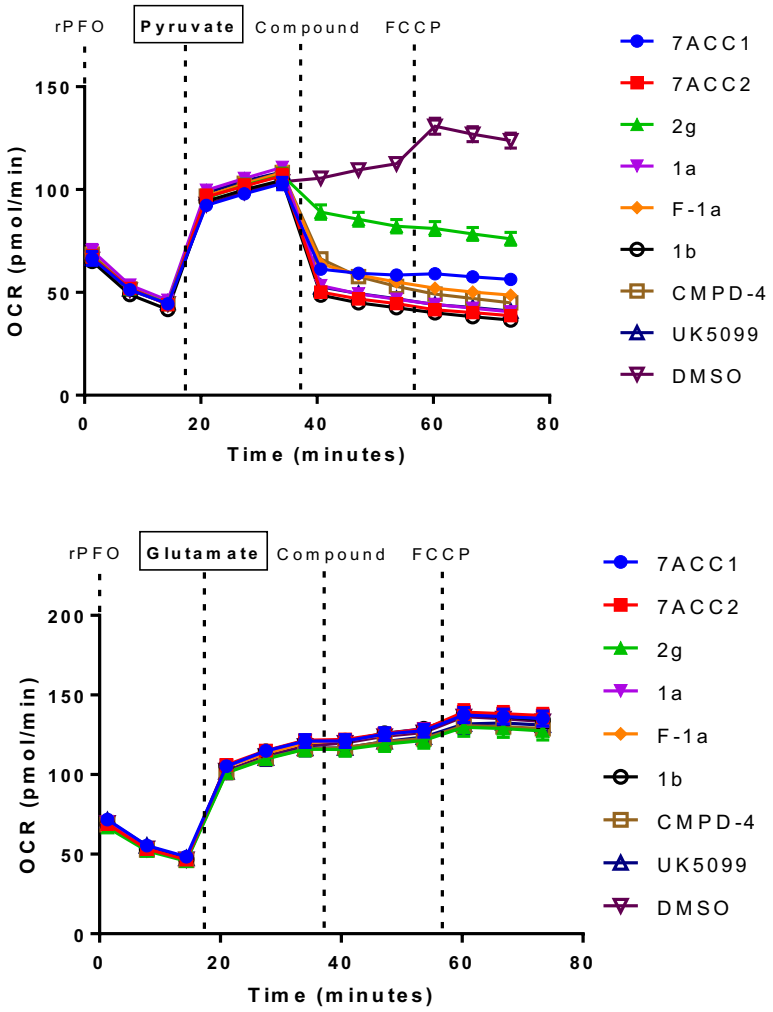

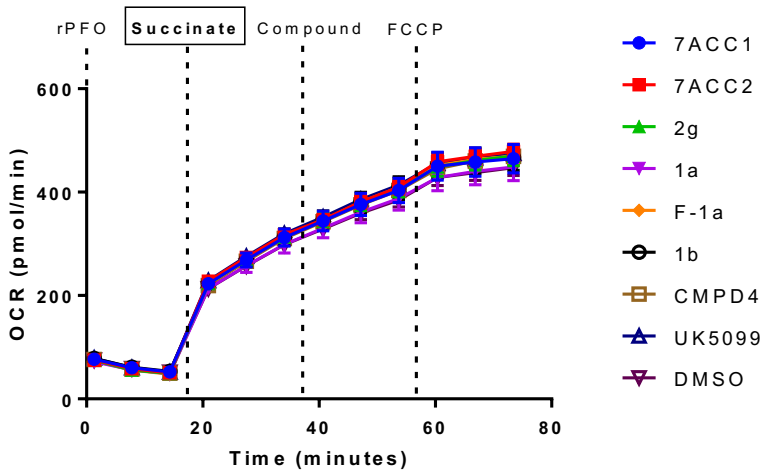

Figure 36. Candidate compounds specifically inhibit pyruvate driven mitochondrial respiration.

Permeabilized mitochondrial assays have revealed that candidate compounds initially developed as MCT inhibitors also exhibit inhibition properties of pyruvate driven respiration consistent with known MPC inhibitor UK5099. In this regard, we developed a SeahorseXFe96 based dose-response method of evaluating the relative potency of candidate compounds toward inhibition of pyruvate driven respiration in permeabilized 4T1 cells (Figures 37-45).

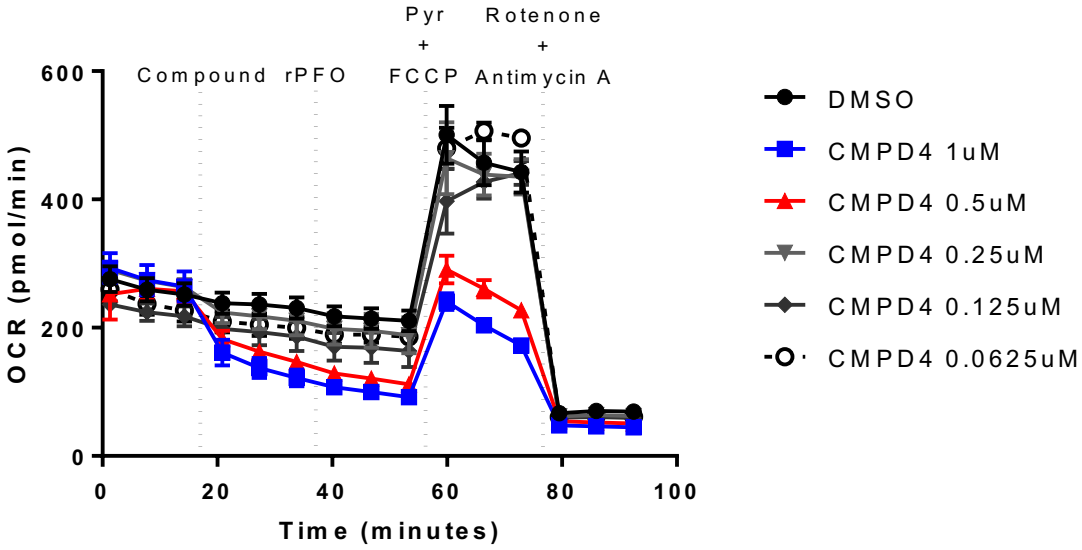

Figure 37. Dose response inhibition of pyruvate driven mitochondrial respiration by **CMPD4** in permeabilized 4T1 cells.

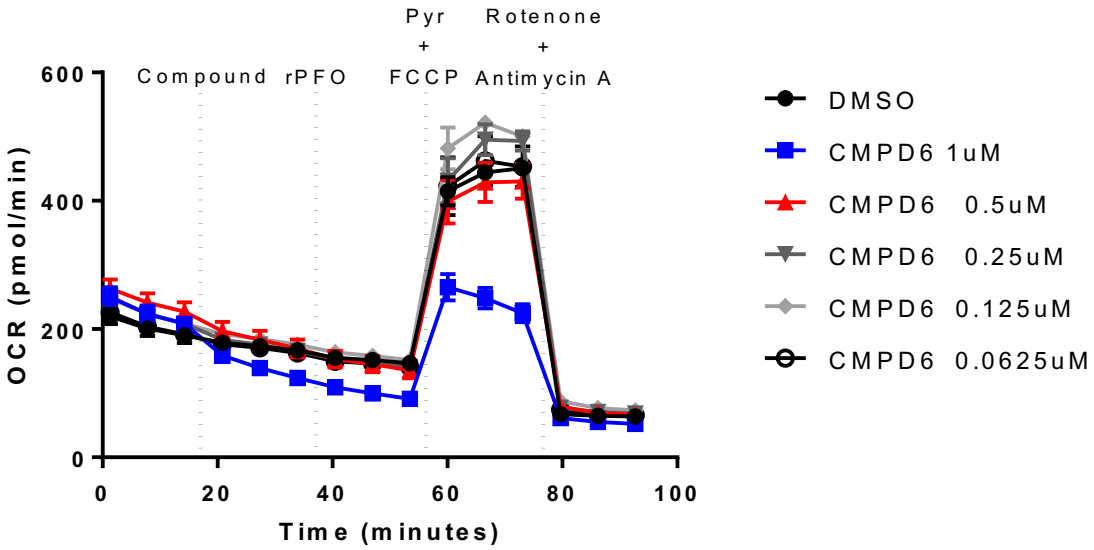

Figure 38. Dose response inhibition of pyruvate driven mitochondrial respiration by **CMPD6** in permeabilized 4T1 cells.

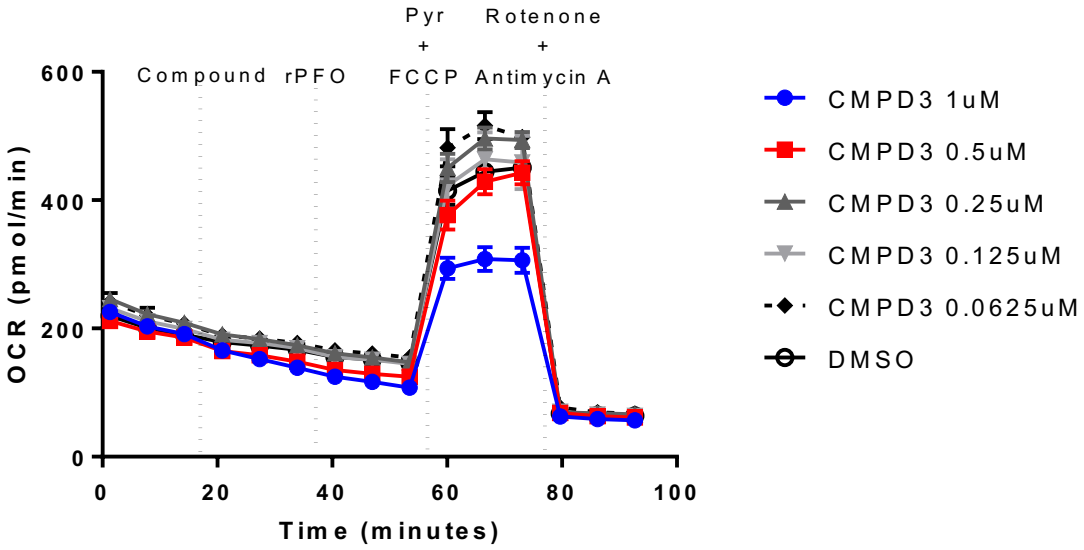

Figure 39. Dose response inhibition of pyruvate driven mitochondrial respiration by **CMPD3** in permeabilized 4T1 cells.

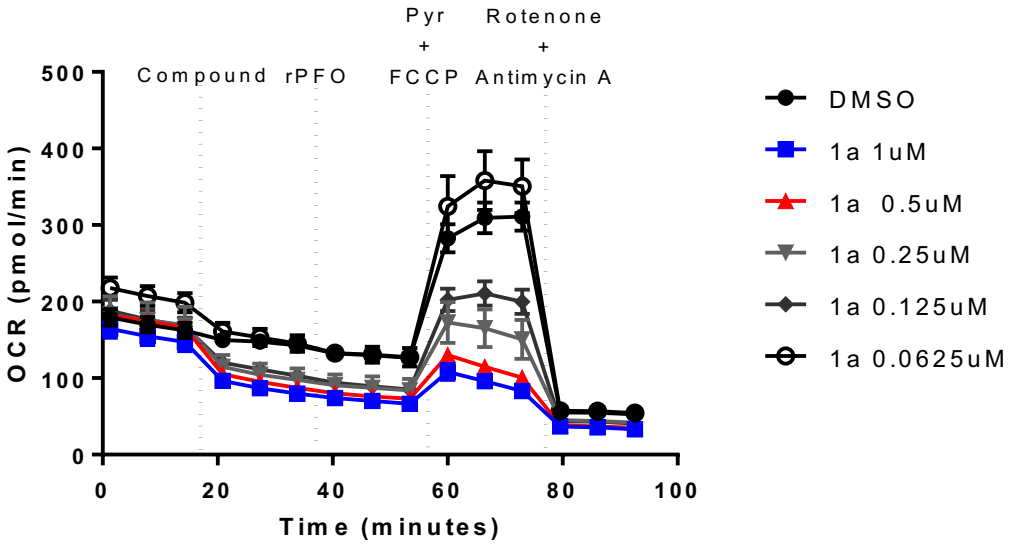

Figure 40. Dose response inhibition of pyruvate driven mitochondrial respiration by **1a** in permeabilized 4T1 cells.

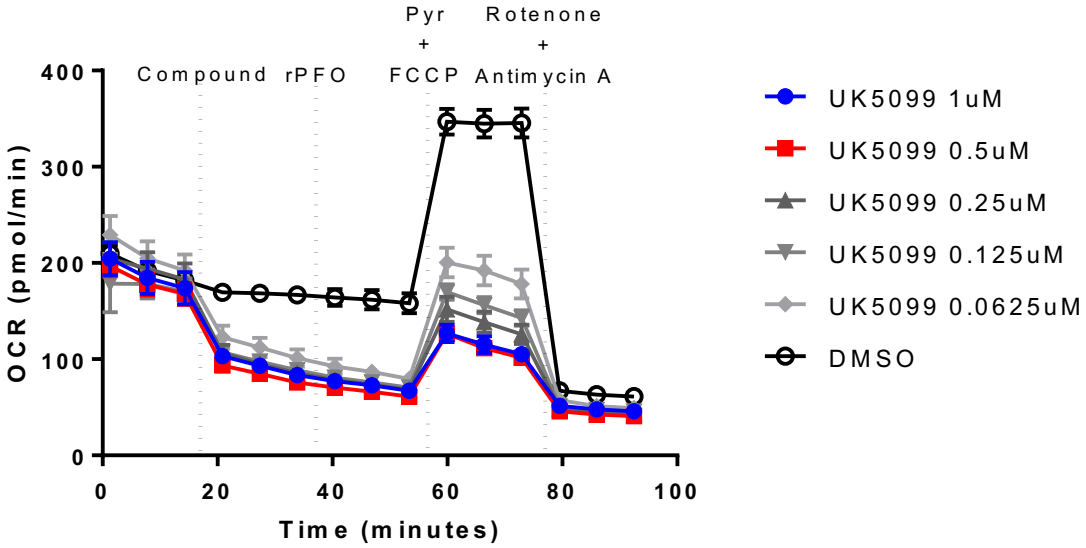

Figure 41. Dose response inhibition of pyruvate driven mitochondrial respiration by **UK5099** in permeabilized 4T1 cells.

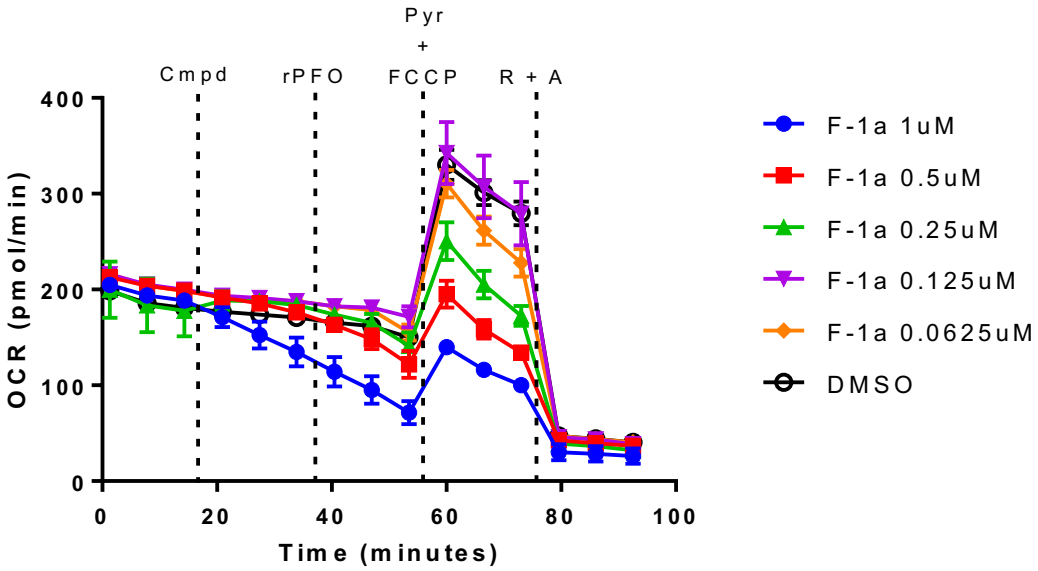

Figure 42. Dose response inhibition of pyruvate driven mitochondrial respiration by **F-1a** in permeabilized 4T1 cells.

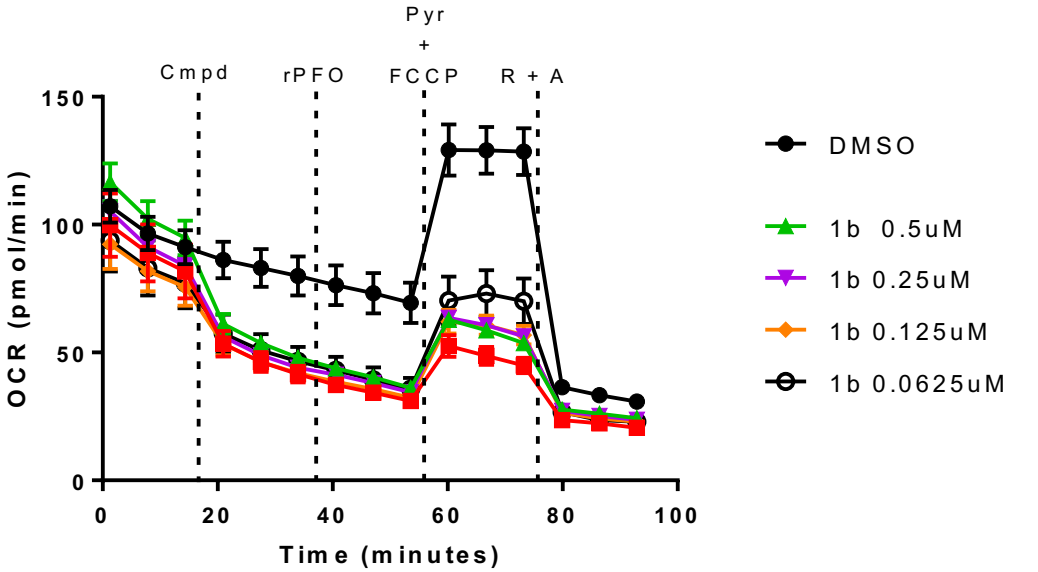

Figure 43. Dose response inhibition of pyruvate driven mitochondrial respiration by **1b** in permeabilized 4T1 cells.

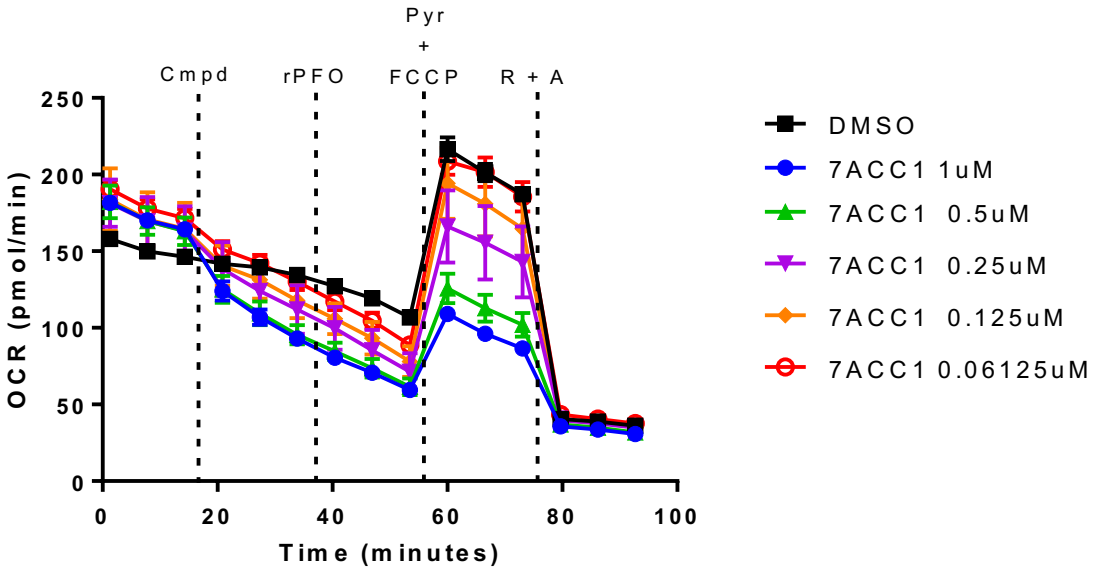

Figure 44. Dose response inhibition of pyruvate driven mitochondrial respiration by **7ACC1** in permeabilized 4T1 cells.

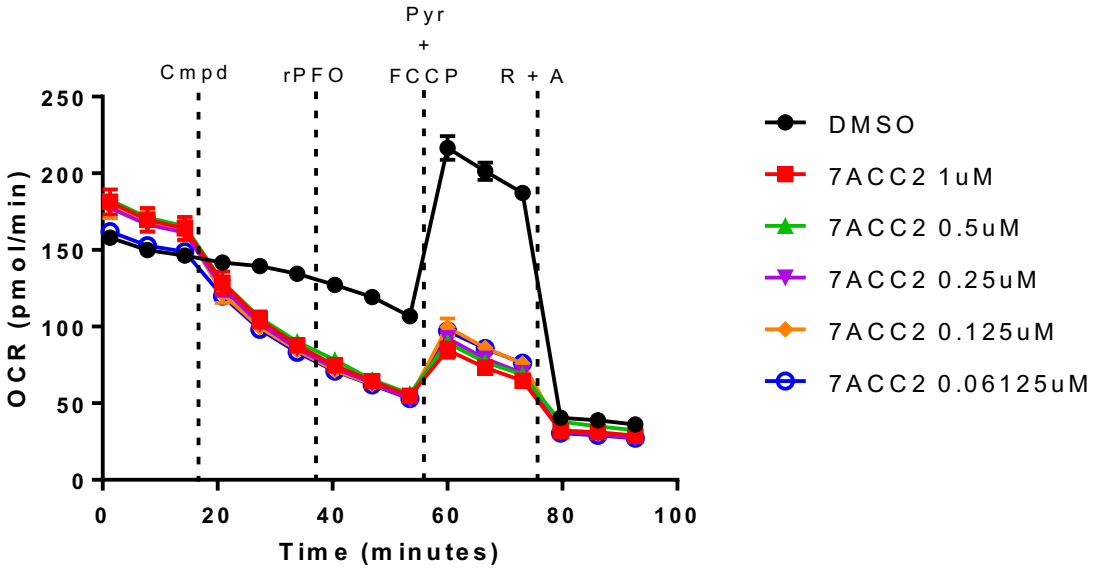

Figure 45. Dose response inhibition of pyruvate driven mitochondrial respiration by **7ACC2** in permeabilized 4T1 cells.

Permeabilized pyruvate driven respiratory assays revealed that candidate compounds inhibited mitochondrial oxygen consumption rates in a dose-dependent fashion suitable

for calculation of 50% inhibitory concentrations (IC_{50}) and comparison of relative potency between our structurally diverse library of candidate inhibitors (Table 15).

Table 15: Pyruvate driven respiration inhibitory concentrations IC_{50}*(μM) values of candidate compounds

Compound	4T1
CMPD-4	0.69
CMPD-6	0.90
CMPD-3	1.0
1a	0.36
F-1a	0.15
1b	0.09
7ACC1	0.60
7ACC2	0.008
UK5099	0.04

To evaluate the relative potency between structurally diverse derivatives, the magnitude of inhibition of pyruvate driven respiration between **1a**, **CMPD-4**, and known MPC inhibitor UK5099 were compared in pertmeabilized 4T1 cells at equal concentrations (1μM, Figure 46). These experiments revealed that although UK5099 exhibited a more potent dose response IC_{50} values, candidate **1a** and **CMPD-4** exhibited slightly enhanced magnitude of inhibition (Figure 46).

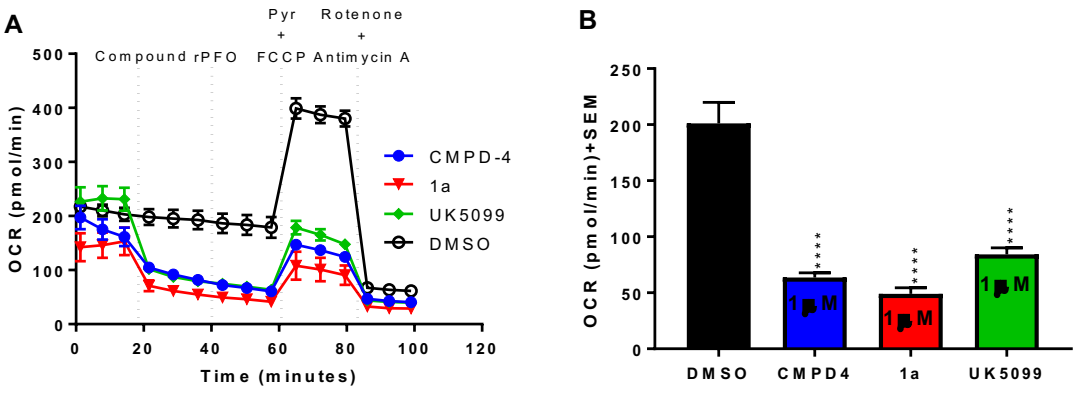

Figure 46. Head-to-head comparison of the inhibition of pyruvate driven respiration of candidate **CMPD-4** and **1a** against known MPC inhibitor UK5099 in permeabilized 4T1

cells. (**A**) Metabolic profile of real-time oxygen consumption rates in both control (DMSO) and treated (1μM CMPD-4 & 1a) cells and (**B**) Graphical representation of FCCP stimulated pyruvate driven respiration.

Literature reports have rigorously indicated that cancer cells, particularly of solid tumor origin – including breast cancer – exhibit the capability to alter their energetic pathways as a function of nutrient and oxygen availability, as well as other microenvironmental stressors. Hence, our altered working hypotheses states that the sole-targeting of either glycolysis or mitochondrial respiration alone is not sufficient to eliminate the tumor, as compensatory energetic mechanisms will result in survival and progression of the tumor. Hence, we envisioned that potent inhbibition of both glycolysis and mitochondrial respiration through rational combination strategies would lead to energetic crisis by inhibiting metabolic plasticity – starving the tumor of energy and biosynthetic building blocks – and eradicating tumor progression. In this regard, we carried out extensive literature search of potent and pharmacologically priveledged inhibitors of glycolysis that would be suitable to combine with our new generation inhibitor of mitochondrial pyruvate respiration **CMPD-4**. In this regard, we identified three glucose transporter 1 (Glut1) inhibitors that have shown to exhibit potent inhibiton of glycolysis and tumor growth in the literature – **STF31**, **WZB117**, and **BAY-876** (Figure 47). To evaluate the relative potency between Glut1 candidates, we carried out glycolysis stress tests of candidate compounds STF31, WZB117, and BAY-876 at equal concentrations. These experiments revealed that BAY-876 exhibited potent inhibition of glycolysis in highly glycolytic breast cancer cell line MDA-MB-231 when compared to STF31 and WZB117 (Figure 48).

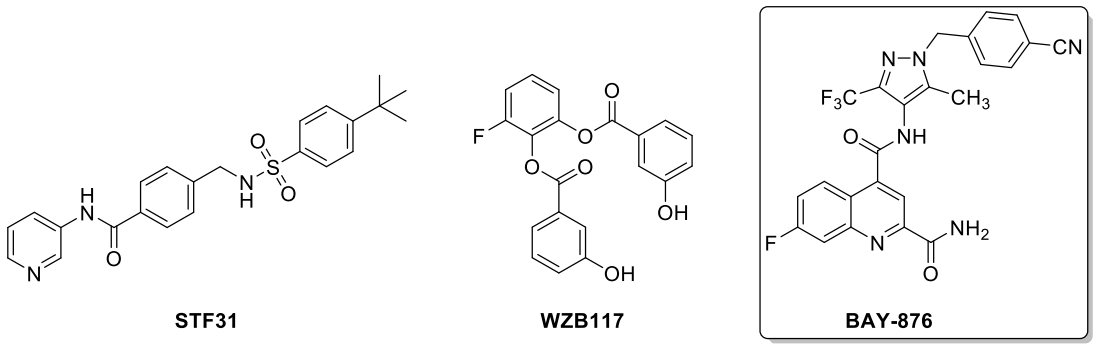

Figure 47. Structures of known Glut1 inhibitors that show anticancer properties.

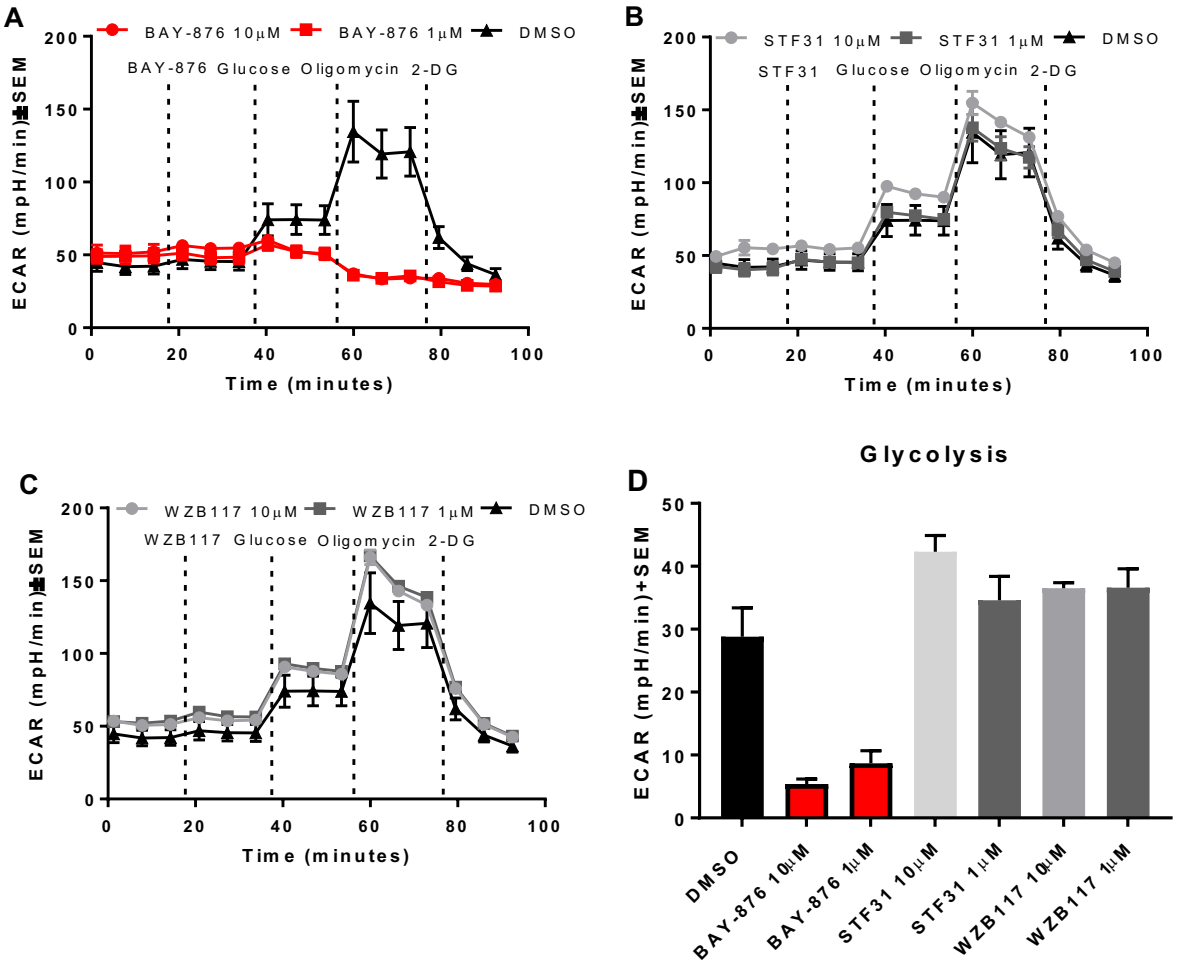

Figure 48. Glycolysis stress test of (**A**) BAY-876, (**B**) STF31, and (**C**) WZB117 in MDA-MB-231 cells. (**D**) Graphical representation of candidate compounds at inhibiting glycolysis at 10 and 1μM.

Encouraged by potent inhibition of glycolysis by BAY-876, we sought to evaluate the ability of BAY-876 and CMPD-4 to inhibit metabolic plasticity in MDA-MB-231 cells. In this regard, we carried out a Seahorse XFe96 mitochondrial stress test of the combination of candidate compounds. In these experiments, inhibition of both mitochondrial respiration and compensatory glycolysis can be simultaneously measured. Gratifyingly, the combination of BAY-876 with candidate mitochondrial pyruvate inhibitor CMPD-4 exhibited inhibition of both mitochondrial respiration and compensatory glycolysis – thereby inhibiting metabolic plasticity in MDA-MB-231 cells (Figure 49).

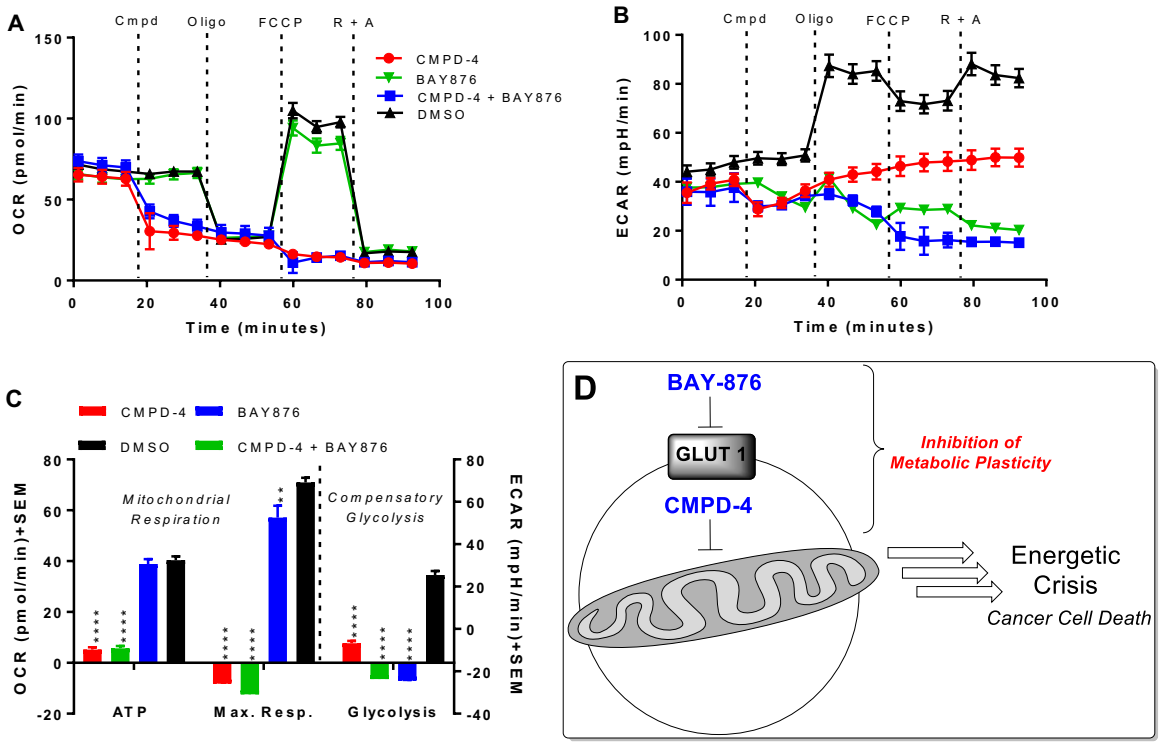

Figure 49. Mitochondrial stress test of candidate compounds enables simultaneous observation of changes in (**A**) oxygen consumption rates and (**B**) extracellular acidification rates in the presence of test compounds and mitochondrial stressors. A rise in extracellular acidification following oligomycin injection is considered compensatory glycolysis. (**C**) Graphical representation of compound effects on mitochondrial respiration and compensatory glycolysis. (**D**) Hypothesis of combination of Glut1 inhibitor **BAY-876** with mitochondrial pyruvate respiration inhibitor **CMPD-4**.

Intrigued by combinatorial inhibition of glycolysis and mitochondrial respiration with BAY-876 and CMPD-4, we sought to understand potential combination synergy in cancer cell proliferation inhibition of the candidate compounds. In this regard, we carried out *in vitro* cancer cell proliferation assays using aggressive stage IV breast cancer cell line 4T1. These results indicated that **BAY-876** and **CMPD-4** exhibited strong synergy in arresting breast cancer cell growth as indicated by combination isobologram analysis (Figure 50).

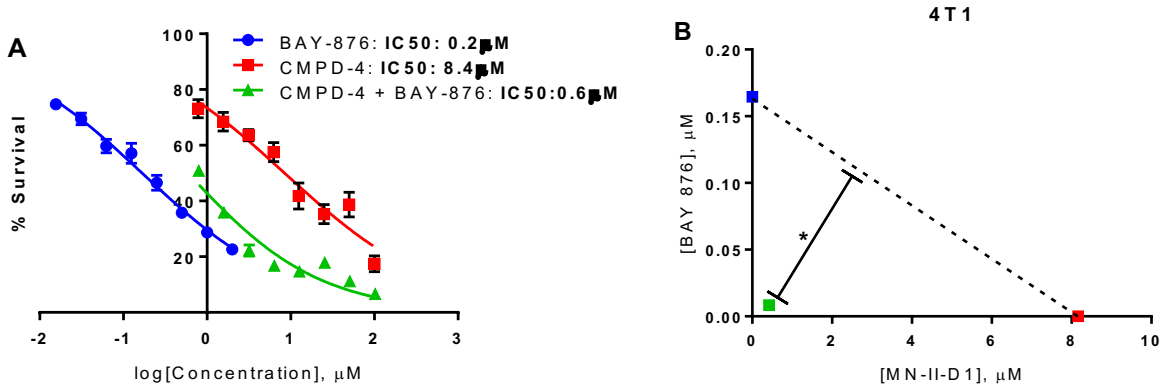

Figure 50. Combination synergy studies of **BAY-876** and **CMPD-4** in 4T1 cells reveal synergistic combination efficacy. (**A**) Log-dose plots and (**B**) isobologram analysis of synergistic combination responses.

Encouraged by synergistic combination, we sought to investigate the *in vivo* systemic toxicity of candidate mitochondrial inhibitors CMPD3-6 to further illustrate the translational potential of mitochondrial targeting agents. These studies indicated that all compounds were well tolerated over the treatment period with no effects on red-blood cell counts (Figure 51A&B). Candidate compounds also did not affect white-blood cell counts, other than a modest but statistically significant decrease in the WBC count in mice treated with CMPD-3 (Figure 51C).

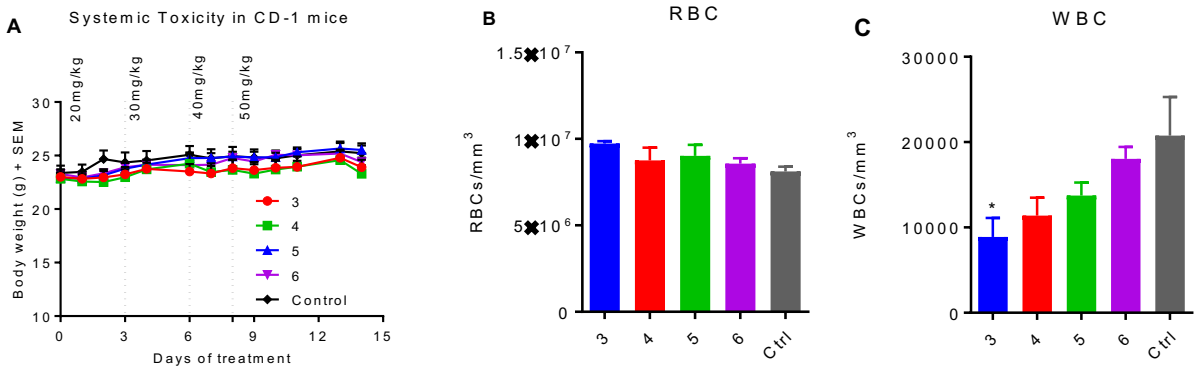

Figure 51. (**A**) Systemic toxicity study of candidate compounds in healthy CD-1 mice. Effect of treatment with candidate compounds on (**B**) red-blood cells (RBC) and (**C**) white blood cells (WBC) from the systemic toxicity study (**A**).

We further investigated the translational potential of the combination by carrying out the combination systemic toxicity study of BAY-876 and lead candidate CMPD-4 in healthy CD-1 mice. These studies indicated that the combination treatment was well tolerated at the doses tested (Figure 52).

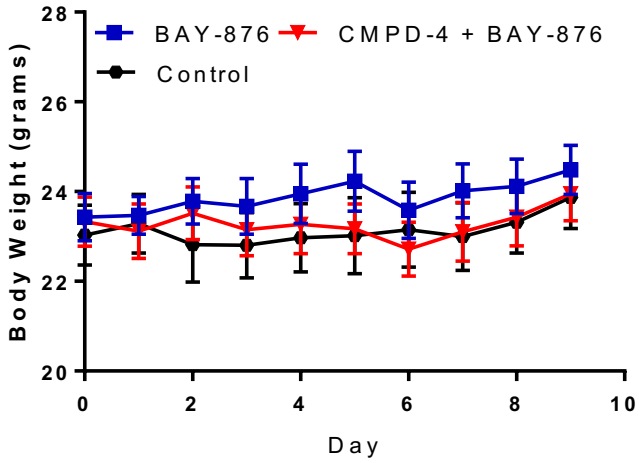

Figure 52. Combination systemic toxicity study of BAY-876 (4mg/kg) and CMPD-4 (40mg/kg) in healthy CD-1 mice.

Based on potent inhibition of mitochondrial pyruvate respiration by **CMPD-4**, inhibition of glycolysis by BAY-876, potent cell proliferation inhibition properties as single agents, synergistic combination antiproliferative effects *in vitro*, and non-toxic nature of these candidates when administered *in vivo* has qualified this combination strategy as a new-generation treatment protocol for aggressive and difficult to treat breast cancers. Since metabolic plasticity has also been identified in other aggressive solid tumors, targeting metabolic processes in rational and combinatorial fashion has the potential for broad spectrum anticancer treatment.

- **What opportunities for training and professional development has the project provided?**
  Initiating PI Mereddy: The project funds have been utilized to pay PI Mereddy's graduate students Dr. Lucas Solano (PhD Integrated Biosciences, Chemical Biology, graduated), Dr. Sravan Jonnalagadda (PhD Integrated Biosciences, Chemical Biology, graduated), Dr. Grady Nelson (PhD Integrated Biosciences, Chemical Biology, graduated), and Dr. Shirisha Jonnalagadda (PhD Integrated Biosciences, Chemical Biology, graduated). The PI has directly worked with these four graduate students on a daily basis that helped them develop various chemical and biological skills required for this particular project. It is highly gratifying to see these students develop proficiency in experimental skills in chemistry, *in vitro* biology and handling of mice including surgical techniques. Dr. Shirisha Jonnalagadda is currently a post-doctoral research fellow at Texas Tech Health Sciences Center. Dr. Sravan Jonnalagadda is currently a post-doctoral fellow at the University of Nebraska Omaha Cancer Center. Dr. Lucas Solano is a post-doctoral fellow at the University of California – Davis Cancer Center. Grady Nelson is a post-doctoral fellow at Memorial Sloan Kettering Cancer Center. Further, Mr.

Conor Ronayne, Mr. Tanner Schumacher, and Mr. Michael Williams have received rigorous training in this regard and are currently working on their PhD in Integrated Biosciences. They along with Mr. Zachary Gardner have also obtained their MS Chemistry degrees over the duration of the project. The PI also had the opportunity to train undergraduate student volunteers Ms. Mackenzie Latterell and Ms. Kaija Kottke, Michael McParlan, and Olivia Neville. These four students have learned synthetic chemistry techniques such as thin layer chromatography, column chromatography, extraction, setting up low and high temperature reactions, characterization of compounds, etc. These students have also been rigorously trained in numerous biological aspects such as cancer cell culture, metabolic assays, screening candidate compounds for biological activity, etc. Some of these undergraduate research students are working in the biomedical industry. Michael McParlan is currently continuing as an undergraduate researcher, with aspirations for graduate or medical school.

Partnering PI Drewes: Ms. Mary Sneve and Mr. Zackory Blankenheim (research technicians) worked with partnering PI Drewes. They learnt several techniques in establishing all the new cell lines and optimizing Seahorse XFe96 assays included in this report.

- **How were the results disseminated to communities of interest?**
  Nothing to Report (Initiating PI Mereddy and Partnering PI Drewes).
- **What do you plan to do during the next reporting period to accomplish the goals?**
  NA. This is the final report of the project.

Impact

- **What was the impact on the principal discipline(s) of the project?**
  Initiating PI Mereddy and Partnering PI Drewes: Vigorous glycolysis along with functional mitochondrial oxidative phosphorylation (OxPhos), is a hallmark of many advanced stage tumors. To facilitate glycolysis, cancer cells upregulate the glucose transporter 1 (Glut1) which imports extracellular glucose for bioenergetic and synthetic needs. Glycolytic metabolites such as pyruvate and lactate are transported between cells by monocarboxylate transporters 1 and 4 (MCT1&4) for further energy production. The energy rich metabolite, pyruvate, is further shuttled into the mitochondrial matrix by the mitochondrial pyruvate carrier (MPC) under conditions that demand TCA cycle and OxPhos processes. The tumor microenvironment is heterogeneous in nature, poorly vascularized at the center, and exists in nutrient-poor conditions. Under these conditions, cancer cells exhibit a catabolic phenotype, where the breakdown of glucose and other macromolecules yield high levels of biosynthetic building blocks, including lactate, that are shuttled out of the cell. These metabolites are then imported by neighboring anabolic cells, where oxygen and nutrients are readily available. In anabolic compartments, glucose and pyruvate are used as fuels to support both glycolysis and OxPhos in these highly proliferative cell types. Metabolic plasticity

between intratumoral catabolic and anabolic compartments is facilitated by Glut1, MPC, and MCT's, and targeting of these transporters has high potential for cancer treatment. In this regard, we have developed MPC/MCT based metabolic inhibitors. The proposed research is innovative because we are the first to discover MPC based MCT1&4 inhibitors and the very first to use targeting of these transporters for anticancer drug discovery and development. Our first generation MPC/MCT inhibitors highly potent, generally non-toxic, water soluble, and effective in arresting the tumor growth *in vivo* as single agents. In fact, the anticancer efficacy of our inhibitors have been evaluated in two in vivo breast cancer models 4T1-luc2 syngraft and MDA-MB-231 xenograft, and also in WiDr colorectal adenocarcinoma and GL261-luc mouse glioma models where they exhibited an efficient tumor growth reduction (~56-77%). In addition, our first generation candidate inhibitors provided significant tumor growth reduction and survival advantages in oral squamous cell carcinoma.

- **What was the impact on other disciplines?**
  The candidate compounds developed during the project period have been utilized by us as well as others for the treatment of a variety of other cancers including colorectal cancer, cervical cancer, oral squamous cell carcinoma, as well as glioblastoma. This clearly indicates the potential of our MPC/MCT inhibitors towards the treatment of several aggressive cancers.
- **What was the impact on technology transfer?**
  Initiating PI Mereddy and Partnering PI Drewes
  U. S. Patent No. 9296728 has been issued on March 29, 2016 based on the lead candidate compound. We have also filed two provisional patent applications on the new candidate compounds discovered during the project period.
- **What was the impact on society beyond science and technology?**
  Nothing to report, Initiating PI Mereddy and Partnering PI Drewes

Changes/Problems

- **Changes in approach and reasons for change**
  Initiating PI Mereddy and Partnering PI L.R. Drewes: Initially, this project was designed to evaluate the pre-clinical efficacy of novel MCT1/4 inhibitors developed in our lab for breast cancer treatment. These first-generation compounds exhibited excellent pharmacological properties with low nanomolar potency for both MCT1 and MCT4. These compounds are also very well tolerated in healthy mice at clinically relevant dosages. In our early aims for this project, we carried out *in vivo* efficacy studies using human and murine breast cancer cell lines in syn- and xenograft tumor models, where these candidates exhibited does dependent tumor growth inhibition. In this regard, we have carried out the *in vivo* pharmacokinetic studies which revealed that these candidates are rapidly eliminated, with low biological half-lives (~30min). Since our primary goal is to develop drug candidates that are suitable for clinical translation, we envisioned that our first generation candidates will be limited in their clinical translation because of unfavorable

pharmacokinetic properties. Further, literature studies and our own experiments have revealed that the cyanocinnamate and coumarin based drug candidates potently inhibit mitochondrial pyruvate transport, and inhibit MCT mediated lactate transport as a feedback mechanism, that can be attributed to inhibition of the mitochondrial pyruvate carrier (MPC). Additionally, our first generation candidates, although potent MCT inhibitors, did not exhibit potent antiproliferative properties in breast cancer cells *in vitro*. To improve the pharmaceutical, anticancer, and MPC inhibitory properties, we have changed our approach and developed several new-generation drug candidates as described in the report.

- **Actual or anticipated problems or delays and actions or plans to resolve them**
  NA, this is the final report.
- **Changes that had a significant impact on expenditures**
  Initiating PI Mereddy and Partnering PI Drewes: We have allocated some of the funds initially budgeted for *in vivo* animal studies toward the development of new generation drug candidates with improved pharmaceutical and pharmacological properties with high potential for clinical translation.
- **Significant changes in use or care of human subjects, vertebrate animals, biohazards, and/or select agents.**
  NA.

Products

- **Publications, conference papers, and presentations**
  - **Journal publications**

    1. Jonnalagadda, S., Jonnalagadda, S. K., Ronayne, C. T., Nelson, G. L., Solano, L. N., Rumbley, J., Holy, J., Drewes, L. R., Mereddy, V. R. (2019) Novel N,N-dialkyl cyanocinnamic acids as monocarboxylate transporter 1 and 4 inhibitors, Oncotarget. 10(24): 2355–2368.
    2. Gurrapu, S., Jonnalagadda, S. K., Alam, M. A., Ronayne, C. T., Nelson, G. L., Solano, L. N., Lueth, E. A., Drewes, L. R., Mereddy, V. R. (2016) Coumarin carboxylic acids as monocarboxylate transporter 1 inhibitors: In vitro and in vivo studies as potential anticancer agents. Bioorg Med Chem Lett. 26, 3282-6.
    3. Cong, A., Pimenta R. M. L., Lee H. B., Mereddy, V. R., Holy, J., Heikal, A. A., (2019) Two-Photon Fluorescence Lifetime Imaging of Intrinsic NADH in Three-Dimensional Tumor Models, Cytometry Part A. 95(1):80-92.
    4. Khammanivong, A., Saha, J., Spartz, A.K., Sorenson, B.S., Bush, A.G., Gopalakrishnan, R., O'Brian, T.D., Jonnalagadda, S., Mereddy, V.R., Drewes, L.R., Dickerson, E.B., (2019) A novel MCT1 and MCT4 dual inhibitor reduces mitochondrial metabolism and inhibits tumor growth of feline oral squamous cell carcinoma, Veterinary and Comparative Oncology. DOI: 10.1111/vco.12551

5. Nelson, G.L., Ronayne, C.T., Solano, L.S., Jonnalagadda, S.K., Jonnalagadda, S., Rumbley, J., Holy, J., Rose-Hellekant, T., Drewes, L.R., Mereddy, V.R., (2019) Development of Novel Silyl Cyanocinnamic Acid Derivatives as Metabolic Plasticity Inhibitors for Cancer Treatment, Scientific Reports, (Manuscript accepted, SREP-19-30760)
Several additional manuscripts are in preparation based on our new generation candidates described in the report.

- **Books or other non-periodical, one-time publications**
  None
- **Other**
  None

- **Website or other internet site**
  None
- **Technologies or techniques**
  None
- **Inventions, patent applications, and/or licenses**
  Mereddy, V. R., Drewes, L. R., Alam, M. A., Jonnalagadda, S. K., Gurrapu, S. (2016). Therapeutic Compounds, US 9296728 B2 20160329.
  We have also filed two provisional patent applications on the new candidate compounds discovered during the project period.
- **Other products**
  None

Participants and Other Collaborating Organizations

- **What individuals have worked on the project?**

Name:	Lester R. Drewes
Project Role:	PI
Researcher Identifier (e.g. ORCID ID):	0000-0002-7440-0387
Nearest person month worked:	3
Contribution to Project:	Research director, administrator, supervisor, data interpreter, author
Funding Support:	NA
Name:	Teresa Rose-Hellekant
Project Role:	Faculty
Researcher Identifier (e.g. ORCID ID):	NA
Nearest person month worked:	1
Contribution to Project:	collaborator, cancer expert
Funding Support:	NA
Name:	Mary Sneve
Project Role:	Researcher

Researcher Identifier (e.g. ORCID ID):	None
Nearest person month worked:	17
Contribution to Project:	lab staff, technical support
Funding Support:	NA
Name:	Zachary Blankenheim
Project Role:	Researcher
Researcher Identifier (e.g. ORCID ID):	None
Nearest person month worked:	10
Contribution to Project:	lab staff, technical support
Funding Support:	NA

- **Has there been a change in the active other support of the PD/PI(s) or senior/key personnel since the last reporting period?**
  No

- **What other organizations were involved as partners?**
  None

Special Reporting Requirements

- **Collaborative Awards**
  None
- **Quad Charts:** NA

Appendices

Publications from this project have been appended.

Published in final edited form as:

Bioorg Med Chem Lett. 2016 July 15; 26(14): 3282–3286. doi:10.1016/j.bmcl.2016.05.054.

Coumarin carboxylic acids as monocarboxylate transporter 1 inhibitors: In vitro and in vivo studies as potential anticancer agents

Shirisha Gurrapu[a], **Sravan K. Jonnalagadda**[a], **Mohammad A. Alam**[b], **Conor T. Ronayne**[b], **Grady L. Nelson**[a], **Lucas N. Solano**[a], **Erica A. Lueth**[b], **Lester R. Drewes**[a,c], and **Venkatram R. Mereddy**[a,b,d,*]

[a]Integrated Biosciences Graduate Program, University of Minnesota, Duluth, MN 55812, United States

[b]Department of Chemistry and Biochemistry, University of Minnesota Duluth, Duluth, MN 55812, United States

[c]Department of Biomedical Sciences, Medical School Duluth, University of Minnesota Duluth, MN 55812, United States

[d]Department of Pharmacy Practice & Pharmaceutical Sciences, University of Minnesota, Duluth, MN 55812, United States

Abstract

Novel *N,N*-dialkyl carboxy coumarins have been synthesized as potential anticancer agents via inhibition of monocarboxylate transporter 1 (MCT1). These coumarin carboxylic acids have been evaluated for their in vitro MCT1 inhibition, MTT cancer cell viability, bidirectional Caco-2 cell permeability, and stability in human and liver microsomes. These results indicate that one of the lead candidate compounds **4a** has good absorption, metabolic stability, and a low drug efflux ratio. Systemic toxicity studies with lead compound **4a** in healthy mice demonstrate that this inhibitor is well tolerated based on zero animal mortality and normal body weight gains compared to the control group. In vivo tumor growth inhibition studies in mice show that the candidate compound **4a** exhibits significant single agent activity in MCT1 expressing GL261-luc2 syngraft model but doesn't show significant activity in MCT4 expressing MDA-MB-231 xenograft model, indicating the selectivity of **4a** for MCT1 expressing tumors.

Keywords

N,N-Dialkyl carboxy coumarin; Tumor glycolysis; Monocarboxylate transporter 1; MCT; Glioblastoma; GL261-luc2; Triple negative breast cancer; MDA-MB-231

Numerous cancer chemotherapeutics have been developed over the past 50 years to improve the quality of patient care and overall survival rate. However, cancer continues to be one of the major killers throughout the world. Suboptimal efficacy, unacceptable side effects, and

*Corresponding author. Tel.: +1 218 726 6776; fax: +1 218 726 7394. vmereddy@d.umn.edu (V.R. Mereddy).

development of chemo-resistance are some of the reasons for treatment failure and patient mortality. Hence, new candidate compounds with novel mechanisms of action, low side effects, and that work on all stages of tumors are urgently needed.

Recent studies indicate that alteration in cellular metabolism is a crucial hallmark of cancer development.[1,2] Therefore, tumor metabolism is an attractive target for developing new cancer therapeutics. [3,4] The metabolic properties of cancer cells differ significantly from those of normal cells. In normal differentiated tissues, cellular energy is generated mainly via an efficient oxidative phosphorylation (OxPhos). In contrast, cancer cells pursue vigorous glycolysis even in the presence of sufficient amounts of oxygen (Warburg effect, WE).[5–10] Glycolysis generates only two moles of ATP per one mole of glucose compared to OxPhos, which can produce up to 38 moles of ATP. To compensate this energy inefficiency, cancer cells upregulate glycolytic enzymes to keep up with the energy requirements of cell proliferation and tumor progression. Maintaining a high level of glycolytic activity is essential for survival, fueling anabolic pathways, tumor advancement, resistance to apoptosis, and invasion and metastasis of cancer cells.[5–11]

Because cancer cells are mainly dependent on glycolysis for their survival and propagation, they need to export the glycolysis end products pyruvic and lactic acids to avoid cytoplasmic acidification that may lead to apoptosis. To accomplish this task, cancer cells upregulate proton-coupled membrane proteins called monocarboxylate transporters (MCTs), which are responsible for transmembrane shuttling of small carboxylates such as lactate, pyruvate, and ketone bodies.[12–18] There are 14 known isoforms of MCTs, but MCTs 1–4 are responsible for transporting these carboxylates. They are also implicated in influx and efflux of lactate by cancer-associated stromal fibroblasts and epithelial cancer cells for energy generation.[19–22] Elevated expression of MCT1 has been identified in a large number of cancers and, therefore, this transporter is a major selective target for broad-spectrum cancer treatment.[23–34] In this regard, we recently developed a series of MCT1 inhibitors based on the α-hydroxy-4-cyanocinnamic acid (CHC) template for potential anticancer applications.[23] Although our earlier CHC based MCT1 inhibitors are potent, the lead compounds suffer from poor oral bioavailability and toxicity at high concentrations. In this regard, we envisioned to utilize a similar but bicyclic coumarin template to improve absorption, distribution, metabolism and elimination properties, decrease systemic toxicity and improve anticancer efficacy. Coumarin is a key structural unit with good pharmaceutical properties that is found in many important medicinal molecules.[35–37] Structure-activity relationship studies using our first generation CHC template indicated that placing *N,N*-dialkyl/diaryl groups at the 4-position demonstrated the most optimized structural moiety for potent MCT1 inhibition. Therefore, we synthesized carboxy coumarins with *N, N*-dialkyl substitution at the 7-position as second generation MCT1 inhibitors (Fig. 1).[25]

Here, we report on the pre-clinical evaluation of novel coumarin carboxylic acids. Included is the synthesis, in vitro MCT1 inhibition, cytotoxicity against two cancer cell lines, in vitro Caco-2 permeability and metabolic stability in mouse and human liver microsomes. Systemic toxicity studies in CD-1 mice, in vivo anticancer efficacy in glioblastoma GL261-luc2 syngraft and MDA-MB-231-luc xenograft mouse models are also reported.

We synthesized *N,N*-dialkyl carboxy coumarins starting from the alkylation of *o*-aminophenol **1** to obtain *N,N*-dialkylated-*o*-aminophenols **2**. These alkylated aminophenols were formylated under Vilsmeier Haack conditions with $POCl_3$ and DMF to obtain the corresponding aldehydes **3** in 60–70% yields. The aldehydes **3**, upon Knoevenagel condensation with diethyl malonate, followed by the treatment with aqueous NaOH at 100 °C and adjusting pH to 7 at room temperature provided carboxy coumarins **4a**–**4e** (Scheme 1).[38]

We then carried out the MCT1 inhibition study of **4a**–**4e** using L-[^{14}C]-lactate uptake on rat brain endothelial-4 cells that predominantly express MCT1.[23] This transport inhibition study revealed carboxy coumarins **4a**–**4e** as potent inhibitors of MCT1 at nanomolar to low micromolar concentrations (Table 1).

Encouraged by excellent inhibition of MCT1, we then evaluated cytotoxicity of compounds **4a**–**4e** in two cancer cell lines that are known to express either MCT1 or MCT4. For this purpose, a predominantly MCT1 expressing cell line, GL261-luc2, and an MCT4 expressing cell line, MDA-MB-231 were chosen (Fig. 2).[39] GL261 is an important and a well-established mouse glioblastoma (GBM) cell line that closely mimics human gliomas.[40,41] MDA-MB-231 is a triple negative breast cancer cell line derived from human tissue.

To determine in vitro toxicity, we evaluated cell viability using 3-(4,5-dimethylthiazol-2-yl)-2,5-diphenyl tetrazolium bromide (MTT) assay.[42,43] This colorimetric assay measures the reduction of MTT to formazan by cellular mitochondrial reductase as a measure of cell viability. Compounds **4a**–**4e** were found to be generally non-cytotoxic at high concentrations as can be expected from MCT inhibitors (Table 2). These results suggest that under in vitro conditions, the cancer cells are able to adapt their metabolism to other pathways to maintain viability. Furthermore, it was reported that potent inhibition of MCT1 did not have any appreciable cytotoxic properties for several solid tumor cell lines.[44] In contrast, in in vivo systems where tumor hypoxia is prevalent, cancer cells are dependent on ATP generation via vigorous glycolysis for essential metabolites, survival, and proliferation. Hence, chronic administration of an MCT1 inhibitor in vivo should hamper the glycolytic process, leading to severe energy crisis and tumor growth inhibition. Based on its excellent MCT1 inhibition, slightly enhanced cytotoxicity, and favorable solubility, compound **4a** was selected for further in vitro and in vivo evaluation.

We then determined its potential oral bioavailability using bidirectional Caco-2 cell monolayer permeability, and its metabolic stability in human and mouse liver microsomes (Tables 3–5).[45,46] Caco-2 cell permeability assays for **4a** in both apical to basolateral (A – B) and basolateral to apical (B – A) directions were carried out to predict its potential oral bioavailability. Caco-2 is a heterogeneous human epithelial colorectal adenocarcinoma cell line that mimics the human enterocytic intestinal layer.[45] This assay estimates human intestinal permeability and drug efflux ratio of the compounds. **4a** showed relatively low A – B and moderate B – A permeability (Table 3). Based on this study, **4a** exhibits much better absorption (~30%) compared to poor absorption of first generation MCT1 inhibitors (3–6%, data not shown). Propranolol (highly permeable), labetalol (moderately permeable), ranitidine (poorly permeable), and colchicine (P-glycoprotein substrate) were used as

controls. The efflux ratio was calculated using the formula $P_{app}(B - A)/P_{app}(A - B)$ and efflux ratio >2 signifies that drug efflux is occurring. **4a** has an efflux ratio of 0.2 indicating that the efflux rate is very low and **4a** may not be a good substrate for drug efflux transporters, which is beneficial for providing anticancer efficacy.

We then determined the metabolic stability (half-life) of **4a** in human and mouse liver microsomes in order to assess its hepatic clearance rate because liver microsomes contain many enzymes that are responsible for drug metabolism. **4a** exhibited good metabolic stability (half-life >60 min) in both human and mouse liver microsomes (Tables 4 and 5). Propranolol, imipramine, verapamil, and terfenadine were used as controls with high, high, medium, and low metabolic stabilities, respectively, in human liver microsomes.

We then evaluated the systemic toxicity profile of **4a** in healthy CD-1 mice.[47] Mice were treated once daily (qd) with **4a** intraperitoneally (ip, 20 mg/kg) and via oral gavage (100 mg/kg). Control mice received the vehicle (10% DMSO in saline). At the end of the study, the treated groups did not show any visible toxic effects or mortality and had no significant difference in body weights compared to the control group (Fig. 3). This study indicates the nontoxic nature of the candidate compound **4a** for in vivo anticancer applications.

We then evaluated anticancer efficacy of **4a** in a flank-based GL261-luc2 tumor syngraft model.[47–49] Group 1 was administered with **4a** (20 mg/kg, ip, qd), group 2 was treated with the clinically used brain tumor drug temozolomide (20 mg/kg, ip, qd) and the control group was given vehicle. At the end of the study, the tumor growth inhibition of compound **4a** and temozolomide was found to be 77% and 81%, respectively, compared to the control group (Fig. 4). This efficacy study demonstrated the therapeutic utility of **4a** for potential anticancer applications.

To determine whether **4a** is capable of exhibiting antitumor properties in high MCT4 and low MCT1 expressing tumors, we evaluated the tumor growth inhibition in an MDA-MB-231-luc flank-based xenograft model.[47,49,50] Group 1 and group 2 mice were administered with compound **4a** at two different dosages of 20 mg/kg, ip, qd and 100 mg/kg, oral gavage, qd. Group 3 was treated with the clinically used breast cancer drug doxorubicin (0.5 mg/kg, ip, 5 days/week). The control group was administered with vehicle (10% DMSO in saline). At the end of the study (day-19), the tumor growth inhibition in groups 1, 2, and 3 were found to be 10%, 13%, and 50% respectively, compared to the control group (Fig. 5). This study indicates that compound **4a** doesn't exhibit significant tumor growth reduction in a predominantly MCT4 expressing tumor model.

In conclusion, we synthesized *N,N*-dialkyl carboxy coumarins as MCT1 inhibitors and carried out in vitro cytotoxicity studies in MCT1 and MCT4 expressing cell lines. Selected inhibitor **4a** was further studied for its in vitro bidirectional Caco-2 cell permeability and metabolic stability in human and mouse liver microsomes. This lead compound **4a** exhibited good absorption, metabolic stability, and a low drug efflux ratio. Systemic toxicity studies in healthy CD-1 mice indicated that compound **4a** was well tolerated and treated animals gained normal body weights with no apparent side effects. The candidate compound **4a** was evaluated for in vivo tumor growth inhibition in predominantly MCT1 expressing GL261-

luc2 glioma syngraft, and MCT4 expressing MDA-MB-231 xenograft mouse models. These in vivo studies indicated that compound **4a** significantly inhibited tumor growth in GL261-luc2 model, but did not exhibit any significant activity in MDA-MB-231-luc model. This emphasizes the importance of high MCT1 expression for the efficacy of these inhibitors. Owing to the importance of glycolysis in tumor progression and the elevated expression of MCT1 in several cancers, we believe that these inhibitors have good potential to be developed as broad-spectrum anticancer agents. **4a** can be used as a single agent and can also be combined with other chemotherapeutic agents with different mechanisms of action to realize their synergistic potential in cancer treatment.

Acknowledgments

This work was supported by University of Minnesota Duluth; Department of Defense Breast Cancer Research Proposal, Break-through Award W81XWH-15-1-0047; Whiteside Clinical Research Institute, Duluth, Minnesota; Center for Pharmaceutical Development, University of Minnesota; Minnesota Partnership for Biotechnology & Medical Genomics; Masonic Cancer Center Brainstorm Mechanism, University of Minnesota; and KAM and Bighley Foundation, University of Minnesota.

References and notes

1. Hanahan D, Weinberg RA. Cell. 2011; 144:646. [PubMed: 21376230]
2. Hanahan D, Weinberg RA. Cell. 2000; 100:57. [PubMed: 10647931]
3. Erez A, DeBerardinis RJ. Nat Rev Cancer. 2015; 15:440. [PubMed: 26084394]
4. Cantor JR, Sabatini DM. Cancer Discovery. 2012; 2:881. [PubMed: 23009760]
5. Peppicelli S, Bianchini F, Calorini L. Oncoscience. 2015; 2:225. [PubMed: 25897425]
6. Ganapathy-Kanniappan S, Geschwind JF. Mol Cancer. 2013; 12:152. [PubMed: 24298908]
7. Ganapathy V, Thangaraju M, Prasad PD. Pharmacol Ther. 2009; 121:29. [PubMed: 18992769]
8. Hsu PP, Sabatini DM. Cell. 2008; 134:703. [PubMed: 18775299]
9. Sonveaux P, Vegran F, Schroeder T, Wergin MC, Verrax J, Rabbani ZN, De Saedeleer CJ, Kennedy KM, Diepart C, Jordan BF, Kelley MJ, Gallez B, Wahl ML, Feron O, Dewhirst MW. J Clin Invest. 2008; 118:3930. [PubMed: 19033663]
10. Gatenby RA, Gillies RJ. Nat Rev Cancer. 2004; 4:891. [PubMed: 15516961]
11. Vander Heiden MG. Nat Rev Drug Discovery. 2011; 10:671. [PubMed: 21878982]
12. Halestrap AP. Mol Aspects Med. 2013; 34:3379.
13. Pinheiro C, Longatto-Filho A, Azevedo-Silva J, Casal M, Schmitt FC, Baltazar F. J Bioenerg Biomembr. 2012; 44:127. [PubMed: 22407107]
14. Pavlides S, Whitaker-Menezes D, Castello-Cros R, Flomenberg N, Witkiewicz AK, Frank PG, Casimiro MC, Wang C, Fortina P, Addya S, Pestell RG, Martinez-Outschoorn UE, Sotgia F, Lisanti MP. Cell Cycle. 2009; 8:3984. [PubMed: 19923890]
15. Spanier, J., Drewes, LR. Drug Transporters: Molecular Characterization and Role in Drug Disposition. You, G., Morris, ME., editors. Wiley Publishers; New York: 2007. p. 147
16. Wang Q, Morris ME. Drug Metab Dispos. 2007; 35:1393. [PubMed: 17502341]
17. Murray CM, Hutchinson R, Bantick JR, Belfield GP, Benjamin AD, Brazma D, Bundick RV, Cook ID, Craggs RI, Edwards S, Evans LR, Harrison R, Holness E, Jackson AP, Jackson CG, Kingston LP, Perry MW, Ross AR, Rugman PA, Sidhu SS, Sullivan M, Taylor-Fishwick DA, Walker PC, Whitehead YM, Wilkinson DJ, Wright A, Donald DK. Nat Chem Biol. 2005; 1:371. [PubMed: 16370372]
18. Halestrap AP, Price NT. Biochem J. 1999; 343:281. [PubMed: 10510291]
19. Sotgia F, Martinez-Outschoorn UE, Lisanti MP. Oncotarget. 2014; 5:7982. [PubMed: 25478627]
20. Wang H, Yang C, Doherty JR, Roush WR, Cleveland JL, Bannister TD. J Med Chem. 2014; 57:7317. [PubMed: 25068893]

21. Witkiewicz AK, Whitaker-Menezes D, Dasgupta A, Philp NJ, Lin Z, Gandara R, Sneddon S, Martinez-Outschoorn UE, Sotgia F, Lisanti MP. Cell Cycle. 2012; 11:1108. [PubMed: 22313602]
22. Lisanti MP, Martinez-Outschoorn UE, Chiavarina B, Pavlides S, Whitaker-Menezes D, Tsirigos A, Witkiewicz A, Lin Z, Balliet R, Howell A, Sotgia F. Cancer Biol Ther. 2010; 10:537. [PubMed: 20861671]
23. Gurrapu S, Jonnalagadda SK, Alam MA, Nelson GL, Sneve MG, Drewes LR, Mereddy VR. ACS Med Chem Lett. 2015; 6:558. [PubMed: 26005533]
24. Doherty JR, Yang C, Scott KE, Cameron MD, Fallahi M, Li W, Hall MA, Amelio AL, Mishra JK, Li F, Tortosa M, Genau HM, Rounbehler RJ, Lu Y, Dang CV, Kumar KG, Butler AA, Bannister TD, Hooper AT, Unsal-Kacmaz K, Roush WR, Cleveland JL. Cancer Res. 2014; 74:908. [PubMed: 24285728]
25. While this work was in progress, two publications have appeared on the utilization of aminocarboxy coumarins as MCT1 inhibitors. Draoui N, Schicke O, Seront E, Bouzin C, Sonveaux P, Riant O, Feron O. Mol Cancer Ther. 2014; 13:1410. [PubMed: 24672058] Draoui N, Schicke O, Fernandes A, Drozak X, Nahra F, Dumont A, Douxfils J, Hermans E, Dogne JM, Corbau R, Marchand A, Chaltin P, Sonveaux P, Feron O, Riant O. Bioorg Med Chem. 2013; 21:7107. [PubMed: 24095010] Draoui N, Feron O, Riant O, Sonveaux P, Schicke O, Fernandes A, Kilonda A, Vanherck J, Marchand A. PCT Int Appl. WO 2014195507 A1 20141211. 2014
26. Sanita P, Capulli M, Teti A, Galatioto GP, Vicentini C, Chiarugi P, Bologna M, Angelucci A. BMC Cancer. 2014; 14:154. [PubMed: 24597899]
27. Baek G, Tse YF, Hu Z, Cox D, Buboltz N, McCue P, Yeo CJ, White MA, DeBerardinis RJ, Knudsen ES, Witkiewicz AK. Cell Rep. 2014; 9:2233. [PubMed: 25497091]
28. Curry JM, Tuluc M, Whitaker-Menezes D, Ames JA, Anantharaman A, Butera A, Leiby B, Cognetti DM, Sotgia F, Lisanti MP, Martinez-Outschoorn UE. Cell Cycle. 2013; 12:1371. [PubMed: 23574725]
29. Mereddy, VR., Drewes, LR., Alam, MA., Sravan, KJ., Gurrapu, S. PCT Int Appl. WO2013109972. 2013.
30. Miranda-Goncalves V, Honavar M, Pinheiro C, Martinho O, Pires MM, Pinheiro C, Cordeiro M, Bebiano G, Costa P, Palmeirim I, Reis RM, Baltazar F. Neuro Oncol. 2013; 15:172. [PubMed: 23258846]
31. Pertega-Gomes N, Vizcaino JR, Miranda-Goncalves V, Pinheiro C, Silva J, Pereira H, Monteiro P, Henrique RM, Reis RM, Lopes C, Baltazar F. BMC Cancer. 2011; 11:312. [PubMed: 21787388]
32. Colen CB, Shen Y, Ghoddoussi F, Yu P, Francis TB, Koch BJ, Monterey MD, Galloway MP, Sloan AE, Mathupala SP. Neoplasia. 2011; 13:620. [PubMed: 21750656]
33. Draoui N, Feron O. Dis Model Mech. 2011; 4:727. [PubMed: 22065843]
34. Hao J, Chen H, Madigan MC, Cozzi PJ, Beretov J, Xiao W, Delprado WJ, Russell PJ, Li Y. Br J Cancer. 2010; 103:1008. [PubMed: 20736947]
35. Kale M, Patwardhan K. Curr Pharma Res. 2014; 4:1150.
36. Pangal A, Gazge M, Mane V, Shaikh JA. Int J Pharm Res Biosci. 2013; 2:168.
37. Jain PK, Joshi H. J Appl Pharm Sci. 2012; 2:236.
38. *Representative procedure for the synthesis of 7-(dibenzylamino)-2-oxo-2H-chromene-3-carboxylic acid* **4a**: To a solution of 3-aminophenol (10 mmol) in 10 mL DMSO (ethanol-H_2O for other alkyl bromides), was added benzyl bromide (40 mmol), potassium carbonate (20 mmol) and refluxed at 80 °C for 12 h. Upon the completion of the reaction, the reaction mixture was extracted with ethyl acetate and water. The organic layer was dried with anhydrous Mg_2SO_4 and evaporated to obtain the 3-(dibenzylamino)phenol. The product was purified via column chromatography. To a solution of 3-(dibenzylamino) phenol (10 mmol) in DMF (60 mmol) was added phosphorous oxychloride dropwise at 0 °C and the reaction mixture was refluxed at 80 °C for 2–4 h. The reaction was quenched in a saturated solution of sodium carbonate and the solid was filtered and washed with hexanes to obtain 4-(dibenzylamino)-2-hydroxybenzaldehyde. To a solution of this aldehyde (10 mmol) in 20 ml ethanol, was added diethyl malonate (20 mmol), acetic acid (5 drops) and piperidine (13 mmol) and refluxed for 8–12 h at 80 °C. Upon the completion of the reaction, the above solution was evaporated and extracted with ethyl acetate. The organic layers were dried with anhydrous $MgSO_4$ and evaporated. The product obtained was further refluxed in 20 ml of 10%

NaOH solution. The reaction was quenched with 3 M HCl (pH 7.0) and extracted with ethyl acetate. The compound was purified by column chromatography (eluted with 100% ethyl acetate) and recrystallized. ^{1}H NMR (500 MHz, $CDCl_3$): δ 12.31 (s, 1H), 8.69 (s, 1H), 7.48–7.23 (m, 11H), 6.86 (dd, J = 8.5, 1.5 Hz, 1H), 6.67 (s, 1H), 4.84 (s, 4H); ^{13}C NMR (125 MHz, $CDCl_3$): 165.53, 164.24, 157.89, 155.60, 150.75, 135.84, 132.23, 129.46, 128.16, 126.52, 112.02, 109.79, 107.24, 98.63, 55.03; Anal. Calcd for $C_{24}H_{19}NO_4$·HCl (421.88): C, 68.33; H, 4.78; N, 3.32. Found: C, 69.22; H, 4.88; N, 3.43.

39. *Western blot analysis of MCT1 and MCT4 expression:* Cultured cells were scraped from culture flasks and immediately frozen. Cells were thawed on ice and solubilized in 200 μL SDS boiling buffer, then centrifuged for 2 min at high speed. The supernatant was collected and diluted 1:5 with deionized H_2O and assayed for protein using the BCA protocol. A volume containing 10 μg was loaded on SDS PAGE gels (Novex) for standard electrophoresis (40 min at 200 V). Proteins were transferred from the gel to nitrocellulose membrane under denaturing conditions (200 mA for 1.75 h). MCT1 and MCT4 were detected using specific antibodies (rabbit polyclonal IgG antibody for MCT1, sc-50324; rabbit polyclonal IgG antibody for MCT4, sc50329; Santa Cruz, Inc.) and visualized using chemiluminescence. For relative quantitation, actin was detected and measured as a control protein.
40. Newcomb EW, Lymberis SC, Lukyanov Y, Shao Y, Schnee T, Devitt M, Rosenstein BS, Zagzag D, Formenti SC. Cell Cycle. 2006; 5:93. [PubMed: 16319534]
41. Winkler F, Kienast Y, Fuhrmann M, Von Baumgarten L, Burgold S, Mitteregger G, Kretzschmar H, Herms J. Glia. 2009; 57:1306. [PubMed: 19191326]
42. Niks M, Otto M. J Immunol Methods. 1990; 130:149. [PubMed: 2358686]
43. *Cell culture conditions and MTT cytotoxicity:* MDA-MB-231 cells (ATCC) were grown in DMEM supplemented with 10% FBS and penicillin-streptomycin (50 U/ml, 50 μg/ml). GL261-luc2 cells (Perkin Elmer) were cultured in DMEM, 10% FBS, 50 μg/mL geneticin and penicillin-streptomycin (50 U/ml, 50 μg/ml). Cells (5×10^3 cells/well) were seeded in 96-well plate and incubated at 37 °C and 5% CO_2 for 24 h. Test compounds were added to the wells in replicate and incubated for 72 h. 10 μL MTT (12 mM in 1X PBS) was added in each well and incubated for 4 h before adding 100 μL SDS (1 g/10 mL 0.01 N HCl) to dissolve formazan precipitate and incubated for further 4 h. Absorbance was recorded at 570 nm. Percent survival was calculated using the formula %survival = (abs test compound/abs of DMSO control) × 100. IC_{50} was obtained using GraphPad by plotting log[concentration] on x-axis and% survival on y-axis.
44. Critchlow, SE., Tate, L. PCT Int Appl. WO 2010089580A1 20100812. 2010.
45. Hidalgo IJ, Raub TJ, Borchardt RT. Gastroenterology. 1989; 96:736. [PubMed: 2914637]
46. Obach RS, Baxter JG, Liston TE, Silber BM, Jones BC, MacIntyre F, Rance DJ, Wastall P. J Pharmacol Exp Ther. 1997; 283:46. [PubMed: 9336307]
47. *Ethical considerations:* The experimental procedure involving animals that were conducted at the University of Minnesota Duluth was in compliance with the U.S. National Institutes of Health Guide for Care and Use of Laboratory Animals and approved by the Institutional Animal Care and Use Committee (IACUC). Studies with protocols 1311-31063A (systemic toxicity, Fig. 3) and 1312-31108A (GL261-luc2 syngraft, Fig. 4) were conducted at University of Minnesota. MDA-MB-231-luc xenograft study (Fig. 5) was conducted by GenScript Corporation (Piscataway, NJ) according to their approved IACUC protocol GS-PAMD1401SN052.
48. *Tumor growth inhibition studies in GL261-luc2 syngraft model:* Tumor cells suspended in 1:1 matrigel-PBS were injected onto the right flank of C57BL/6 mice (5×10^6 GL261-luc2 cells). The mice were randomly assigned into groups (n = 6, male and female mice). Treatment was started when tumor volume reached 200 mm^3. Tumors were measured by caliper every two or three days and tumor volumes calculated using the formula $V = (ab^2)/2$ where ‘a’ is the long diameter of the tumor and ‘b’ is the short diameter of the tumor. Mice were euthanized at the end of the study and tumors were isolated and weighed. The inhibition amount was determined using the formula % inhibition = [(C − T)/C] × 100 where C is average tumor weight of the control group and T is the average tumor weight of the test group.
49. *Statistical analysis:* Statistics were computed using GraphPad Prism version 6.0. Mann-Whitney test was used to compare the treated and untreated groups for all in vivo tumor syngraft/xenograft studies. A P-value of <0.05 was considered significant.

50. *Tumor growth inhibition studies in MDA-MB-231 xenograft model:* Tumor cells suspended in 1:1 matrigel-PBS were injected on right flank of female SCID mice (10×10^6 MDA-MB-231 cells). The mice were randomly assigned into groups ($n = 6$). Treatment was initiated when the average tumor volume was ~100 mm^3. Mice were euthanized at the end of the study and tumors were isolated and weighed. Tumor growth inhibition was calculated as above in Ref. 49.

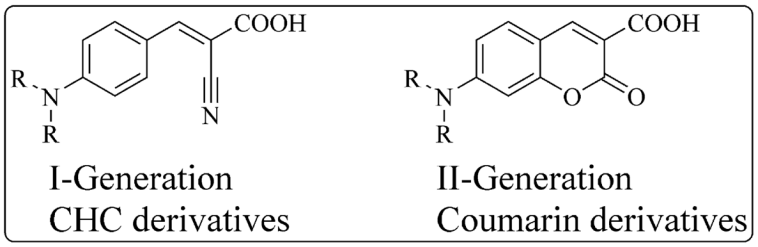

Figure 1.
CHC and coumarin derivatives.

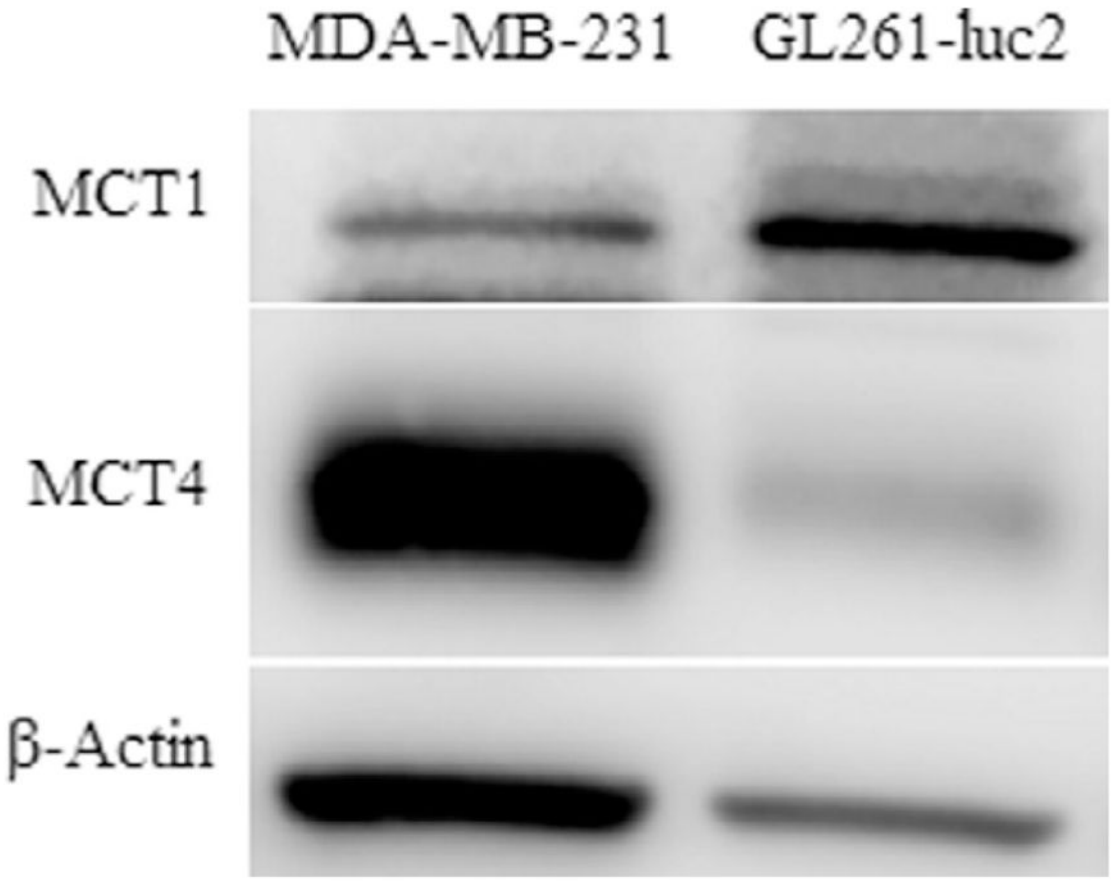

Figure 2.
Western blot analysis of MCT1 and MCT4 expression in GL261-luc2 and MDA-MB-231 cell lines.

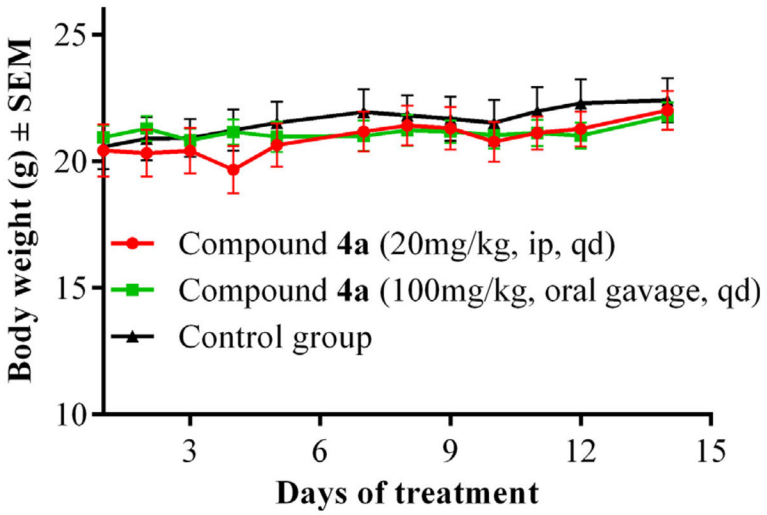

Figure 3.
Body weight changes in systemic toxicity study of compound **4a** in CD-1 mice.

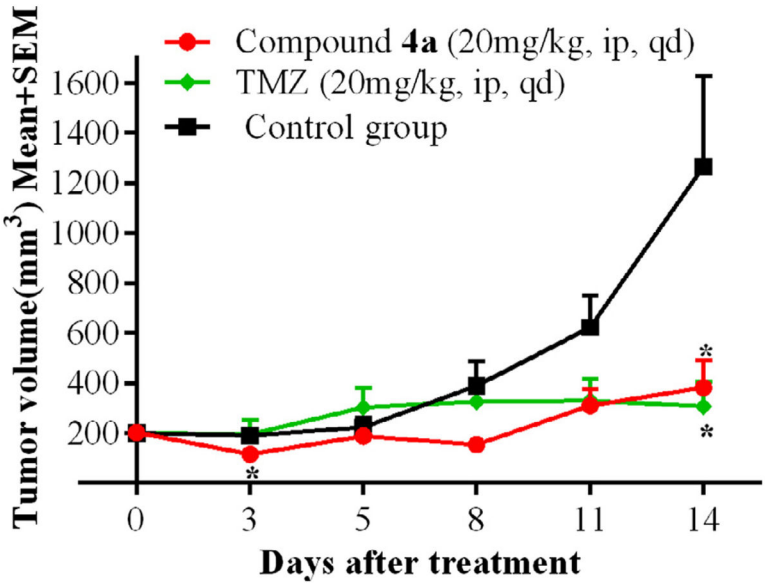

Figure 4.

Tumor growth inhibition study with compound **4a** in GL261-luc2 tumor syngraft model. N = 6; $^{*}P < 0.05$.

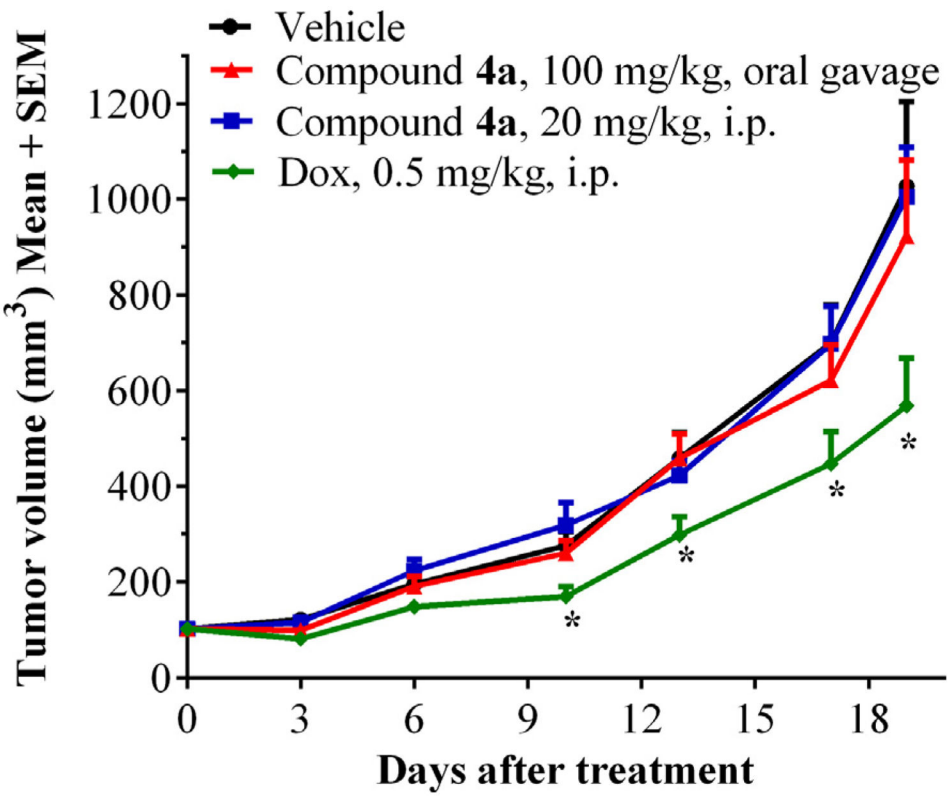

Figure 5.

Tumor growth inhibition study with compound **4a** in MDA-MB-231-luc tumor xenograft model. N = 6; $^{*}P < 0.05$.

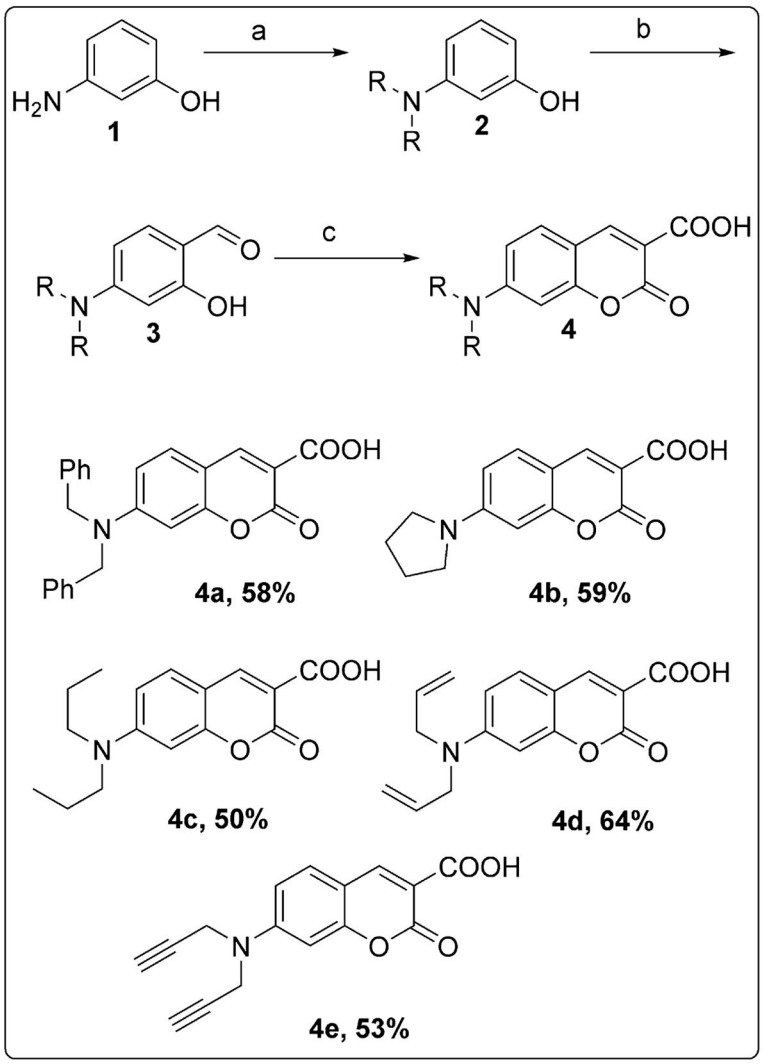

Scheme 1.

Synthesis of 7-(dialkylamino)-2-oxo-2H-chromene-3-carboxylic acid. (a) alkyl bromide, K_2CO_3, DMSO or EtOH, 80 °C, 12 h; (b) $POCl_3$, DMF, 0 °C to 80 °C, 2–4 h; (c) (i) diethyl malonate, piperidine, CH_3COOH, EtOH, 80 °C, 8–12 h (ii) 10% NaOH, 100 °C, 2 h (iii) 3 M HCl, pH 7.0; reported yields are from the reaction of **3** to **4.**

Table 1

MCT1 IC_{50} * (μM) values of amino carboxy coumarins

Compounds	MCT1 IC_{50} in μM
4a	0.09 ± 0.01
4b	0.38 ± 0.08
4c	0.45 ± 0.05
4d	0.17 ± 0.04
4e	0.21 ± 0.02

* Average ± SEM of minimum three separate experimental values.

Table 2

MTT assay IC_{50} * values of amino carboxy coumarins in MDA-MB-231, GL261-luc2 and MIA PaCa-2 cell lines

Compounds	GL261-luc2	MDA-MB-231
4a	>0.25	0.24 ± 0.01
4b	>0.25	>0.25
4c	>0.25	>0.25
4d	>0.25	>0.25
4e	>0.25	>0.25

* IC_{50} values reported in mM, average ± SEM of minimum three separate experimental values.

Table 3

In vitro Caco-2 monolayer permeability (pH 6.5/7.4, at 10 μM)

A – B permeability (Caco-2, pH 6.5/7.4)		
Compounds	**Permeability (10^{-6} cm/s) Mean***	**Percent recovery (%) Mean***
4a	32	34
Propranolol	40.9	67
Labetalol	8.5	66
Ranitidine	ND**	ND**
Colchicine	0.3	75
B – A permeability (Caco-2, pH 6.5/7.4)		
4a	6.4	55
Propranolol	41.5	80
Labetalol	36.5	72
Ranitidine	3.7	85
Colchicine	15.3	81

* Mean of two experiments.

** ND = not determined.

Table 4

Intrinsic clearance in human liver microsomes (0.1 μM)

Intrinsic clearance (liver microsomes, human)				
Compounds	**Half-life***			**Cl_{int}**
	Trial 1	**Trial 2**	**Mean**	
4a	922.2	>60	>60	<115.5
Propranolol	334.4	373	>60	<115.5
Imipramine	213.9	194.4	>60	<115.5
Verapamil	21.1	21.5	21	324.8
Terfenadine	9.8	9.1	9	736.8

* Half-life is reported in minutes, mean value of two experiments.

Table 5

Intrinsic clearance in mice liver microsomes (0.1 μM)

Intrinsic clearance (liver microsomes, mouse)				
Compounds	**Half-life***			**Cl_{int}**
	Trial 1	**Trial 2**	**Mean**	
4a	90.6	73.5	>60	<115.5
Propranolol	9.1	9.5	9	744.5
Imipramine	15.7	15.4	16	446.2
Verapamil	17.6	17.5	18	394.6
Terfenadine	7.5	6.1	7	1027.4

* Half-life is reported in minutes, mean value of two experiments.

www.oncotarget.com Oncotarget, 2019, Vol. 10, (No. 24), pp: 2355-2368

Research Paper

Novel N,N-dialkyl cyanocinnamic acids as monocarboxylate transporter 1 and 4 inhibitors

Shirisha Jonnalagadda[1], Sravan K. Jonnalagadda[1], Conor T. Ronayne[1], Grady L. Nelson[1], Lucas N. Solano[1], Jon Rumbley[1,2], Jon Holy[1,3], Venkatram R. Mereddy[1,2,4] and Lester R. Drewes[1,3]

[1]Integrated Biosciences Graduate Program, University of Minnesota, Duluth, MN 55812, USA

[2]Department of Pharmacy Practice & Pharmaceutical Sciences, University of Minnesota, Duluth, MN 55812, USA

[3]Department of Biomedical Sciences, Medical School Duluth, University of Minnesota, Duluth, MN 55812, USA

[4]Department of Chemistry and Biochemistry, University of Minnesota, Duluth, MN 55812, USA

Correspondence to: *Lester R. Drewes,* ***email:*** *ldrewes@d.umn.edu*
Venkatram R. Mereddy, ***email:*** *vmereddy@d.umn.edu*

Keywords: monocarboxylate transporter 1 inhibitor; monocarboxylate transporter 4 inhibitor; 2-alkoxy-*N,N*-dialkyl cyanocinnamic acid; cancer; metabolism

Received: *December 02, 2018* ***Accepted***: *February 22, 2019* ***Published***: *March 22, 2019*

ABSTRACT

Potent and dual monocarboxylate transporter (MCT) 1 and 4 inhibitors have been developed for the first time as potential anticancer agents based on α-cyanocinnamic acid structural template. Candidate inhibitors 1–9 have been evaluated for *in vitro* cell proliferation against MCT1 and MCT4 expressing cancer cell lines. Potential MCT1 and MCT4 binding interactions of the lead compound 9 have been studied through homology modeling and molecular docking prediction. *In vitro* effects on extracellular flux via glycolysis and mitochondrial stress tests suggest that candidate compounds 3 and 9 disrupt glycolysis and OxPhos efficiently in MCT1 expressing colorectal adenocarcinoma WiDr and MCT4 expressing triple negative breast cancer MDA-MB-231 cells. Fluorescence microscopy analyses in these cells also indicate that compound 9 is internalized and concentrated near mitochondria. *In vivo* tumor growth inhibition studies in WiDr and MDA-MB-231 xenograft tumor models in mice indicate that the candidate compound 9 exhibits a significant single agent activity.

INTRODUCTION

Metabolic reprogramming is now recognized as a critical hallmark of cancer and by understanding and manipulating the energetics of tumor metabolism, new therapeutic strategies may be developed for the treatment of cancer [1–8]. The survival and progression of tumors is accompanied by a significant increase in the metabolic enzymes and transporters, along with the cooperative reprogramming of other cells in the stromal compartment including cancer associated fibroblasts that assist tumor growth [9–13].

Glycolysis is generally amplified in cancer cells to keep up with bioenergetic and biosynthetic demands for rapid cell proliferation [14–17]. Anabolic and proliferative cancer cells also utilize the catabolic by-products of glycolysis such as lactate and pyruvate to fuel TCA cycle and mitochondrial OxPhos for further ATP generation to meet synthetic and energetic needs [14–17]. These metabolic transformations that support tumor progression result in overexpression of numerous enzymes and transporters, hence, provide an opportunity for pharmacological intervention [18, 19]. Several studies also recognize the importance of mitochondrial OxPhos to generate a large portion of ATP in cancer cells [20–22]. OxPhos also plays an important role in cancer cell survival, drug resistance, relapse, and metastasis. OxPhos intermediates are utilized in the TCA cycle and many are shuttled into numerous biosynthetic pathways including fatty acids, amino acids, and nucleotides. In this regard, inhibition of OxPhos will lead to severe ATP depletion and dysfunction of the TCA cycle, again starving cancer cells of critical components for cell survival and proliferation [20–22].

Monocarboxylic acid transport is one of the metabolic targets wherein the flux of small ketone bodies such as lactic acid and pyruvic acid occurs to support metabolic demands in cancer cells [23–29]. Monocarboxylic acid transporters (MCTs) are members of the solute carrier family 16 (SCL16 family) and consist of 14 known isoforms. Of these, only MCTs 1–4 have been shown to catalyze the bidirectional proton-linked transport of monocarboxylates such as lactate, pyruvate, and some ketone bodies. MCTs are present in the cell membrane and are centrally involved in glycolysis to efflux the end product lactate out of the tumor cells to avoid the decrease in intracellular pH which may lead to apoptosis [23–29]. MCT1 and MCT4 are encoded by the genes SCL16A1 and SLC16A3 and they also play an active role in the shuttling of lactate from glycolytic cancer cells into the neighboring oxidative cells for energy generation via mitochondrial OxPhos [9–13]. Hence, MCT1 and MCT4 are important therapeutic targets for metabolism-directed cancer treatments [30–37].

RESULTS

2-Methoxy-4-N,N-dialkyl cyanocinnamic acids are dual MCT1 and MCT4 inhibitors

Several recent studies have reported the importance of MCT1 and MCT4 in various cancers [23–37]. These studies indicate that elevated expression of MCT1 and/or MCT4 is correlated with poor patient prognosis and increased patient mortality in cancer patients [23–37]. Therefore, targeting MCT1 and/or MCT4 is of high therapeutic importance. In this regard, our previous structure activity relationship studies using CHC (Figure 1A) template indicated that placing *N,N*-dialkyl/diaryl groups at the 4-position and a methoxy (-OMe) group at the 2-position proved to be the most optimized structural moiety for MCT1 inhibition [32, 33]. L-[^{14}C]-lactate uptake studies on MCT1 expressing rat brain endothelial-4 (RBE4) cells revealed several 2-methoxy-4-*N,N*-dialkyl cyanocinnamic acids 1–9 as potent inhibitors of MCT1 at low nanomolar concentrations in our earlier study (Figure 1B) [32, 33].

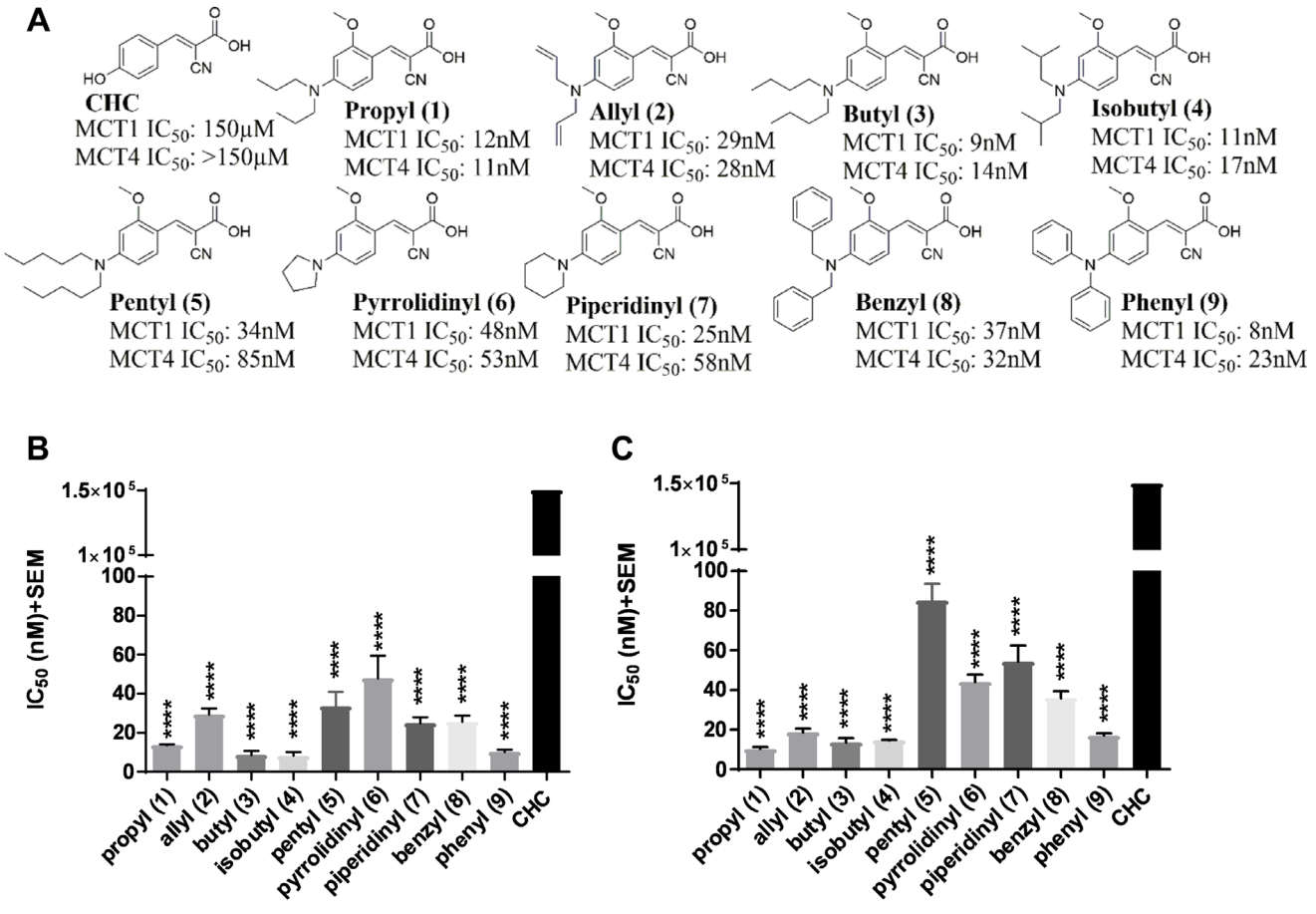

Figure 1: MCT1 and MCT4 lactate uptake inhibition. (**A**) Chemical structures of 2-methoxy-4-*N,N*-dialkyl cyanocinnamic acids 1–9. Bar graphs of (**B**) MCT1 inhibition and (**C**) MCT4 inhibition using lactate uptake study with compounds 1–9 in comparison to CHC. The final average ± sem of at least three independent experimental values were calculated. Repeated measures one-way ANOVA was used to calculate statistical significance ($P < 0.05$) between test compounds and CHC. $^{****}P < 0001$.

Table 1: SRB IC_{50}* (μM) values of 2-methoxy *N,N*-dialkyl cyanocinnamates in MDA-MB-231 and WiDr cell lines

Compound	MDA-MB-231	WiDr
Propyl (1)	>25	>25
Allyl (2)	>25	>25
Butyl (3)	>25	>25
Isobutyl (4)	>25	>25
Pyrrolidinyl (6)	>25	>25
Piperidinyl (7)	>25	>25
Benzyl (8)	>25	>25
Phenyl (9)	>25	4.2 ± 0.4

*The experiments were carried out in duplicate wells and the average ± sem values of minimum three separate experiments was calculated.

Because compounds 1–9 exhibited potent MCT1 inhibition, we investigated if these candidates would also inhibit the MCT4 function. For this purpose, a triple negative breast cancer (TNBC) cell line MDA-MB-231 was utilized. These cells predominantly express MCT4 as confirmed by Western blot and quantitative PCR analysis (Supplementary Figure 1). Upon evaluation of compounds 1–9 using L-[^{14}C]-lactate uptake study, they were also found to exhibit excellent inhibitory activity against MCT4 (Figure 1C, Supplementary Table 1). Compared to CHC ($IC_{50} \geq 150$ μM), compounds 1–9 exhibited several thousand-fold greater potency in inhibiting MCT1 (IC_{50} 8–48 nM) [32, 33] and MCT4 (IC_{50} 11–85 nM). Furthermore, compounds 1–9 were equally potent against both MCT1 and MCT4. These results constitute the first report of dual inhibition of MCT1 and MCT4 in nanomolar potency using small molecules.

MCT1 and MCT4 inhibitors do not affect cell proliferation in MDA-MB-231 and WiDr cells

Encouraged by dual inhibition of MCT1/4, we then evaluated cell proliferation of compounds 1–9 using SRB assay. MCT1 expressing cells WiDr and MCT4 expressing cells MDA-MB-231 were chosen for this assay (Supplementary Figure 1A). Compounds 1–8 did not show any appreciable cell proliferation inhibition up to 25 μM in both MDA-MB-231 and WiDr cell lines. Although compound 9 exhibited an IC_{50} of 4.2 μM in WiDr cell line, it did not show any activity in MDA-MB-231 cell line (Table 1).

Glycolysis stress test of compound 9 result in potent inhibition of glycolysis

To evaluate the metabolic profile of these MCT1 and MCT4 inhibitors, extracellular flux using Seahorse XFe96® assay was performed. Based on the lipophilic structural features and enhanced cell proliferation inhibition properties of these compounds, it is quite possible that they interact with intracellular organelles, including the mitochondria. In this regard, we chose candidate compound 9 based on its potent MCT1 and MCT4 inhibition and previously demonstrated ability to reduce tumor growth in a WiDr mouse xenograft model [32, 33]. To further investigate the metabolic implications of MCT1 and MCT4 inhibition, we also compared compound 9 with AZD3965 and CHC. AZD3965 is a known MCT1 inhibitor with no significant MCT4 inhibition activity [36, 37] For these studies, we utilized WiDr and MDA-MB-231 cells.

In the GST, three parameters namely glycolysis, glycolytic capacity and glycolytic reserve were measured. Our results show that compound 9 decreased glycolytic capacity in MCT1 expressing WiDr and MCT4 expressing MDA-MB-231 cells at 30 μM, whereas, AZD3965 decreased glycolytic capacity only in WiDr at 30 μM (Figure 2A–2C, Supplementary Figure 2A–2B). A similar trend was observed in glycolytic reserve for candidate 9 in both cell lines, and it completely arrested glycolytic reserve implying energy is not generated via glycolysis or other proton producing metabolic pathways. CHC and AZD3965 decreased glycolytic reserve only in MCT1 expressing WiDr. It is interesting to note that compound 9 showed significantly greater inhibition of glycolytic parameters compared to AZD3965 and CHC in WiDr and MDA-MB-231 cells (Figure 2A–2C). AZD3965 did not exhibit significant difference in the inhibition of glycolytic parameters compared to CHC.

Mitochondrial stress test of compound 9 result in significant inhibition of mitochondrial parameters

The MST results indicated that compound 9 significantly decreased maximal respiration, ATP production and spare respiratory capacity in WiDr and MDA-MB-231 cells as observed by the decrease in OCR (Figure 2D–2G, Supplementary Figure 2C–2D). CHC and AZD3695 did not affect these parameters in the two cell

lines implying these compounds don't inhibit or effect mitochondrial OxPhos. While candidate compound 9 significantly increased proton leak in both the cell lines, CHC and AZD3965 did not affect proton leak in either cells (Figure 2F), indicating that a significant portion of 9 is also internalized into the cytoplasm, causing disruption of mitochondrial function.

Compounds 2 and 9 result in significant inhibition of glycolytic and mitochondrial parameters

To further explore the potential of compounds in crossing the cell membrane and effecting cellular metabolic properties we also investigated compound 3 and compared it to compound 9. Compound 3 has two butyl groups and one phenyl ring, whereas compound 9 has three phenyl rings, and both compounds are equipotent in terms of MCT1 and MCT4 inhibition. In GST, both butyl 3 and phenyl 9 showed a significant decrease in glycolytic capacity and glycolytic reserve compared to control at 30 μM in WiDr (Figure 3A–3C, Supplementary Figure 3A–3B). Interestingly, compound 9 exhibited a significant difference in the above-mentioned glycolysis parameters compared to 3, making it superior to the compound 3. Similar glycolytic inhibition trends were also observed in MDA-MB-231 with compound 3 (Figure 3A–3C). In this case also candidate 9 was found to be superior compared to 3 in disrupting glycolysis. For MST, while 3 and 9 decreased maximal respiration, ATP production,

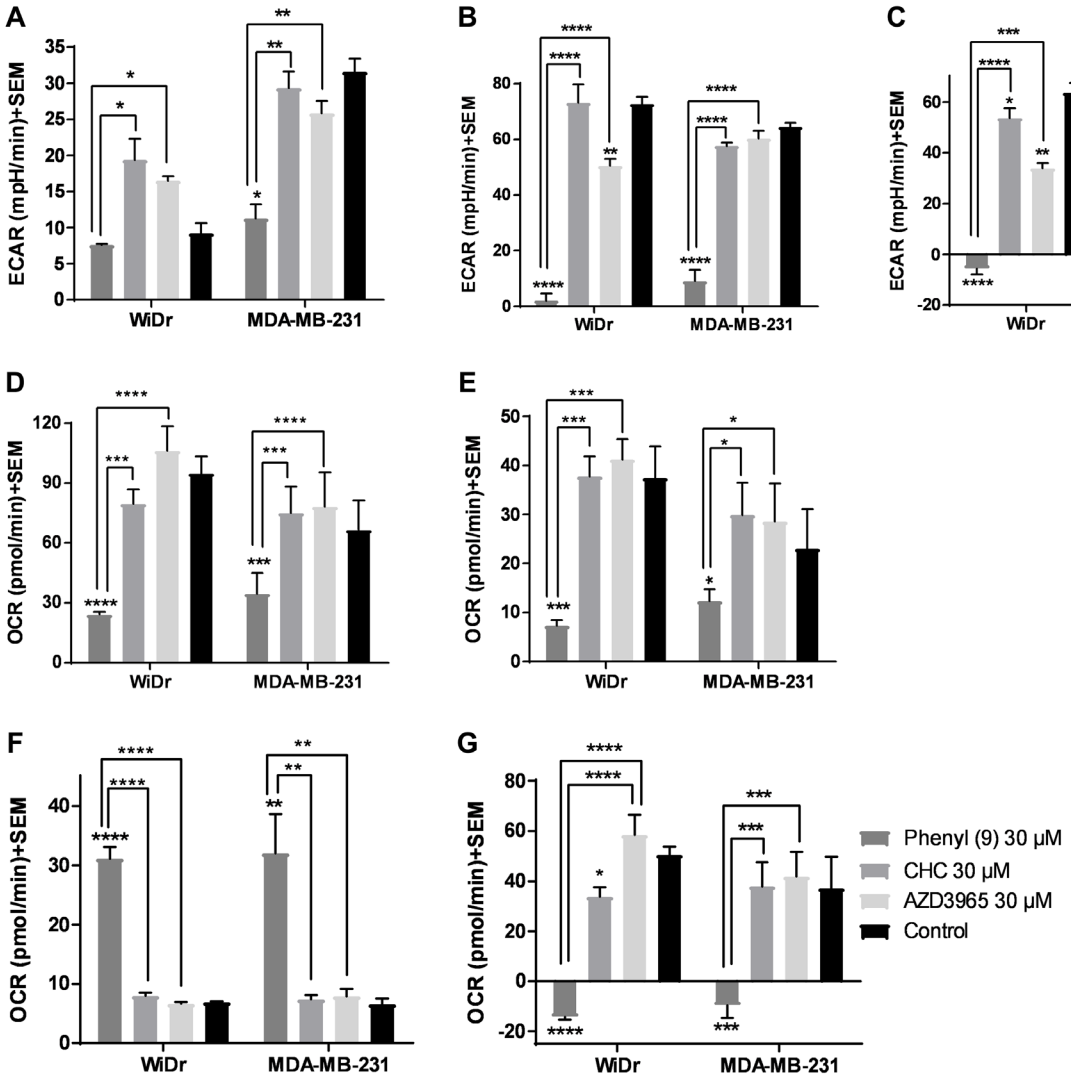

Figure 2: Glycolysis and mitochondrial stress tests of compound 9, CHC, and AZD3965. (**A–C**) represent the parameters from glycolysis stress test: (**A**) glycolysis, (**B**) glycolytic capacity, and (**C**) glycolytic reserve of compounds at 30 μM concentration in MCT1 expressing WiDr and MCT4 expressing MDA-MB-231 cells. (**D–G**) represent the parameters from mitochondrial stress test: (**D**) maximal respiration, (**E**) ATP production, (**F**) proton leak, and (**G**) spare respiratory capacity in WiDr and MDA-MB-231 cells. The ECAR and OCR values of were calculated using wave software. The average + SEM values of at least three independent experimental values were calculated. $^{*}P < 0.05$, $^{**}P < 0.01$, $^{***}P < 0.001$, $^{****}P < 0.0001$.

and spare respiratory capacity, compound 9 exhibited superior inhibition properties over compound 3 in the above-studied parameters (Figure 3D–3G, Supplementary Figure 3C–3D). A similar profile was observed for proton leak in which candidate 9 significantly increased proton leak compared to compound 3 in WiDr (Figure 3F).

MitoTracker staining indicates that compound 9 localizes in areas near mitochondria

Our studies showed that compound 9 is fluorescent (470/40 excitation, 525/50 barrier filters) and can be imaged with a fluorescein or GFP filter set (Supplementary Figures 4 and 5). To investigate cellular uptake and localization of compound 9, we have carried out fluorescence microscopy studies in WiDr and MDA-MB-231 cells, along with MitoTracker red to test for mitochondrial perturbation. Interestingly, it was observed that compound 9 was internalized in both cell lines (Figure 4A and 4B). In MDA-MB-231 cells, compound 9 localized to granular regions of cytoplasm (Figure 4C and 4D). In both cell lines, compound 9 was concentrated in areas near mitochondria, but did not appear to co-localize with most mitochondria (Figure 4E and 4F).

Homology modeling of and computational inhibitor docking to human MCT1 and MCT4 indicate that the phenyl rings in compound 9 are involved in hydrophobic interactions

To understand the potential molecular interactions of MCT1 and MCT4 inhibitors, homology modeling and

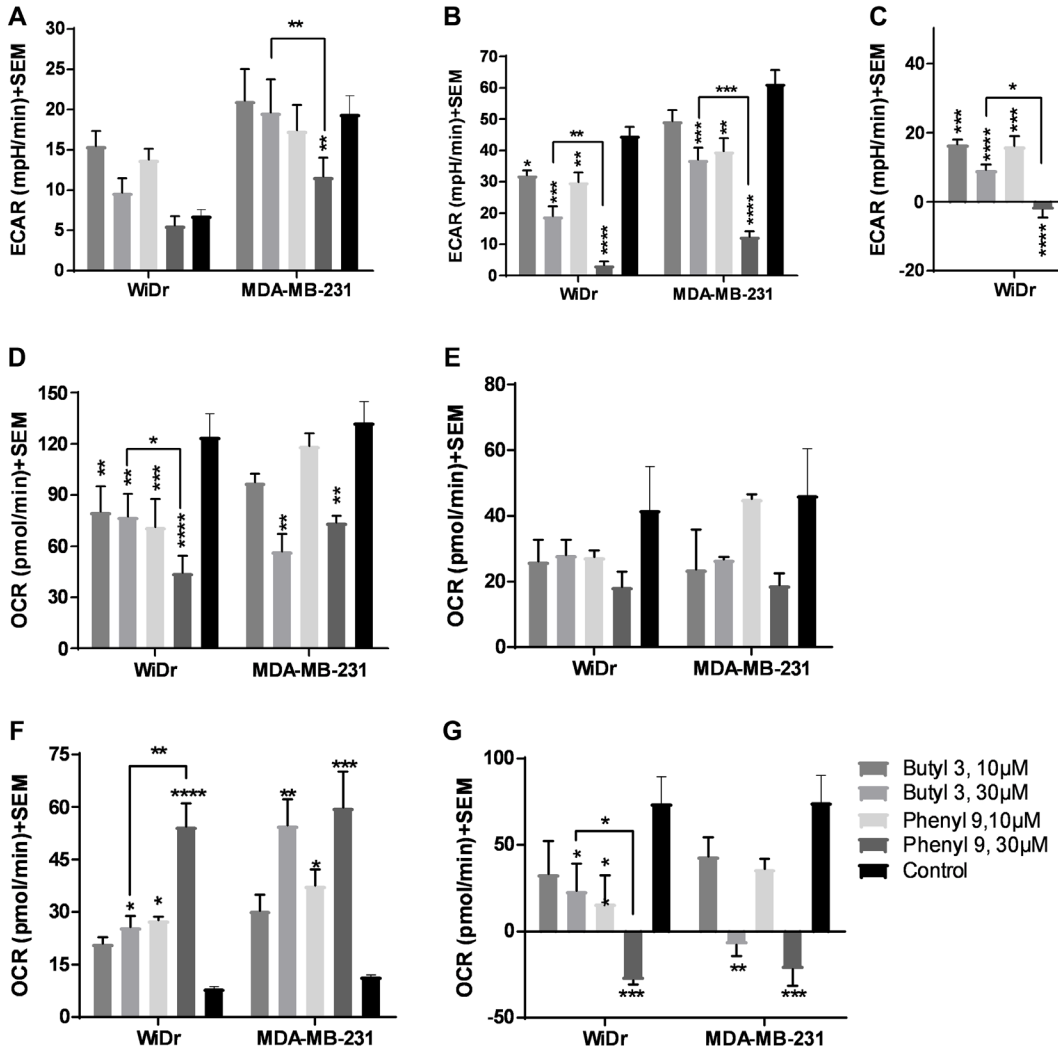

Figure 3: Glycolysis and mitochondrial stress tests of compounds 3 and 9. (**A–C**) represent the parameters from glycolysis stress test: (**A**) glycolysis, (**B**) glycolytic capacity, and (**C**) glycolytic reserve of compounds at 30 μM concentration in WiDr and MDA-MB-231 cells. (**D–G**) represent the parameters from mitochondrial stress test: (**D**) maximal respiration, (**E**) ATP production, (**F**) proton leak, and (**G**) spare respiratory capacity in WiDr and MDA-MB-231 cells. The ECAR and OCR values of were calculated using wave software. The average + SEM values of at least three independent experimental values were calculated. $^{*}P < 0.05$, $^{**}P < 0.01$, $^{***}P < 0.001$, $^{****}P < 0.0001$.

computational docking studies were performed. Optimal homology models were selected primarily based on an evaluation of charged residue rotamer orientation in the transmembrane spans. The resulting human MCT1 structure was compared to a previously reported rat MCT1 homology model based on an *E. coli* glycerol-3-phosphate transporter template [38]. For comparison, we analyzed the residues involved in inhibitor binding between our human MCT1 structure and compound 9. In order to achieve an unbiased ligand/inhibitor binding pocket search, our inspection area included the entire transmembrane spanning domain and extended into the inward-open aqueous surface of MCT1 and MCT4. The best ranked docking pose of compound 9 to both MCT1 and MCT4 was determined to be nearly structurally indistinguishable (Figure 5). Compound 9 is surrounded by a number of aliphatic and aromatic side chains. The binding affinity of compound 9 was estimated to be –9.2 kcal/mol for MCT1 and –9.6 kcal/mol for MCT4, consistent with the compounds high affinity for both proteins determined

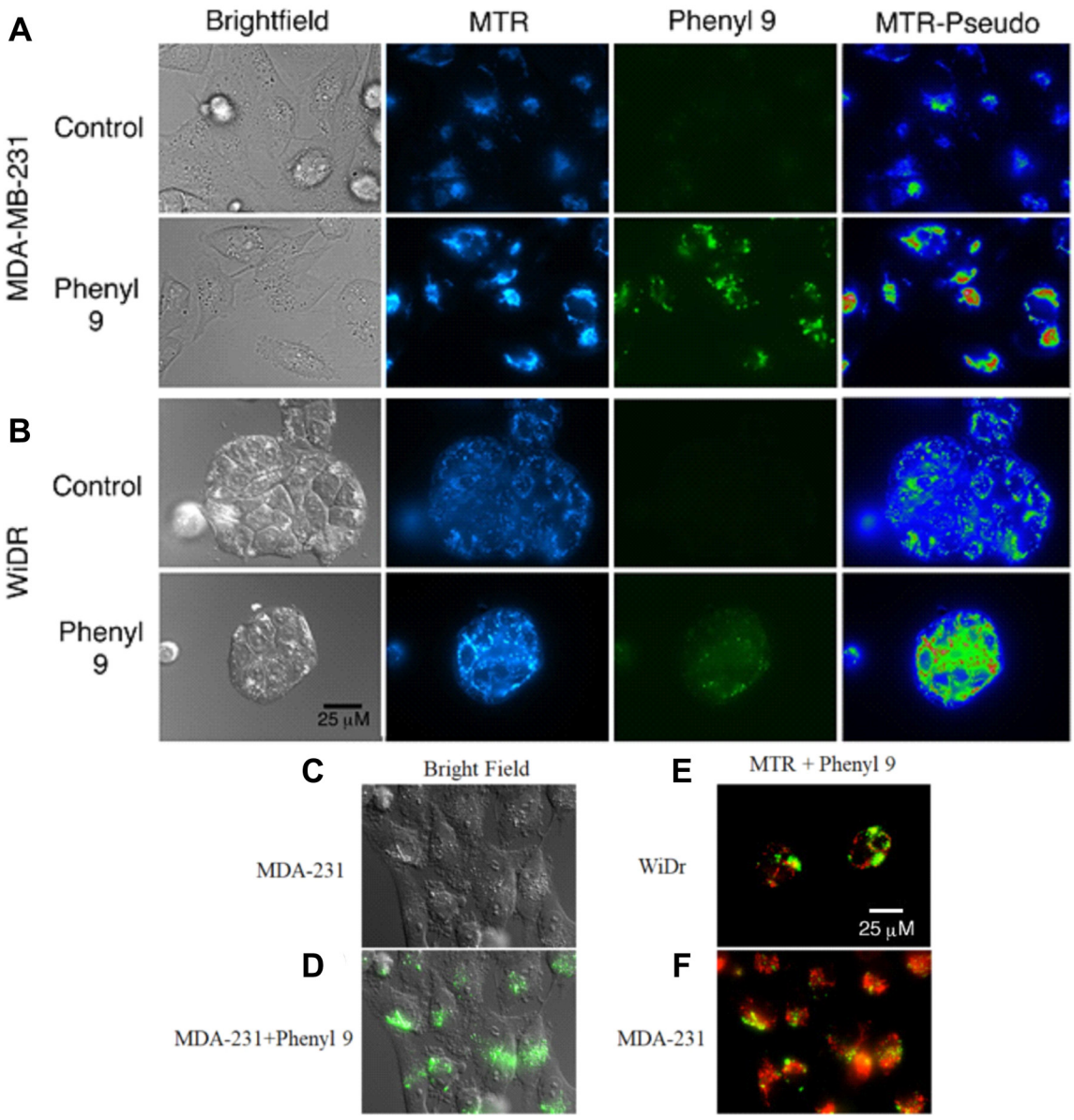

Figure 4: Mitotracker red staining in compound 9 treated MDA-MB-231 and WiDr cell lines. Representative pictures of (**A**) MDA-MB-231 and (**B**) WiDr cells after exposure to compound 9 (green) for 1 hour and MitoTracker red (MTR) for 15 minutes. Compound 9 is localized in regions of higher mitochondrial density in WiDr cell line. MTR-Pseudo images show the MTR signal pseudocolored using the Rainbow RGB LUT of the FIJI software program, to demonstrate mitochondrial hyperpolarization after addition of compound 9. (**C, D**) Compound 9 localizes to granular regions of MDA-MB-231 cells. Compound 9 localizes to regions near to, but does not overlap with, most mitochondria (red) in both (**E**) WiDr and (**F**) MDA-MB-231 cells. Images are representative of multiple fields of view from three independent experiments. Scale bar, 25 µm.

experimentally. The estimated binding affinity of parent compound CHC for MCT1 was –6.4 kcal/mol, an approximately 220-fold lower affinity. Further, of the top 18 binding poses determined for compound 9 binding to MCT1, 13 of 18 occupied the same binding site while 6 of 18 poses occupied the analogous MCT4 site. Only 2 of 18 poses for parent compound CHC binding to MCT1 were structurally similar, a surrogate for binding specificity.

Nancolas et al. determined the best binding pose of AstraZeneca MCT1 inhibitor AR-C155858 to the homology model of rat MCT1 [39]. A small list of amino acids determined to form hydrogen bonds with inhibitor were identified. Although our inhibitor is quite structurally distinct from AR-C155858, the residues contacting inhibitor in our study were highly analogous or structurally very near the rat MCT1 residues. Analogous amino acids included Tyr34, Arg306, Ser364, Leu367 and Glu391 in rat MCT1 and Tyr34, Arg313, Ser371, Leu374 and Glu398 identified in the human MCT1/compound 9 complex (Supplementary Table 2).

Compound 3 reduces the tumor burden in MCT1 expressing WiDr xenograft model

Our earlier studies indicated that candidate compound 9 exhibited significant tumor growth inhibition in WiDr tumor model [32, 33]. Although compound 3 exhibits inferior effects on glycolytic and mitochondrial properties compared to 9, we investigated its anticancer efficacy in a WiDr tumor model for *in vivo* comparison with compound 9. The butyl derivative 3 exhibited similar tumor growth inhibition to that of compound 9 (Figure 6A).

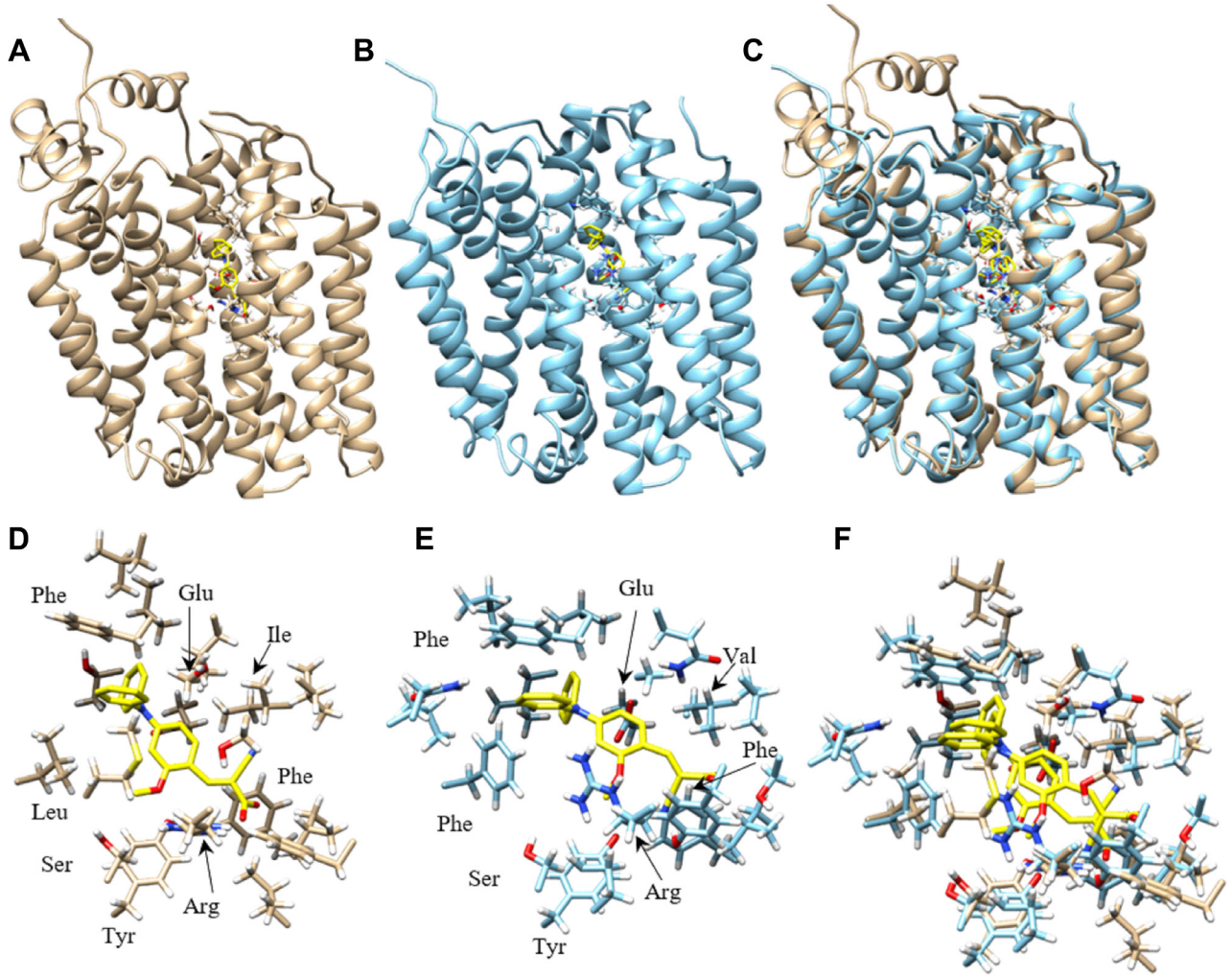

Figure 5: Homology model of human MCT1 and MCT4 docked with compound 9. Most favorable compound 9 binding pose to human MCT1 and MCT4 were represented. (**A**) Cα ribbon homology structure of MCT1 with docked compound 9 (yellow) and binding site residues within 4.5 Å shown. (**B**) Cα ribbon homology structure of MCT4 with docked compound 9 (yellow) and binding site residues within 4.5 Å shown. (**C**) Overlay of MCT1 and MCT4 homology models and their respective best compound 9 docking pose. (**D**) Compound 9 (yellow) and residue forming its binding site in MCT1, all residues within 4.5 Å are shown. (**E**) Compound 9 (yellow) and residue forming its binding site in MCT1, all residues within 4.5 Å are shown. (**F**) Overlay of most favorable binding pose of compound 9 for MCT1 and MCT4 and all residues within 4.5 Å. Models were displayed with Chimera.

Compound 9 not only inhibits tumor growth in WiDr, but also in MCT4 expressing MDA-MB-231 tumor model

Based on good tumor growth inhibition with compound 9 in WiDr tumor model, and also based on its superior metabolic disruption properties compared to 3, compound 9 was further advanced for *in vivo* studies in the MCT4 expressing MDA-MB-231 tumor xenograft model. Group-1 was administered with compound 9, group-2 was given a combination of compound 9 and clinical breast cancer drug doxorubicin (AKSci catalog # E518), and group-3 was treated with doxorubicin alone. Group-4 was assigned as a control group and treated with vehicle (10% DMSO in saline). The treatment was continued up to 18 days and on day 20, the mice were euthanized and tumor masses isolated and weighed. Tumor growth inhibitions were found to be 58, 67 & 48% in groups 1, 2 and 3, respectively based on tumor volume (Figure 6B) and 56, 67 & 52% in groups 1, 2 and 3, respectively based on isolated tumor weights (Figure 6C). These studies clearly exhibit the potential of MCT1/4 inhibitors in TNBC treatment. Our *in vivo* pharmacokinetic studies also indicated that peak plasma concentration was observed at 15 minutes and most of the compound was eliminated in less than one hour [32]. Due to these reasons, higher dosages of compound 9 were required to produce significant anticancer efficacy *in vivo*. In all these studies, <20% of body weight loss was observed.

DISCUSSION

MCT1 and MCT4 are upregulated in various cancers and the presence of either of these markers is linked with poor patient prognosis [23–37]. MCT1 and MCT4 are frequently credited with lactate transport in and out of cells, respectively. However, shuttling of lactate via MCTs is bidirectional and dependent on the pH and anion gradients [40]. Hence, low intracellular pH favors lactate efflux and high intracellular pH favors lactate influx.

Based on their excellent MCT1 inhibition activity in low nanomolar potency [32, 33], the candidate compounds 1–9 were evaluated for MCT4 inhibition. All compounds exhibited similar inhibitory profile for both

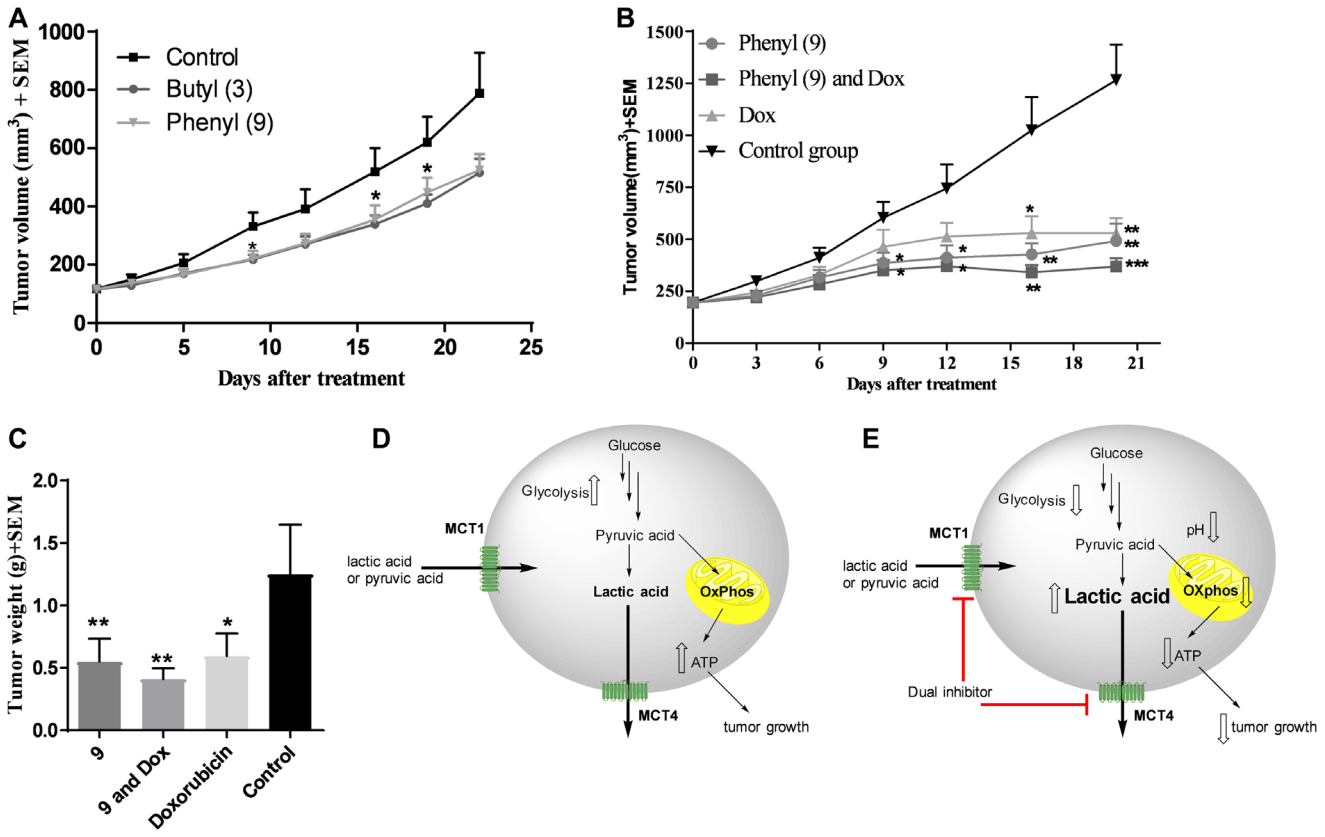

Figure 6: *In vivo* xenograft studies in WiDr and MDA-MB-231 tumor models. (**A**) WiDr tumor xenograft study of compound 3 and compound 9. Mice ($n = 8$) were treated with 8 mg/kg of compound 3, intraperitoneally, two times a day. (**B**) Tumor growth inhibition study with compound 9 in MDA-MB-231 tumor xenograft model ($n = 6$). Mice were treated with compound 9 (70 mg/kg, ip, bid until day-4; qd from day-5), a combination of 9 and doxorubicin (0.5 mg/kg, ip, five days a week), and doxorubicin. (**C**) Tumor growth inhibition based on isolated tumor mass. $^{*}P < 0.05$, $^{**}P < 0.01$, $^{***}P < 0.001$, $^{****}P < 0.0001$. Schematic representation of (**D**) untreated tumor cells and (**E**) inhibition of MCT1 and MCT4 and decreased glycolysis and mitochondrial OxPhos in compound 9 treated tumor cells. Upward hollowed arrow indicates "increase" in function/amount and downward hollowed arrow indicates "decrease" in function/amount.

MCT1 and MCT4 with slight preference for MCT1 over MCT4 (Figure 1B). Based on these results, the mode of action of compounds appears to be similar for MCT1 and MCT4. In this regard, potential MCT1 and MCT4 binding interactions have been studied through homology modeling and molecular docking prediction (Figure 5).

The structures of inward-open human MCT1 and MCT4 generated here appear to be of sufficient quality to identify the binding site and reason for dual specificity of compound 9. The binding site amino acids for compound 9 in MCT1 and MCT4 were predicted to be identical based on model. The concordance of binding site residues for AstraZeneca AR-C155858 inhibitor binding to a rat MCT1 model, although not fully expected for such a structurally distinct inhibitor, lends confidence in the results obtained here. The lipophilic phenyl groups of compound 9 binding to MCT1 and MCT4 is characterized by a number of hydrophobic contacts, including aromatic stacking to phenylalanine in both proteins. The extensive hydrophobic contact surface likely leads to a dramatic increase in affinity over CHC, supplemented by several putative hydrogen bonds. All polar atoms in compound 9 are immediately adjacent to one or more polar side chains, including conserved Tyr34, Ser154/156 and Arg313/278 (Figure 5). The 2-methoxy group specifically interacts with Tyr34, another strong contributor to specificity and high affinity over CHC. Of the residues within 4.5Å of compound 9 the most obvious unsatisfied interaction is that of conserved Glu398/363, also identified in the binding site of AstraZeneca inhibitor AR-C155858 in rat MCT1 [39].

Since compounds 1–9 exhibited potent dual MCT1 and MCT4 inhibition, we then evaluated cell proliferation studies of these compounds in cancer cell lines. SRB assay results indicate that compound 9 significantly inhibits cell proliferation of WiDr cells (Table 1). This is not surprising as it is known that potent inhibition of MCT may not lead to corresponding levels of cell proliferation inhibition [30]. *In vitro*, cells are exposed to supraphysiological levels of oxygen, nutrients, and growth factors which may render them more resistant to some types of metabolic perturbation. Also, the tumor microenvironment *in vivo* can be expected to include more drug targets than a single cultured cell line, due to the presence of potentially metabolically-coupled stromal cells, and other cell signaling effects.

In GST, MDA-MB-231 produced high ECAR indicating that these cells pursue glycolysis as a dominant energy source, whereas WiDr are less glycolytic in nature compared to MDA-MB-231 as evidenced by the low ECAR in the control wells in the presence of glucose (Figure 2A). In MDA-MB-231 and WiDr cells, 9 lead to a significant disruption in glycolytic capacity and glycolytic reserve. CHC, being a weak MCT1 and MCT4 inhibitor, did not affect glycolysis and glycolytic capacity in both the cell lines. Being a selective MCT1 inhibitor, AZD3965 decreased glycolytic capacity and glycolytic reserve only in WiDr. However, candidate 9 was found to be superior to AZD3965 in inhibiting glycolytic parameters. AZD3965 did not show any glycolysis inhibition in MCT4 expressing MDA-MB-231.

We then investigated if 9 would disrupt mitochondrial OxPhos. Our results from MST suggest that 9 crosses the plasma membrane and effects mitochondria by causing an increase in proton leak and inhibiting ATP production (Figure 2E, 2F). Treatment with 9 was found to prevent the cells from meeting their energy demands by not only decreasing glycolytic reserve (Figure 2C), but also efficiently suppressing spare respiratory capacity (Figure 2G) leading to an even greater energy crisis in both GST and MST. These results suggest that compound 9 has pleiotropic activities effecting glycolysis and mitochondrial OxPhos. In this study, CHC at 30 μM resulted in a very limited effect on mitochondria, and AZD3965 did not affect any mitochondrial parameters indicating that this compound is more selective towards plasma membrane MCT1 inhibition.

We also investigated the efficacy of another MCT inhibitor 3 on glycolysis and mitochondrial parameters and compared it to 9. Although compound 3 exhibited significant inhibition of GST and MST parameters (Figure 3A–3G), compound 9 was still found to exhibit superior efficacy compared to 3. CHC and other related cyanocinnamic acid derivatives have been previously reported as inhibitors of the mitochondrial pyruvate carrier (MPC) [41, 42]. The MPC plays a vital role in the coupling of glycolysis and mitochondrial respiratory processes by shuttling cytosolic pyruvate into the mitochondria where it can be utilized in the TCA cycle and OxPhos [43]. It is quite possible that the ability of compounds 3 and 9 to disrupt mitochondrial respiration may in part be due to inhibition of mitochondrial pyruvate uptake through interaction with the MPC.

Although MST results indicated significant inhibition in mitochondrial activity, fluorescence studies using both compound 9 and MitoTracker CMXROS did not reveal obvious co-localization of 9 in mitochondria (Figure 4). Cells exposed to 9 did not exhibit significant decrease in mitochondrial membrane potential in the time frames tested but rather, an apparent and acute hyperpolarization of the mitochondria. This observation was surprising as we had observed large amounts of proton leak in MST (Figures 2F and 3F) and may be due to a lack of glucose in media during microscopy experiments. Most of the compound 9 fluorescence appeared to reside in vesicular structures, which raises the possibility that it is being concentrated in endosomes, or lysosomes. It is currently unknown how the fluorescence characteristics of 9 are affected by distinct microenvironments associated with different organelles and cellular locations (e.g., pH or membrane polarization status). Hence, the fluorescence observed in these experiments may not represent the full extent of its actual intracellular

distribution. Nevertheless, it is apparent that it enters both MDA-MB-231 and WiDr cells to readily detectable levels, and so a difference in cell entry does not appear to be the primary mechanism underlying the different sensitivities of these two lines to 9.

We then investigated the efficacy of candidate compounds 3 and 9 in WiDr mouse xenograft models. Treatment with compounds 3 and 9 in mice for three weeks provided equal efficacy with 35% and 33% tumor growth reduction, respectively [32, 33] (Figure 6A). Encouraged by these *in vivo* results, we further advanced 9 for efficacy studies in MDA-MB-231 xenograft model as a single agent and also in combination with a clinical breast cancer drug doxorubicin. Compound 9 showed significant tumor growth inhibition in both the cases (Figure 6B and 6C). We attribute the anticancer efficacy properties of dual MCT1 and MCT4 inhibitor 9 to a combination of direct or indirect effects resulting in metabolic disruption via inhibition of glycolysis and mitochondrial respiration (Figure 6D and 6E), along with cell cycle disruption (Supplementary Figure 6).

In conclusion, we developed 2-alkoxy-*N,N*-dialkyl cyanocinnamates 1–9 as potent and dual MCT1 and MCT4 inhibitors with activities at low nM concentrations. We carried out *in vitro* cell proliferation inhibition studies of these inhibitors in MCT1 and MCT4 expressing cancer cells and identified compound 9 as a lead candidate for further studies. Homology modeling and molecular docking prediction of compound 9 indicated that phenyl rings were involved in hydrophobic interactions and polar functional groups formed several putative hydrogen bonds with amino acid restudies of MCT1 and MCT4. Compounds 3 and 9 were evaluated for their glycolysis and mitochondrial OxPhos inhibition properties using extracellular flux assays. These compounds showed significant inhibition of glycolytic capacity, glycolytic reserve, maximal respiration, and spare respiratory capacity in MCT1 expressing WiDr and MCT4 expressing MDA-MB-231 cells. Compound 9 was found to be superior to 3 in inhibiting glycolytic and mitochondrial parameters in both cell lines. Florescence microscopy studies provided further proof that 9 was internalized and concentrated in areas near mitochondria in MDA-MB-231 and WiDr cells. Compound 3 was evaluated for its *in vivo* efficacy in WiDr tumor model in mice and compared it with 9 and this study indicated that both these inhibitors exhibited similar anticancer efficacy. Compound 9 was further advanced for *in vivo* study in MDA-MB-231 tumor xenograft models in mice and these results indicated that 9 significantly inhibited tumor growth as a single agent. These findings constitute the first report on the discovery of dual and potent MCT1 and MCT4 inhibitors with significant mitochondrial OxPhos inhibition properties. Owing to the importance of MCTs in tumor metabolism in several cancers, we believe that these inhibitors have good potential to be developed as broad-spectrum anticancer agents.

MATERIALS AND METHODS

Cell lines and culture conditions

MDA-MB-231 cells (ATCC, 2015) were grown in DMEM supplemented with 10% FBS and penicillin-streptomycin (50 U/ml, 50 µg/ml, Invitrogen). WiDr cells (ATCC, 2017) were cultured in MEM medium supplemented with 10% FBS (Atlanta Biologicals) and penicillin-streptomycin (50 U/ml, 50 µg/ml). For *in vitro* experiments, after seeding, cells were incubated at 37°C in 5% CO_2 for 18–24 hours before the addition of test compounds.

MCT4 inhibition assay

In this study, an L-[^{14}C]-lactate based transport assay was developed by us to quantify MCT4 transport and its inhibition by test compounds. Previously, for MCT1 transport study, the pH of HEPES buffer with L-[^{14}C]-lactate was maintained at 7.43 and lactate influx was quantified under this pH gradient condition. 2×10^5 cells/mL were used for the MCT1 assay and the plates were incubated for 20 minutes after the addition of test compounds [32, 33]. For the MCT4 transport assay, the pH of HEPES buffer with L-[^{14}C]-lactate was adjusted to 7.0 such that lactate influx into the cells was aided by the pH gradient. 4×10^5 MDA-MB-231 cells/mL and incubation with test compounds for one hour was found to be optimal for isotope readings for this study. Test compounds were diluted to working concentration in HEPES buffer (140 mM NaCl, 5 mM KCl, 2 mM $CaCl_2$, 2 mM $MgCl_2$, 10 mM HEPES, pH 7.0) containing 3 µM L-[^{14}C]-lactate (Perkin Elmer) and 2 µM L-lactate. Cells (24-well plate) were washed twice with 500 µL HEPES buffer and allowed to equilibrate for 15–20 minutes at 37°C. HEPES buffer was replaced with 250 µL test solution. After 1 hour, media was replaced with 500 µL ice-cold stop buffer (0.1 mM CHC solution in HBS, pH 7.4) and the plates were placed on ice. Cells were washed twice with ice-cold stop buffer and solubilized using 250 µL of 0.1 M NaOH in 5% Triton-X (Millipore Sigma). A 150 µL aliquot from each well was added to 4 mL EcoLite(+)™ scintillation fluid (MP Biomedicals) and radioactivity was determined by scintillation spectrometry. Inhibition by each test solution was calculated as a percentage of the maximum control uptake. CHC and dimethylsulfoxide (DMSO) were used as controls.

Sulforhodamine-B (SRB) cell proliferation inhibition assay

Cells (5×10^4 cells/mL) were cultured in 48-well plates. Test compounds were dissolved in DMSO (final concentration of DMSO is <0.1%) and were added to culture wells at various concentrations in replicate and incubated for 72 hours. Growth medium was removed and the wells were washed with PBS and dried. SRB (0.5% in 1% acetic acid) was added to the wells and incubated for

30–45 minutes. The wells were washed 3 times with 1% acetic acid and dried. The cellular protein was dissolved in trizma base (10 mM, pH 10.2) and absorbance was recorded at 540 nm. Percent survival was calculated using the formula $\%Survival = \frac{Abs_{test\ compound}}{Abs_{control}} \times 100$.

Seahorse XFe96® assessment of glycolysis and mitochondrial respiration

Extracellular acidification rates (ECAR) and oxygen consumption rates (OCR) were recorded in real-time for glycolysis stress test (GST) and mitochondrial stress test (MST), respectively, using Agilent Seahorse XFe96® analyzer [44, 45].

Fluorescent microscopy studies

MDA-MB-231 or WiDr cells (5×10^4 cells/mL) were seeded in MatTek glass-bottom dishes (MatTek Corp, #P35G010C) and incubated for 48 hours and exposed to compound 9 (30 μM) for 1 h. MitoTracker Red CMXROS (Invitrogen, M7512, 100 nM) was added 15 minutes prior to imaging. Media was then aspirated and replaced with PBS + 5% FBS for imaging. Cells were imaged using a Nikon TE2000 epifluorescent microscope and a Photometrics Dyno CCD camera.

Homology modeling of and molecular docking to human MCT1 and MCT4 structures

Structures were generated for human MCT1 and MCT4 by homology modeling with MODELLER 9.18 using inward-open human glucose transporter 1 as a structural template, PDB file: 5eqi [46, 47]. Due to minimal sequence similarity, we generated a final template alignment by consensus sequence alignment guided by consensus transmembrane spanning domain prediction followed by manual adjustment to eliminate gaps in the putative transmembrane spanning domains. The last 50 C-terminal amino acids were deleted but are not part of a transmembrane spanning domain. As with the homology model of rat MCT1 previously built by Manoharan, et. al., we consider the models synthesized to be of intermediate quality but predictive in nature [38]. Autodock Vina was used to dock parent compound CHC and compound 9 to the inward open homology models [48]. From estimated individual binding energies, a crude difference between CHC and compound 9 affinity was calculated. Further, the number of poses nearly identical to the most favorable docked pose was used as a surrogate for binding specificity.

Ethics statement

The animal studies were approved and conducted by GenScript Corporation (Piscataway, NJ, USA) according to their approved IACUC protocols.

Tumor growth inhibition studies

Tumor cells suspended in 1:1 matrigel-PBS were injected on right flank of female SCID mice ($n = 6$ mice/group, 10^7 MDA-MB-231 cells) or right flank of female athymic nude mice ($n = 8$ mice/group, 5×10^6 WiDr cells). Tumors were measured using calipers every 2–3 days and tumor volumes were calculated using the formula $V = ab^2/2$ where 'a' is the long diameter of the tumor and 'b' is the short diameter of the tumor. Tumor growth inhibition was determined using the formula % inhibition = $[(C - T)/C] \times 100$ where C is average tumor weight of the control group and T is the average tumor weight of the test group.

Statistical analysis

Statistics were computed using GraphPad Prism 6.0. For *in vitro* studies, repeated measures one-way ANOVA and for *in vivo* studies, Mann-Whitney test were used to compare the treated and untreated groups. A *P*-value of < 0.05 was considered significant.

Abbreviations

α-cyano-4-hydroxy cinnamic acid: CHC; monocarboxylate transporter: MCT; oxidative phosphorylation: OxPhos; sulforhodamine-B: SRB; dimethylsulfoxide: DMSO; extracellular acidification rate: ECAR; oxygen consumption rate: OCR; glycolysis stress test: GST; mitochondrial stress test: MST; rat brain endothelial-4: RBE4; triple negative breast cancer: TNBC; mitochondrial pyruvate carrier: MPC.

Author contributions

VRM performed the *in vitro* and *in vivo* study design and contributed to draft the manuscript, LRD designed MCT4 inhibition assay and Seahorse XFe96 experiments; SJ and SKJ performed MCT4 inhibition, Seahorse XFe96 studies, statistical analysis and drafted the manuscript; CTR and JH designed and conducted florescence and flow cytometry studies, GLN and LNS cultured cells and carried out all the cell proliferation studies, JR designed and performed homology modeling of and molecular docking to human MCT1 and MCT4 structures. All authors read and approved the final manuscript.

ACKNOWLEDGMENTS

We thank Zachary Blankenheim for excellent assistance in performing Seahorse XFe96 related assays.

CONFLICTS OF INTEREST

The authors declare no conflicts of interest. A patent has been issued to the University of Minnesota.

FUNDING

This work was supported by University of Minnesota Duluth; Department of Defense Breast Cancer Research Proposal, Breakthrough Award (grant number W81XWH-15-1-0047, VRM); Department of Defense Breast Cancer Research Award (grant number W81XWH-15-1-0060, LRD), Whiteside Clinical Research Institute, Duluth, Minnesota.

REFERENCES

1. Fritz V, Fajas L. Metabolism and proliferation share common regulatory pathways in cancer cells. Oncogene. 2010; 29:4369–77. https://doi.org/10.1038/onc.2010.182.
2. Hanahan D, Weinberg RA. Hallmarks of cancer: the next generation. Cell. 2011; 144:646–74. https://doi.org/10.1016/j.cell.2011.02.013.
3. Cantor JR, Sabatini DM. Cancer cell metabolism: one hallmark, many faces. Cancer Discov. 2012; 2:881–98. https://doi.org/10.1158/2159-8290.CD-12-0345.
4. Pecqueur C, Oliver L, Oizel K, Lalier L, Vallette FM. Targeting metabolism to induce cell death in cancer cells and cancer stem cells. Int J Cell Biol. 2013; 2013:805975. https://doi.org/10.1155/2013/805975.
5. Pavlova NN, Thompson CB. The Emerging Hallmarks of Cancer Metabolism. Cell Metab. 2016; 23:27–47. https://doi.org/10.1016/j.cmet.2015.12.006.
6. Lee N, Kim D. Cancer Metabolism: Fueling More than Just Growth. Mol Cells. 2016; 39:847–54. https://doi.org/10.14348/molcells.2016.0310.
7. DeBerardinis RJ, Chandel NS. Fundamentals of cancer metabolism. Sci Adv. 2016; 2:e1600200. https://doi.org/10.1126/sciadv.1600200.
8. Kalyanaraman B. Teaching the basics of cancer metabolism: developing antitumor strategies by exploiting the differences between normal and cancer cell metabolism. Redox Biol. 2017; 12:833–42. https://doi.org/10.1016/j.redox.2017.04.018.
9. Martinez-Outschoorn UE, Balliet RM, Rivadeneira DB, Chiavarina B, Pavlides S, Wang C, Whitaker-Menezes D, Daumer KM, Lin Z, Witkiewicz AK, Flomenberg N, Howell A, Pestell RG, et al. Oxidative stress in cancer associated fibroblasts drives tumor-stroma co-evolution: A new paradigm for understanding tumor metabolism, the field effect and genomic instability in cancer cells. Cell Cycle. 2010; 9:3256–76. https://doi.org/10.4161/cc.9.16.12553.
10. Pavlides S, Vera I, Gandara R, Sneddon S, Pestell RG, Mercier I, Martinez-Outschoorn UE, Whitaker-Menezes D, Howell A, Sotgia F, Lisanti MP. Warburg meets autophagy: cancer-associated fibroblasts accelerate tumor growth and metastasis via oxidative stress, mitophagy, and aerobic glycolysis. Antioxid Redox Signal. 2012; 16:1264–84. https://doi.org/10.1089/ars.2011.4243.
11. Martinez-Outschoorn UE, Lin Z, Whitaker-Menezes D, Howell A, Lisanti MP, Sotgia F. Ketone bodies and two-compartment tumor metabolism: stromal ketone production fuels mitochondrial biogenesis in epithelial cancer cells. Cell Cycle. 2012; 11:3956–63. https://doi.org/10.4161/cc.22136.
12. Lee M, Yoon JH. Metabolic interplay between glycolysis and mitochondrial oxidation: the reverse Warburg effect and its therapeutic implication. World J Biol Chem. 2015; 6:148–61. https://doi.org/10.4331/wjbc.v6.i3.148.
13. Fu Y, Liu S, Yin S, Niu W, Xiong W, Tan M, Li G, Zhou M. The reverse Warburg effect is likely to be an Achilles' heel of cancer that can be exploited for cancer therapy. Oncotarget. 2017; 8:57813–25. https://doi.org/10.18632/oncotarget.18175.
14. Ganapathy V, Thangaraju M, Prasad PD. Nutrient transporters in cancer: relevance to Warburg hypothesis and beyond. Pharmacol Ther. 2009; 121:29–40. https://doi.org/10.1016/j.pharmthera.2008.09.005.
15. Ganapathy-Kanniappan S, Geschwind JF. Tumor glycolysis as a target for cancer therapy: progress and prospects. Mol Cancer. 2013; 12:152. https://doi.org/10.1186/1476-4598-12-152.
16. Liberti MV, Locasale JW. The Warburg Effect: How Does it Benefit Cancer Cells? Trends Biochem Sci. 2016; 41:211–218. https://doi.org/10.1016/j.tibs.2015.12.001.
17. Jiang B. Aerobic glycolysis and high level of lactate in cancer metabolism and microenvironment. Genes Dis. 2017; 4:25–27. https://doi.org/10.1016/j.gendis.2017.02.003.
18. Granchi C, Fancelli D, Minutolo F. An update on therapeutic opportunities offered by cancer glycolytic metabolism. Bioorg Med Chem Lett. 2014; 24:4915–25. https://doi.org/10.1016/j.bmcl.2014.09.041.
19. Roy D, Sheng GY, Herve S, Carvalho E, Mahanty A, Yuan S, Sun L. Interplay between cancer cell cycle and metabolism: Challenges, targets and therapeutic opportunities. Biomed Pharmacother. 2017; 89:288–96. https://doi.org/10.1016/j.biopha.2017.01.019.
20. Marchetti P, Guerreschi P, Mortier L, Kluza J. Integration of Mitochondrial Targeting for Molecular Cancer Therapeutics. Int J Cell Biol. 2015; 2015:283145. https://doi.org/10.1155/2015/283145.
21. Weinberg SE, Chandel NS. Targeting mitochondria metabolism for cancer therapy. Nat Chem Biol. 2015; 11:9–15. https://doi.org/10.1038/nchembio.1712.
22. Kim HK, Noh YH, Nilius B, Ko KS, Rhee BD, Kim N, Han J. Current and upcoming mitochondrial targets for cancer therapy. Semin Cancer Biol. 2017; 47:154–67. https://doi.org/10.1016/j.semcancer.2017.06.006.
23. Halestrap AP. The SLC16 gene family - structure, role and regulation in health and disease. Mol Aspects Med. 2013; 34:337–49. https://doi.org/10.1016/j.mam.2012.05.003.
24. Baltazar F, Pinheiro C, Morais-Santos F, Azevedo-Silva J, Queirós O, Preto A, Casal M. Monocarboxylate transporters

as targets and mediators in cancer therapy response. Histol Histopathol. 2014; 29:1511–24. https://doi.org/10.14670/HH-29.1511.

25. Jones RS, Morris ME. Monocarboxylate Transporters: Therapeutic Targets and Prognostic Factors in Disease. Clin Pharmacol Ther. 2016; 100:454–63. https://doi.org/10.1002/cpt.418.

26. Ruan Y, Zeng F, Cheng Z, Zhao X, Fu P, Chen H. High expression of monocarboxylate transporter 4 predicts poor prognosis in patients with lung adenocarcinoma. Oncol Lett. 2017; 14:5727–34. https://doi.org/10.3892/ol.2017.6964.

27. Latif A, Chadwick AL, Kitson SJ, Gregson HJ, Sivalingam VN, Bolton J, McVey RJ, Roberts SA, Marshall KM, Williams KJ, Stratford IJ, Crosbie EJ. Monocarboxylate Transporter 1 (MCT1) is an independent prognostic biomarker in endometrial cancer. BMC Clin Pathol. 2017; 17:27. https://doi.org/10.1186/s12907-017-0067-7.

28. Payen VL, Hsu MY, Rädecke KS, Wyart E, Vazeille T, Bouzin C, Porporato PE, Sonveaux P. Monocarboxylate transporter MCT1 promotes tumor metastasis independently of its activity as a lactate transporter. Cancer Res. 2017; 77:5591–601. https://doi.org/10.1158/0008-5472.CAN-17-0764.

29. Johnson JM, Cotzia P, Fratamico R, Mikkilineni L, Chen J, Colombo D, Mollaee M, Whitaker-Menezes D, Domingo-Vidal M, Lin Z, Zhan T, Tuluc M, Palazzo J, et al. MCT1 in Invasive Ductal Carcinoma: Monocarboxylate Metabolism and Aggressive Breast Cancer. Front Cell Dev Biol. 2017; 5:27. https://doi.org/10.3389/fcell.2017.00027.

30. Critchlow SE, Tate L. Use of a MCT1 inhibitor in the treatment of cancers expressing MCT1 over MCT4. WO 2010089580, World Intellectual Property Organization, 2010. https://patents.google.com/patent/WO2010089580A1/en.

31. Draoui N, Schicke O, Seront E, Bouzin C, Sonveaux P, Riant O, Feron O. Antitumor activity of 7-aminocarboxycoumarin derivatives, a new class of potent inhibitors of lactate influx but not efflux. Mol Cancer Ther. 2014; 13:1410–18. https://doi.org/10.1158/1535-7163.MCT-13-0653.

32. Gurrapu S, Jonnalagadda SK, Alam MA, Nelson GL, Sneve MG, Drewes LR, Mereddy VR. Monocarboxylate transporter 1 inhibitors as potential anticancer agents. ACS Med Chem Lett. 2015; 6:558–61. https://doi.org/10.1021/acsmedchemlett.5b00049.

33. Mereddy VR, Drewes LR, Alam MA, Jonnalagadda SK, Gurrapu S. Therapeutic Compounds. US 9296728B2, United States Patent and Trademark Office, 2016. https://app.dimensions.ai/details/patent/US-9296728-B2.

34. Gurrapu S, Jonnalagadda SK, Alam MA, Ronayne CT, Nelson GL, Solano LN, Lueth EA, Drewes LR, Mereddy VR. Coumarin carboxylic acids as monocarboxylate transporter 1 inhibitors: *in vitro* and *in vivo* studies as potential anticancer agents. Bioorg Med Chem Lett. 2016; 26:3282–86. https://doi.org/10.1016/j.bmcl.2016.05.054.

35. Parnell KM, McCall J. MCT4 Inhibitors for Treating Disease. US 20160362378A1, United States Patent and Trademark Office, 2016. https://patents.google.com/patent/US20160362378A1/en.

36. Curtis NJ, Mooney L, Hopcroft L, Michopoulos F, Whalley N, Zhong H, Murray C, Logie A, Revill M, Byth KF, Benjamin AD, Firth MA, Green S, et al. Pre-clinical pharmacology of AZD3965, a selective inhibitor of MCT1: DLBCL, NHL and Burkitt's lymphoma anti-tumor activity. Oncotarget. 2017; 8:69219–36. https://doi.org/10.18632/oncotarget.18215.

37. Noble RA, Bell N, Blair H, Sikka A, Thomas H, Phillips N, Nakjang S, Miwa S, Crossland R, Rand V, Televantou D, Long A, Keun HC, et al. Inhibition of monocarboxyate transporter 1 by AZD3965 as a novel therapeutic approach for diffuse large B-cell lymphoma and Burkitt lymphoma. Haematologica. 2017; 102:1247–57. https://doi.org/10.3324/haematol.2016.163030.

38. Manoharan C, Wilson MC, Sessions RB, Halestrap AP. The role of charged residues in the transmembrane helices of monocarboxylate transporter 1 and its ancillary protein basigin in determining plasma membrane expression and catalytic activity. Mol Membr Biol. 2006; 23:486–98. https://doi.org/10.1080/09687860600841967.

39. Nancolas B, Sessions RB, Halestrap AP. Identification of key binding site residues of MCT1 for AR-C155858 reveals the molecular basis of its isoform selectivity. Biochem J. 2015; 466:177–88. https://doi.org/10.1042/BJ20141223.

40. Juel C, Halestrap AP. Lactate transport in skeletal muscle - role and regulation of the monocarboxylate transporter. J Physiol. 1999; 517:633–42. https://doi.org/10.1111/j.1469-7793.1999.0633s.x.

41. Divakaruni AS, Wallace M, Buren C, Martyniuk K, Andreyev AY, Li E, Fields JA, Cordes T, Reynolds IJ, Bloodgood BL, Raymond LA, Metallo CM, Murphy AN. Inhibition of the mitochondrial pyruvate carrier protects from excitotoxic neuronal death. J Cell Biol. 2017; 216:1091–105. https://doi.org/10.1083/jcb.201612067.

42. Divakaruni AS, Wiley SE, Rogers GW, Andreyev AY, Petrosyan S, Loviscach M, Wall EA, Yadava N, Heuck AP, Ferrick DA, Henry RR, McDonald WG, Colca JR, et al. Thiazolidinediones are acute, specific inhibitors of the mitochondrial pyruvate carrier. Proc Natl Acad Sci USA. 2013; 110:5422–27. https://doi.org/10.1073/pnas.1303360110.

43. Vacanti NM, Divakaruni AS, Green CR, Parker SJ, Henry RR, Ciaraldi TP, Murphy AN, Metallo CM. Regulation of substrate utilization by the mitochondrial pyruvate carrier. Mol Cell. 2014; 56:425–35. https://doi.org/10.1016/j.molcel.2014.09.024.

44. TeSlaa T, Teitell MA. Techniques to monitor glycolysis. Methods Enzymol. 2014; 542:91–114. https://doi.org/10.1016/B978-0-12-416618-9.00005-4.

45. Jitschin R, Hofmann AD, Bruns H, Giessl A, Bricks J, Berger J, Saul D, Eckart MJ, Mackensen A, Mougiakakos

D. Mitochondrial metabolism contributes to oxidative stress and reveals therapeutic targets in chronic lymphocytic leukemia. Blood. 2014; 123:2663–72. https://doi.org/10.1182/blood-2013-10-532200.

46. Šali A, Blundell TL. Comparative protein modelling by satisfaction of spatial restraints. J Mol Biol. 1993; 234:779–815. https://doi.org/10.1006/jmbi.1993.1626.

47. Kapoor K, Finer-Moore JS, Pedersen BP, Caboni L, Waight A, Hillig RC, Bringmann P, Heisler I, Müller T, Siebeneicher H, Stroud RM. Mechanism of inhibition of human glucose transporter GLUT1 is conserved between cytochalasin B and phenylalanine amides. Proc Natl Acad Sci USA. 2016; 113:4711–16. https://doi.org/10.1073/pnas.1603735113.

48. Trott O, Olson AJ. AutoDock Vina: improving the speed and accuracy of docking with a new scoring function, efficient optimization, and multithreading. J Comput Chem. 2010; 31:455–61.

ACS Medicinal Chemistry Letters

Letter

pubs.acs.org/acsmedchemlett

Monocarboxylate Transporter 1 Inhibitors as Potential Anticancer Agents

Shirisha Gurrapu,[†] Sravan K. Jonnalagadda,[†] Mohammad A. Alam,[‡] Grady L. Nelson,[†] Mary G. Sneve,[§] Lester R. Drewes,*[,§] and Venkatram R. Mereddy*[,†,‡,∥]

[†]Integrated Biosciences Graduate Program, [‡]Department of Chemistry and Biochemistry, [§]Department of Biomedical Sciences, Medical School Duluth, and [∥]Department of Pharmacy Practice & Pharmaceutical Sciences, University of Minnesota Duluth, Duluth, Minnesota 55812, United States

Supporting Information

ABSTRACT: Potent monocarboxylate transporter 1 inhibitors (MCT1) have been developed based on α-cyano-4-hydroxycinnamic acid template. Structure−activity relationship studies demonstrate that the introduction of *p*-*N*, *N*-dialkyl/diaryl, and *o*-methoxy groups into cyanocinnamic acid has maximal MCT1 inhibitory activity. Systemic toxicity studies in healthy ICR mice with few potent MCT1 inhibitors indicate normal body weight gains in treated animals. *In vivo* tumor growth inhibition studies in colorectal adenocarcinoma (WiDr cell line) in nude mice xenograft models establish that compound **27** exhibits single agent activity in inhibiting the tumor growth.

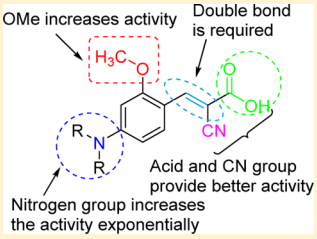

KEYWORDS: *Warburg effect, reverse Warburg effect, monocarboxylate transporter 1, α-cyano-4-hydroxycinnamic acid, colorectal adenocarcinoma*

Vigorous glycolysis is the hallmark of many advanced stage tumors.[1−5] Malignant tumors are heterogeneous in nature, and tumor microenvironment contains aerobic and hypoxic regions.[1] Tumor hypoxia leads to cancer advancement, metastasis, treatment failure, and patient mortality as these cells become resistant to standard chemo- and radiation therapy. Under hypoxic conditions, cancer cells consume glucose that is metabolized to lactate, ketone, and other energy rich molecules.[1] The transport of these energy rich metabolites occurs via monocarboxylate transporters (MCTs).[1,4,6,7] They are members of the solute carrier 16 gene family consisting of 14 known MCT isoforms (SLC16A1−14).[6,7] Of these, MCTs 1−4 have been shown to transport monocarboxylates such as lactate, pyruvate, and some ketone bodies.[1,6,7] MCT1 expression is elevated in an array of human tumors, and therefore, these transporters can be major selective targets for antitumor therapy.[1,8−14] Recently, Lisanti et al. have carried out extensive studies to explain the glycolytic process in epithelial cancer cells.[15−18] These studies strongly indicate that cancer cells initiate oxidative stress in their neighboring fibroblasts resulting in mitochondrial dysfunction and aerobic glycolysis (Warburg effect). These fibroblasts then produce lactate and pyruvate, which are taken up by adjacent cancer cells via MCT1 for mitochondrial oxidative phosphorylation and further proliferation. In essence, tumor associated stromal fibroblasts and epithelial cancer cells develop a metabolic symbiotic relationship (reverse Warburg effect).[15−18]

Owing to the importance of MCT1 in the above-mentioned tumor related biological events, development of MCT1 inhibitors should be of immense importance in broad-spectrum cancer treatment. In this regard, we initiated a project on the discovery of novel MCT1 inhibitors as potential anticancer agents based on α-cyano-4-hydroxycinnamic acid (CHC).[19] Although CHC has been in biochemical usage as a low affinity MCT1 inhibitor (IC_{50} >100 μM), the derivatives of CHC have not been studied to improve its potency. We envisioned the systematic design, synthesis, and evaluation of several CHC analogues to understand the structure−activity relationship (SAR) and obtain lead molecules that inhibit MCT 1 at low concentrations for potential development as anticancer agents.

There are five positions of substitution on the CHC template (Scheme 1A), and we chose *p*-hydroxyl replacement as the starting point. For initial studies, hydroxyl group was substituted with alkyl (methyl, ethyl, **1**−**2**), electron withdrawing (F, Cl, Br, CN, and NO_2, **3**−**7**), and electron donating groups (methoxy, 3,4-methylenedioxy, **8**−**9**). These CHC derivatives of α-cyanocinnamic acids were synthesized from corresponding aldehydes via Knoevenagel type condensation (**1**−**9**, Scheme 1B).[20]

The compounds **1**−**9** were evaluated for their MCT1 inhibition activity via [^{14}C]-lactate uptake assay on rat brain endothelial 4 cells (RBE4). We utilized this cell line for initial lactic acid transport studies as they highly express MCT1 as confirmed by Western blotting.[21,22] Gratifyingly, compounds **1**−**9** have exhibited several times higher potency (~0.5−100 μM) than the parent CHC molecule (Scheme 1B).

We then explored the role of cyano (−CN), carboxylic acid (−COOH), and olefinic functionalities in CHC by replacing −CN group with H atom, replacing −COOH and introducing two −CN groups, removal of the −CN group, and also

Received: January 29, 2015
Accepted: March 19, 2015
Published: March 19, 2015

DOI: 10.1021/acsmedchemlett.5b00049
ACS Med. Chem. Lett. 2015, 6, 558−561

Scheme 1[a]

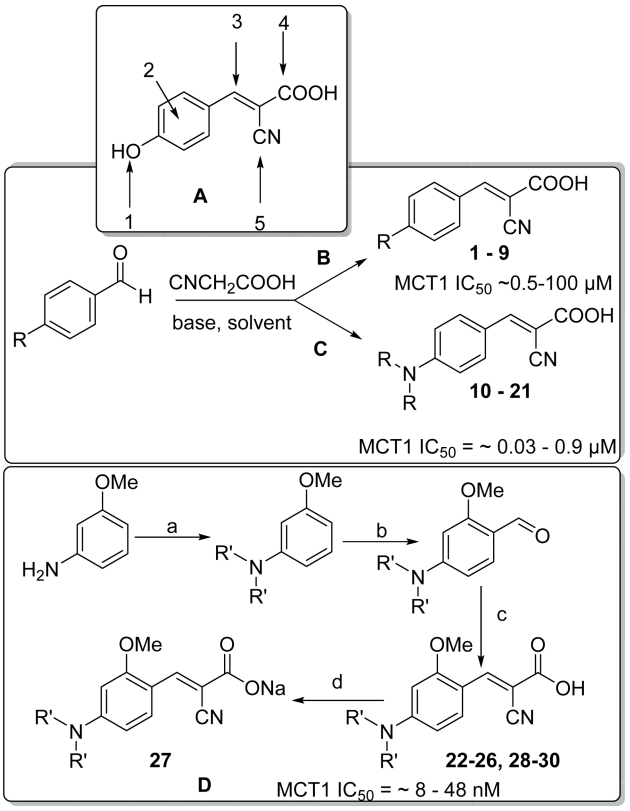

[a]Reagents and conditions: (a) Alkyl bromide, K_2CO_3, tetrabutylammonium bromide, H_2O/ethanol or isopropanol, 100 °C, 8−24 h; (b) (i) $POCl_3$/DMF 0−80 °C, 2−4 h; (ii) Na_2CO_3; (c) $CNCH_2COOH$, piperidine, CH_3CN, 80 °C, 8−20 h; (d) $NaHCO_3$, MeOH−H_2O, rt, overnight.

reduction of the olefin. In all these cases, we did not observe any appreciable MCT1 inhibition activity when compared to CHC (data not shown).

We then introduced *N,N*-dialkyl group in place of hydroxyl moiety owing to the biological significance of nitrogen atom in many pharmaceutical compounds. Condensation of commercially available *p*-(*N,N*-dimethyl) benzaldehyde with cyanoacetic acid in the presence of piperidine provided the corresponding cyanocinnamic acid **10** in ∼72% yield. To our delight, **10** exhibited potent MCT1 inhibition activity with a mean IC_{50} = 0.14 μM. Taking **10** as a lead derivative, we further explored the SAR (Table 1) by structural modification on the nitrogen atom. In this regard, we synthesized several *p-N,N*-dialkyl and aryl substituted cyanocinnamic acids starting from aniline (Scheme 1C). Dialkylation of aniline followed by Vilsmeier−Haack formylation[23] and subsequent base-mediated condensation with cyanoacetic acid provided cinnamic acids **11**−**21** in good yields (Scheme 1C and Table 1). Compounds **11**−**21** upon evaluation of their MCT1 inhibition activities on RBE4 cell line exhibited a clear pattern of SAR. From these studies, it was found that increasing the alkyl chain increased the potency up to four carbon chain length (**11**−**13**, 13−66 nM, Table 1). Further increase in the chain length to pentyl **15** and hexyl **16** decreased the activity. Aryl-substituted cyanocinnamic acid **19** also showed excellent activity (26 nM). Cyclic amines such as pyrrolidine **20** and piperidine **21** decreased the activity to a moderate range of IC_{50} values (70 and 142 nM, Table 1).

Table 1. MCT1 IC_{50} Values of *N,N*-Dialkyl/Aryl Cyanocinnamic Acids

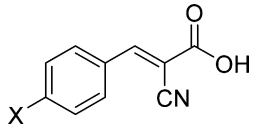

Sl. No.	X	% yield[a]	MCT1 IC_{50} (μM)[b]
10	*N,N*-dimethyl	72	0.14 ± 0.05
11	*N,N*-diethyl	75	0.07 ± 0.02
12	*N,N*-dipropyl	67	0.01 ± 0.01
13	*N,N*-dibutyl	65	0.03 ± 0.00
14	*N,N*-diisobutyl	61	0.10 ± 0.05
15	*N,N*-dipentyl	70	0.14 ± 0.02
16	*N,N*-dihexyl	68	0.88 ± 0.18
17	*N,N*-diallyl	60	0.11 ± 0.03
18	*N,N*-dipropargyl	62	0.40 ± 0.02
19	*N,N*-diphenyl	76	0.03 ± 0.00
20	pyrrolidinyl	62	0.07 ± 0.01
21	piperidinyl	67	0.14 ± 0.03

[a]Starting from aldehydes. [b]Average IC_{50} values of minimum three separate experiments. Values reported as avg ± SEM.

On the basis of the significantly improved activity of *N,N*-dialkyl series, we further carried out SAR studies by introducing substitutions at the 2-position of the aromatic ring (Scheme 1A). For initial studies, we started with cyanocinnamic acid **22** derived from *o*-methoxy-*N,N*-dipropyl benzaldehyde. Compound **22** exhibited higher MCT1 inhibitory activity (IC_{50} = 12 nM) compared to its nonmethoxy derivative **12**. To understand further SAR of this lead candidate, we introduced several alkyl and aryl substitutions on the nitrogen atom. The required aldehydes were synthesized from *m*-anisidine (Scheme 1D). Alkylation of *m*-anisidine with alkyl halides in the presence of K_2CO_3 and catalytic tetrabutylammonium bromide followed by Vilsmeier−Haack formylation[23] provided the corresponding aldehydes. These aldehydes were then condensed with cyanoacetic acid in the presence of piperidine to synthesize cyanocinnamic acids **22**−**30** (Scheme 1D and Table 2). MCT1-based [^{14}C]-lactate uptake studies on RBE4 cells revealed that these derivatives **22**−**30** have superior inhibitory activity (IC_{50}

Table 2. MCT1 IC_{50} Values of *o*-Methoxy *p-N,N*-Dialkyl/Aryl Cyanocinnamic Acids

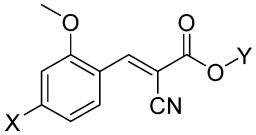

Sl. No.	X	Y	% yield[a]	MCT1 IC_{50} (nM)[c]
22	*N,N*-dipropyl	H	62	12 ± 1
23	*N,N*-dibutyl	H	60	9 ± 1
24	*N,N*-diisobutyl	H	58	11 ± 4
25	*N,N*-dipentyl	H	74	34 ± 7
26	*N,N*-diphenyl	H	66	8 ± 1
27	*N,N*-diphenyl	Na	78[b]	11 ± 3
28	*N,N*-diallyl	H	70	29 ± 2
29	pyrrolidinyl	H	68	48 ± 20
30	piperidinyl	H	85	25 ± 5

[a]Starting from aldehydes. [b]Starting from acid. [c]Average IC_{50} values of minimum three separate experiments. Values reported as avg ± SEM.

DOI: 10.1021/acsmedchemlett.5b00049
ACS Med. Chem. Lett. 2015, 6, 558−561

= 8−48 nM) when compared to their nonmethoxy homologues **10**−**21** (Table 1). In fact, cyanocinnamic acids **22**−**24** and **26** have exhibited inhibitory activity in low nanomolar range (8−12 nM, Table 2).

We chose **26** as a representative example for further evaluation based on its potent MCT1 inhibitory profile. To improve the water solubility, we prepared its sodium salt **27** by treating the corresponding acid **26** with $NaHCO_3$ in methanol−water. The sodium salt **27** has water solubility of ∼1 mg/mL. Compound **27** retained its potent MCT1 inhibitory activity (11 nM, Table 2). Similarly, we have also synthesized sodium salts of **29** and **30**, and they exhibited water solubility of >7 mg/mL. Having achieved the initial goal of discovering potent MCT1 inhibitors, we then carried out systemic toxicity analysis of some of these derivatives in healthy ICR mice.

Compound **27** was chosen for initial studies, and the mice were treated with **27** in 0.1% DMSO in saline for 3 weeks (6.67 mg/kg, ip, bid). All mice survived, and weight gains were similar when compared to the control group (Supporting Information). We then carried out another study with increased dosages of 50 mg/kg, oral gavage, bid, and 50 mg/kg, ip, qd. In these cases also, all mice survived, and weight gains were similar to the control group (Supporting Information). Because of the higher water solubility of sodium salts of **29** and **30**, toxicity studies were carried out at the higher dosage of 70 mg/kg/ip/bid. In these cases also, no animal mortality was observed, and the body weight gains were similar to the control group (Supporting Information).

We also carried out a preliminary pharmacokinetic analysis of **27** in ICR mice. Sixty ICR mice were divided into two groups and group 1 was administered with **27** intraperitoneally and group 2 intragastrically at 100 mg/kg. Blood samples were collected at different time points (n = 3 for each time point). The peak plasma concentrations were observed at 0.25 h for group 1 and 0.30 h for group 2. In both the cases, compound **27** was completely eliminated from the system within 24 h (Supporting Information).

Encouraged by the generally nontoxic nature of potent MCT1 inhibitors in healthy animals, we next carried out the *in vivo* tumor growth inhibition study with **27** using flank-based tumor xenografts in nude mice. For initial studies, we utilized a MCT1 expressing and highly tumorigenic colorectal adenocarcinoma cell line WiDr.[1] These cancer cells (7×10^6) in 1:1 PBS−matrigel were inoculated into the flank of female BALB/c nude mice and allowed to grow until the tumor volume reached ∼100 mm^3 (∼3 weeks). Mice were administered with **27** by intraperitoneal injection (10 mg/kg, bid) and by oral gavage (50 mg/kg, bid). The treatment was continued for 3 weeks, and tumor volumes were determined with calipers every 3 days (Figure 1). At the end of the study, mice were euthanized, and tumors were isolated and weighed to validate the caliper measurements. On the basis of these studies, ∼29% and 45% tumor growth inhibition was observed in ip and oral gavage groups, respectively.

Similarly, another *in vivo* tumor growth inhibition study was conducted by starting the treatment from day 6 following WiDr tumor inoculation. This time, **27** was administered at a higher dosage of 100 mg/kg, oral gavage, qid and 50 mg/kg, ip, bid in groups 1 and 2, respectively. By the end of the study (21 days, tumor volumes in Figure 2), 56% and 45% tumor growth inhibition was observed in groups 1 and 2, respectively, based on the weights of the isolated tumors.

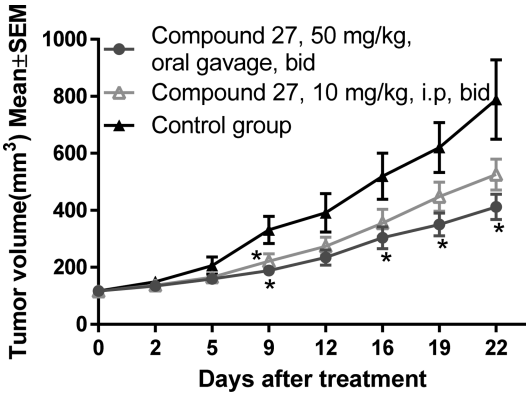

Figure 1. *In vivo* efficacy with **27** as a single agent in WiDr tumor xenograft model: WiDr cells were implanted subcutaneously in the right flanks of female BALB/c nude mice. After tumors reached ∼100 mm^3, mice were randomly assigned to three groups (n = 8 mice per group). Group 1 was administered with 50 mg/kg, oral gavage, bid; group 2 was treated with 10 mg/kg, ip, bid. Tumor volumes were recorded every 3−4 days. The study was carried out for 22 days. Mann−Whitney test was used to compute significance. *$P \leq 0.05$.

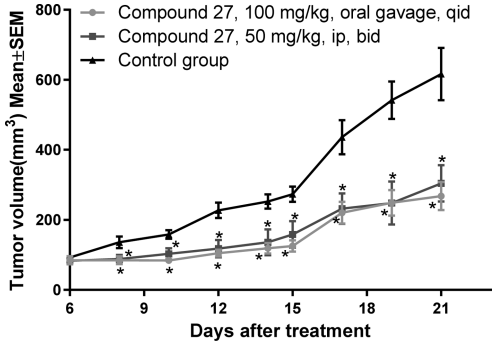

Figure 2. *In vivo* efficacy with **27** in WiDr tumor xenograft model: WiDr cells were implanted subcutaneously in the right flank of female BALB/c nude mice. Treatments were started on day 6 of implant. Mice were randomly assigned to three groups (n = 8 mice per group). Group 1 was administered with 100 mg/kg, oral gavage, qid; group 2 received 50 mg/kg, ip, bid. Tumor volumes were recorded every 2 days. The study was carried out for 21 days. Mann−Whitney test was used to compare the treated and untreated groups. *$P \leq 0.05$.

These studies clearly demonstrate that MCT1 inhibitors have potential to develop them as anticancer agents. However, detailed mechanistic studies need to be conducted with low MCT1 expressing cell line or with MCT1 knock out cell lines to evaluate the *in vivo* anticancer efficacy of **27**. Also, studies to determine whether efficacy is directly due to MCT1 inhibition and whether any potential off-target effects are present must be conducted.

In conclusion, we have carried out a systematic SAR study of CHC and discovered several potent MCT1 inhibitors that are active at low nanomolar concentration. Preliminary *in vivo* toxicology studies indicate that these potent inhibitors are well tolerated without significant serious side effects. *In vivo* anticancer efficacy studies in MCT1 expressing colorectal cancer (WiDr) indicate an efficient tumor growth reduction. In general, these MCT1 inhibitors are highly potent, easy to synthesize, water-soluble, generally nontoxic, orally bioavailable, and effective in arresting the tumor growth *in vivo* as single agents. We believe that MCT1 inhibitors can be developed as single agent cancer chemotherapeutics and that they should

DOI: 10.1021/acsmedchemlett.5b00049
ACS Med. Chem. Lett. 2015, 6, 558−561

also be highly amenable for combination therapy with other drugs with different mechanisms of action. The potential outcome of this project will be a new class of broad spectrum anticancer agents with higher affinity and specificity than previously available.

■ ASSOCIATED CONTENT

Supporting Information

Synthetic methods and procedures of all the compounds, spectroscopic data, and elemental analysis, and *in vitro* and *in vivo* biological protocols. This material is available free of charge via the Internet at http://pubs.acs.org.

■ AUTHOR INFORMATION

Corresponding Authors

*(L.R.D.) E-mail: ldrewes@d.umn.edu. Tel: 218-726-7925.
*(V.R.M.) E-mail: vmereddy@d.umn.edu. Tel: 218-726-6766.

Funding

This work was supported by Engebretson Drug Discovery Program, College of Pharmacy, University of Minnesota; Whiteside Clinical Research Institute, Duluth, Minnesota; and Minnesota Partnership for Biotechnology and Medical Genomics.

Notes

The authors declare the following competing financial interest(s): A patent application has been filed, but it has not been licensed nor has generated any revenue to date.

■ ABBREVIATIONS

CHC, α-cyano-4-hydroxycinnamic acid; MCT, monocarboxylate transporter; IC_{50}, the concentration of test compound causing 50% transport inhibition; SAR, structure−activity relationship; RBE4, rat brain endothelial 4 cells; K_2CO_3, potassium carbonate; $NaHCO_3$, sodium bicarbonate; SEM, standard error of the mean; ICR mice, mice initiated at Institute for Cancer Research; DMSO, dimethyl sulfoxide; PBS, phosphate buffered saline; ip, intraperitoneal; qd, once daily; bid, twice daily; qid, four times daily

■ REFERENCES

(1) Sonveaux, P.; Végran, F.; Schroeder, T.; Wergin, M. C.; Verrax, J.; Rabbani, Z. N.; De Saedeleer, C. J.; Kennedy, K. M.; Diepart, C.; Jordan, C. F.; Kelley, M. J.; Gallez, B.; Wahl, M. L.; Feron, M.; Dewhirst, M. W. Targeting lactate-fueled respiration selectively kills hypoxic tumor cells in mice. *J. Clin. Invest.* **2008**, *11*, 3930−3942.
(2) Ganapathy, V.; Thangaraju, M.; Prasad, P. D. Nutrient transporters in cancer: Relevance to Warburg hypothesis and beyond. *Pharmacol. Ther.* **2009**, *121*, 29−40.
(3) Lunt, S. Y.; Vander, H. M. Aerobic glycolysis: Meeting the metabolic requirements of cell proliferation. *Annu. Rev. Cell Dev. Biol.* **2011**, *27*, 441−464.
(4) Ganapathy, K. S.; Geschwind, J. F. Tumor glycolysis as a target for cancer therapy: Progress and prospects. *Mol. Cancer* **2013**, *12*, 152.
(5) Miran, J.; Sung, S. K.; Jinhwa, L. Cancer cell metabolism: Implications for therapeutic targets. *Exp. Mol. Med.* **2013**, *45*, e45.
(6) Halestrap, A. P.; Price, N. T. The proton-linked monocarboxylate transporter (MCT) family: Structure, function and regulation. *Biochem. J.* **1999**, *343*, 281−299.
(7) Halestrap, A. P. The SLC16 gene family: Structure, role and regulation in health and disease. *Mol. Aspects Med.* **2013**, *34*, 337−349.
(8) Sonveaux, P.; Copetti, T.; Saedeleer, C. J. D.; Vegran, F.; Verrax, J.; Kennedy, K. M.; Moon, E. J.; Dhup, S.; Danhier, P.; Frerart, F.; Gallez, B.; Ribeiro, A.; Michiels, C.; Dewhirst, M. W.; Feron, O. Targeting the lactate transporter mct1 in endothelial cells inhibits lactate-induced HIF-1 activation and tumor angiogenesis. *PLoS One* **2012**, *7*, e33418.
(9) Doherty, J. R.; Yang, C.; Scott, K. E.; Cameron, M. D.; Fallahi, M.; Li, W.; Hall, M. A.; Amelio, A. L.; Mishra, J. K.; Li, F.; Tortosa, M.; Genau, H. M.; Rounbehler, R. J.; Lu, Y.; Dang, C. V.; Kumar, K. G.; Butler, A. A.; Bannister, T. D.; Hooper, A. T.; Unsal-Kacmaz, K.; Roush, W. R.; Cleveland, J. L. Blocking lactate export by inhibiting the myc target MCT1 disables glycolysis and glutathione synthesis. *Cancer Res.* **2014**, *74*, 908−920.
(10) Wang, H.; Yang, C.; Doherty, J. R.; Roush, W. R.; Cleveland, J. L.; Bannister, T. D. Synthesis and structure activity relationships of pteridine dione and trione monocarboxylate transporter 1 inhibitors. *J. Med. Chem.* **2014**, *57*, 7317−7324.
(11) Critchlow, S. E.; Tate, L. Use of a MCT1 inhibitor in the treatment of cancers expressing MCT1 over MCT4. PCT Int. Appl. WO 2010089580A1 20100812, 2010.
(12) Draoui, N.; Schicke, O.; Fernandes, A.; Drozak, X.; Nahra, F.; Dumont, A.; Douxfils, J.; Hermans, E.; Dogné, J. M.; Corbau, R.; Marchand, A.; Chaltin, P.; Sonveaux, P.; Feron, O.; Riant, O. Synthesis and pharmacological evaluation of carboxycoumarins as a new antitumor treatment targeting lactate transport in cancer cells. *Bioorg. Med. Chem.* **2013**, *21*, 7107−7117.
(13) Zhao, Z.; Wu, M. S.; Zou, C.; Tang, Q.; Lu, J.; Liu, D.; Wu, Y.; Yin, J.; Xie, X.; Shen, J.; Kang, T.; Wang, J. Downregulation of MCT1 inhibits tumor growth, metastasis and enhances chemotherapeutic efficacy in osteosarcoma through regulation of the NF-κB pathway. *Cancer Lett.* **2014**, *342*, 150−158.
(14) Draoui, N.; Schicke, O.; Seront, E.; Bouzin, C.; Sonveaux, P.; Riant, O.; Feron, O. Antitumor activity of 7-aminocarboxycoumarin derivatives, a new class of potent inhibitors of lactate influx but not efflux. *Mol. Cancer Ther.* **2014**, *13*, 1410−1418.
(15) Pavlides, S.; Whitaker-Menezes, D.; Castello-Cros, R.; Flomenberg, N.; Witkiewicz, A. K.; Frank, P. G.; Casimiro, M. C.; Wang, C.; Fortina, P.; Addya, S.; Pestell, R. G.; Martinez-Outschoorn, U. E.; Sotgia, F.; Lisanti, M. P. The reverse Warburg effect: Aerobic glycolysis in cancer associated fibroblasts and the tumor stroma. *Cell Cycle* **2009**, *8*, 3984−4001.
(16) Witkiewicz, A. K.; Dasgupta, A.; Sammons, S.; Er, O.; Potoczek, M. B.; Guiles, F.; Sotgia, F.; Brody, J. R.; Mitchell, E. P.; Lisanti, M. P. Loss of stromal caveolin-1 expression predicts poor clinical outcome in triple negative and basal-like breast cancers. *Cancer Biol. Ther.* **2010**, *10*, 135−143.
(17) Lisanti, M. P.; Martinez-Outschoorn, U. E.; Chiavarina, B.; Pavlides, S.; Whitaker-Menezes, D.; Tsirigos, A.; Witkiewicz, A.; Lin, Z.; Balliet, R.; Howell, A.; Sotgia, F. Understanding the lethal drivers of tumor-stroma co-evolution. *Cancer Biol. Ther.* **2010**, *10*, 537−542.
(18) Agnieszka, K. W.; Whitaker-Menezes, D.; Dasgupta, A.; Philp, N. J.; Lin, Z.; Gandara, R.; Sneddon, S.; Martinez-Outschoorn, U. E.; Sotgia1, F.; Lisanti, M. P. Using the reverse Warburg effect to identify high-risk breast cancer patients. *Cell Cycle.* **2012**, *11*, 1108−1117.
(19) Mereddy. V. R.; Drewes L. R.; Alam, M. A.; Jonnalagadda, S. K.; Gurrapu, S. Therapeutic compounds. PCT Appl. WO 2013109972A2, 2013.
(20) Freeman, F. Properties and reactions of ylidenemalononitriles. *Chem. Rev.* **1980**, *80*, 329−350.
(21) Drewes, L. R.; Spanier, J. A. Monocarboxylate transporters. *Drug Transp.* **2007**, 147−170.
(22) Smith, J. P.; Drewes, L. R. Modulation of monocarboxylic acid transporter-1 kinetic function by the cAMP signaling pathway in rat brain endothelial cells. *J. Biol. Chem.* **2006**, *281*, 2053−2060.
(23) Campaigne, E.; Archer, W. L. Formylation of dimethylaniline. *Org. Synth.* **1953**, *33*, 27.

DOI: 10.1021/acsmedchemlett.5b00049
ACS Med. Chem. Lett. 2015, 6, 558−561

Received: 13 August 2019 | Revised: 30 September 2019 | Accepted: 22 October 2019

DOI: 10.1111/vco.12551

Veterinary and Comparative Oncology WILEY

ORIGINAL ARTICLE

A novel MCT1 and MCT4 dual inhibitor reduces mitochondrial metabolism and inhibits tumour growth of feline oral squamous cell carcinoma

Ali Khammanivong[1] | Jhuma Saha[1] | Angela K. Spartz[2] | Brent S. Sorenson[1] | Alexander G. Bush[1] | Derek M. Korpela[1] | Raj Gopalakrishnan[3,4] | Shirisha Jonnalagadda[5] | Venkatram R. Mereddy[5] | Timothy D. O'Brien[4,6,7] | Lester R. Drewes[4,8] | Erin B. Dickerson[1,4,9]

[1]Department of Veterinary Clinical Sciences, College of Veterinary Medicine, University of Minnesota, St. Paul, Minnesota

[2]Department of Laboratory Medicine and Pathology, University of Minnesota, Minneapolis, Minnesota

[3]Department of Diagnostic and Biological Sciences, School of Dentistry, University of Minnesota, Minneapolis, Minnesota

[4]Masonic Cancer Center, University of Minnesota, Minneapolis, Minnesota

[5]Department of Chemistry and Biochemistry, University of Minnesota, Duluth, Minnesota

[6]Department of Veterinary Population Medicine, College of Veterinary Medicine, University of Minnesota, St. Paul, Minnesota

[7]Stem Cell Institute, University of Minnesota, Minneapolis, Minnesota

[8]Department of Biomedical Sciences, University of Minnesota Medical School Duluth, Duluth, Minnesota

[9]Animal Cancer Care and Research Program, University of Minnesota, St. Paul, Minnesota

Correspondence
Erin B. Dickerson, Department of Veterinary Clinical Sciences, College of Veterinary Medicine, University of Minnesota, St. Paul, MN.
Email: edickers@umn.edu

Funding information
Morris Animal Foundation, Grant/Award Number: D15FE-020; The National Institutes of Health, Grant/Award Number: P30 CA77598; U.S. Department of Defense, Grant/Award Numbers: W81XWH-15-1-0047, W81XWH-15-1-0060; College of Veterinary Medicine, University of Minnesota

Abstract

Monocarboxylate transporters (MCTs) support tumour growth by regulating the transport of metabolites in the tumour microenvironment. High MCT1 or MCT4 expression is correlated with poor outcomes in human patients with head and neck squamous cell carcinoma (HNSCC). Recently, drugs targeting these transporters have been developed and may prove to be an effective treatment strategy for HNSCC. Feline oral squamous cell carcinoma (OSCC) is an aggressive and treatment-resistant malignancy resembling advanced or recurrent HNSCC. The goals of this study were to investigate the effects of a previously characterized dual MCT1 and MCT4 inhibitor, MD-1, in OSCC as a novel treatment approach for feline oral cancer. We also sought to determine the potential of feline OSCC as a large animal model for the further development of MCT inhibitors to treat human HNSCC. In vitro, MD-1 reduced the viability of feline OSCC and human HNSCC cell lines, altered glycolytic and mitochondrial metabolism and synergized with platinum-based chemotherapies. While MD-1 treatment increased lactate concentrations in an HNSCC cell line, the inhibitor failed to alter lactate levels in feline OSCC cells, suggesting an MCT-independent activity. In vivo, MD-1 significantly inhibited tumour growth in a subcutaneous xenograft model and prolonged overall survival in an orthotopic model of feline OSCC. Our results show that MD-1 may be an effective therapy for the treatment of feline oral cancer. Our findings also support the further investigation of feline OSCC as a large animal model to inform the development of MCT inhibitors and future clinical studies in human HNSCC.

KEYWORDS

Feline oral squamous cell carcinoma, Head and neck cancer, MCT1, MCT4, metabolism, metabolic coupling

1 | INTRODUCTION

Cancer cells rewire their metabolism to promote cell proliferation, survival, tumour growth and long-term maintenance, and there is abundant interest in developing therapies to selectively target these aberrant metabolic pathways.[1-4] A common feature of altered cancer cell metabolism is an increase in glucose uptake and consumption, leading to the production of high levels of lactate, even in the presence of adequate oxygen.[5] The "Warburg effect," a unique process where tumour cells use aerobic glycolysis, was first described by Otto Warburg in the 1920s.[6] Aerobic glycolysis has been proposed as an adaptive mechanism used by cancer cells to support the generation of nucleotides, lipids and proteins required for uncontrolled cell proliferation.[7,8] However, it only partially explains metabolic tumour cell reprogramming, since many tumour types exhibit metabolic heterogeneity.[9-11] Tumour metabolic heterogeneity has led to the idea of the "reverse Warburg effect," a two-compartment model wherein cancer cells and cancer-associated fibroblasts (CAFs) become metabolically coupled.[12-14] In this model, CAFs undergo glycolysis and generate high levels of energy-rich fuels, such as lactate and ketone bodies, which are taken up by the cancer cells and metabolized via oxidative phosphorylation (OXPHOS).[12,15,16] By exploiting the metabolically rich fuels produced by CAFs, cancer cells can efficiently produce the adenosine triphosphate (ATP) and the metabolites necessary to promote cellular proliferation and tumour growth.[17-19]

Monocarboxylate transporters (MCTs) are members of the solute carrier 16 gene family, which consists of 14 different isoforms.[20,21] These proton-linked membrane transporters move single-carboxylate molecules, including pyruvate, lactate and ketone bodies, in and out of cells.[20-22] Evidence suggests MCT1 and MCT4, encoded by the *SLC16A1* and the *SLC16A3* genes, respectively, support metabolic coupling between cancer cells and CAFs.[23-25] MCT1 expression is elevated in a variety of human tumours, where it is associated with the increased uptake of lactate by cancer cells exhibiting high levels of OXPHOS.[22,26] In contrast, MCT4 expression is often higher in glycolytic CAFs, which export lactic acid.[27,28] Confirmation of this metabolic symbiosis in vivo, at least in part, has been supported using biopsies from human breast cancer and head and neck squamous cell carcinoma (HNSCC, head and neck cancer).[25,29]

Head and neck cancers comprise 3% of the cancer burden in the United States each year, and the 5-year survival rate for patients with HNSCC continues to hover around 60%.[30] The increased expression of either MCT1 or MCT4 has been shown to correlate with poor outcomes in patients with HNSCC,[29,31-33] suggesting that targeting these transporters may be an effective treatment strategy. AZD3965 is a highly potent MCT1 inhibitor currently in Phase I/II clinical trials in diffuse B cell lymphomas, Burkitt Lymphoma and advanced solid tumours (NCT01791595, ClinicalTrials.gov). Because AZD3965 selectively inhibits MCT1, it may not be suitable for treatment of HNSCC or other cancers because of the potential compensatory activity of MCT4, which it does not inhibit. Hence, inhibitors that target both MCT1 and MCT4 may be more effective for the treatment of HNSCC, and their evaluation in pre-clinical and clinical models of head and neck cancer will be needed to assess their suitability for clinical translation.[34-36]

Feline oral squamous cell carcinoma (OSCC) shares many clinical and biological features of human HNSCC, and it has been proposed as a naturally occurring, large-animal model for human head and neck cancer.[37-41] Feline OSCC is a devastating disease that accounts for approximately 60% to 80% of all oral tumours in domestic cats.[37,42] Because the disease is typically diagnosed at the advanced stages, it often involves local structural invasion and regional lymph node metastasis, contributing to a poor prognosis.[43,44] Currently, there are no effective treatments for feline OSCC, and 1-year survival rates remain at less than 10%.[43,44] Surgery is generally ineffective at controlling local disease or improving overall survival, and only modest gains have been noted with the addition of radio- or chemotherapy.[45-48] Studies assessing MCT expression have not been undertaken for feline OSCC, and the metabolic properties of these tumours remain largely unstudied.

Here, we sought to investigate the effects of a previously characterized dual MCT1 and MCT4 inhibitor, MD-1,[35,36] on OSCC cell viability and tumour growth as a novel treatment approach for feline oral cancer. We also sought to determine the potential of feline OSCC as a large animal model for the further development of MCT inhibitors to treat human HNSCC.

2 | MATERIALS AND METHODS

2.1 | MD-1

MD-1 was provided by Dr Venkatram Mereddy (University of Minnesota Duluth, Minnesota) and was solubilized in dimethylsulfoxide (DMSO). The synthesis (Compound 27[35]), anti-tumour activity (Compound 27[35]; Compound 9[36]) and inhibition of metabolic activity for MD-1 (Compound 9[36]) were described previously.

2.2 | Cell lines and culture conditions

The feline OSCC lines SCCF1, SCCF2 and SCCF3 were provided by Dr Thomas Rosol (Ohio State University). SCCF1 was previously established and characterized from a primary laryngeal tumour,[49] while SCCF2 and SCCF3 were established from bone-invasive gingival and lingual feline tumours, respectively.[50] The human HNSCC cell lines TR146, UMSCC-17B and SCC-58 were provided by Dr Mark Herzberg (University of Minnesota). TR146 was established and characterized from a metastatic buccal carcinoma.[51] UMSCC-17B was established from a metastatic laryngeal head and neck tumour,[52] and SCC-58 was established from a primary tumour of the oral cavity.[53] All of the cell lines were cultured on standard tissue-culture treated flasks in Dulbecco Modified Eagle Medium/Ham F-12 50:50 mix (DMEM/F-12) (Corning, Mediatech, Manassas, Virginia) supplemented with L-glutamine, 10% FBS (Atlanta Biologicals, Flowery Branch, Georgia), 1% HEPES (Mediatech Inc., Manassas, Virginia) and 0.1%

Primocin (Invivogen, San Diego, California) at 37°C in a humidified, 5% CO_2 atmosphere, unless otherwise specified.

2.3 | RNA sequencing, gene coregulation and pathway analysis

RNA sequencing (RNA-seq) analysis of human HNSCC data from The Cancer Genome Atlas (TCGA) was performed as previously described.[54] Differentially regulated genes (fold-change ≥ 1.9, false discovery rate or FDR < 0.05) were further interrogated for coregulation in HNSCC based on Pearson correlation analysis across all tumour samples. Correlation coefficient (*r*) of ≤−0.45 or ≥0.45 and FDR < 0.05 were used as cut-off criteria. For RNA-seq analysis of human HNSCC and feline OSCC cell lines, total RNA was extracted from cells grown as heterogeneous monolayer cultures or sphere-enriched cancer stem cell (CSC)-like cultures (orospheres) as previously described.[54] Three independent replicate monolayer and orosphere cultures of human TR146, UMSCC-17B and SCC-58 (three additional replicates of SCC-58 orospheres were also included, for a total n = 6) HNSCC cell lines were analysed. For feline OSCC lines, three independent replicates of SCCF1, SCCF2 and SCCF3 monolayer cultures were used, but only SCCF1 and SCCF3 formed orospheres and were included in the analysis (n = 3 independent repeats each). RNA quality analysis was performed for each sample using Agilent Bioanalyzer (Agilent Technologies, Santa Clara, California) and only samples with RNA integrity number > 8.0 were submitted for library preparation using Illumina v4 chemistry and sequencing using Illumina HiSeq 2500, 50 bp paired-end read, high output mode (University of Minnesota Genomics Center) at a depth of approximately 20 million reads. FASTQ analysis was performed for each sequencing data with a mean quality score of >35. Sequencing data was then mapped to either the human HG38 reference genome (for human HNSCC lines) or the *Felis catus* 5.0 reference genome (for feline OSCC lines) from ensemble.org using MapSplice 2.2.[55] Transcript abundance was calculated using Subread featureCounts,[56] and total transcript count values were collapsed to the gene level based on median counts representing total mRNA expression levels. Expression value of each gene was further normalized to total reads and presented as reads per million. Differential expression analysis was performed using signal-to-noise ratio and fold-change statistical analysis using GENE-E/Morpheus (https://software.broadinstitute.org/GENE-E/; https://software.broadinstitute.org/morpheus/). Gene pathway and functional analysis were performed using Ingenuity Pathway Analysis (IPA; Qiagen, Redwood, California).

2.4 | Immunoblotting

All cell lines were plated at 50% to 60% confluency in cell culture flasks containing DMEM/F-12 cell culture medium and allowed to adhere overnight. Flasks were then incubated under normoxic (21% O_2) or hypoxic (1% O_2) conditions for 24 hours before treating with MD-1. Hypoxia was achieved by displacing air in the humidified hypoxic chamber with nitrogen gas using an automated injector while maintaining the CO_2 level at 5% and temperature at 37°C. The hypoxic chamber was set to 1% O_2 overnight prior to the start of the experiment, and the O_2 level was monitored continuously throughout the experiment with a digital sensor system. The cells were then washed with phosphate buffered saline (PBS), removed from the flasks with trypsin, pelleted and washed two times with PBS. Washed pellets were frozen and stored at −80°C. Whole cell lysates were prepared as previously described,[41,57] and the protein concentrations were determined using the Pierce BCA protein assay kit (Thermo Fisher Scientific). Immunoblotting was performed as described previously.[41,57,58] Specifically, equal amounts of protein were loaded onto Mini-PROTEIN TGX precast protein gels (4%-15%) or Criterion TGX precast SDS-PAGE gels (Bio-Rad, Hercules, California) and separated by gel electrophoresis. The proteins were then transferred to nitrocellulose membranes, and the membranes blocked for 1 hour at room temperature using the Odyssey Blocking Buffer diluted 1:1 in Tris-buffered saline (TBS) (LI-COR Biosciences, Lincoln, Nebraska) or iBind ×1 FD Buffer (Invitrogen, Carlsbad, California). The membranes were then incubated with the primary antibodies for MCT1 (1:1000, TA321555; Origene, Rockville, Maryland), MCT4 (1:1000, sc-50329; Santa Cruz Biotechnology, Dallas, Texas), lactate dehydrogenase B (LDHB) (1:1000, sc-100775; Santa Cruz Biotechnology), or Tom20 (1:1000, sc-17764; Santa Cruz Biotechnology) diluted in either Odyssey Blocking Buffer overnight at 4°C or iBind ×1 FD Buffer overnight at room temperature. Normalization was performed by either REVERT total protein staining (LI-COR Biosciences) immediately after transfer or by incubating with β-actin antibody (1:5000, Mouse IgG monoclonal, A5441; Sigma-Aldrich, St. Louis, Missouri). The membranes were washed with TBS plus 0.5% Tween 20 and incubated with goat anti-rabbit and anti-mouse secondary antibodies (1:10 000) (LI-COR Biosciences, Catalogue Nos. 92632211 and 92668070), respectively, conjugated to infrared dyes. Proteins were detected using a LI-COR Odyssey imager, and the protein levels were quantified using LI-COR Image Studio software.

2.5 | Immunohistochemistry

Eight formalin-fixed, paraffin-embedded human HNSCC tumour blocks representing invasive disease were obtained from the University Oral Pathology Laboratory, University of Minnesota (Minneapolis, Minnesota) after obtaining appropriate IRB approval. Five feline OSCC tumour blocks were obtained from the College of Veterinary Medicine, Colorado State University (Fort Collins, Colorado). The samples were sectioned into 4 μm sections and mounted on glass slides for haematoxylin staining and immunohistochemistry (IHC). The human HNSCC and the feline OSCC cell lines were used to establish the conditions for IHC analysis of the human and feline FFPE tumour sections once expression of the relevant antigens had been confirmed in the cell lines by immunoblotting. Human HNSCC and feline OSCC cell lines were embedded in paraffin as described[59] and used as positive controls for MCT1, MCT4, LDHB and translocase of outer mitochondrial membrane 20 (TOMM20) expressions; unstained sections

exposed only to secondary antibody served as negative controls. For staining of cell lines or tumour sections, antigen retrieval was performed using a citrate buffer target retrieval solution (Dako 1699; Agilent, Santa Clara, California) at 95°C for 30 minutes. Sections were then treated with 0.3% hydrogen peroxide (H312-500; Fisher Chemical) for 5 minutes, followed by blocking for 15 minutes at room temperature with Protein Block-Serum Free solution (Dako, X0909). Sections were incubated with an anti-MCT1 primary antibody (1:800 dilution, TA321555), an anti-MCT4 antibody (1:200 dilution, sc-50329), an anti-LDHB antibody (1:100 dilution, sc-100775), or an anti-Tom20 antibody (1:200, sc-17764) for 30 minutes at room temperature. Sections were washed and incubated with either a peroxidase-conjugated anti-rabbit secondary antibody (Rabbit Envision, Dako, K4003) or a peroxidase-conjugated anti-mouse secondary antibody (Mouse Envision, Dako, K4001) for 30 minutes at room temperature. Colour development was performed using 3,3-diaminobenzidine tetra-hydrochloride (DAB) (Dako, K3468) for 5 minutes at room temperature. The slides were counterstained with haematoxylin and coverslipped for microscopic evaluation. Samples were assessed for staining, and the levels and distribution of MCT1, MCT4, LDHB and TOMM20 expressions were evaluated by a board-certified veterinary pathologist (T.D.O.). All immunohistochemical processing and staining were carried out through the Comparative Pathology Shared Resource, University of Minnesota, Twin Cities.

2.6 | Cell viability assay

SCCF1, SCCF2, SCCF3, TR146, UMSCC-17B and SCC-58 cells were plated in 96-well cell culture plates at a density of 1×10^4 cells/well. After allowing the cells to adhere to the plate in DMEM/F12 under standard culture conditions, cells were treated with increasing concentrations of MD-1 (0.5-150 μM). DMSO-treated cells were included as a vehicle control, and all treatments were conducted in triplicate. The concentrations chosen for these assays were based on previously published studies and the PK parameters for MD-1.[35,36] Cells were incubated under standard normoxic or hypoxic conditions for 24 hours followed by treatment with MD-1 for 48 hours. Cell viability was assessed by using a CyQUANT Cell Proliferation Assay kit (Thermo Fisher Scientific, Waltham, Massachusetts), according to the manufacturer's instructions. Fluorescence emission at 520 nm was measured using a TECAN Infinite m200 PRO plate reader (Tecan US, Morrisville, North Carolina), and the values were standardized to total cell number using a standard curve for each cell line. The experiments were repeated a minimum of three times, and the data were plotted using GraphPad Prism version 6.0 hours software (GraphPad, San Diego, California) to enable statistical analysis and estimation of the relative IC50 values.

2.7 | Lactic acid assay

L-lactate in cell culture medium and cell culture extracts was assayed enzymatically using a commercially available L-Lactate Assay Kit (Eton Bioscience, San Diego, California). Briefly, cell culture samples were stored at −80°C and assayed after appropriate dilution with water. Cell cultures were quickly washed with ice-cold buffer, stored frozen, extracted and assayed. Samples (8 μL) were incubated with assay buffer and enzyme reagent (992 μL) for 30 minutes before quantification at 570 nm in a plate reader. Samples were assayed in duplicate and concentrations calculated using a standard curve. The data are representative of at least three independent experiments for each cell line.

2.8 | Metabolic analysis

A Seahorse XF^{e}96 Extracellular Flux Analyzer (Seahorse Biosciences, North Billerica, Massachusetts) was used to measure the oxygen consumption rate (OCR) and extracellular acidification rate (ECAR) of cancer cells in vitro in the presence or absence of MD-1. Human HNSCC and feline OSCC cell lines were plated in XF96-well plates containing 80 μL of growth medium at cell densities that were optimized for each line (12 000-19 000 cells/well) 18 hours prior to the start of the assay to attain a confluence level of approximately 85% to 95%. Sensor cartridges were pre-incubated for the same length of time in XF Calibrant solution (Seahorse Biosciences). On the day of the assay, growth medium was replaced with 175 μL of Assay Medium, which contained Seahorse XF Base Medium supplemented with 2.5 mM L-glutamine for the Glycolysis Stress Test or 17.5 mM glucose, 2.5 mM L-glutamine, and 0.5 mM sodium pyruvate for the Mitochondria Stress Test, both of which were adjusted to pH 7.4 at 37°C. Medium replacement was carried out using a Seahorse XF Prep Station according to the manufacturer's instructions (Seahorse Biosciences). Plates were maintained for 1 hour at 37°C in a non-CO_2 incubator prior to the assay.

Assay Medium was used to reconstitute Seahorse kit reagents according to the manufacturer's instructions and to dilute MD-1 to the appropriate concentrations. After three initial measurements of basal ECAR and OCR, injection of MD-1 (10 μM), vehicle DMSO, and an additional control containing only assay medium commenced. For the Glycolysis Stress Test, sequential injections of glucose (10 mM), oligomycin (1 or 2 μM, depending on the cell line) and 2-deoxyglucose (50 mM) followed. For the Mitochondria Stress test, sequential injections of oligomycin (1-2 μM, depending on the cell line), FCCP (0.125 μM) and rotenone and antimycin A (0.5 μM) are followed. Three measurements of ECAR and OCR were recorded after every injection for both assay types.

After completion of the assays, cells were fixed with ice-cold methanol containing 1% acetic acid and kept at −20°C for a minimum of 4 hours. The methanol/acetic acid mixture was removed and cells were washed twice with cold ×1 PBS before being dried at 37°C. Cellular protein concentration per well was determined using a Pierce BCA Protein Assay Kit for normalization of Seahorse ECAR and OCR data. The data are representative of at least three independent experiments for each cell line.

2.9 | Synergy studies

Cell lines were plated and cultured in 96-well plates as described above, and incubated with increasing concentrations of carboplatin

(Hospira, Inc., Lake Forest, Illinois) (SCCF1, SCCF2 and SCCF3), cisplatin (Accord Healthcare, Inc., Durham, North Carolina) (TR146, SCC-58 and UMSCC-17B), MD-1, or a combination of both drugs using a diagonal constant ratio combination design, as described by Chou.[41] After an incubation period of 48 hours under standard cell culture conditions, cell viability was assessed using a CyQUANT Cell Proliferation assay as described above. The Combination Index was determined using the Compusyn software package (www.combosyn.com) as previously described.[41]

2.10 | Mice

Six-week-old female, athymic nude mice (strain J:Nu) were obtained from The Jackson Laboratory (Bar Harbour, Maine). All protocols for this study were approved by the University of Minnesota Institutional Animal Care and Use Committee.

2.11 | Tumour xenografts

2.11.1 | Orthotopic model

Two experiments were carried out to assess orthotopic (floor of the mouth, FOM) growth of SCCF3 cells and the tumour responses to MD-1. For the first experiment, four mice were used to validate the orthotopic model. All the mice showed successful implantation. For the second experiment, two groups of nine mice were used to establish significance. In this experiment, only 15 mice showed successful implantation. Mice were divided into two groups (vehicle-treated control, n = 7; MD-1-treated, n = 8) to determine the effects of MD-1 on tumour growth.

Animals were assigned to separate cages (three to four animals each) in random order for each experiment. The animals in each cage received the same treatment. SCCF3 cells expressing YFP and firefly luciferase were injected into the FOM. Mice were anaesthetized with xylazine (10 mg/kg body weight, intraperitoneally [IP]) and ketamine (100 mg/kg, IP), and 5×10^4 cells suspended in 100 μL of a 1:1 mixture of sterile PBS and Matrigel (Corning/BD Biosciences, Belford, Massachusetts) were injected into the FOM using a tuberculin syringe with 29-gauge needle. Tumour growth was monitored every 2 to 3 days by in vivo imaging, as described.[60] Bioluminescence imaging (Xenogen IVIS spectrum, Calliper Life Sciences, Hopkinton, Massachusetts) was carried out after injection of D-luciferin (Gold Biotechnology, St. Louis, Missouri) following isoflurane inhalant anaesthesia. Bioluminescence intensity with respect to the tumour size was analysed using Living Image Software (Calliper Life Sciences). Mice were treated two times per day, approximately 8 hours apart, with the drug diluent solution (PBS + 1% Tween-20) or MD-1 (25 mg/kg) by IP injection. The dose of MD-1 chosen for these assays was based on previously published studies and the PK parameters for MD-1.[35,36] Mice were observed until tumour endpoint criteria were reached (ill thrift, pain, difficulty eating or drinking or severe weight loss), at which time the mice were humanely euthanized with pentobarbital sodium and sodium phenytoin solution (Beuthanasia-D Special, Schering-Plough Animal Health, Union, New Jersey). Primary FOM tumours were excised and fixed in 10% neutral-buffered formalin, and processed for routine histological examination.

2.11.2 | Subcutaneous model

For the subcutaneous tumour model, 5×10^5 SCCF3 cells were suspended in 100 μL of PBS and injected subcutaneously over the right flank using a 25-gauge needle. For this experiment, eight mice per group were used to establish significance. All mice, except for one, showed successful implantation. Mice were divided into four groups (vehicle-treated control, n = 7; MD-1-treated, n = 8; carboplatin-treated, n = 8; MD-1 and carboplatin-treated, n = 8) to determine the effects of MD-1 and carboplatin on tumour growth and to evaluate drug synergy in vivo.

Once mean tumour size reached approximately 50 mm^3, animals were randomly assigned to separate cages (four animals each). Mice were injected IP with the drug diluent solution (PBS + 1% Tween-20), MD-1 (25 mg/kg), carboplatin (75 mg/kg), or MD-1 and carboplatin (25 and 75 mg/kg, respectively). Mice were injected twice daily with vehicle control or MD-1 as above, and twice weekly with carboplatin. All the animals in each cage received the same treatment. Mice were observed until the tumour endpoint criteria were reached (tumour reaching 2 cm^3, ill thrift, pain, or severe weight loss). Tumour growth was monitored by measuring the width (W) and length (L) of the tumours using callipers, and the tumour volume was calculated using the formula $V = W \times (L)^2 \times (\pi/6)$.[61] As above, all mice were humanely euthanized using Beuthanasia-D Special.

2.12 | Statistical analysis

All experiments were performed with at least three independent replicates to ensure consistency and reproducibility. Pair-wise comparison analysis was performed using two-sample unpaired Student t test with unequal variance using GraphPad Prism (GraphPad Software, Inc., San Diego, California), unless noted otherwise. A P value of less .05 was considered statistically significant.

3 | RESULTS

3.1 | MCT1 is coregulated with gene networks associated with cancer progression of HNSCC

To understand the significance of MCT1 in tumour growth and progression, and as a candidate for targeted anti-tumour therapy, we performed correlation analysis of genes differentially regulated in HNSCC using RNA-seq data from TCGA database as previously reported.[54] We identified 52 genes upregulated in HNSCC strongly correlated with SLC16A1 (MCT1) and 27 genes downregulated in HNSCC showing an inverse correlation with MCT1 (Figure 1A,B). The identified genes appeared to be coregulated with MCT1 and were associated with increased tumour

cell survival, proliferation, migration and metastatic invasion, and decreased cell death signalling (Figure 1C), processes essential for tumorigenesis and aggressive disease progression.

3.2 | MCT1 and MCT4 are expressed in human and feline oral tumours

Using RNA-seq data from TCGA and a panel of HNSCC and OSCC cell lines (human: UMSCC-17B, TR146 and SCC-58; feline: SCCF1, SCCF2 and SCCF3), we determined that both human and feline cells expressed similarly high levels of MCT1. For the human samples, expression in the established cell lines was similar to primary HNSCC tumours, which was significantly higher relative to the normal adjacent tissues ($P < .0001$) (Figure 2A). Because high expression of MCT1 has been associated with enriched CSC populations in glioblastoma (neurospheres)[62] and breast cancer (mammospheres),[63] we evaluated the expression of MCT1 in sphere cell populations enriched from the HNSCC (orospheres)[57,64] and OSCC cell lines. Differences in MCT1 expression were not observed in the heterogeneous monolayers (representing bulk tumour cells) and sphere cultures.

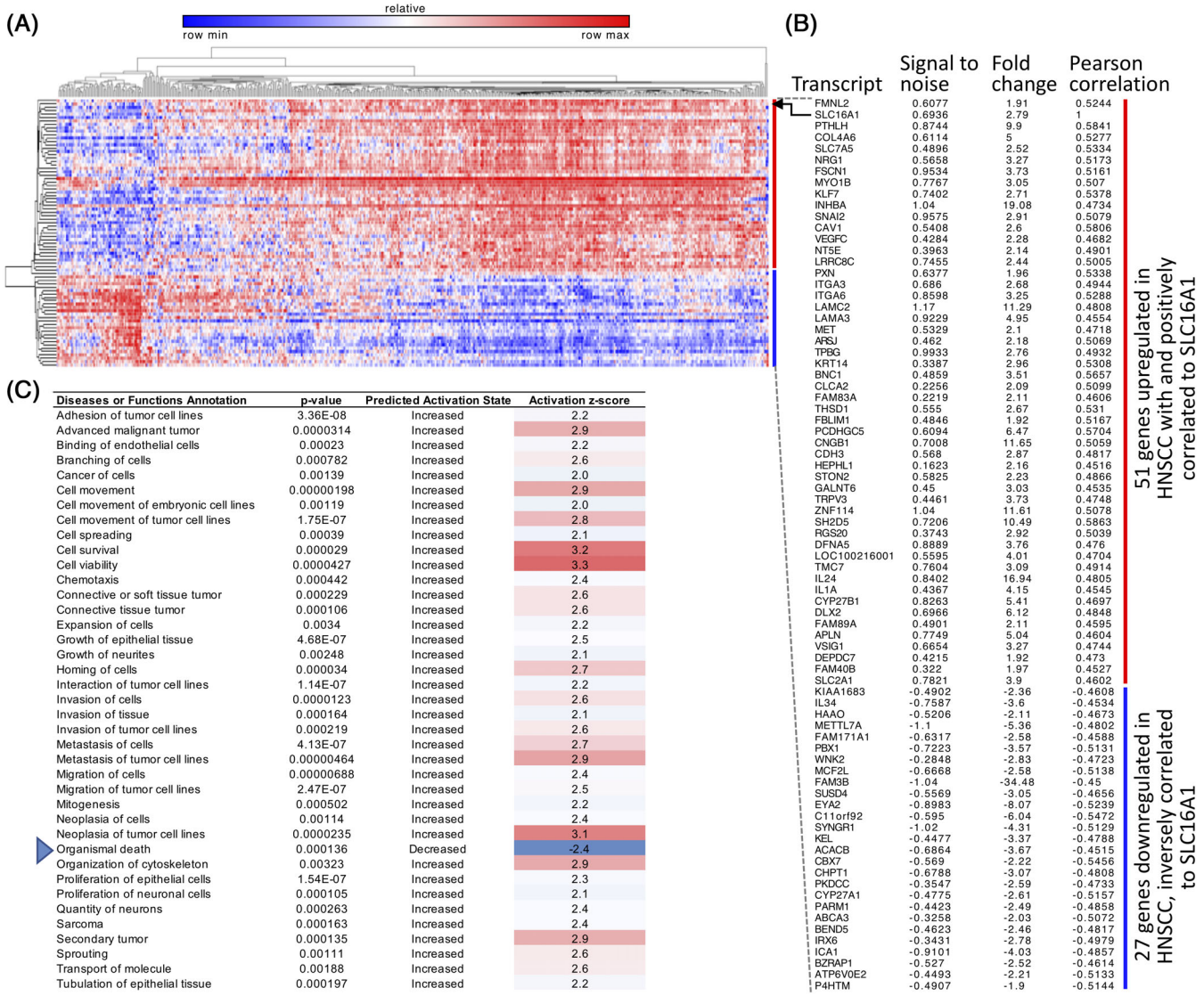

FIGURE 1 MCT1 is coregulated with gene networks associated with cancer progression of HNSCC. (A) Two-dimensional hierarchical clustering of differentially regulated genes (fold-change ≥ 1.9, FDR < 0.05) in HNSCC RNA-seq data from TCGA showing strong correlation (–0.45 ≥ r ≥ 0.45, FDR < 0.05) with MCT1 (SLC16A1). Heatmap shown as relative gene expression levels (measured by transcript abundance) in HNSCC tumour samples (n = 521). Blue and red are low and high expression levels, respectively, as indicated by the scale bar. Horizontal dendrogram shows clustering of HNSCC samples (columns) and vertical dendrogram shows clustering of genes (rows). (B) List of differentially regulated genes showing positive and negative correlations to MCT1. Statistical signal-to-noise ratio, fold change and Pearson correlation coefficient (relative to MCT1) are shown for each gene transcript. (C) Functional analysis of genes correlated to MCT1 in HNSCC by IPA. Blue and red indicate levels of decreased and increased predicted activation state, respectively, of each listed disease or biological function based the activation z-score values. FDR, false discovery rate; HNSCC, head and neck squamous cell carcinoma; IPA, Ingenuity Pathway Analysis; TCGA, The Cancer Genome Atlas

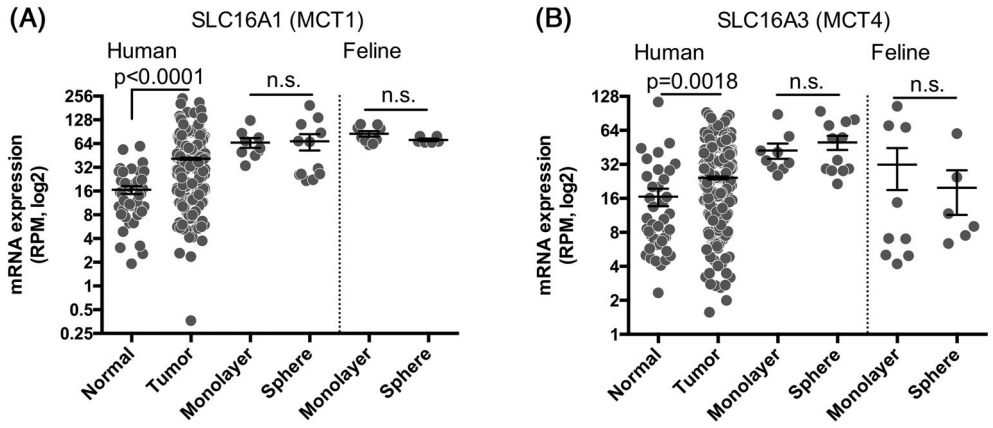

FIGURE 2 MCT1 and MCT4 are expressed in human and feline oral tumours. mRNA expression of (A) MCT1 and (B) MCT4 in normal adjacent tissue (n = 41), tumour (n = 521), monolayer cultures (TR146, n = 3; UMSCC-17B, n = 3; SCC-58, n = 3) and orospheres (sphere) (TR146 and UMSCC-17B with n = 3; SCC-58, n = 6) of human HNSCC and feline OSCC-derived cell lines (SCCF1, SCCF2, SCCF3 for monolayers and SCCF1 and SCCF3 for spheres; n = 3 each). Lines and error bars indicate mean ± SE. Statistical analysis was performed using two-tailed Student unpaired *t* test with equal variance. *P* value indicates statistical significance and n.s. indicates not significant between each pair. HNSCC, head and neck squamous cell carcinoma; OSCC, oral squamous cell carcinoma

The gene expression of MCT4 was significantly higher in primary tumours relative to the normal adjacent tissues in human samples (Figure 2B), and it was relatively high in both the human and feline carcinoma cells; although, expression in normal feline oral tissues was not available for comparison. We also evaluated the expression of MCT4 in the sphere cell populations, since higher levels of MCT4 have been shown to be associated with the CSC marker CD133 in neurospheres.[65] Differences in the expression of MCT4 between the sphere-enriched cells and the monolayer cells was not observed in both the human and feline cells.

We next used immunoblotting and IHC to validate the protein expression of MCT1 and MCT4 in the human and feline cell line panels and in primary tumours. Expression in all cell lines was evaluated after growth under normoxic (21% atmospheric O_2 level) and hypoxic (1% O_2 level) conditions since hypoxia has been shown to induce the expression of MCT4.[66] The expression levels of MCT1 were similar under both normoxic and hypoxic conditions in all cell lines, except for feline cell line, SCCF1 (Figure 3A,B), where MCT1 expression was increased under hypoxia. On the other hand, the expression of MCT4 was increased under hypoxia in all three human HNSCC cell lines. In the feline cell lines, the expression of MCT4 was relatively lower or below detectable limits compared with the levels in the human cell lines, and hypoxic responses were inconsistent (Figure 3A,C).

IHC analysis of MCT1 expression in primary tumour samples showed a similar membranous staining pattern in both human and feline tumour tissues (Figure 3D, top left and center panels), as previously described.[29] MCT1 staining was reproducible in a feline FOM xenograft model generated by injecting SCCF3 cells orthotopically (Figure 3D top right panel). MCT1 staining was not observed in the stroma of the human (Figure S1A) or the feline (Figure 3D, top centre panel) tissues. Membranous MCT4 staining was observed in the human carcinoma cells (Figure 3D bottom left panel), and a more diffuse and weaker staining pattern was observed in the stromal components (Figure S1B), consistent with previously reported findings.[29] Staining for MCT4 was relatively weaker in the feline tumours and the FOM tissues. In contrast to the membranous localization observed in the human tumours, staining for MCT4 in the feline OSCC tumours was more diffuse and distributed in both the cytoplasm and the nuclei of the epithelial cancer cells (Figure 3D, bottom centre and right panels). We also did not detect staining for MCT4 in the tumour stroma in feline OSCC. While these results suggest a similar role for MCT1 in human and feline oral tumours, they also suggest that MCT4 may not support a similar mechanism of metabolic symbiosis in feline OSCC.

3.3 | MD-1 reduces the viability of human HNSCC and feline OSCC cell lines

Based on the expression of MCT1 and MCT4 in the human and feline cell lines, we treated the cell lines with MD-1, a previously characterized dual inhibitor of MCT1 and MCT4.[35] MD-1 reduced the viability of the human and feline cells in a concentration-dependent manner (Figure 4). While MD-1 effectively inhibited the viability of the human UMSCC-17B HNSCC cells under both normoxia and hypoxia (Figure 4A; IC50: 50 and 58 μM, respectively), responses by human SCC-58 and TR146 (Figure 4B,C) and feline SCCF1 and SCCF2 lines were similar under both conditions (Figure 4D,E; IC50 ranging from 96 to 326 μM), and these cell lines were more resistant to MD-1 overall. SCCF3 was highly sensitive to MD-1 (IC50 of 9 and 13 μM in normoxia and hypoxia, respectively) (Figure 4F) relative to responses observed in the other cell lines. SCCF3 expresses relatively higher levels of MCT4 compared with the other feline OSCC lines (Figure 3), which may explain its strong sensitivity to MD-1.

We next determined if MD-1 increased the intracellular levels of lactic acid, since MD-1 was previously shown to increase intracellular

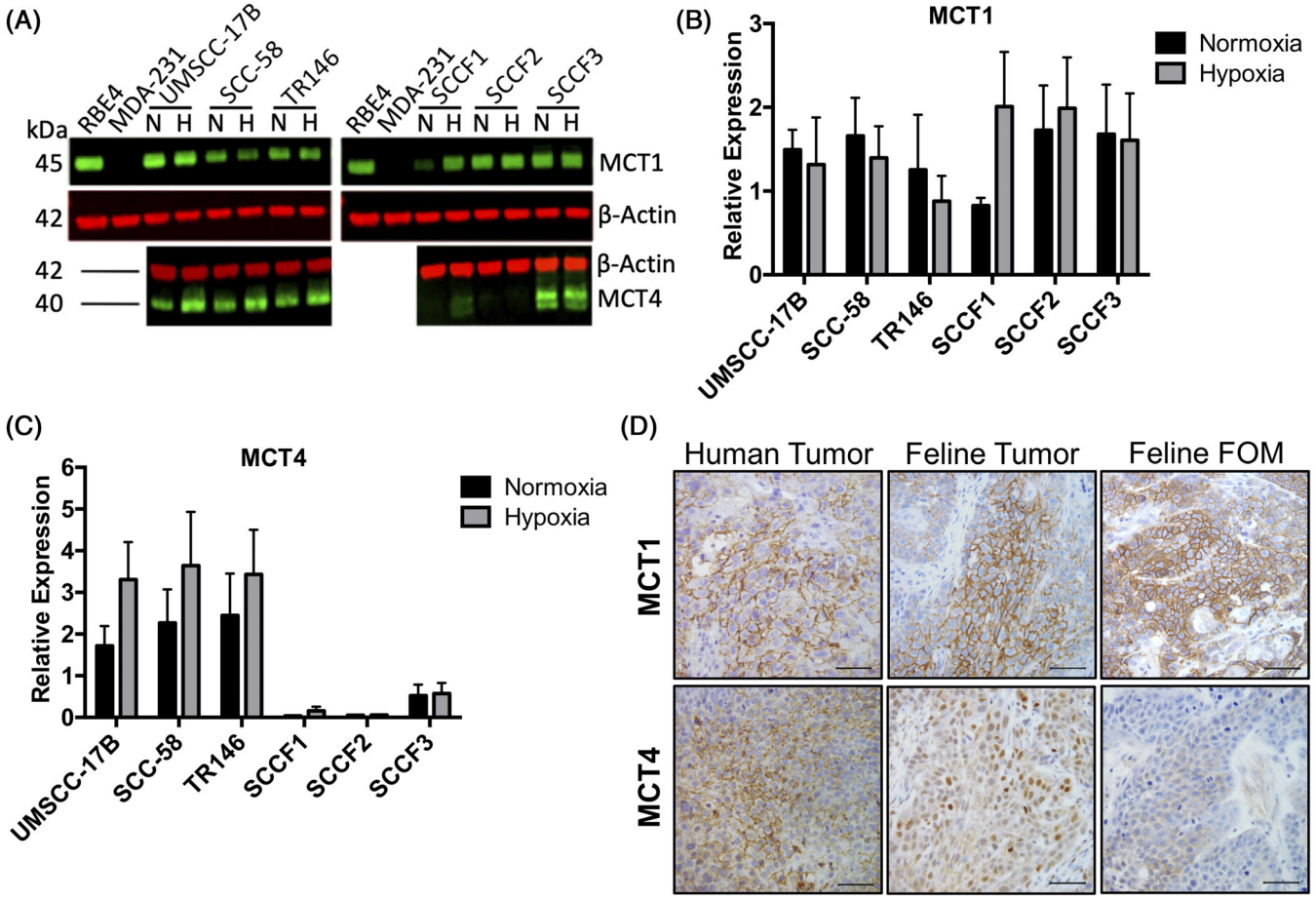

FIGURE 3 Protein expression of MCT1 and MCT4 in the human and feline cell line panels and in primary tumours by immunoblotting and immunohistochemistry. (A) Representative immunoblot for MCT1 and MCT4 in human HNSCC cell lines (left) and feline OSCC cell lines (right) under normoxia (N; 21% O_2), with hypoxia (H; 1% O_2). MDA-MB-231 (MDA-231) was used as a positive control for MCT4 and RBE4 was used as a positive control for MCT1 expression. Immunoblotting was performed twice, independently to confirm detection and summarized in (B) for MCT1 and (C) for MCT4. Data shown as mean ± SE. (D) Immunohistochemical staining of primary oral and FOM tumours. MCT1 (top row) and MCT4 (bottom row) staining in human HNSCC, feline OSCC, and feline FOM tumour. The brown colour indicates positive staining for each transporter and counterstained with haematoxylin for nuclei (blue). Original magnification: ×40, scale bar 50 μm. OSCC, oral squamous cell carcinoma; FOM, floor of the mouth

lactate concentrations in other tumour cell lines.[36] Analysis of lactate concentrations was performed in TR146, as a representative human cell line, and in SCCF1 and SCCF3 cells, since these lines were the most resistant and most sensitive OSCC lines to MD-1 treatment. We also used SCCF3 cells since we wanted to determine whether the relatively high expression of MCT4 in this line might contribute to the intracellular accumulation of lactic acid because of inhibition of both transporters by MD-1. Treatment with MD-1 significantly (P = .034) increased the intracellular levels of lactic acid in TR146 cells 24 hours after the addition of MD-1 (Figure 5A). Interestingly, significant changes in intracellular lactate concentrations were not observed in the SCCF1 or SCCF3 cell lines (Figure 5B,C).

Because MD-1 did not affect intracellular lactate accumulation in SCCF1 or SCCF3 cells, we considered that other transporters could compensate for MCT1 or MCT4 activity. MCT2 is a bidirectional transporter of lactate, and its expression has been reported in breast cancer, non-small cell lung cancer, colon cancer and ovarian cancer.[67,68] Using the RNA-seq data generated from the panel of OSCC cell lines, we determined that the expression of MCT2 (SLC16A7) was approximately 15-fold higher in the feline OSCC cell lines than the levels expressed by the human cell lines (Figure S2), suggesting that MCT2 could offset the inhibition induced by MD-1.

3.4 | MD-1 alters the metabolism in HNSCC and OSCC cell lines

Previous studies showed that MD-1 disrupted glycolysis and OXPHOS in the MCT1 expressing colorectal adenocarcinoma cell line, WiDr, and the MCT4 expressing cell line MDA-MB-231, a triple-negative breast cancer cell line.[36] Hence, we sought to determine if MD-1 reduced cell viability by altering glycolytic and mitochondrial metabolism. Because the in vitro metabolic profiles of the cell lines have not yet been described, we first established their energy profiles

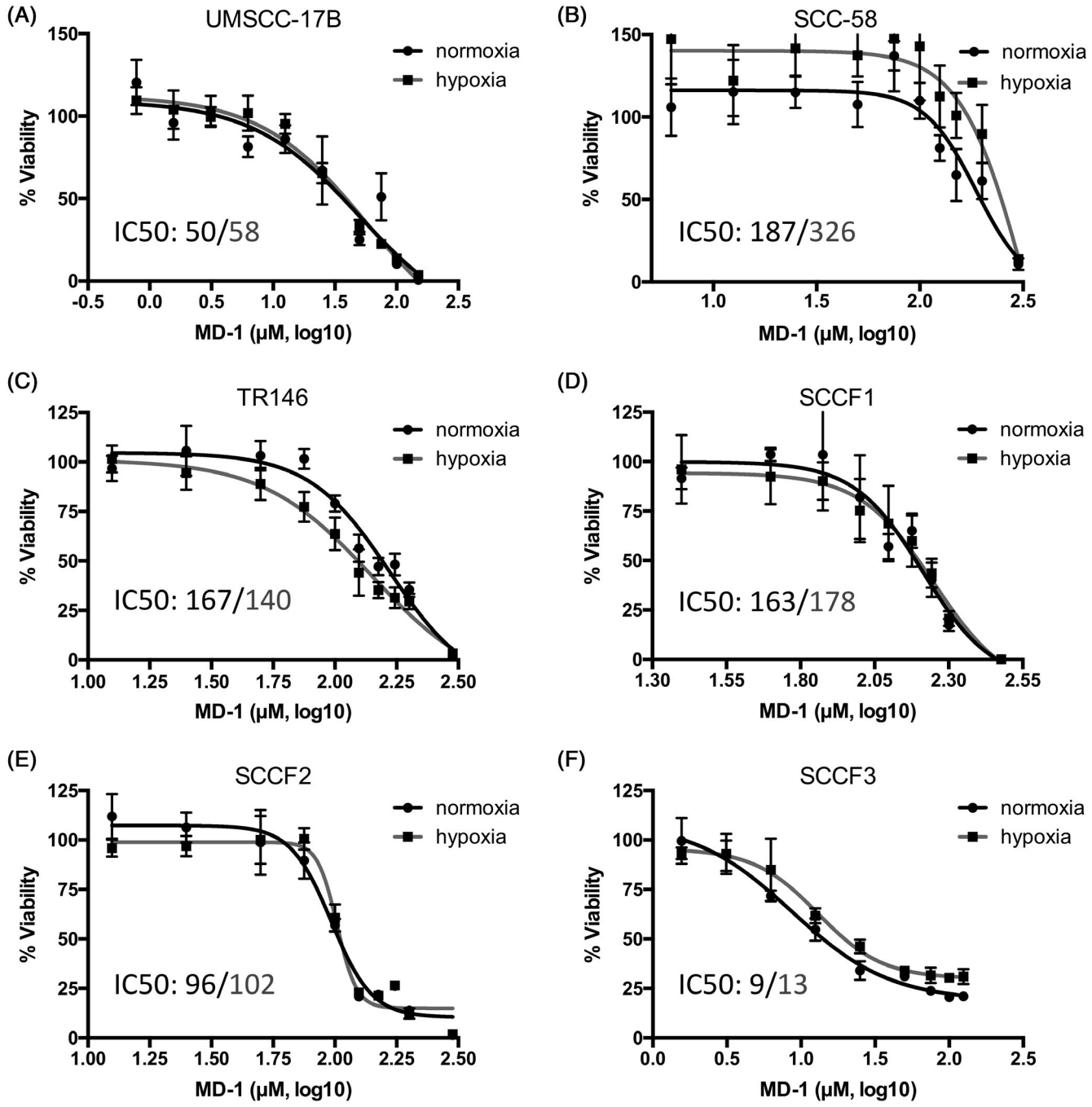

FIGURE 4 MD-1 reduces the viability of human HNSCC and feline OSCC cell lines. Cell viability of human HNSCC cell lines (A) UMSCC-17B, (B) SCC-58 and (C) TR146 and feline OSCC cell lines (D) SCCF1, (E) SCCF2 and (F) SCCF3 treated with increasing concentrations of MD-1 for 48 hour under normoxia and hypoxia. Non-linear least square (ordinary) fit regression was performed using GraphPad Prism to estimate IC50 values for each cell line under normoxia (black) and hypoxia (grey). Data shown as mean ± SD (n = 4 for each cell line). HNSCC, head and neck squamous cell carcinoma; OSCC, oral squamous cell carcinoma

by simultaneously measuring glycolysis and mitochondrial respiration using a Seahorse analyser. The human cell lines and SCCF3 exhibited high levels of glycolytic activity (Figure 6A). The profiles for the SCCF1 and SCCF2 cell lines, which express relatively low levels of MCT4 (Figure 3), were more energetic, suggesting that these cells preferentially used both the glycolytic and the mitochondrial metabolic pathways. The human and the SCCF1 cell lines exhibited similar basal levels of respiration, ATP production, proton leak, maximum respiration, spare respiratory capacity and nonmitochondrial O_2 consumption (Figure 6B). Higher levels of basal respiration, ATP production and maximum respiration were observed for SCCF2 and SCCF3. Basal and compensatory glycolytic proton efflux rates (PER) and percent PER from glycolysis were strikingly similar between the human and feline cells (Figure 6C,D).

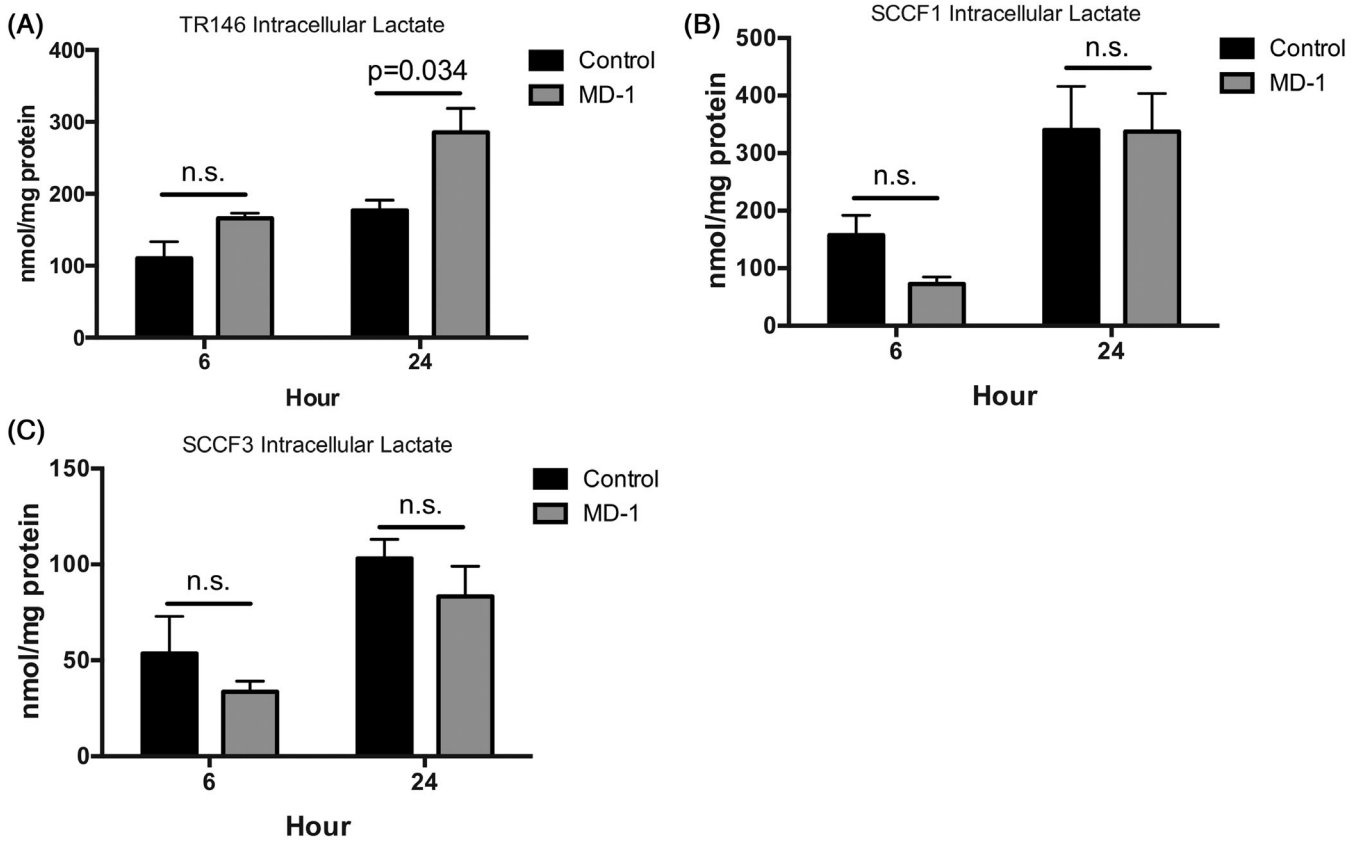

FIGURE 5 Intracellular lactate accumulation as an indicator MD-1 inhibition. Intracellular lactate levels in representative (A) human HNSCC (n = 3) and (B) SCCF1 (n = 3) and (C) SCCF3 (n = 4) feline OSCC cells treated with 10 μM MD-1 for 6 and 24 hour relative to the vehicle control. Data shown as mean ± SE (with 3 to 4 independent repeats). HNSCC, head and neck squamous cell carcinoma; OSCC, oral squamous cell carcinoma

Although not consistent across all cell lines tested, treatment with MD-1 (10 μM) induced significant changes in both the ECAR (Figure 7A) and OCR (Figure 7B). Mitochondrial stress analysis using a Mito Stress test kit showed that MD-1 significantly modified mitochondrial metabolism, including a marked reduction in ATP production and proton coupling efficiency (Figure 7C,D), and an increase in proton leak (Figure 7E) in all cell lines. Maximum respiration and spare respiration capacity were also significantly decreased by MD-1 in most of the cell lines (Figure 7F,G). Changes in nonmitochondrial respiration (O_2 consumption rate) with MD-1 treatment were not observed (Figure 7H).

Curry et al previously used TOMM20, to identify cells rich in mitochondria undergoing OXPHOS, and LDHB, to identify cells that preferentially used glycolysis, to establish cellular metabolic compartments in HNSCC.[29] Because MD-1 disrupted glycolytic and OXPHOS metabolism in both HNSCC and OSCC cell lines, we evaluated the expression of TOMM20 and LDHB as potential markers for mitochondrial and stromal metabolism, respectively, in OSCC. We first confirmed that commercially available antibodies against mouse Tom20 and human LDHB recognized the feline proteins by testing for their expression in feline OSCC cell lines using immunoblotting (Figure 8A); human SCC-58 cells were used as a positive control. Analysis by IHC in eight human HNSCC (Figure 8B) and five feline OSCC (Figure 8C) samples, TOMM20 protein expression was strongest in the epithelial cancer cell population, as compared with the adjacent tumour stroma. In contrast to HNSCC samples, where the strongest LDHB expression was found in the stromal cells (Figure 8D), expression of LDHB protein in feline OSCC tumours was strongest in the cancer cell population, with little to no staining found in the tumour stroma (Figure 8E).

3.5 | MD-1 inhibits tumour growth, but fails to synergize with chemotherapy in vivo

To evaluate the anti-tumour activity of MD-1 alone and in combination with chemotherapy, we performed in vitro synergy studies of MD-1 in combination with cisplatin (for human cells) or carboplatin (for feline cells) chemotherapy. As a single agent, MD-1 was shown above to be cytotoxic to carcinoma cells in a concentration-dependent manner (Figure 4). The human and feline cell lines were sensitive to cisplatin or carboplatin, respectively, (Table 1). MD-1 (20-50 μM) synergized (CI ≤ 0.9) with both chemotherapies (6.25-100 μM, depending on the drug and the cell line) over a wide range of concentrations in vitro (Figure 9A).

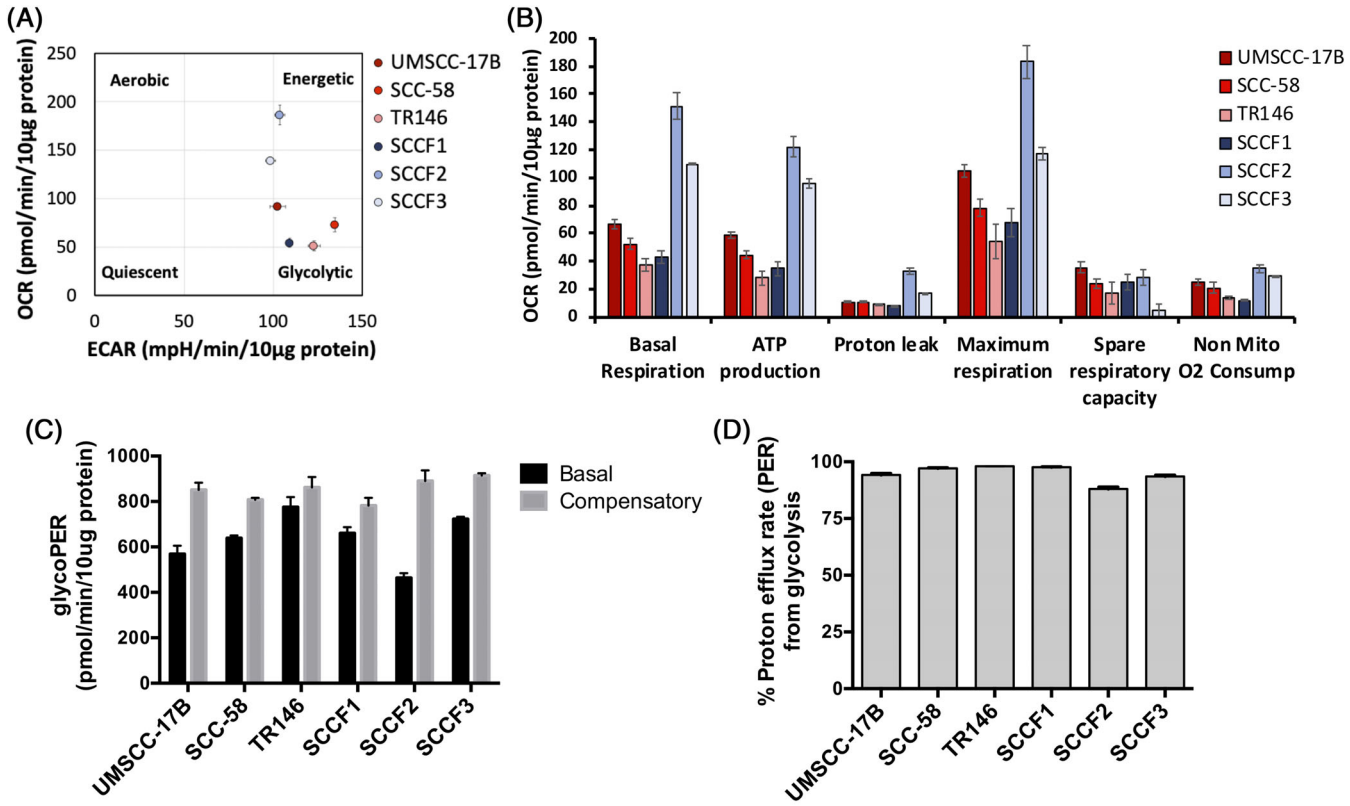

FIGURE 6 Basal metabolic activities of human HNSCC and feline OSCC cells. (A) Energy profiles of human and feline carcinoma cells based on OCR relative to ECAR. (B) Basal respiration, adenosine triphosphate (ATP) production, proton leak, maximum respiration, spare respiration and nonmitochondrial oxygen consumption levels in human and feline carcinoma cells. (C) Basal and compensatory glycolytic proton efflux rates (PER) and (D) percent PER in both human and feline carcinoma cells. All data shown as mean ± SE (n = 3 independent repeats). ECAR, extracellular acidification rate; HNSCC, head and neck squamous cell carcinoma; OCR, oxygen consumption rate; OSCC, oral squamous cell carcinoma

To investigate the anti-tumour effects of MD-1, we performed both subcutaneous and FOM orthotopic xenograft models in athymic nude mice using feline SCCF3 cells, since this cell line was found to be highly sensitive to MD-1 in vitro. We also chose SCCF3 for xenografts because of its dual expression of MCT1 and MCT4. MD-1 (25 mg/kg b.i.d. for ~2 weeks) significantly inhibited tumour growth in the subcutaneous model but failed to synergize with carboplatin (75 mg/kg every 3 days) (Figure 9B). Similar tumour growth inhibition by MD-1 treatment (25 mg/kg b.i.d. for ~10 days) was also observed in a FOM model (Figure 9C), although significance on each day of tumour measurement could not be established in this model because of high variations in the vehicle control treatment group. Nonetheless, MD-1 treatment significantly extended the overall survival in mice in the FOM tumour model compared with the vehicle control (Figure 9D).

Marked differences in tumour morphology between MD-1 and vehicle control treatments were not observed when samples from the control and treatment groups were examined in the FOM model. However, H&E staining appears to show darker nuclei in MD-1 treated tissues (Figure S3A-D), which may be associated with growth arrest. Immunohistochemical staining for MCT1 and MCT4 showed similar membranous and diffused patterns, respectively, in both MD-1- and vehicle-treated tumours (Figure S4A-D). The TOMM20 and the LDHB staining were also similar between the two groups (Figure S5A-D).

4 | DISCUSSION

Our investigation establishes two key steps in the development of MD-1 as a therapeutic strategy for the treatment of oral cancer in cats and humans. First, we demonstrate that MD-1 kills feline OSCC cell lines and reduces tumour growth. Viability and metabolic assays showed that MD-1 euthanized feline and human oral cancer cells and disrupted glycolytic and mitochondrial metabolism. This is in line with previous studies suggesting that metabolic disruption contributes to the anticancer properties of MD-1.[36] MD-1 also reduced tumour growth in subcutaneous and orthotopic tumour models. These observations are consistent with previous data showing that MD-1, and one of its derivatives, inhibited tumour growth in WiDR and MDA-MD-231 tumour xenograft models.[35,36] Taken together, our results suggest that MD-1 represents a viable therapeutic intervention in feline OSCC.

Second, we demonstrate the existence of metabolic heterogeneity in feline oral tumours. We observed high protein expression of

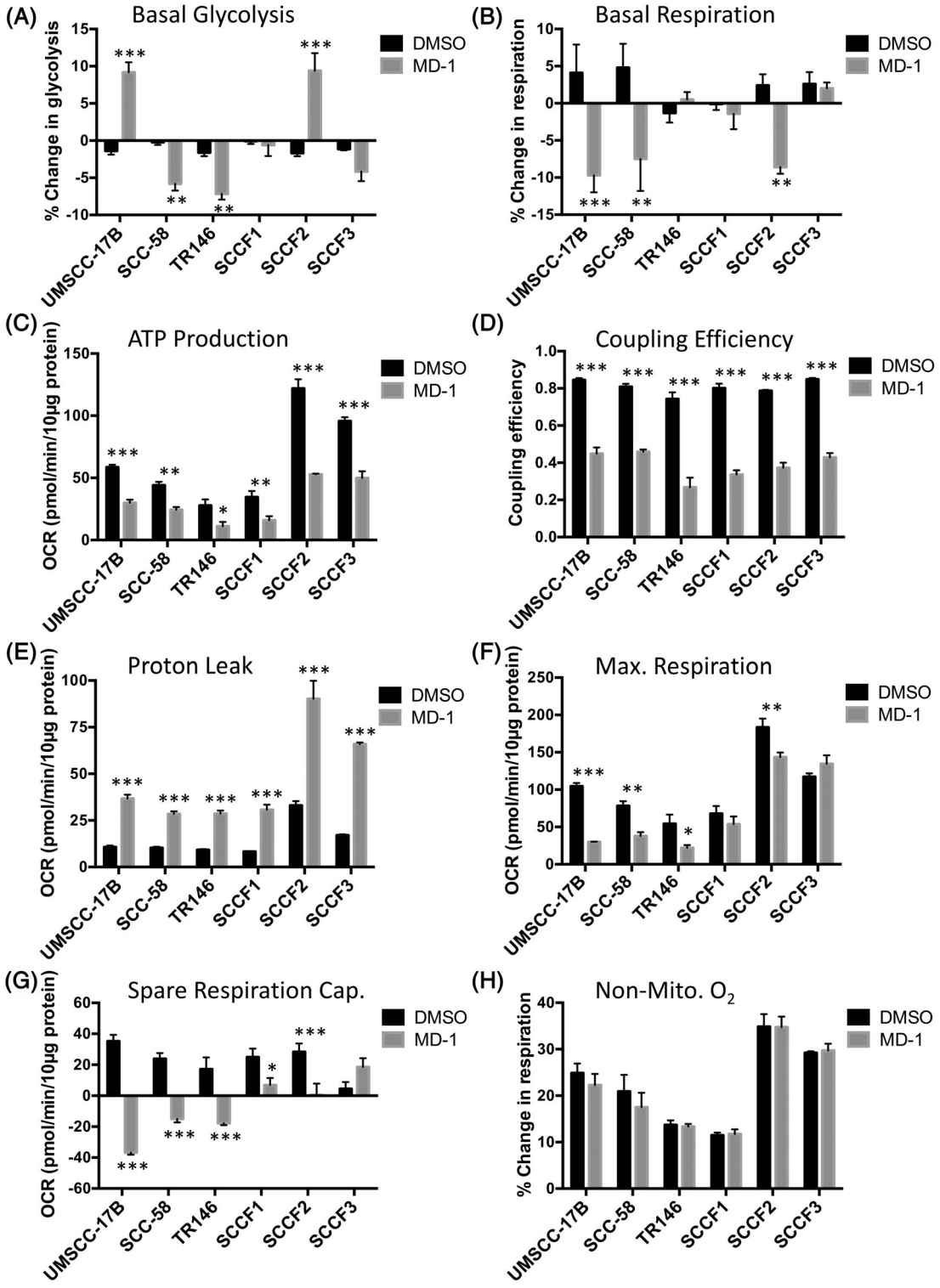

FIGURE 7 MD-1 alters the metabolism in human HNSCC and feline OSCC cells. Percent changes in basal (A) glycolysis and (B) respiration in carcinoma cells treated with 10 µM MD-1 relative to the vehicle control (DMSO). Changes in (C) ATP production, (D) proton coupling efficiency, (E) proton leak, (F) maximum respiration, (G) spare respiration capacity and (H) nonmitochondrial oxygen consumption in carcinoma cells with 10 µM MD-1 treatment relative to the vehicle control (DMSO). All data shown as mean ± SE (n = 3 independent repeats). HNSCC, head and neck squamous cell carcinoma; OSCC, oral squamous cell carcinoma

MCT1 and TOMM20 in the epithelial cancer cell population in feline OSCC, consistent with previous observations that this cell population is metabolically programmed to use mitochondrial metabolism (OXPHOS).[29] In contrast to human HSNCC cell lines and tissues, we found that protein expression of MCT4 is relatively lower in feline OSCC cell lines and tissues, and like LDHB expression, was not a

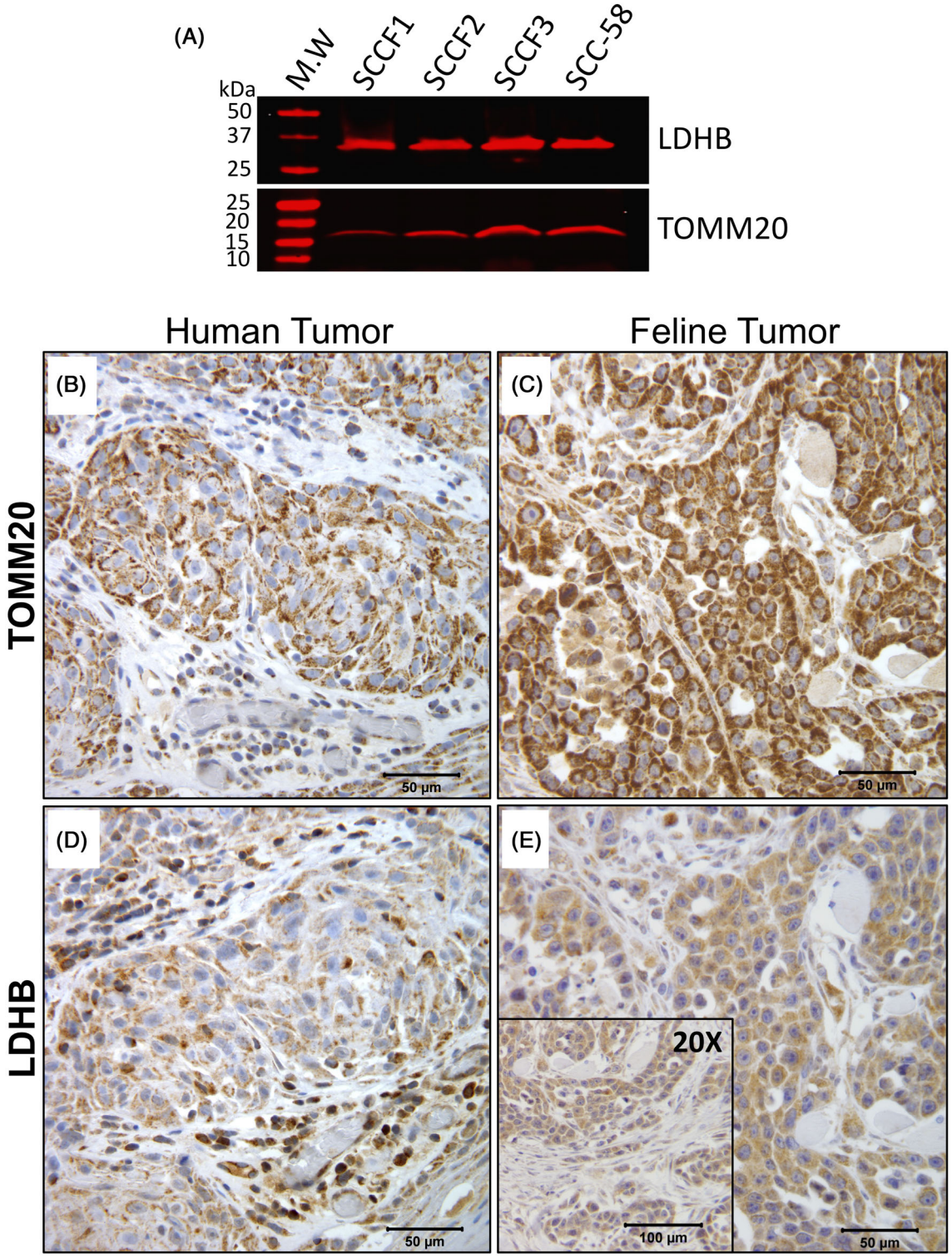

FIGURE 8 Protein expression of TOMM20 and LDHB as mitochondrial and stromal metabolic markers, respectively, in human HNSCC and feline OSCC tumours. (A) Immunoblotting of LDHB and TOMM20 in three feline OSCC cell lines and a human HNSCC cell line (SCC-58) as a positive control to validate proper protein detection using anti-human LDHB and TOMM20 primary antibodies. Immunohistochemical staining of (B and C) TOMM20 and (D and E) LDHB in human and feline tumours. Inset in (E) shown at ×20 magnification to visualize little to no staining in the stromal compartment. The brown colour indicates positive staining for each protein marker with haematoxylin counterstain for nuclei (blue). Original magnification: ×40, scale bar 50 µm. HNSCC, head and neck squamous cell carcinoma; LDHB, lactate dehydrogenase B; OSCC, oral squamous cell carcinoma; TOMM20, translocase of outer mitochondrial membrane 20

prominent feature of the tumour stroma (glycolytic compartment). While these observations suggest that different metabolic compartments (oxidative versus glycolytic) also exist within feline OSCC, the glycolytic compartment may not be marked by MCT4 or LDHB expression, as in human HNSCC. Collectively, our results support the further investigation of MD-1 as a novel treatment approach for oral cancer in cats. Our data also support additional studies regarding feline OSCC as a large animal model to more fully assess MD-1, or similar compounds, for the treatment of human HNSCC.

TABLE 1 IC50 values for human HNSCC cell lines in response to cisplatin and feline OSCC lines in response to carboplatin

Cell line	Cisplatin or carboplatin IC50 (μM)
UMSCC-17B	13.36
TR146	5.36
SCC-58	30.84
SCCF1	91.20
SCCF2	292.90
SCCF3	91.75

Despite the clinical efforts to identify effective treatments for feline OSCC, very few studies have investigated the metabolic processes that may promote the development and the progression of these tumours. MCT4 was recently shown to be a driver of tumour growth in human HNSCC, where it was found to be critical for the progression from oral dysplasia to invasive disease.[69] Increased expression of MCT4 in patients with HNSCC has also been shown to correlate with poor outcomes,[29,32,33] indicating that inhibitors targeting MCT4 could have clinical benefits for patients with HSNCC. The limited protein expression of MCT4 in some of the feline OSCC cell lines along with its variable expression in feline tumours suggests that MCT4 may not play a similar role in feline OSCC. MCT4 is upregulated by hypoxia,[66] and we confirmed induction of MCT4 expression under hypoxic growth conditions in our human HNSCC cell line panel. In contrast, significant increases were not observed in

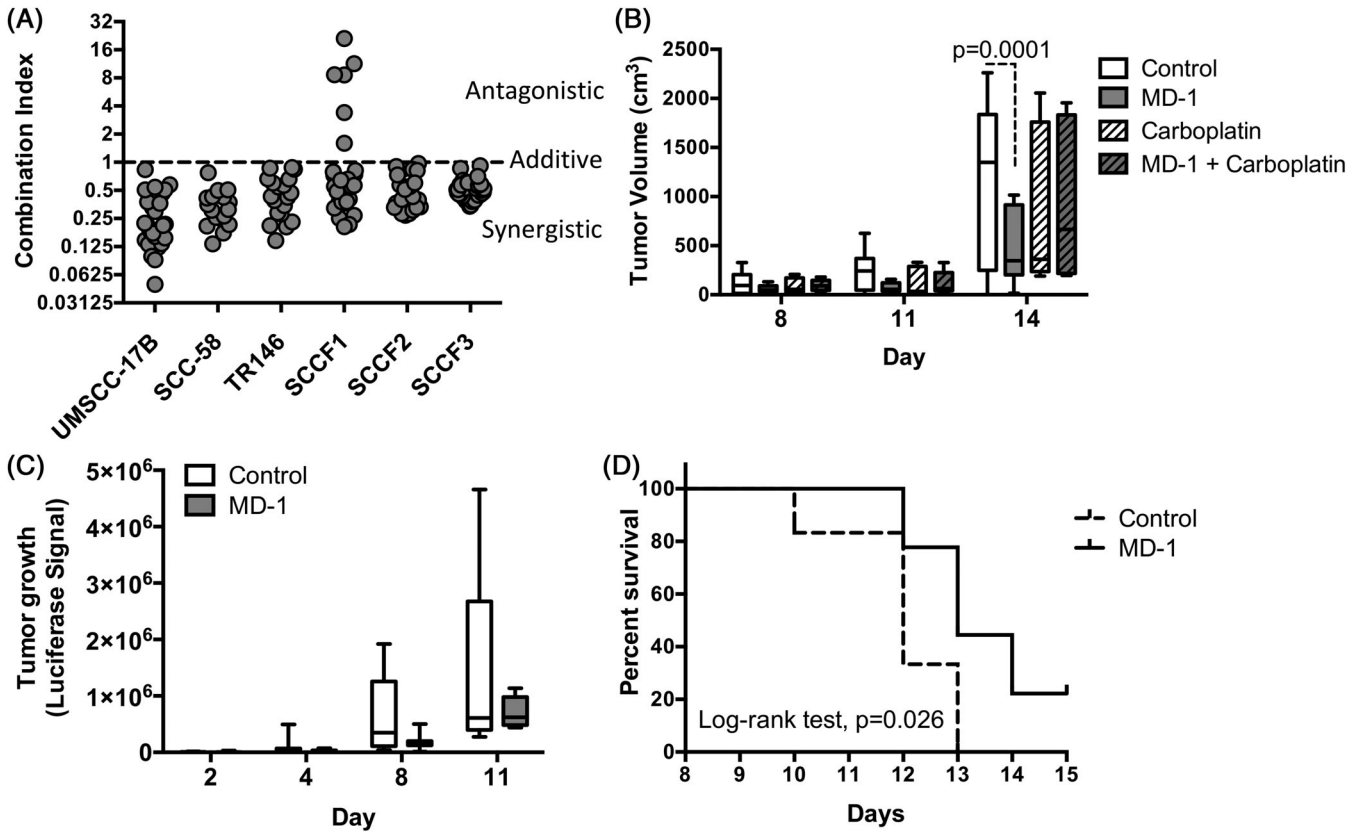

FIGURE 9 Synergy observed in combination treatments of MD-1 and chemotherapy in vitro and inhibition of tumour growth by MD-1. (A) CI of combined treatments with MD-1 (from 20 to 50 μM) and cisplatin (from 6.25 to 100 μM for human HNSCC lines) or carboplatin (from 6.25 to 100 μM for feline OSCC lines) specific to each cell line in vitro. CI ≤0.9, synergistic; 0.9 < CI ≤1, additive; CI > 1, antagonistic. Horizontal dashed line indicates CI = 1. (B) Feline SCCF3 subcutaneous xenograft tumour growth (measured in volume) at 8, 11 and 14 days following treatment with MD-1 alone (25 mg/kg b.i.d. for ~2 weeks), carboplatin alone (75 mg/kg every 3 days), or in combination relative to the vehicle control. Box and whiskers shown with median ± range (minimum and maximum). (C) Feline SCCF3 FOM orthotopic tumour growth over time following MD-1 treatment (25 mg/kg b.i.d. for ~10 days). Box and whiskers shown with median ± range (minimum and maximum). (D) Kaplan-Meier survival plot of feline SCCF3 FOM animals shown in (C) following treatment with MD-1. Curve comparison was performed using log-rank (Mantel-Cox) test, with a *P* value = 0.026. CI, Combination index; FOM, floor of the mouth; HNSCC, head and neck squamous cell carcinoma; OSCC, oral squamous cell carcinoma

feline OSCC cells. MCT4 has also been shown to facilitate lactic acid export by glycolytic cancer cells. Increased levels of intracellular lactate in response to MD-1 were previously confirmed in MDA-MB-231 cells, which predominantly express MCT4 and were used to validate the dual MCT1/MCT4 targeting of MD-1.[36] While a significant increase in intracellular lactate was observed in human TR146 cells, similar increases were not observed in the feline SCCF1 or SCCF3 line. The lack of accumulation in SCCF3 cells was especially surprising, since these cells are highly sensitive to MD-1 inhibition, and they show relatively higher expression of MCT4 compared with SCCF1 and SCCF2. Although the protein sequences for feline MCT1 and MCT4 are 88% identical to the human proteins, MD-1 may not bind with high affinity to the feline transporters. In future studies, a more sensitive radiolabeled L-[^{14}C]-lactic acid uptake assay could be used in combination with feline OSCC cell lines expressing human MCT1 or MCT4 to address MD-1 specificity. Genetic ablation of MCT1 and MCT4 should also be carried out in the OSCC cell lines to evaluate the effects of the transporters on OSCC cell proliferation and viability in vitro.

Alternatively, other MCT transporters may play a larger role in lactate transport in feline OSCC. Although MCT1 and MCT4 are the most widely expressed MCT isoforms in cancer cells, the expression of other MCTs that transport lactate, such as MCT2, has been documented in multiple cancers types.[67,68] MCT2 has also been shown to transport β-hydroxybutyrate from adipocytes into breast cancer cells, leading to the activation of tumour-promoting genes and enhancement of tumour growth.[70] We found that the expression of MCT2 was approximately 15-fold higher in the feline OSCC cell lines than the levels expressed by the human cell lines. Because MCT2 is a bidirectional lactate transporter, it may compensate for inhibition of MCT1 or MCT4 activity. Based on our observations, further studies, including evaluation of MCT2 protein expression in both cell lines and primary tumours, are warranted to determine the role of MCT2 in lactate transport in feline OSCC and whether MCT2 overcomes the inhibitory effects of MD-1.

The inability of MD-1 to affect the intracellular accumulation of lactate in feline OSCC cells prompted us to investigate alternative modes of action for the effects of the inhibitor on cell viability. Consistent changes in basal glycolysis across the human and feline cell line panels were not induced by MD-1. In contrast, MD-1 consistently reduced coupling efficiency and ATP in all lines and triggered a concomitant increase in protein leak. MD-1 also significantly reduced the spare respiratory capacity in all the cell lines, except for SCCF3, suggesting that MD-1 reduced cell viability by limiting metabolic flexibility and the ability of the cells to meet their energy demands. These changes are consistent with a decrease in bioenergy related functions observed in previous studies following the treatment of MDA-MD-231 and WiDr cells with MD-1.[36]

Chemoresistance has previously been shown to depend on increased levels of intracellular ATP to maintain key survival pathways.[71] More recent work has associated resistance to platin-based chemotherapies with increases in mitochondrial function.[72] Based on our observations that MD-1 disrupted glycolytic and OXPHOS metabolism, we hypothesized that MD-1 would synergize with carboplatin or cisplatin, used as the standard of care for feline OSCC and human HNSCC, respectively.[45,73-75] Drug synergy and drug additivity were observed in all cell lines for both species across a range of concentrations. In contrast, carboplatin failed to synergize with MD-1 in a subcutaneous xenograft model generated by inoculating immunodeficient mice with the SCCF3 cell line. The current reason for this discrepancy is unknown, but may be because of ineffective penetration of carboplatin and/or MD-1 into the tumour microenvironment. Based on our results, other combinatorial strategies may yield more effective outcomes in vivo. For example, recent reports showed that combining the MCT1 inhibitor, AZD3965, with metformin, a drug used to treat type-2 diabetes and an inhibitor of mitochondrial complex I, was more effective than single-agent therapy.[23,76] Synthetic lethality was also observed when metformin was combined with a newly identified dual MCT1/MCT4 inhibitor, syrosingopine.[34] Further investigations into the metabolic basis underlying the MD-1 induced changes in bioenergetics are needed to more fully understand its mode of action and to support the identification of potential combinatorial strategies.

To translate the inhibitory effects of MD-1 that we observed *in vitro*, we developed subcutaneous and FOM orthotopic xenograft models in nude mice based on a previously published study.[50] MD-1 significantly suppressed tumour growth in the subcutaneous model, but as mentioned above, failed to synergize with carboplatin. MD-1 as a single agent was further confirmed to significantly extended overall survival in a FOM model; however, the effect of MD-1 in this model is somewhat modest. While this may be because of the small sample sizes used in the study, a more likely factor is the rapid tumour growth observed in the FOM model, which provided only a short treatment window and may have limited our ability to fully assess the effects of MD-1. We were also unable to evaluate the significance of MD-1 on tumour growth in the FOM model because of the high variability in tumour growth observed in the control group. Future studies using a larger sample size and evaluating the in vivo effects of MD-1 in orthotopic models generated from the SCCF1 or the SCCF2 lines should be carried out since these lines are more resistant to MD-1 in vitro and exhibit little to no expression of MCT4. Because MD-1 treatment promoted lactate accumulation in the HNSCC cell line TR146, MD-1 may be a more effective inhibitor of human HNSCC.

In summary, we show that MD-1 reduces cell viability, alters glycolytic and OXPHOS activity and synergizes with platin-based chemotherapies in vitro in both feline OSCC and human HNSCC. We also show that MD-1 inhibits tumour growth in a xenograft model of feline OSCC. The activity of MD-1 in the xenograft model was superior to carboplatin alone, supporting the clinical translation of MD-1 for the treatment of feline cancer. Although our study highlights potential differences in the mode of action of MD-1 in OSCC and HNSCC, the remarkably similar response across many of our assays and the discovery that MD-1 promotes the accumulation of lactic acid in human HNSCC cells suggests it may be an effective therapeutic for HNSCC patients. To our knowledge, ours is the first report to identify metabolic symbiosis in feline OSCC and to suggest the potential

therapeutic value of targeting these mechanisms as a strategy to treat this disease.

ACKNOWLEDGEMENTS

This work was supported by grant D15FE-020 from Morris Animal Foundation (E.B.D., T.D.O. and L.R.D.), the Comparative Medicine Signature Program of the College of Veterinary Medicine, University of Minnesota (E.B.D., T.D.O. and L.R.D) and the Department of Defense grants W81XWH-15-1-0047 (V.R.M) and W81XWH-15-1-0060 (L.R.D.). The National Institutes of Health (NIH) Comprehensive Cancer Center Support Grant to the Masonic Cancer Center, University of Minnesota (P30 CA077598) provided support for genomics, bioimaging and comparative pathology services. The authors gratefully acknowledge donations to the Animal Cancer Care and Research Program of the University of Minnesota that helped support this project.

DISCLOSURE OF CONFLICTS OF INTEREST

The authors have no conflicts of interest to report. A patent (US No. 9573888B2) for MD-1 has been issued to the University of Minnesota.

DATA AVAILABILITY STATEMENT

The data that support the findings of this study are available from the corresponding author upon reasonable request.

ORCID

Erin B. Dickerson https://orcid.org/0000-0002-9757-4961

REFERENCES

1. Luengo A, Gui DY, Vander Heiden MG. Targeting metabolism for cancer therapy. *Cell Chem Biol*. 2017;24:1161-1180.
2. Martinez-Outschoorn UE, Peiris-Pages M, Pestell RG, Sotgia F, Lisanti MP. Cancer metabolism: a therapeutic perspective. *Nat Rev Clin Oncol*. 2017;14:113.
3. Mullard A. Cancer metabolism pipeline breaks new ground. *Nat Rev Drug Discov*. 2016;15:735-737.
4. Mullard A. Diabetes drug shows promise in Parkinson disease. *Nat Rev Drug Discov*. 2017;16:593.
5. Kennedy KM, Dewhirst MW. Tumor metabolism of lactate: the influence and therapeutic potential for MCT and CD147 regulation. *Future Oncol*. 2010;6:127-148.
6. Warburg O, Wind F, Negelein E. The metabolism of tumors in the body. *J Gen Physiol*. 1927;8:519-530.
7. Boroughs LK, DeBerardinis RJ. Metabolic pathways promoting cancer cell survival and growth. *Nat Cell Biol*. 2015;17:351-359.
8. Vander Heiden MG, Cantley LC, Thompson CB. Understanding the Warburg effect: the metabolic requirements of cell proliferation. *Science*. 2009;324:1029-1033.
9. Gatenby RA, Smallbone K, Maini PK, et al. Cellular adaptations to hypoxia and acidosis during somatic evolution of breast cancer. *Br J Cancer*. 2007;97:646-653.
10. Lee M, Yoon JH. Metabolic interplay between glycolysis and mitochondrial oxidation: the reverse Warburg effect and its therapeutic implication. *World J Biol Chem*. 2015;6:148-161.
11. Migneco G, Whitaker-Menezes D, Chiavarina B, et al. Glycolytic cancer associated fibroblasts promote breast cancer tumor growth, without a measurable increase in angiogenesis: evidence for stromal-epithelial metabolic coupling. *Cell Cycle*. 2010;9:2412-2422.
12. Pavlides S, Whitaker-Menezes D, Castello-Cros R, et al. The reverse Warburg effect: aerobic glycolysis in cancer associated fibroblasts and the tumor stroma. *Cell Cycle*. 2009;8:3984-4001.
13. Sotgia F, Whitaker-Menezes D, Martinez-Outschoorn UE, et al. Mitochondrial metabolism in cancer metastasis: visualizing tumor cell mitochondria and the "reverse Warburg effect" in positive lymph node tissue. *Cell Cycle*. 2012;11:1445-1454.
14. Yoshida GJ. Metabolic reprogramming: the emerging concept and associated therapeutic strategies. *J Exp Clin Cancer Res*. 2015;34:111.
15. Lisanti MP, Martinez-Outschoorn UE, Chiavarina B, et al. Understanding the "lethal" drivers of tumor-stroma co-evolution: emerging role(s) for hypoxia, oxidative stress and autophagy/mitophagy in the tumor micro-environment. *Cancer Biol Ther*. 2010;10:537-542.
16. Witkiewicz AK, Dasgupta A, Sammons S, et al. Loss of stromal caveolin-1 expression predicts poor clinical outcome in triple negative and basal-like breast cancers. *Cancer Biol Ther*. 2010;10:135-143.
17. Danhier P, Banski P, Payen VL, et al. Cancer metabolism in space and time: beyond the Warburg effect. *Biochim Biophys Acta Bioenerg*. 1858;2017:556-572.
18. Arcucci A, Ruocco MR, Granato G, Sacco AM, Montagnani S. Cancer: an oxidative crosstalk between solid tumor cells and cancer associated fibroblasts. *Biomed Res Int*. 2016;2016:4502846.
19. Bonuccelli G, Whitaker-Menezes D, Castello-Cros R, et al. The reverse Warburg effect: glycolysis inhibitors prevent the tumor promoting effects of caveolin-1 deficient cancer associated fibroblasts. *Cell Cycle*. 2010;9:1960-1971.
20. Halestrap AP. Monocarboxylic acid transport. *Compr Physiol*. 2013;3:1611-1643.
21. Halestrap AP. The SLC16 gene family - structure, role and regulation in health and disease. *Mol Aspects Med*. 2013;34:337-349.
22. Sonveaux P, Vegran F, Schroeder T, et al. Targeting lactate-fueled respiration selectively kills hypoxic tumor cells in mice. *J Clin Invest*. 2008;118:3930-3942.
23. Doherty JR, Cleveland JL. Targeting lactate metabolism for cancer therapeutics. *J Clin Invest*. 2013;123:3685-3692.
24. Fiaschi T, Marini A, Giannoni E, et al. Reciprocal metabolic reprogramming through lactate shuttle coordinately influences tumor-stroma interplay. *Cancer Res*. 2012;72:5130-5140.
25. Whitaker-Menezes D, Martinez-Outschoorn UE, Lin Z, et al. Evidence for a stromal-epithelial "lactate shuttle" in human tumors: MCT4 is a marker of oxidative stress in cancer-associated fibroblasts. *Cell Cycle*. 2011;10:1772-1783.
26. De Saedeleer CJ, Copetti T, Porporato PE, Verrax J, Feron O, Sonveaux P. Lactate activates HIF-1 in oxidative but not in Warburg-phenotype human tumor cells. *PLoS One*. 2012;7:e46571.
27. Chiche J, Le Fur Y, Vilmen C, et al. In vivo pH in metabolic-defective Ras-transformed fibroblast tumors: key role of the monocarboxylate transporter, MCT4, for inducing an alkaline intracellular pH. *Int J Cancer*. 2012;130:1511-1520.
28. Dimmer KS, Friedrich B, Lang F, Deitmer JW, Broer S. The low-affinity monocarboxylate transporter MCT4 is adapted to the export of lactate in highly glycolytic cells. *Biochem J*. 2000;350(Pt 1):219-227.
29. Curry JM, Tuluc M, Whitaker-Menezes D, et al. Cancer metabolism, stemness and tumor recurrence: MCT1 and MCT4 are functional biomarkers of metabolic symbiosis in head and neck cancer. *Cell Cycle*. 2013;12:1371-1384.
30. Siegel RL, Miller KD, Jemal A. Cancer statistics, 2019. *CA Cancer J Clin*. 2019;69:7-34.
31. Bovenzi CD, Hamilton J, Tassone P, et al. Prognostic indications of elevated MCT4 and CD147 across cancer types: a meta-analysis. *Biomed Res Int*. 2015;2015:242437.
32. Simoes-Sousa S, Granja S, Pinheiro C, et al. Prognostic significance of monocarboxylate transporter expression in oral cavity tumors. *Cell Cycle*. 2016;15:1865-1873.

33. Zhu J, Wu YN, Zhang W, et al. Monocarboxylate transporter 4 facilitates cell proliferation and migration and is associated with poor prognosis in oral squamous cell carcinoma patients. *PLoS One*. 2014; 9:e87904.
34. Benjamin D, Robay D, Hindupur SK, et al. Dual inhibition of the lactate transporters MCT1 and MCT4 is synthetic lethal with metformin due to NAD+ depletion in cancer cells. *Cell Rep*. 2018;25:3047-3058. e4.
35. Gurrapu S, Jonnalagadda SK, Alam MA, et al. Monocarboxylate transporter 1 inhibitors as potential anticancer agents. *ACS Med Chem Lett*. 2015;6:558-561.
36. Jonnalagadda S, Jonnalagadda SK, Ronayne CT, et al. Novel N,N-dialkyl cyanocinnamic acids as monocarboxylate transporter 1 and 4 inhibitors. *Oncotarget*. 2019;10:2355-2368.
37. Cannon CM. Cats, cancer and comparative oncology. *Vet Sci*. 2015;2: 111-126.
38. Cannon CM, Trembley JH, Kren BT, et al. Therapeutic targeting of protein kinase CK2 gene expression in feline oral squamous cell carcinoma: a naturally occurring large-animal model of head and neck cancer. *Hum Gene Ther Clin Dev*. 2017;28:80-86.
39. Martin CK, Dirksen WP, Carlton MM, et al. Combined zoledronic acid and meloxicam reduced bone loss and tumour growth in an orthotopic mouse model of bone-invasive oral squamous cell carcinoma. *Vet Comp Oncol*. 2015;13:203-217.
40. Supsavhad W, Dirksen WP, Martin CK, Rosol TJ. Animal models of head and neck squamous cell carcinoma. *Vet J*. 2016;210:7-16.
41. Walz JZ, Saha J, Arora A, Khammanivong A, O'Sullivan MG, Dickerson EB. Fatty acid synthase as a potential therapeutic target in feline oral squamous cell carcinoma. *Vet Comp Oncol*. 2018;16:E99-E108.
42. Stebbins KE, Morse CC, Goldschmidt MH. Feline oral neoplasia: a ten-year survey. *Vet Pathol*. 1989;26:121-128.
43. Hayes AM, Adams VJ, Scase TJ, Murphy S. Survival of 54 cats with oral squamous cell carcinoma in United Kingdom general practice. *J Small Anim Pract*. 2007;48:394-399.
44. Liptak JM, Withrow SJ. Cancer of the gastrointestinal tract. In: Withrow SJ, Page R, Vail D, eds. *Withrow and MacEwen's Small Animal Oncology*. St. Louis, Missouri: Elsevier; 2013.
45. Fidel J, Lyons J, Tripp C, Houston R, Wheeler B, Ruiz A. Treatment of oral squamous cell carcinoma with accelerated radiation therapy and concomitant carboplatin in cats. *J Vet Intern Med*. 2011;25:504-510.
46. Fidel JL, Sellon RK, Houston RK, Wheeler BA. A nine-day accelerated radiation protocol for feline squamous cell carcinoma. *Vet Radiol Ultrasound*. 2007;48:482-485.
47. Fox LE, Rosenthal RC, King RR, et al. Use of cis-bis-neodecanoato-trans-R,R-1,2-diaminocyclohexane platinum (II), a liposomal cisplatin analogue, in cats with oral squamous cell carcinoma. *Am J Vet Res*. 2000;61:791-795.
48. Poirier VJ, Kaser-Hotz B, Vail DM, Straw RC. Efficacy and toxicity of an accelerated hypofractionated radiation therapy protocol in cats with oral squamous cell carcinoma. *Vet Radiol Ultrasound*. 2013;54: 81-88.
49. Tannehill-Gregg S, Kergosien E, Rosol TJ. Feline head and neck squamous cell carcinoma cell line: characterization, production of parathyroid hormone-related protein, and regulation by transforming growth factor-beta. *In Vitro Cell Dev Biol Anim*. 2001;37:676-683.
50. Martin CK, Dirksen WP, Shu ST, et al. Characterization of bone resorption in novel in vitro and in vivo models of oral squamous cell carcinoma. *Oral Oncol*. 2012;48:491-499.
51. Rupniak HT, Rowlatt C, Lane EB, et al. Characteristics of four new human cell lines derived from squamous cell carcinomas of the head and neck. *J Natl Cancer Inst*. 1985;75:621-635.
52. Worsham MJ, Chen KM, Meduri V, et al. Epigenetic events of disease progression in head and neck squamous cell carcinoma. *Arch Otolaryngol Head Neck Surg*. 2006;132:668-677.
53. Lee Y, Yang X, Huang Y, et al. Network modeling identifies molecular functions targeted by miR-204 to suppress head and neck tumor metastasis. *PLoS Comput Biol*. 2010;6:e1000730.
54. Khammanivong A, Sorenson BS, Ross KF, et al. Involvement of calprotectin (S100A8/A9) in molecular pathways associated with HNSCC. *Oncotarget*. 2016;7:14029-14047.
55. Wang K, Singh D, Zeng Z, et al. MapSplice: accurate mapping of RNA-seq reads for splice junction discovery. *Nucleic Acids Res*. 2010; 38:e178.
56. Liao Y, Smyth GK, Shi W. featureCounts: an efficient general purpose program for assigning sequence reads to genomic features. *Bioinformatics*. 2014;30:923-930.
57. Khammanivong A, Gopalakrishnan R, Dickerson EB. SMURF1 silencing diminishes a CD44-high cancer stem cell-like population in head and neck squamous cell carcinoma. *Mol Cancer*. 2014;13:260.
58. Matson CT, Drewes LR. Immunoblot detection of brain vascular proteins. *Methods Mol Med*. 2003;89:479-487.
59. Khammanivong A, Gorden BH, Frantz AM, Graef AJ, Dickerson EB. Identification of drug-resistant subpopulations in canine hemangiosarcoma. *Vet Comp Oncol*. 2016;14:e113-e125.
60. Kim JH, Frantz AM, Anderson KL, et al. Interleukin-8 promotes canine hemangiosarcoma growth by regulating the tumor microenvironment. *Exp Cell Res*. 2014;323:155-164.
61. Dickerson EB, Akhtar N, Steinberg H, et al. Enhancement of the anti-angiogenic activity of interleukin-12 by peptide targeted delivery of the cytokine to alphavbeta3 integrin. *Mol Cancer Res*. 2004;2: 663-673.
62. Takada T, Takata K, Ashihara E. Inhibition of monocarboxylate transporter 1 suppresses the proliferation of glioblastoma stem cells. *J Physiol Sci*. 2016;66:387-396.
63. Lamb R, Harrison H, Hulit J, Smith DL, Lisanti MP, Sotgia F. Mitochondria as new therapeutic targets for eradicating cancer stem cells: quantitative proteomics and functional validation via MCT1/2 inhibition. *Oncotarget*. 2014;5:11029-11037.
64. Krishnamurthy S, Nor JE. Orosphere assay: a method for propagation of head and neck cancer stem cells. *Head Neck*. 2013;35:1015-1021.
65. Lim KS, Lim KJ, Price AC, Orr BA, Eberhart CG, Bar EE. Inhibition of monocarboxylate transporter-4 depletes stem-like glioblastoma cells and inhibits HIF transcriptional response in a lactate-independent manner. *Oncogene*. 2014;33:4433-4441.
66. Ullah MS, Davies AJ, Halestrap AP. The plasma membrane lactate transporter MCT4, but not MCT1, is up-regulated by hypoxia through a HIF-1alpha-dependent mechanism. *J Biol Chem*. 2006;281:9030-9037.
67. Eilertsen M, Andersen S, Al-Saad S, et al. Monocarboxylate transporters 1-4 in NSCLC: MCT1 is an independent prognostic marker for survival. *PLoS One*. 2014;9:e105038.
68. Pinheiro C, Reis RM, Ricardo S, Longatto-Filho A, Schmitt F, Baltazar F. Expression of monocarboxylate transporters 1, 2, and 4 in human tumours and their association with CD147 and CD44. *J Biomed Biotechnol*. 2010;2010:427694.
69. Bisetto S, Whitaker-Menezes D, Wilski NA, et al. Monocarboxylate transporter 4 (MCT4) knockout mice have attenuated 4NQO induced carcinogenesis; a role for MCT4 in driving oral squamous cell cancer. *Front Oncol*. 2018;8:324.
70. Huang CK, Chang PH, Kuo WH, et al. Adipocytes promote malignant growth of breast tumours with monocarboxylate transporter 2 expression via beta-hydroxybutyrate. *Nat Commun*. 2017;8:14706.
71. Zhou Y, Tozzi F, Chen J, et al. Intracellular ATP levels are a pivotal determinant of chemoresistance in colon cancer cells. *Cancer Res*. 2012;72:304-314.
72. Cruz-Bermudez A, Laza-Briviesca R, Vicente-Blanco RJ, et al. Cisplatin resistance involves a metabolic reprogramming through ROS and PGC-1alpha in NSCLC which can be overcome by OXPHOS inhibition. *Free Radic Biol Med*. 2019;135:167-181.

73. Pignon JP, le Maitre A, Maillard E, Bourhis J, Group M-NC. Meta-analysis of chemotherapy in head and neck cancer (MACH-NC): an update on 93 randomised trials and 17,346 patients. *Radiother Oncol*. 2009;92:4-14.
74. Shapiro LQ, Sherman EJ, Riaz N, et al. Efficacy of concurrent cetuximab vs. 5-fluorouracil/carboplatin or high-dose cisplatin with intensity-modulated radiation therapy (IMRT) for locally-advanced head and neck cancer (LAHNSCC). *Oral Oncol*. 2014;50:947-955.
75. Chen D, Cheng J, Yang K, Ma Y, Yang F. Retrospective analysis of chronomodulated chemotherapy versus conventional chemotherapy with paclitaxel, carboplatin, and 5-fluorouracil in patients with recurrent and/or metastatic head and neck squamous cell carcinoma. *Onco Targets Ther*. 2013;6:1507-1514.
76. Beloueche-Babari M, Wantuch S, Casals Galobart T, et al. MCT1 inhibitor AZD3965 increases mitochondrial metabolism, facilitating combination therapy and noninvasive magnetic resonance spectroscopy. *Cancer Res*. 2017;77:5913-5924.

SUPPORTING INFORMATION

Additional supporting information may be found online in the Supporting Information section at the end of this article.

How to cite this article: Khammanivong A, Saha J, Spartz AK, et al. A novel MCT1 and MCT4 dual inhibitor reduces mitochondrial metabolism and inhibits tumour growth of feline oral squamous cell carcinoma. *Vet Comp Oncol*. 2019;1–18. https://doi.org/10.1111/vco.12551

Received: 29 January 2019 | Revised: 27 March 2019 | Accepted: 14 April 2019

DOI: 10.1002/jlcr.3739

SPECIAL ISSUE ARTICLE

WILEY Journal of Labelled Compounds and Radiopharmaceuticals

Development and radiosynthesis of the first ^{18}F-labeled inhibitor of monocarboxylate transporters (MCTs)

Masoud Sadeghzadeh[1] | Rareş-Petru Moldovan[1] | Steffen Fischer[1] | Barbara Wenzel[1] | Friedrich-Alexander Ludwig[1] | Rodrigo Teodoro[1] | Winnie Deuther-Conrad[1] | Shirisha Jonnalagadda[2] | Sravan K. Jonnalagadda[2] | Emilis Gudelis[3] | Algirdas Šačkus[3] | Kei Higuchi[4] | Vadivel Ganapathy[4] | Venkatram R. Mereddy[2] | Lester R. Drewes[5] | Peter Brust[1]

[1] Department of Neuroradiopharmaceuticals, Helmholtz-Zentrum Dresden-Rossendorf, Institute of Radiopharmaceutical Cancer Research, Research Site Leipzig, Leipzig, Germany

[2] Department of Chemistry and Biochemistry, Department of Pharmacy Practice and Pharmaceutical Sciences, University of Minnesota, Duluth, Minnesota, USA

[3] Institute of Synthetic Chemistry, Kaunas University of Technology, Kaunas, Lithuania

[4] Department of Cell Biology and Biochemistry, Texas Tech University Health Sciences Center, Lubbock, Texas, USA

[5] Department of Biomedical Sciences, University of Minnesota Medical School Duluth, Duluth, Minnesota, USA

Correspondence
Masoud Sadeghzadeh, Department of Neuroradiopharmaceuticals, Helmholtz-Zentrum Dresden-Rossendorf, Institute of Radiopharmaceutical Cancer Research, Research Site Leipzig, Permoserstraße 15, 04318, Leipzig, Germany.
Email: m.sadeghzadeh@hzdr.de

Funding information
The Alexander von Humboldt Foundation

Monocarboxylate transporters 1 and 4 (MCT1 and MCT4) are involved in tumor development and progression. Their expression levels are related to clinical disease prognosis. Accordingly, both MCTs are promising drug targets for treatment of a variety of human cancers. The noninvasive imaging of these MCTs in cancers is regarded to be advantageous for assessing MCT-mediated effects on chemotherapy and radiosensitization using specific MCT inhibitors. Herein, we describe a method for the radiosynthesis of [^{18}F]**FACH** (*(E)*-2-cyano-3-{4-[(3-[^{18}F]fluoropropyl)(propyl)amino]-2-methoxyphenyl}acrylic acid), as a novel radiolabeled MCT1/4 inhibitor for imaging with PET. A fluorinated analog of α-cyano-4-hydroxycinnamic acid (**FACH**) was synthesized, and the inhibition of MCT1 and MCT4 was measured via an L-[^{14}C]lactate uptake assay. Radiolabeling was performed by a two-step protocol comprising the radiosynthesis of the intermediate *(E)/(Z)*-[^{18}F]***tert*-Bu-FACH** (*tert*-butyl *(E)/(Z)*-2-cyano-3-{4-[(3-[^{18}F]fluoropropyl)(propyl)amino]-2-methoxyphenyl}acrylate) followed by deprotection of the *tert*-butyl group. The radiofluorination was successfully implemented using either K[^{18}F]F-$K_{2.2.2}$-carbonate or [^{18}F]TBAF. The final deprotected product [^{18}F]**FACH** was only obtained when [^{18}F]***tert*-Bu-FACH** was formed by the latter procedure. After optimization of the deprotection reaction, [^{18}F]**FACH** was obtained in high radiochemical yields (39.6 ± 8.3%, end of bombardment (EOB) and radiochemical purity (greater than 98%).

KEYWORDS
[^{18}F]FACH, α-cyano-4-hydroxycinnamic acid (α-CHC), monocarboxylate transporters (MCTs), positron emission tomography (PET), radiofluorination

1 | INTRODUCTION

Monocarboxylate transporters (MCTs) belong to the solute carrier 16 (SLC16) gene family and comprise of 14 isoforms, each having a unique distribution and different sequence homology.[1] Among them, MCT1 and MCT4 act as H^+-linked transporters of short-chain monocarboxylates (e.g., pyruvate, L-lactate, and ketone

bodies) across the plasma membrane of mammalian cells.[2-4] They have also been shown to play an important role in supporting the lactate oxidation pathway and facilitating metabolic symbiosis between hypoxic tumor cells and normoxic tumor cells by facilitating the release of lactate from the former and the uptake of lactate in the latter.[5] Cancer cells avoid cytoplasmic acidification that may lead to apoptosis by facilitated efflux of pyruvate and lactate produced during glycolysis.[5,6] Accordingly, upregulation of MCTs, in particular of MCT1 and MCT4, was observed in a large number of tumors.[7-13] Consequently, these two isoforms are known as major selective targets for the treatment of a broad spectrum of cancers such as high-grade gliomas, neuroblastomas, soft-tissue sarcoma, colorectal carcinomas, lung cancer, cervical cancer, and triple-negative breast carcinoma.[7-13] It has been shown that inhibition of MCT1 and/or MCT4 can block tumor growth through disruption of lactate transport and the glycolytic pathway of cell energy metabolism.[14]

The development and preclinical evaluation of several MCT inhibitors including α-cyanocinnamate derivatives, quinolinethiophene amides such as AZD3965 and AR-C155858 as well as bioflavenoids such as quercetin, phenyl pyruvate, and phloretin (Figure 1A) have been reported.[1,15-17] Among these drugs, AZD3965, initially developed as an immunosuppressor,[17] is currently being evaluated as an anticancer agent in phase I clinical trials (NCT01791595) for patients with prostate cancer, gastric cancer, or diffuse large B cell lymphoma.[18] Although having relatively low inhibitory activity towards MCT1 (IC_{50} ~100 μM), α-cyano-4-hydroxycinnamic acid (α-CHC) was the first MCT1 inhibitor reported.[19] More recently, we reported a comprehensive structure-activity relationship (SAR) study on a new series of α-CHC derivatives as MCT1 inhibitors.[7,8] Accordingly, we have also described the synthesis of the most potent inhibitors in this series and reported on their *in vivo* tumor growth inhibition in WiDr tumor-bearing mice for potential anticancer applications.[7,8]

In this context, it is also of high interest to attain a more detailed understanding of the function and regulation of MCTs in living animals and humans by positron emission tomography (PET). From the diagnostic perspective, the involvement of MCT1 and MCT4 in the glycolytic metabolism of cancer cells makes them valuable imaging biomarkers for many tumors. However, during the last decade, only a few substrates and inhibitors of MCTs were investigated as PET tracers (Figure 1B) for *in vivo* investigation of MCTs.[20-22]

We have focused on α-CHC derivatives as lead compounds to develop a novel ^{18}F-labeled ligand targeting MCTs for tumor imaging with PET. To achieve this aim, *(E)*-2-cyano-3-(4-(dipropylamino)-2-methoxyphenyl) acrylic acid **(I)** (Figure 2) appeared to be appropriate because it shows a high MCT1 inhibition (IC_{50} = 12 ± 1 nM).[7,8] Based on **I**, **FACH**, a **f**luorinated **α-CH**C derivative (*(E)*-2-cyano-3-{4-[(3- fluoropropyl) (propyl)amino]-2-methoxyphenyl} acrylic acid), has been developed in the present study and considered as a candidate for ^{18}F-labeling (Figure 2). Herein, we report on the chemical synthesis, measurement of MCTs inhibition, and radiosynthesis of the first ^{18}F-labeled MCTs inhibitor [^{18}F]**FACH**.

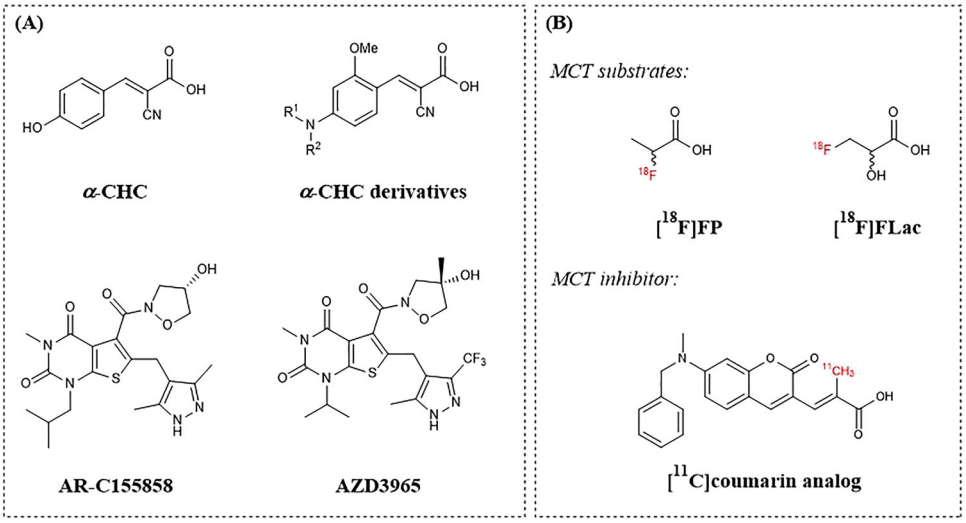

FIGURE 1 (A) Selected potent monocarboxylate transporters (MCTs) inhibitors; (B) Recently developed ^{18}F- and ^{11}C-labeled MCT-targeting tracers[15-22]

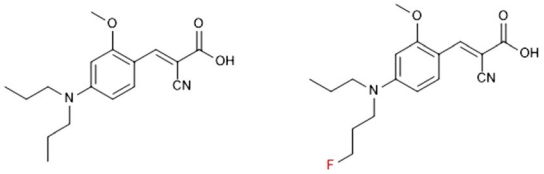

FIGURE 2 The potent monocarboxylate transporter 1 (MCT1) inhibitor (**I**) and its fluorinated analog (**FACH**) developed in the present study

2 | MATERIALS AND METHODS

2.1 | Organic syntheses

2.1.1 | General methods

Unless otherwise noted, moisture-sensitive reactions were conducted under dry nitrogen or argon. All chemicals and reagents were purchased from commercial sources and used without further purification. For thin-layer chromatography (TLC), Silica gel 60 F254 plates (Merck KGaA, Darmstadt, Germany) were used. Flash chromatography (fc) was performed using Silica gel 60, 40 to 64 μm (Merck). Room temperature was 21°C. For mass spectrometry (MS), Finnigan MAT GCQ (Thermo Finnigan MAT GmbH, Bremen, Germany) was used. ^{1}H and ^{13}C spectra were recorded on VARIAN "MERCURY plus" (300 MHz for ^{1}H NMR and 75 MHz for ^{13}C NMR) and VARIAN "MERCURY plus" and BRUKER DRX-400 (400 MHz for ^{1}H NMR, 101 MHz for ^{13}C NMR, and 377 MHz for ^{19}F NMR); δ in ppm related to tetramethylsilane; coupling constants (J) are given with 0.1-Hz resolution. Multiplicities of NMR signals are indicated as follows: s (singlet), d (doublet), t (triplet), sext (sextuplet), m (multiplet), dd (doublet of doublets), dt (doublet of triplets), and dq (doublet of quintets). Electrospray ionization (ESI)/Ion trap mass spectra (LRMS) were recorded with a Bruker Esquire 3000 plus instrument (Billerica, MA, USA). High-resolution mass spectra were recorded on a FT-ICR APEX II spectrometer (Bruker Daltonics; Bruker Corporation, Billerica, MA, USA) using ESI in positive ion mode.

2.1.2 | General procedure for synthesis of the reference compounds and precursor

1-Bromopropane (2.55 mL, 28 mmol, 1.0 eq) and potassium carbonate (8.4 g, 60 mmol, 2.1 eq) were added to a solution of *m*-anisidine (6.0 mL, 84 mmol, 3 eq) in 50mL acetonitrile (ACN) and refluxed overnight. Upon the completion of the reaction, 100 mL 5% aqueous $NaHCO_3$ solution was added, and the mixture was extracted with ethyl acetate (EtOAc, 3 × 50 mL). The organic layer was dried with anhydrous Mg_2SO_4 and evaporated. The residue was purified by column chromatography (silica, EtOAc/isohexane (IH) = 0.5:9.5 to 1:9) to give the monoalkylated aniline (52% yield, TLC [silica gel, EtOAc/IH, 2:8]: R_f = 0.65). 1-Iodo-3-fluoropropane (2.65 mL, 20 mmol, 1.8 eq) and potassium carbonate (4.2 g, 30 mmol, 2.7 eq) were added to a solution of 3-methoxy-*N*-propylaniline (1.82 g, 11 mmol, 1.0 eq) in 50mL ACN and refluxed overnight. Upon the completion of the reaction, 100 mL 5% aqueous $NaHCO_3$ solution was added, and the mixture was extracted with EtOAc (3 × 50 mL). The organic layer was dried with anhydrous Mg_2SO_4 and evaporated. $POCl_3$ (1.0 mL, 11 mmol, 1.1 eq) was added dropwise to a solution of dialkylated aniline (10 mmol, 1.0 eq) in *N,N*-dimethylformamide (DMF, 4.65 mL, 60 mmol, 6.0 eq) at 0°C, and the reaction mixture was refluxed at 80°C for 2 to 4 hours. The reaction was quenched with saturated Na_2CO_3, and the solid was filtered and washed with n-hexane to obtain the corresponding *N,N*-disubstituted benzaldehyde. Cyanoacetic acid (or *tert*-butyl cyanoacetate) (15 mmol, 3.0 eq) and piperidine (0.5 mL, 5 mmol, 1.0 eq) were added to a solution of substituted benzaldehyde (5 mmol, 1.0 eq) in 20mL ACN and refluxed overnight at 80°C. Upon the completion of the reaction, the above solution was poured into a mixture of 3 M HCl (10 mL) in ice. The solution was stirred for 10 to 15 minutes, and the solid was filtered using a Büchner funnel. The final compounds were obtained in pure form by column chromatography.

N-(3-Fluoropropyl)-3-methoxy-*N*-propylaniline (**2**) (colorless oil, 96% yield). TLC (silica gel, EtOAc/IH, 2:8): R_f = 0.82. ^{1}H NMR (400 MHz, DMSO-d_6) δ 7.13 (t, J = 8.6 Hz, 1H), 6.45-6.06 (m, 3H), 4.42 (dt, J = 47.1, 5.4 Hz, 2H), 3.79 (s, 3H), 3.45 (t, J = 7.1 Hz, 2H), 3.23 (t, J = 7.1 Hz, 2H), 2.05 (dq, J = 28.4 Hz, 2H), 1.69 (sext, J = 7.6 Hz, 2H), 0.99 (t, J = 7.4 Hz, 3H).

4-[(3-Fluoropropyl)(propyl)amino]-2-methoxybenzaldehyde (**3**) (yellow solid, greater than 98% yield). TLC (silica gel, EtOAc/IH, 2:8): R_f = 0.18. ^{1}H NMR (400 MHz, chloroform-*d*) δ 10.15 (s, 1H), 7.71 (d, J = 8.9 Hz, 1H), 6.30 (dd, J = 8.9, 2.3 Hz, 1H), 6.12 (d, J = 2.4 Hz, 1H), 4.55 (dt, J = 47.1, 5.4 Hz, 2H), 3.90 (s, 3H), 3.58 (t, J = 7.2 Hz, 2H), 3.35 (t, J = 7.2 Hz, 2H), 2.06 (dq, J = 28.3 Hz, 2H), 1.69 (sext, J = 7.4 Hz, 2H), 0.99 (t, J = 7.4 Hz, 3H); ^{13}C NMR (101 MHz, chloroform-*d*) δ 187.2, 164.0, 154.1, 130.7, 114.6, 104.4, 92.9, 81.4 (d, J = 164.9 Hz), 55.2, 52.8, 47.0 (d, J = 3.5 Hz), 28.4 (d, J = 20.1 Hz), 20.5, 11.3.

(*E*)-2-Cyano-3-{4-[(3-fluoropropyl)(propyl)amino]-2-methoxyphenyl}acrylic acid (**FACH**) (yellow solid, 90% yield). TLC (silica gel, EtOAc/IH, 1:1): R_f = 0.33. ^{1}H NMR (400 MHz, DMSO-d_6) δ 8.40 (s, 1H), 8.18 (d, J = 9.2 Hz, 1H), 6.50 (dd, J = 9.3, 2.4 Hz, 1H), 6.19 (d, J = 2.4 Hz, 1H), 4.51 (dt, J = 47.4, 5.6 Hz, 1H), 3.86 (s, 3H), 3.67–3.46 (m, 2H), 3.38 (t, J = 7.6 Hz, 2H), 1.94 (dq, J = 26.8 Hz, 2H), 1.58 (sext, J = 7.4 Hz, 2H), 0.89 (t, J = 7.4 Hz, 3H); ^{13}C NMR (101 MHz, DMSO-d_6) δ 165.8, 162.1, 154.5, 146.7, 130.3, 118.9, 108.2, 105.9, 93.8, 91.6, 82.2 (d, J = 164.9 Hz), 56.1, 52.2, 46.9 (d, J = 4.8 Hz), 28.4 (d, J = 19.3 Hz), 20.6, 11.5; ^{19}F NMR (377 MHz, DMSO-d_6) δ -219.3. HRFT-MS (ESI+): m/z = 343.1422 (calcd. 343.1428 for $C_{17}H_{21}FN_2O_3Na^+$ $[M + Na]^+$).

tert-Butyl *(E)/(Z)*-2-cyano-3-{4-[(3-fluoropropyl)(propyl)amino]-2-methoxyphenyl}acrylate (***(E)/(Z)-tert*-Bu-FACH**) (yellow solid, greater than 98% yield). TLC (silica gel, EtOAc/IH, 1:1): R_f = 0.50. ^{1}H NMR (400 MHz, chloroform-*d*) δ 8.56 (s, 1H), 8.36 (d, J = 9.0 Hz, 1H), 6.33 (dd, J = 9.2, 2.5 Hz, 1H), 6.09 (d, J = 2.5 Hz, 1H), 4.52 (dt, J = 47.2, 5.4 Hz, 2H), 3.84 (s, 3H), 3.65–3.48 (m, 2H), 3.42–3.27 (m, 2H), 2.01 (dq, J = 26.6 Hz, 2H), 1.65 (sext, J = 7.6 Hz, 2H), 1.55 (s, 9H), 0.96 (t, J = 7.3 Hz, 3H); ^{13}C NMR (101 MHz, chloroform-*d*) δ 163.6, 161.8, 153.1, 147.2, 131.1, 118.3, 110.0, 105.3, 94.8, 93.7, 82.1, 81.3 (d, J = 165.2 Hz), 55.4, 53.2, 47.3 (d, J = 3.5 Hz), 28.4 (d, J = 20.1 Hz), 28.1 (s, 3C), 20.5, 11.3; ^{19}F NMR (282 MHz, chloroform-*d*) δ -220.9. HRFT-MS (ESI+): m/z = 377.2233 (calcd. 377.2235 for $C_{21}H_{30}FN_2O_3$ $[M + H]^+$).

3-[(3-Methoxyphenyl)(propyl)amino]propan-1-ol (**5**). 3-Bromo-1-propanol (1.81 mL, 20 mmol, 1.8 eq) and potassium carbonate (4.2 g, 30 mmol, 2.7 eq) were added to a solution of 3-methoxy-*N*-propylaniline (1.82 g, 11 mmol, 1.0 eq) in 50mL ACN and refluxed overnight. The work-up was performed as described in the general procedure (yellow oil, 88% yield). TLC (silica gel, EtOAc/IH, 2:8): R_f = 0.19. ^{1}H NMR (400 MHz, chloroform-*d*) δ 7.15 (t, J = 8.1 Hz, 1H), 6.38 (dd, J = 8.4, 2.4 Hz, 1H), 6.34-6.10 (m, 2H), 3.82 (s, 3H), 3.74 (t, J = 6.0 Hz, 2H), 3.44 (t, J = 7.1 Hz, 2H), 3.34-3.16 (m, 2H), 2.03 (s, 1H), 1.91-1.76 (m, 2H), 1.64 (sext, J = 7.4 Hz, 2H), 0.95 (t, J = 7.4 Hz, 3H); ^{13}C NMR (101 MHz, chloroform-*d*) δ 160.9, 149.6, 129.9, 105.8, 100.6, 99.3, 60.8, 55.1, 53.3, 48.1, 30.2, 20.3, 11.5.

3-[(3-Methoxyphenyl)(propyl)amino]propyl acetate (**6**). Acetyl chloride (2.4 mL, 33 mmol, 1.5 eq) and pyridine (5.3 mL, 66 mmol, 3.0 eq) was added to a solution of alcohol **5** (5.0 g, 22 mmol, 1.0 eq) in 50mL dichloromethane (DCM), and the resulting mixture was allowed to react at room temperature overnight. The reaction was quenched by the addition of 50mL ice cold water, the phases were separated, and the organic phase was dried with anhydrous Mg_2SO_4 and evaporated to give **6** as yellowish oil, which was used in the next reaction without further purification. TLC (silica gel, EtOAc/IH, 2:8): R_f = 0.55. ^{1}H NMR (400 MHz, chloroform-*d*) δ 7.14 (t, J = 8.1 Hz, 1H), 6.46–6.07 (m, 3H), 4.14 (t, J = 6.3 Hz, 2H), 3.81 (s, 3H), 3.39 (t, J = 7.3 Hz, 2H), 3.24 (t, J = 7.7 Hz, 2H), 2.10 (s, 3H), 1.95 (t, J = 7.1 Hz, 2H), 1.63 (m, 2H), 0.94 (t, J = 7.4 Hz, 3H); ^{13}C NMR (101 MHz, chloroform-*d*) δ 171.1, 160.9, 149.3, 129.9, 105.3, 100.3, 98.8, 62.4, 55.1, 53.1, 47.8, 26.6, 21.0, 20.4, 11.4.

3-[(4-Formyl-3-methoxyphenyl)(propyl)amino]propyl acetate (**7**) (yellow oil, 79% yield). TLC (silica gel, EtOAc/IH, 2:8): R_f = 0.11. ^{1}H NMR (400 MHz, chloroform-*d*) δ 10.19 (s, 1H), 7.76 (d, J = 8.9 Hz, 1H), 6.39 (dd, J = 8.9, 2.3 Hz, 1H), 6.29 (s, 1H), 4.16 (t, J = 6.2 Hz, 2H), 3.93 (s, 3H), 3.57–3.42 (m, 2H), 3.42–3.25 (m, 2H), 2.10 (s, 3H), 2.01 (m, 2H), 1.71 (m, 2H), 0.99 (t, J = 7.4 Hz, 3H).

4-[(3-Hydroxypropyl)(propyl)amino]-2-methoxybenzaldehyde (**8**). A solution of K_2CO_3 (7.0 g, 50 mmol, 5.0 eq) in 70 mL H_2O was added to a solution of **7** (2.5 g, 10 mmol, 1.0 eq) in 75 mL MeOH, and the reaction mixture was stirred for 30 minutes at room temperature. An aqueous saturated NaCl solution (50 mL) was added followed by addition of 100 mL DCM. The resulting phases were separated, and the organic phase was dried with anhydrous Mg_2SO_4 and evaporated to give **8** as yellowish oil, which was used in the next reaction without further purification. TLC (silica gel, EtOAc/IH, 1:1): R_f = 0.15. ^{1}H NMR (400 MHz, chloroform-*d*) δ 10.16 (s, 1H), 7.73 (d, J = 8.9 Hz, 1H), 6.38 (d, J = 9.0 Hz, 1H), 6.28 (s, 1H), 3.91 (s, 3H), 3.76 (t, J = 5.8 Hz, 2H), 3.57 (t, J = 7.3 Hz, 2H), 3.36 (dd, J = 8.6, 6.9 Hz, 2H), 1.97–1.84 (m, 2H), 1.70 (sext, J = 7.5 Hz, 2H), 0.98 (t, J = 7.4 Hz, 3H).

tert-Butyl *(E)/(Z)*-2-cyano-3-{4-[(3-hydroxypropyl)(propyl)amino]-2-methoxyphenyl}acrylate (**9**) (yellow solid, 90%). TLC (silica gel, EtOAc/IH, 1:1): R_f = 0.18. ^{1}H NMR (300 MHz, chloroform-*d*) δ 8.56 (s, 1H), 8.35 (d, J = 9.2 Hz, 1H), 6.38 (dd, J = 9.1, 2.4 Hz, 1H), 6.20 (s, 1H), 3.85 (s, 3H), 3.73 (t, J = 5.8 Hz, 2H), 3.55 (dd, J = 8.1, 6.4 Hz, 2H), 3.38–3.28 (m, 2H), 1.92–1.84 (m, 2H), 1.67 (dt, J = 9.4, 7.4 Hz, 2H), 1.57 (s, 9H), 0.95 (t, J = 7.4 Hz, 3H). ^{13}C NMR (75 MHz, chloroform-*d*) δ 165.5, 162.3, 154.3, 148.1, 131.2, 118.6, 109.2, 105.3, 93.1, 91.0, 59.7, 55.4, 52.8, 52.6, 47.8, 30.1, 20.6, 14.2, 11.4. HRFT-MS (ESI+): m/z = 375.2340 (calcd. 375.2278 for $C_{21}H_{31}N_2O_4^+$ $[M + H]^+$).

tert-Butyl *(E)/(Z)*-2-cyano-3-{2-methoxy-4-{[3-[(methylsulfonyl)oxy]propyl](propyl)amino} phenyl}acrylate (**10**). Methanesulfonyl chloride (30 μL, 0.4 mmol,

1.2 eq) and triethylamine (Et_3N, 130 μL, 0.9 mmol, 3.0 eq) were added to a solution of alcohol **9** (100 mg, 0.3 mmol, 1.0 eq) in 5mL DCM, and the reaction mixture was stirred for 30 minutes at room temperature. The reaction was quenched by addition of 10mL saturated aqueous $NaHCO_3$ solution. The aqueous solution was extracted with DCM (2 × 10 mL), and the combined organic phases were washed with brine (10 mL) and dried over $MgSO_4$. Evaporation of the solvent under reduced pressure afforded quantitatively the corresponding mesylate **10** as yellow solid with greater than 98% yield. TLC (silica gel, EtOAc/IH, 1:1): R_f = 0.22. ^{1}H NMR (400 MHz, chloroform-*d*) δ 8.57 (t, *J* = 0.5 Hz, 1H), 8.36 (dd, *J* = 9.2, 0.5 Hz, 1H), 6.32 (dd, *J* = 9.2, 2.4 Hz, 1H), 6.07 (d, *J* = 2.5 Hz, 1H), 4.30 (t, *J* = 5.8 Hz, 2H), 3.85 (s, 3H), 3.64–3.48 (m, 2H), 3.42–3.26 (m, 2H), 3.03 (s, 3H), 2.15–2.01 (m, 2H), 1.67 (sext, *J* = 7.6 Hz, 2H), 1.55 (s, 9H), 0.96 (t, *J* = 7.4 Hz, 3H). ^{13}C NMR (101 MHz, chloroform-*d*) δ 163.6, 161.9, 153.3, 147.2, 131.1, 118.40, 109.67, 105.03, 94.59, 93.15, 82.15, 67.35, 55.46, 52.98, 47.22, 37.45, 28.10, 27.20, 20.60, 11.4. HRFT-MS (ESI+): *m/z* = 453.2134 (calcd. 453.2054 for $C_{22}H_{33}N_2O_6S^+$ $[M + H]^+$).

2.2 | [^{14}C]Lactate uptake assay for assessment of MCT1 and MCT4 inhibition

Inhibition of MCT1-mediated lactate transport was determined using the rat brain endothelial cell line (RBE4, a gift from F. Roux research group) as previously described.[7,8] Polymerase chain reaction (PCR) analysis and Western Blot demonstrated that only the MCT1 isoform is expressed by RBE4 cells (data not shown). For determination of the inhibition of MCT4-mediated transport, MB-231 cells were used because these cells express exclusively MCT4 as determined by PCR and Western Blot (data not shown). For both cell lines, an L-[^{14}C]lactate (Perkin Elmer, Waltham, MA, USA) based transport assay was implemented to quantify the transport of lactate via the respective MCT and the inhibition thereof by **FACH**. Cells were seeded at 4 × 10^5 cells/mL in 24-well culture dishes. After 24 hours, cells were washed twice with 500μL HEPES buffer and allowed to equilibrate for 15 to 20 minutes at 37°C. Afterwards, cells were incubated for 1 hour in the presence of L-[^{14}C]lactate and different concentrations (100 pM-1 μM) of the respective test compound. The dimethylsulfoxide (DMSO, Fisher scientific, Waltham, Massachusetts, USA) stock solution of **FACH** was diluted to the respective working concentration in HEPES buffer (140mM NaCl, 5mM KCl, 2mM $CaCl_2$, 2mM $MgCl_2$, 10mM HEPES, pH 7.0) containing 3μM L-[^{14}C]lactate and 2μM L-lactate. α-CHC (Millipore sigma, Milwaukee, USA) and DMSO were used as positive and vehicle controls. The incubation was terminated by replacing the incubation medium with 500μL ice-cold HEPES buffer (containing 0.1mM α-CHC, pH 7.4) and transferring the plates on ice. Cells were washed twice with ice-cold HEPES buffer and finally solubilized using 250 μL of 0.1M NaOH in 5% Triton-X (Millipore Sigma, Milwaukee, USA). A 150μL aliquot from each well was added to 4mL EcoLite(+)^{TM} scintillation fluid (MP Biomedicals, Ohio, USA), and radioactivity was determined by scintillation spectrometry. The inhibition of L-[^{14}C] lactate uptake by each test solution was calculated as a percentage of the maximum control uptake, and IC_{50} values were calculated using GraphPad PRISM (Graphpad software, San Diego, USA).

2.3 | [^{14}C]Nicotinate uptake assay for assessment of SMCT1 inhibition

The uptake assays were performed by using [^{14}C] nicotinate (sodium salt, molar activity, 50 mCi/mmol, Perkin Elmer, Waltham, MA, USA) in mouse skeletal muscle cell line, C2C12 (American Type Culture Collection (ATCC), Manassas, VA, USA). The cells, as adherent monolayers suitable for uptake measurements, were cultured in DMEM (Corning Cellgro, Manassas, VA, USA) supplemented with 10% fetal bovine serum (Atlanta Biologicals, Norcross, GA, USA) and 100 mU/mL penicillin and 100 μg/mL streptomycin. Measurement of [^{14}C] nicotinate uptake was made in C2C12 cells monolayers cultured in 24-well plates. On the day of uptake measurement, the culture plates were kept in a water bath at 37°C. The cells were washed with transport buffer, and then the transport medium (250 μL) containing [^{14}C] nicotinate (33 μM) with or without the inhibitors (1-1000 μM) was added to each well. The final concentration of DMSO was adjusted to 0.5% in the uptake buffer. The cells were incubated at 37°C for 3 minutes and then washed twice with ice-cold transport buffer to terminate the uptake. The cells were then lysed in 1% sodium dodecyl sulfate/0.2 N NaOH and used for measurement of radioactivity by scintillation spectroscopy (scintillation fluid: Bio-safeII, Research Products International, Mount Prospect, IL, USA; scintillation counter: LS-6500, Beckman Coulter, Fullerton, CA, USA). Two different uptake buffers were used. The Na^+-containing buffer consisted of 25 mM Hepes/Tris (pH 7.5), 140 mM NaCl, 5.4 mM KCl, 1.8 mM $CaCl_2$, 0.8 mM $MgSO_4$, and 5 mM D-glucose; the Na^+-free buffer consisted of the same components except for the equimolar replacement of NaCl with *N*-methyl-D-glucamine chloride. The difference in uptake between the two buffers yielded Na^+-dependent

uptake, which was taken as a measure of SMCT1-mediated uptake activity. Data are expressed as means ± SE, and the IC_{50} values were calculated from nonlinear regression using the program Graphpad Prism 7 software (GraphPad Software, La Jolla, California, USA).

2.4 | Radiochemistry

2.4.1 | General methods

A Nirta XL target filled with $[^{18}O]H_2O$ (Hyox 18 enriched water, Rotem Industries Ltd., Arava, Israel) attached to the Cyclone 18/9 (iba RadioPharma Solutions, Belgium) was irradiated with fixed energy proton beam to produce no-carrier-added $[^{18}F]$fluoride via the $[^{18}O(p,n)^{18}F]$ nuclear reaction. Discover PET Wave Microwave (CEM, NC, USA) was used for the azeotropic drying process of $[^{18}F]$fluoride. Radio-thin layer chromatography (radio-TLC) analyses were carried out on silica gel (Polygram SIL G/UV254) and aluminum oxide (Polygram Alox N/UV254) pre-coated plates developed with EtOAc/n-hexane 1:1 (for $[^{18}F]$***tert*-Bu-FACH**) and DCM/MeOH 8:2 (for $[^{18}F]$**FACH**), respectively. The plates were exposed to storage phosphor screens (BAS-MS2025, FUJIFILM Co., Tokyo, Japan) and recorded using the Amersham Typhoon RGB Biomolecular Imager (GE Healthcare Life Sciences, Freiburg, Germany). Images were quantified with the Image Quant TL8.1 software (GE Healthcare Life Sciences, Freiburg, Germany).

Analytical high performance liquid chromatography (HPLC) analyses were performed on a JASCO LC-2000 system (JASCO Labor- und Datentechnik, Gross-Umstadt, Germany), incorporating a PU-2080 Plus pump, AS-2055 Plus auto injector (100 μL sample loop), and a UV-2070 Plus detector coupled with a gamma radioactivity HPLC detector (Gabi Star, Raytest Isotopenmessgeräte GmbH, Straubenhardt, Germany). Data analysis was performed with the Galaxie chromatography software (Agilent Technologies, Santa Clara, USA) using the chromatograms obtained at 210 and 254 nm. Semi-preparative HPLC separations were performed on a JASCO LC-2000 system, including a PU-2080-20 pump, a UV/vis-2075 detector coupled with a gamma radioactivity HPLC detector with slightly modified measurement geometry (Gabi Star, Raytest Isotopenmessgeräte GmbH), and a fraction collector (Advantec CHF- 122SC, Dublin, CA, USA). Data analysis was performed with the Galaxie chromatography software (Agilent Technologies, Santa Clara, USA) using the chromatograms obtained at 254 nm. The ammonium acetate (NH_4OAc) and ammonium formate (NH_4HCO_2) concentrations (20 mM NH_4OAc/NH_4HCO_2 aq.) correspond to the concentrations in the aqueous component of an eluent mixture.

2.4.2 | General procedure for radiosynthesis of $[^{18}F]$FACH by using $K[^{18}F]F\text{-}K_{2.2.2}$-carbonate complex

No-carrier-added $[^{18}F]$fluoride (1-2 GBq) in 1 mL of H_2O was trapped on a Chromafix 30 PS-HCO_3-cartridge (Macherey-Nagel GmbH & Co. KG, Düren, Germany). $NaHCO_3$ (15 mL, 0.5 M) and H_2O (10 mL) were used for cartridge preconditioning. The activity was eluted with 300 μL of an aqueous solution of potassium carbonate (K_2CO_3, 1.5 mg, 10.5 μmol) into a 4-mL V-shape vial containing Kryptofix 2.2.2 ($K_{2.2.2}$, 11.2 mg, 29.5 μmol) in 1 mL of ACN. The aqueous $[^{18}F]$fluoride was azeotropically dried under vacuum and nitrogen flow within 7 to 10 minutes using a single-mode microwave device (75 W, at 50°C-60°C, power cycling mode). Two times 1.0 mL of ACN were added during the drying procedure, and the final complex was dissolved in 500 μL of ACN or DMSO. Thereafter, certain volumes of the $K[^{18}F]F\text{-}K_{2.2.2}$-carbonate complex, which correspond to the required amount of the complex, was added to a solution of 2 mg of precursor **10** in 500 μL of ACN or DMSO. Radiofluorination was performed under conventional heating at different temperatures in a total volume of 750 μL. To determine the radiochemical yields of the products by radio-HPLC and radio-TLC, samples were taken from each crude reaction mixture at different time points after cooling the vial on ice to less than 30°C.

After cooling the vial to room temperature, HCl (2.0 and 6.0 N) or trifluoroacetic acid (TFA) was added to the crude mixture, and the deprotection reaction was performed during different reaction times at different temperatures. Thereafter, aqueous 2.0 M NaOH or saturated Na_2CO_3 was used for neutralization of the reaction mixture. In case of performing the deprotection in DCM, the evaporation of ACN and re-dissolving the residue in 100 μL of dry DCM was needed. Evaporation of remaining TFA was considered as an alternative for neutralization when ACN or DCM were used as solvent. In this case, volatile solvents were evaporated at room temperature under vacuum and a gentle stream of argon.

2.4.3 | General procedure for radiosynthesis of $[^{18}F]$FACH by using $[^{18}F]$TBAF

The aqueous solution of no-carrier-added $[^{18}F]$fluoride was added to a solution of 50 μL of tetra-n-butylammonium bicarbonate (0.075 M) in 1 mL of ACN

to a V-shape reaction vial. The aqueous [^{18}F]fluoride was azeotropically dried under vacuum and nitrogen flow within 7 to 10 minutes using a single-mode microwave device (75 W, at 50°C-60°C, power cycling mode). Two times 1.0 mL of ACN were added during the drying procedure, and the final complex was dissolved in 250 μL of ACN ready for labeling. A solution of 2 mg of precursor **10** in 500 μL of *tert*-BuOH or ACN was added to the reaction vial, sealed and mixed. The mixture with a total volume of 750 μL was heated at 100°C for up to 20 minutes. After completion of the reaction, the reaction mixture was allowed to cool to less than 40°C, and the solvents were evaporated under vacuum and a gentle stream of argon at 40°C for 6 to 10 minutes. Thereafter, 100 μL of fresh ACN was added to the residue, and then 400 μL of TFA were slowly added. The deprotection was conducted at room temperature for up to 20 minutes. Sampling was carried out at desired time points to determine the optimized reaction time for both steps. Neutralization was performed by addition of the required amount of Et_3N to adjust the pH to 4 to 5 and subjected to a semi-preparative RP-HPLC for isolation of [^{18}F]**FACH** (46% ACN/20 mM NH_4HCO_2, pH = 4-5, 3.5 mL/min, Reprosil-Pur C18-AQ column, 250 mm × 10 mm; 5 μm; Dr. Maisch HPLC GmbH, Ammerbuch-Entringen, Germany). The collected radiotracer fraction was diluted with 40 mL of H_2O to perform final purification by sorption on a Sep-Pak C18 light cartridge (Waters, Milford, MA, USA) and successive elution with 0.75 mL of ethanol. The solvent was reduced under a gentle argon stream, and the desired radiotracer was formulated in sterile isotonic saline containing 10% EtOH (v/v).

Identity and radiochemical purity of [^{18}F]**FACH** was confirmed by radio-HPLC (gradient and isocratic modes) and radio-TLC (SIL G/UV254, DCM/MeOH 8:2). For analytical radio-HPLC, a Reprosil-Pur C18-AQ column (250 mm × 4.6 mm; 5 μm; Dr. Maisch HPLC GmbH; Germany) and an eluent mixture containing ACN mixed with aqueous 20mM NH_4OAc or NH_4HCO_2 was used with a flow of 1.0 mL/min (see supporting information). Molar activity was determined based on a calibration curve carried out under isocratic HPLC conditions (46% ACN/aq. 20 mM NH_4HCO_2, pH = 4-5) using chromatograms obtained at 210 nm.

3 | RESULTS AND DISCUSSION

3.1 | Organic chemistry and transporter inhibition

In order to develop a fluorinated analog of the lead compound **I**, we replaced one of the propyl groups attached to the amino function by a fluoropropyl group. The synthesis of compound **I** was previously described in three steps starting from *m*-anisidine in 67% overall yield.[7] A similar synthetic approach was used to synthesize the new fluorinated derivative **FACH** (Scheme 1). Additionally, the carbonic acid protected derivative ***tert*-Bu-FACH** was synthesized, as this compound would necessarily be an intermediate in the ^{18}F-radiosynthesis. Briefly, *N,N*-dialkylated anisidine **2** was formed via two consequence alkylation reactions on *m*-anisidine **1** followed by a Vilsmeier-Haack formylation to give compound **3** in 49% yield (three steps).[23] The Knoevenagel condensation reaction of aldehyde **3** with cyanoacetic acid and *tert*-butyl cyanoacetate afforded **FACH** and ***tert*-Bu-FACH** in 44% and 48% overall yields, respectively (Scheme 1). The characterization of ***tert*-Bu-FACH** by HPLC and LC-MS (liquid chromatography-mass spectrometry) revealed that a mixture of *E*- and *Z*-isomers was obtained whereas the *E*-isomer was the predominant product (*E*/*Z* = 96:4; Figure S2.1 and S2.2). According to the reported ^{1}H NMR data, the chemical shift for the alkene hydrogen in the *Z*-isomer could be distinguishable in coumarin analogs.[22] However, in our case, the characterization of ***(Z)-tert*-Bu-FACH** was not possible by NMR analyses probably because of the very low ratio of *Z*-isomer compared to the *E*-isomer (Figure S3.1-S3.3).

In order to determine the inhibitory potency of **FACH** towards MCT1 and MCT4, an L-[^{14}C]lactate uptake assay was performed using RBE4 and MDA-MB-231 cells,

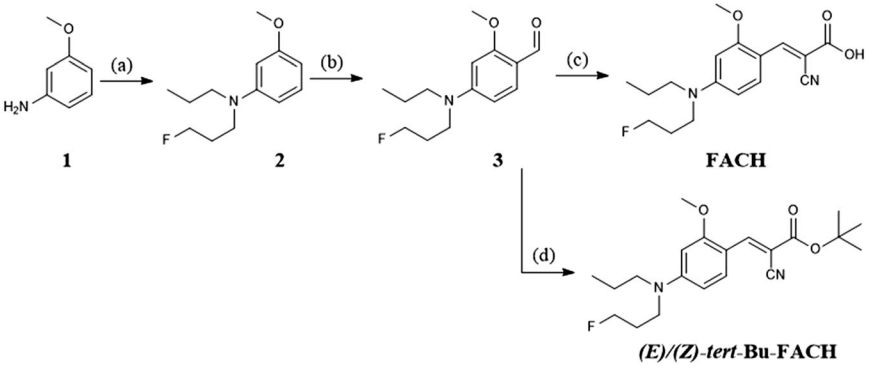

SCHEME 1 Synthesis of the reference compounds **FACH** and ***tert*-Bu-FACH**: (a) *i.* Br $(CH_2)_3$, K_2CO_3, acetonitrile (ACN), reflux, overnight, 52%; *ii.* I $(CH_2)_3F$, K_2CO_3, ACN, reflux, 96%; (b) $POCl_3$/DMF, 80°C, 98%; (c) cyanoacetic acid, piperidine, ACN, reflux, 90%; (d) *tert*-butyl cyanoacetate, piperidine, ACN, reflux, 98%

respectively.[7,8] **FACH** revealed high MCT1 and MCT4 inhibition (IC_{50} = 11.0 nM and 6.5 nM, respectively; Figure S4.1) comparable to the corresponding lead compound **I** (Figure 2). The high MCT4 inhibition found for **FACH** is favorable for further investigations considering the high density of MCT4 in several tumors cells (e.g., brain, breast, and prostate).[9-13] The inhibitory potency of FACH towards SMCT1 was also investigated using an [^{14}C]nicotinate uptake assay performed on C2C12 cells. These cells are widely used as a model for skeletal muscle cells and express the Na^+-dependent MCT SMCT1 and the H^+-dependent MCTs at the mRNA level. Both classes of transporters are known to transport nicotinate, but only the nicotinate uptake that is Na^+-dependent represents SMCT1 transport activity. As such, the transport activity of SMCT1 was monitored by subtracting the nicotinate uptake in the absence of Na^+ from that in the presence of Na^+. FACH revealed the higher IC_{50} value of 77.8 μM compared with the α-CHC compound (IC_{50} = 13.9 μM), which is known as a nonspecific MCTs inhibitor (Figure S4.2).

For the radiosynthesis of the new PET radioligand [^{18}F]**FACH**, a precursor compound with a suitable leaving group for nucleophilic aliphatic substitution with [^{18}F]fluoride is required. Furthermore, protection of the carboxylic acid group was performed to prevent its interference in the radiofluorination step. The synthesis route is depicted in Scheme 2. Starting with the reaction of 3-methoxy-*N*-propylaniline **4** with 3-bromo-1-propanol afforded 3-[(3-methoxyphenyl)(propyl) amino]propan-1-ol **5** in 88% yield. In order to avoid side reactions in the formylation step, conversion of the alcoholic group to its corresponding acetate **6** was performed. Removal of the protecting group after Vilsmeier-Haack formylation afforded the aldehyde **8**, which was subjected to the Knoevenagel condensation with *tert*-butyl cyanoacetate to give the protected alcohol **9**. The mesylate precursor **10** was finally prepared by treating the alcohol **9** with methanesulfonyl chloride and trimethylamine in 62% overall yield (Scheme 2). According to the ^{1}H NMR data, a mixture of *E*- and *Z*-isomers of the mesylate precursor **10** was found. Further, HPLC and LC-MS analyses revealed an approximate ratio of 4:1 for isomer *E* to *Z* (Figure S2.3 and S2.4). The chemical purity of the mesylate precursor **10** was estimated to be greater than 95% including both isomers.

3.2 | Radiochemistry

For the radiosynthesis of [^{18}F]**FACH**, a two-step approach including radiofluorination and deprotection was applied (Scheme 3). An alkali metal fluoride/cryptand complex such as K[^{18}F]F-$K_{2.2.2}$-carbonate is a reagent traditionally used for aliphatic

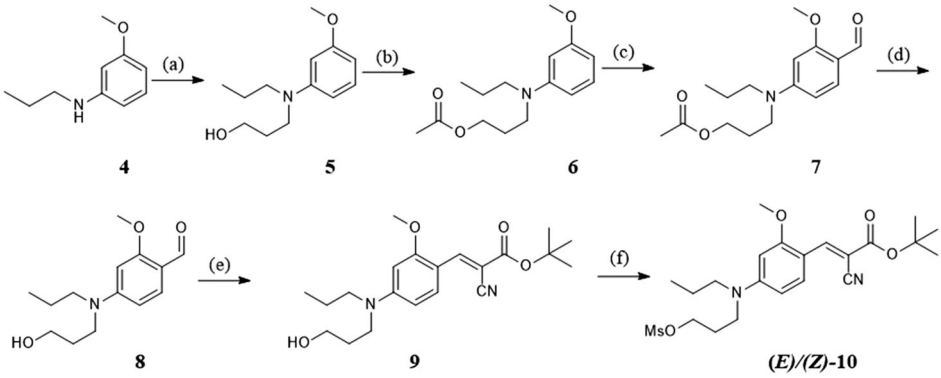

SCHEME 2 Synthesis of precursor **10**: (a) Br $(CH_2)_3OH$, K_2CO_3, acetonitrile (ACN), reflux, 88%; (b) AcCl, pyridine, dichloromethane (DCM), R.T.; (c) $POCl_3$/DMF, 80 °C, 79%; (d) K_2CO_3, MeOH/H_2O (1:1), 30 minutes, R.T.; (e) *tert*-butyl cyanoacetate, piperidine, ACN, reflux, 90%; (f) MsCl, Et_3N, DCM, 30 minutes, greater than 98%

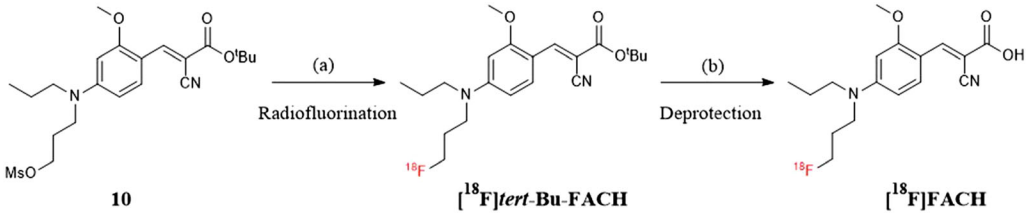

SCHEME 3 Two-step approach for the radiosynthesis of the novel monocarboxylate transporter (MCT) radioligand [^{18}F]**FACH**: (a) K[^{18}F]F-$K_{2.2.2}$-carbonate complex or [^{18}F]TBAF, acetonitrile (ACN), 15 minutes, 100°C; (b) *i.* trifluoroacetic acid (TFA), ACN, 15 minutes, r.t.; *ii.* Et_3N

nucleophilic substitution with ^{18}F-fluoride.[24-28] This system is generally strongly basic, which restricts its synthetic utility for base-sensitive precursors because it generates various side reactions, such as eliminations of alkyl halides or sulfonates to form alkenes.[29] On the other hand, tetraalkylammonium salts, such as Bu_4NHCO_3,[30] are milder reagents with enhanced solubility in organic solvents and have been widely used as an alternative to the Kryptofix 2.2.2/K_2CO_3. In the current study, we investigated both agents for the radiosynthesis of [^{18}F]**FACH**.

3.2.1 | Radiosynthesis of [^{18}F]FACH using K[^{18}F]F-$K_{2.2.2}$-carbonate complex

Optimization of the radiofluorionation via the K[^{18}F]F-$K_{2.2.2}$-carbonate system was accomplished by varying the amount of complex, solvent, reaction time, and temperature. Attempts to obtain the intermediate [^{18}F]***tert*-Bu-FACH** in a reasonable radiochemical yield (RCY) are summarized in Table 1. The radiofluorination was investigated in two solvents including DMSO and ACN using 11.2 mg (29.5 μmol) of $K_{2.2.2}$, 1.5 mg (10.5 μmol) of K_2CO_3 and aqueous solution of no-carrier-added [^{18}F] fluoride (hereinafter referred to as 100 mol% of K[^{18}F]F-$K_{2.2.2}$-carbonate complex) at a fixed concentration of the precursor **10** (2 mg, 4.4 μmol). In all cases, RCYs were higher in DMSO compared with ACN (Table 1).

Surprisingly, the amounts of $K_{2.2.2}$ and K_2CO_3 showed significant impact on the RCYs in both solvents based on the radio-HPLC analyses of the crude reaction mixture (Figure 3). While, only radiolabeled by-products were formed using 200 mol% of the K[^{18}F]F-$K_{2.2.2}$-carbonate complex in DMSO and ACN (Table 1, entries 1 and 5; Figure 3), by decreasing the complex amount to 100 mol%, [^{18}F]***tert*-Bu-FACH** was detected in both solvent systems (Table 1, entries 2 and 6). Interestingly, further decrease of the basicity of the system (complex amount 50 mol%, entries 3 and 7, Table 1) promoted a substantial increase in the RCYs of [^{18}F]***tert*-Bu-FACH** in both solvent systems investigated. However, the radiochemical yield was decreased when less than 50 mol% of the complex was used (Table 1, entry 4). In both solvents, the RCYs were diminished when the reactions were carried out at longer times or at higher temperatures (Table 1). Finally, the highest RCY for [^{18}F]***tert*-Bu-FACH** was obtained using 50 mol% K[^{18}F]F-$K_{2.2.2}$-carbonate complex in DMSO at 100°C in 20-minute reaction time. Under this labeling condition, the ratio between *E*- and *Z*-isomers of [^{18}F]***tert*-Bu-FACH** was found to be 99:1%.

The deprotection reaction was investigated using different concentrations of hydrochloric acid and TFA at different reaction times and temperatures (Table 2). The deprotection of [^{18}F]***tert*-Bu-FACH** in DMSO by using both acids did not afford [^{18}F]**FACH**, and the formation of radioactive by-products was observed (Table 2, entries 1 and 2). Assuming that DMSO is not suitable as solvent for the deprotection step, we then performed the radiofluorination in ACN. The first attempts for removal of the *tert*-butyl group in ACN by using both acids also failed, because of the conversion of [^{18}F]***tert*-Bu-FACH** to radioactive by-products (Table 2, entries 3 and 4; Figure S5.1). This fact might be associated to (a) the thermal instability of [^{18}F]**FACH**, (b) the remaining K[^{18}F]F-$K_{2.2.2}$-carbonate complex, or (c) the presence of water in the reaction mixture. Neither conducting the reaction at lower temperatures (at 40°C or even at room temperature) nor removing the K[^{18}F]F-$K_{2.2.2}$-carbonate complex by using solid-phase extraction resulted in the formation of [^{18}F]**FACH**. However, the deprotection of [^{18}F]***tert*-Bu-FACH** by using TFA in ACN under dry conditions afforded [^{18}F]**FACH** with RCY of 14.6 ± 6.4%

TABLE 1 Investigated parameters for radiosynthesis of [^{18}F]***tert*-Bu-FACH**[a]

Entry	Solvent	K[^{18}F]F-$K_{2.2.2}$-carbonate complex, mol%	Temperature, °C	Time, min	Radiochemical yield, %[b]
1	DMSO	200	110, 130, 150	10, 20, 30	0
2	DMSO	100[c]	110, 120, 135	10, 20, 30	22.3 ± 5.5
3	**DMSO**	**50**	**135**	**20**	**45.0 ± 9.5**
4	DMSO	20	135	20	20-31 (n = 2)
5	ACN	200	90, 100, 110	5, 10, 15, 20	0
6	ACN	100	90, 100, 110	5, 10, 15, 20	19.7 ± 2.1
7	**ACN**	**50**	**100**	10, **15**, 20	**38.7 ± 14.9**

Abbreviations: ACN, acetonitrile; DMSO, dimethylsulfoxide.

[a]In all experiments, 2 mg (4.4 μmol) of precursor **10** was used in a total reaction volume of 750 μL.

[b]The radiochemical yields (RCYs) were determined based on the radio-HPLC analysis of the crude reaction mixture (n ≥ 3, nonisolated).

[c]100 mol% of K[^{18}F]F-$K_{2.2.2}$-carbonate complex represents 11.2 mg (29.5 μmol) of Kryptofix 2.2.2 and 1.5 mg (10.5 μmol) of K_2CO_3.

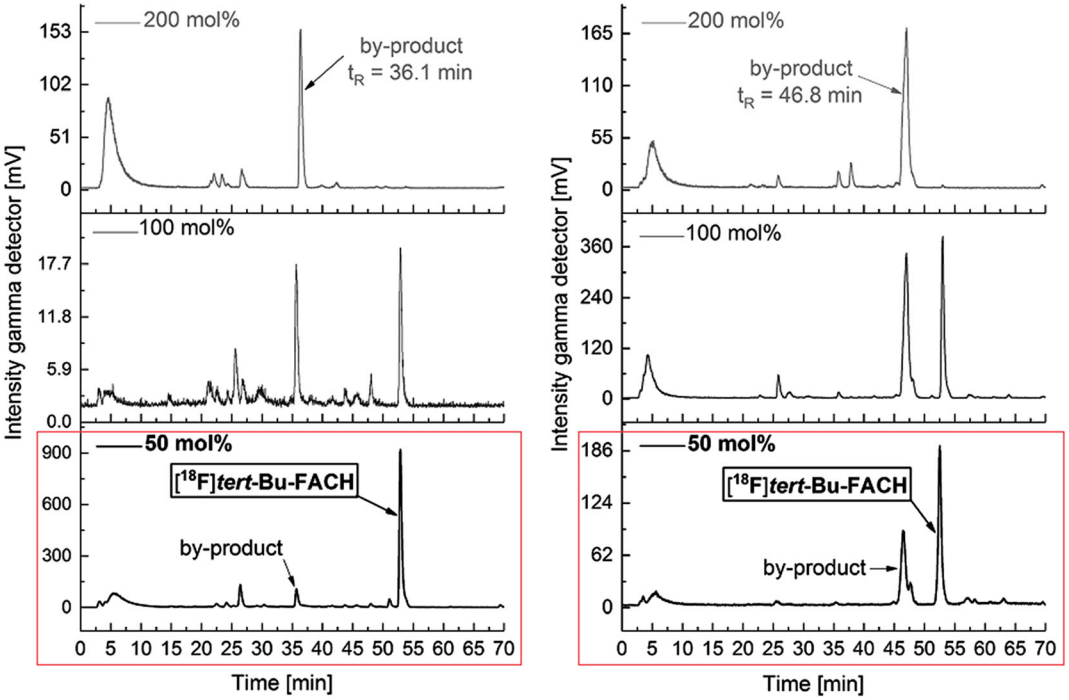

FIGURE 3 Representative radio-HPLC chromatograms showing the effect of different amounts of the K[^{18}F]F-$K_{2.2.2}$-carbonate complex on the radiochemical yields of [^{18}F]***tert*-Bu-FACH** in dimethylsulfoxide (DMSO) at 135°C (left) and acetonitrile (ACN) at 100°C (right); condition **A** was applied for HPLC measurements (see supporting infromation)

TABLE 2 Investigated parameters for the formation of [^{18}F]**FACH**

Entry	Solvent	Acid	Temperature, °C	Time, min	Radiochemical yield, %[a]
1	DMSO	HCl (2,6 N)	85, 100, 115	5, 10, 15, 20	0
2	DMSO	TFA	85	10, 20	0
3	ACN	HCl (2,6 N)	r.t., 40, 85	5, 10	0
4	ACN	TFA/H_2O	r.t., 40, 85	10, 15, 20	0
5	ACN	TFA	r.t., 40, 85	10, 15, 20	14.6 ± 6.4[b]
6	DCM	TFA	r.t., 40	10, 15, 20	26.7 ± 2.9[b]

Abbreviations: ACN, acetonitrile; DMSO, dimethylsulfoxide; TFA, trifluoroacetic acid.

[a]The radiochemical yields were determined based on radio-TLC and radio-HPLC analyses of the crude reaction mixture (n ≥ 3, non-isolated)

[b]Evaporation of TFA was needed before separation.

(Table 2, entry 5). When dry DCM was used instead of ACN, [^{18}F]**FACH** was synthesized with RCYs of 26.7 ± 2.9% based on radio-HPLC of the crude reaction mixture (n = 3). Higher RCYs could be obtained at room temperature indicating that milder conditions prevent the formation of side products. However, subsequent attempts to neutralize the reaction mixture by using saturated Na_2CO_3 or 2.0 N NaOH revealed the decomposition of [^{18}F]**FACH** resulting in the same by-products as observed in our initial deprotection experiments (Figure S5.1), thus supporting the assumption of the impact of water on the stability of [^{18}F]**FACH** in the crude reaction mixture.

3.2.2 | Radiosynthesis of [^{18}F]FACH using [^{18}F]TBAF

As an alternative radiosynthetic route for radiofluorination, tetrabutylammonium [^{18}F]fluoride ([^{18}F]TBAF) was used. First, the radiofluorination was investigated in a mixture of *tert*-BuOH and ACN (2:1) using 50 μL of tetrabutylammonium hydrogen carbonate (0.075 M, aqueous solution) and an aqueous solution of no-carrier-added [^{18}F]fluoride at a fixed concentration of the precursor **10** (2 mg, 4.4 μmol) at different temperatures. In comparison with the radiofluorination using the K[^{18}F]F-$K_{2.2.2}$-carbonate system, RCYs of about 80%

were obtained after 20 minutes at 100°C as determined via radio-TLC and radio-HPLC analyses (Figure 4A, n = 3). Interestingly, the formation of *(Z)*-[^{18}F]***tert*-Bu-FACH** was time- and temperature-dependent with the highest RCY of 27% at 110°C after 20 minutes based on the radio-HPLC of the crude reaction mixture (Figure 4A,B). Nevertheless, the occurrence of the undesired *Z*-isomer did not diminish the formation of the final product, because after deprotection with TFA only the more stable *E*-isomer of [^{18}F]**FACH** could be detected, as confirmed by coinjection of the nonradioactive reference compound **FACH** (Figure S5.2). The deprotection of *(E)/(Z)*-[^{18}F]***tert*-Bu-FACH** with TFA at room temperature afforded [^{18}F]**FACH** with RCYs of approximately 20%. Radio-HPLC analysis revealed an incomplete deprotection under these conditions as well as the formation of a new radioactive by-product, which might be a result of the presence of *tert*-BuOH in the crude mixture (Figure S5.2). Neither excess TFA nor longer reaction times promoted a complete deprotection of the intermediate [^{18}F]***tert*-Bu-FACH**.

Therefore, the possibility of implementing the radiofluorination in pure ACN was investigated. The radiofluorination in pure ACN rendered both isomers after 15 minutes at 100°C with only slightly decreased RCYs (63.3 ± 10.8% and 7.6 ± 4.0% for *E*- and *Z*-isomers [n = 11, nonisolated], respectively), compared with *tert*-BuOH/ACN (2:1) (71.9 ± 13.2% and 4.6 ± 2.0% for *E*- and *Z*-isomers [n = 4, nonisolated], respectively). Furthermore, no radioactive by-products were observed by deprotection of *(E)/(Z)*-[^{18}F]***tert*-Bu-FACH** with TFA in pure ACN at room temperature (Figure S5.3).

Upon completion of the reaction after 15 minutes, the excess TFA was neutralized with Et_3N. The radiotracer was isolated by semi-preparative RP-HPLC with 46% ACN/20 mM NH_4HCO_2 aq., pH 4 to 5 as eluent (Figure 5A). [^{18}F]**FACH** was then purified, concentrated via solid-phase extraction, and formulated in saline containing 10% (v/v) of EtOH for better solubility. Analytical radio-HPLC of the final product, co-eluted with the nonradioactive reference compound, confirmed the identity of the desired product (Figure 5B). At the end, [^{18}F]**FACH** was obtained with a RCY of 39.6 ± 8.3% (n = 10, end of bombardment (EOB)), high radiochemical purity (greater than 98%) and molar activities between 42 and 100 GBq/μmol (EOS), based on starting activities of 1 to 2 GBq.

3.2.3 | The effect of pH on the deprotonation of [^{18}F]FACH

Interestingly, during further radio-HPLC experiments, two species of [^{18}F]**FACH** were observed, which were corresponding to two species of the reference compound **FACH** observed under the same conditions (Figure 6). We therefore assumed that either deprotonation of the carboxylic acid group (Figure 6A) or photocatalytic *E* to *Z* isomerization[22] might be considered as possible mechanisms for the formation of these two forms. In order to investigate the hypothesis of an pH-dependent equilibrium between the two species of [^{18}F]**FACH**, a set of experiments was performed at which the pH value of the sample solutions was varied from 2.5 to 11.3. Only one HPLC signal was observed at pH values less than 5.5, which is probably related to the neutral form of [^{18}F]**FACH** (Figure 6B, left). When the pH values were higher than 6, a second HPLC signal at lower retention time was observed, which can be designated to the

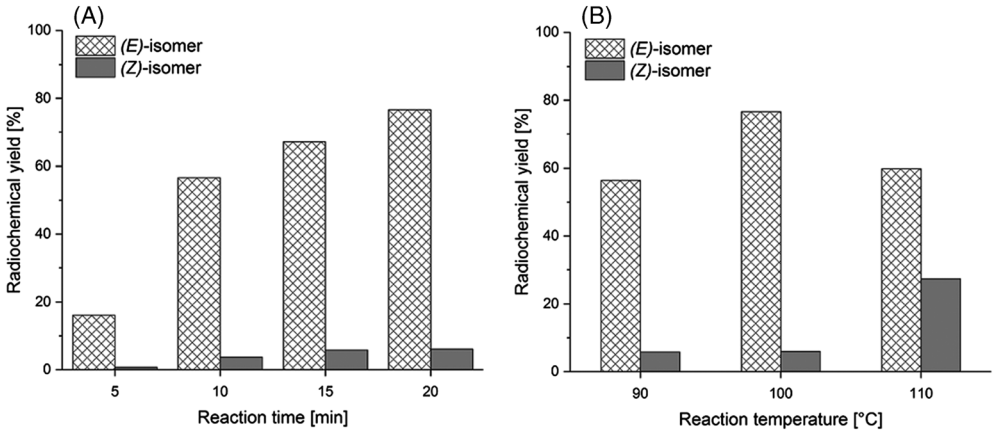

FIGURE 4 The effect of the reaction time and temperature on the radiochemical yields of *(E)- and (Z)*-[^{18}F]***tert*-Bu-FACH** in *tert*-BuOH/acetonitrile (ACN) (2:1): A, the reaction was accomplished at 100°C, and samples were taken at different time points; B, the reactions were carried out at different temperatures for 20 minutes (n = 2)

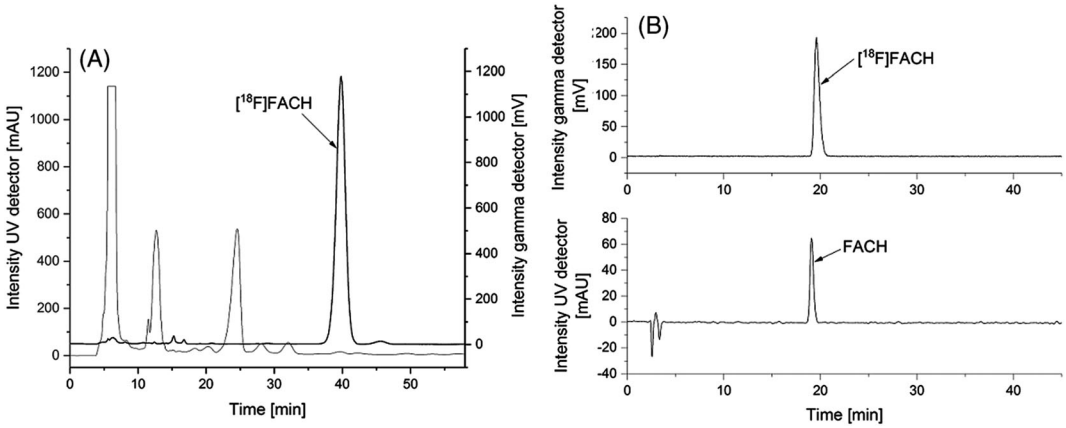

FIGURE 5 A, Representative semi-preparative radio- and UV-HPLC chromatograms of [^{18}F]**FACH** (conditions: Reprosil-Pur C18-AQ, 250 mm × 10 mm, 46% acetonitrile (ACN)/20 mM NH_4HCO_2 aq., pH = 4-5, flow: 3.5 mL/min); B, Representative analytical radio- and UV-HPLC chromatograms of [^{18}F]**FACH** co-eluted with the reference **FACH** (conditions: Reprosil-Pur C18-AQ, 250 mm × 4.6 mm, 46% ACN/20 mM NH_4HCO_2 aq., pH = 4-5, flow: 1.0 mL/min)

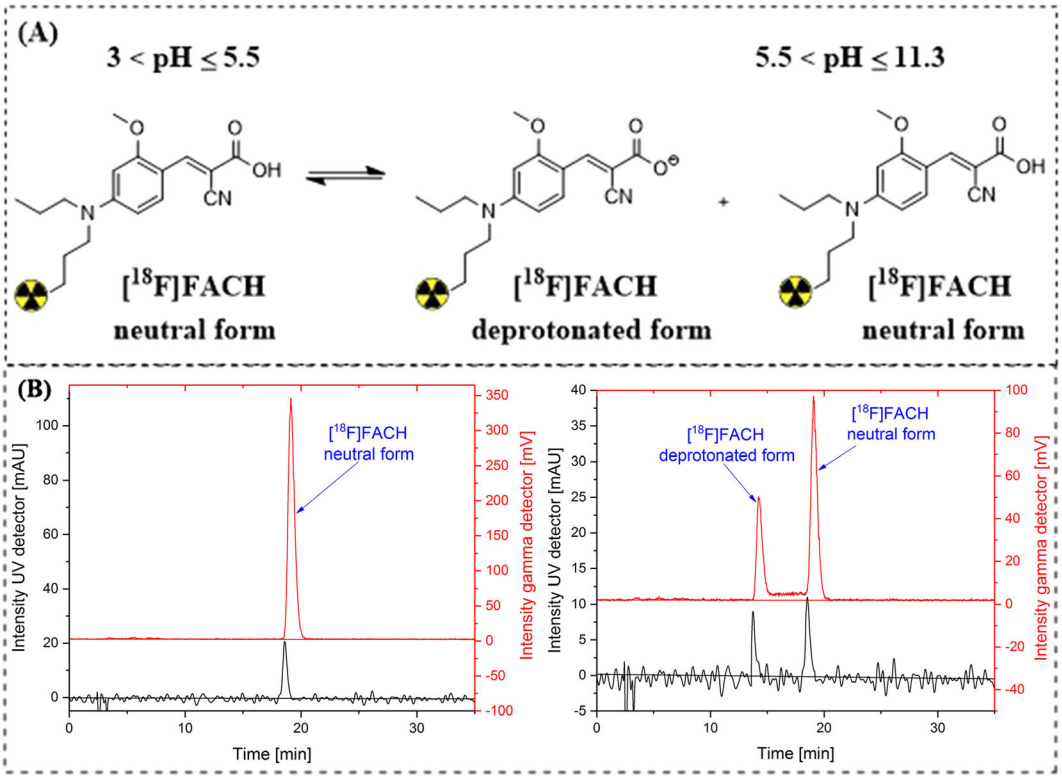

FIGURE 6 A, Proposed pH-dependent equilibrium between neutral and deprotonated forms of [^{18}F]**FACH**; B, Analytical radio- and UV-HPLC chromatograms represent two forms of [^{18}F]**FACH** at different pH (column: Reprosil-Pur C18-AQ, 250 × 4.6 mm, particle size: 5 μm; eluent: 46% ACN/20 mM NH_4HCO_2 aq., pH = 4-5; flow: 1 mL/min)

deprotonated form of [^{18}F]**FACH** (Figure 6B, right; Figure S5.4). Based on these findings, the possibility of photocatalytic *E* to *Z* isomerization was investigated by exposing sample solutions of [^{18}F]**FACH** and **FACH** at pH value of 5 to daylight. After a reasonable exposure time, the formation of a second species did not occur as proven by UV- and radio-HPLC analyses.

4 | CONCLUSIONS

The new fluorinated α-CHC derivative, **FACH**, showed high MCT1 and MCT4 inhibition comparable to the lead compound **I**, which made it suitable for the development of a novel ^{18}F-labeled radiotracer for PET imaging of MCTs. We herein investigated the use of the K[^{18}F]F-

$K_{2.2.2}$-carbonate complex and [^{18}F]TBAF as phase transfer catalysts for radiosynthesis of the intermediate [^{18}F]***tert*-Bu-FACH** and explored the influence of multiple reaction parameters to obtain [^{18}F]**FACH**. Our experiments revealed a base-sensitive behavior when using the conventional K[^{18}F]F-$K_{2.2.2}$-carbonate system as well as the formation of undesirable by-products during the deprotection step. By using the milder basic [^{18}F]TBAF system in ACN, the RCY of *(E)/(Z)*-[^{18}F]***tert*-Bu-FACH** was nearly doubled in comparison with the K[^{18}F]F-$K_{2.2.2}$-carbonate system. Moreover, [^{18}F]TBAF offered a relevant route for the radiosynthesis of [^{18}F]**FACH** via a two-step one-pot strategy. [^{18}F]**FACH** was finally obtained in high radiochemical yield and purity within a reliable and reproducible radiosynthesis route, which is intended to be translated to an automated module device for large-scale production of the radiotracer. This newly developed radiotracer is expected to enable PET investigations of solid tumors expressing MCTs.

ACKNOWLEDGEMENTS

The Alexander von Humboldt Foundation and the University of Minnesota Duluth are acknowledged for financial supports. We are thankful to Dr. Karsten Franke for providing [^{18}F]fluoride as well as Dr. Matthias Scheunemann for his scientific supports. We also thank the staff of the Institute of Analytical Chemistry, Department of Chemistry and Mineralogy of the University of Leipzig, for recording and processing the NMR and HR-MS spectra.

ORCID

Masoud Sadeghzadeh https://orcid.org/0000-0002-6844-6637

REFERENCES

1. Halestrap AP, Meredith D. The SLC16 gene family-from monocarboxylate transporters (MCTs) to aromatic amino acid transporters and beyond. *Pflugers Arch*. 2004;447(5):619-628.
2. Bröer S, Schneider H-P, Bröer A, Rahman B, Hamprecht B, Deitmer JW. Characterization of the monocarboxylate transporter 1 expressed in Xenopus laevis oocytes by changes in cytosolic pH. *Biochem J*. 1998;333(1):167-174.
3. Dimmer K-S, Friedrich B, Florian L, Deitmer JW, Bröer S. The low-affinity monocarboxylate transporter MCT4 is adapted to the export of lactate in highly glycolytic cells. *Biochem J*. 2000;350(1):219-227.
4. Fox JEM, Meredith D, Halestrap AP. Characterisation of human monocarboxylate transporter 4 substantiates its role in lactic acid efflux from skeletal muscle. *J Physiol*. 2000;529(2):285-293.
5. Ponizovskiy MR. Warburg effect mechanism as the target for theoretical substantiation of new possibility cancer disease treatment. *Crit Rev Eukaryot Gene Expr*. 2011;21(1):13-28.
6. Koppenol WH, Bounds PL, Dang CV. Otto Warburg's contributions to current concepts of cancer metabolism. *Nat Rev Cancer*. 2011;11(5):325-337.
7. Gurrapu S, Jonnalagadda SK, Alam MA, et al. Monocarboxylate transporter 1 inhibitors as potential anticancer agents. *ACS Med Chem Lett*. 2015;6(5):558-561.
8. Mereddy VR, Drewes LR, Alam MA, Jonnalagadda SK, Gurrapu S. Therapeutic compounds. Google Patents; 2016, US 9,296,728 B2.
9. Doherty JR, Yang C, Scott KE, et al. Blocking lactate export by inhibiting the Myc target MCT1 Disables glycolysis and glutathione synthesis. *Cancer Res*. 2013;74(3):908-920.
10. Fang J, Quinones QJ, Holman TL, et al. The H^+-linked monocarboxylate transporter (MCT1/SLC16A1): a potential therapeutic target for high-risk neuroblastoma. *Mol Pharmacol*. 2006;70(6):2108-2115.
11. Sanità P, Capulli M, Teti A, et al. Tumor-stroma metabolic relationship based on lactate shuttle can sustain prostate cancer progression. *BMC Cancer*. 2014;14(1):154-167.
12. Baek G, Tse Yan F, Hu Z, et al. MCT4 defines a glycolytic subtype of pancreatic cancer with poor prognosis and unique metabolic dependencies. *Cell Rep*. 2014;9(6):2233-2249.
13. Curry JM, Tuluc M, Whitaker-Menezes D, et al. Cancer metabolism, stemness and tumor recurrence: MCT1 and MCT4 are functional biomarkers of metabolic symbiosis in head and neck cancer. *Cell Cycle*. 2013;12(9):1371-1384.
14. Cairns RA, Harris IS, Mak TW. Regulation of cancer cell metabolism. *Nat Rev Cancer*. 2011;11(2):85-95.
15. Poole RC, Halestrap AP. Transport of lactate and other monocarboxylates across mammalian plasma membranes. *Am J Physiol-Cell Physiol*. 1993;264(4):C761-C782.
16. Meredith D, Christian H. The SLC16 monocaboxylate transporter family. *Xenobiotica*. 2008;38(7-8):1072-1106.
17. Murray CM, Hutchinson R, Bantick JR, et al. Monocarboxylate transporter MCT1 is a target for immunosuppression. *Nat Chem Biol*. 2005;1(7):371-376.
18. https://clinicaltrials.gov/ct2/show/NCT01791595.
19. Wang X, Levi A, Halestrap A. Substrate and inhibitor specificities of the monocarboxylate transporters of single rat heart cells. *Am J Physiol Heart Circ Physiol*. 1996;270(2):H476-H484.
20. Graham K, Müller A, Lehmann L, Koglin N, Dinkelborg L, Siebeneicher H. [^{18}F] Fluoropyruvate: radiosynthesis and initial biological evaluation. *J Label Compd Radiopharm*. 2014;57(3):164-171.
21. Van Hée VF, Labar D, Dehon G, et al. Radiosynthesis and validation of (±)-[^{18}F]-3-fluoro-2-hydroxypropionate ([^{18}F]-FLac) as a PET tracer of lactate to monitor MCT1-dependent lactate uptake in tumors. *Oncotarget*. 2017;8(15):24415-24428.
22. Tateishi H, Tsuji AB, Kato K, et al. Synthesis and evaluation of ^{11}C-labeled coumarin analog as an imaging probe for detecting monocarboxylate transporters expression. *Bioorg Med Chem Lett*. 2017;27(21):4893-4897.

23. Vilsmeier A, Haack A. Über die Einwirkung von Halogenphosphor auf Alkyl-formanilide. Eine neue Methode zur Darstellung sekundärer und tertiärer p-Alkylaminobenzaldehyde. *Eur J Inorg Chem*. 1927;60(1):119-122.
24. Gokel GW. In: Stoddart JF, ed. *Crown ethers and cryptands: monographs in supramolecular chemistry*. London: Royal Society of Chemistry; 1991:190.
25. Dehmlow EV, Dehmlow SS. *Phase transfer catalysis*. 499 Weinheim: Wiley-VCH; 1993.
26. Jacobson O, Kiesewetter DO, Chen X. Fluorine-18 radiochemistry, labeling strategies and synthetic routes. *Bioconjug Chem*. 2014;26(1):1-18.
27. Li S, Schmitz A, Lee H, Mach RH. Automation of the radiosynthesis of six different ^{18}F-labeled radiotracers on the AllinOne. *EJNMMI Radiopharm Chem*. 2017;1(1):15-33.
28. Wiemer J, Steinbach J, Pietzsch J, Mamat C. Preparation of a novel radiotracer targeting the EphB4 receptor via radiofluorination using spiro azetidinium salts as precursor. *J Label Compd Radiopharm*. 2017;60(10):489-498.
29. Pilcher AS, Ammon HL, DeShong P. Utilization of tetrabutylammonium triphenylsilyldifluoride as a fluoride source for nucleophilic fluorination. *J Am Chem Soc*. 1995;117(18):5166-5167.
30. Cox DP, Terpinski J, Lawrynowicz W. "Anhydrous" tetrabutylammonium fluoride: a mild but highly efficient source of nucleophilic fluoride ion. *J Org Chem*. 1984;49(17):3216-3219.

SUPPORTING INFORMATION

Additional supporting information may be found online in the Supporting Information section at the end of the article.

How to cite this article: Sadeghzadeh M, Moldovan R-P, Fischer S, et al. Development and radiosynthesis of the first ^{18}F-labeled inhibitor of monocarboxylate transporters (MCTs). *J Label Compd Radiopharm*. 2019;62:411–424. https://doi.org/10.1002/jlcr.3739

Development of Novel Silyl Cyanocinnamic Acid Derivatives as Metabolic Plasticity Inhibitors for Cancer Treatment

Grady L. Nelson, [1]

Conor T. Ronayne, [1]

Lucas N. Solano, [1]

Sravan K. Jonnalagadda, [1]

Shirisha Jonnalagadda, [1]

Jon Rumbley, [1,4]

Jon Holy, [1,3]

Teresa Rose-Hellekant, [1,3]

Lester R. Drewes, [1,3]

Venkatram R. Mereddy, [1✉,2,4]

Email vmereddy@d.umn.edu

[1] Integrated Biosciences Graduate Program, University of Minnesota, Duluth, MN, 55812 USA

[2] Department of Chemistry and Biochemistry, University of Minnesota Duluth, Duluth, MN, 55812 USA

[3] Department of Biomedical Sciences, Medical School Duluth, University of Minnesota, Duluth, MN, 55812 USA

[4] Department of Pharmacy Practice & Pharmaceutical Sciences, University of Minnesota, Duluth, MN, 55812 USA

Received: 9 August 2019 / Accepted: 14 November 2019

Abstract

Novel silyl cyanocinnamic acid derivatives have been synthesized and evaluated as potential anticancer agents. *In vitro* studies reveal that lead derivatives **2a** and **2b** have enhanced cancer cell proliferation inhibition properties when compared to the parent monocarboxylate transporter (MCT) inhibitor cyano-hydroxycinnamic acid (CHC). Further, candidate compounds exhibit several-fold more potent MCT1 inhibition properties as determined by lactate-uptake studies, and these studies are supported by MCT homology modeling and computational inhibitor-docking studies. *In vitro* effects on glycolysis and mitochondrial metabolism also illustrate that the lead derivatives **2a** and **2b** lead to significant effects on both metabolic pathways. *In vivo* systemic toxicity and efficacy studies in colorectal cancer cell WiDr tumor xenograft demonstrate that candidate compounds are well tolerated and exhibit good single agent anticancer efficacy properties.

Introduction

Tumor growth requires increased energetic and biosynthetic demands in a microenvironment that typically varies in oxygen and nutrient distribution due to differences in tumor cell proximity to blood vessels[1, 2]. A common strategy employed by malignant cells to deal with these conditions involves reprogramming

their metabolism toward aerobic glycolysis (Warburg Effect)[3, 4, 5, 6]. This molecular reprogramming is a critical hallmark of solid tumors and is an important target for cancer treatment[1, 2, 3, 4, 5, 6].

AQ1

AQ2

AQ3

AQ4

Increased glycolysis results in the generation of byproducts such as lactic acid leading to an initial decrease in the internal pH; compensated by the elevated expression of monocarboxylate transporters (MCTs) and other transporters that efflux the acidic components and decrease the external pH[7, 8]. Interestingly, it has been recently shown that extracellular lactate can be taken up by MCTs in neighboring proliferating cancer cells (Reverse Warburg Effect) and utilized in the mitochondrial TCA cycle and oxidative phosphorylation (OxPhos)[9, 10, 11, 12]. Exchanges between anabolic and catabolic compartments facilitate tumor growth and have also been shown to promote resistance to chemo- and radiation therapies[13]. These metabolic specializations are distinct from normal cells and the resulting upregulation of numerous glycolytic enzymes and transporters provide an opportunity for pharmacological intervention[12, 14]. Similar to glycolysis, mitochondrial OxPhos also plays an integral part in ATP production and contributes to the biosynthetic demands of rapidly proliferating cancer cells. Depending on nutrient availability, tumor cells can develop metabolic plasticity switching between glycolysis and OxPhos or exhibit an intermediate phenotype to maximize their chances of survival[12, 14].

AQ5

Metabolic plasticity is responsible for maintaining energetic homeostasis and to facilitate this plasticity, cancer cells increase the expression of MCTs. MCTs regulate the transport of lactate, pyruvate as well as other ketone bodies to support the metabolic demands in cancer cells[15, 16]. Specifically, MCTs 1 and 4 are the primary transporters involved in transporting glycolytic by-products in and out of the cells, respectively; supplying oxidative cells with TCA metabolites, and circumventing a rapid decrease in intracellular pH[12, 16, 17]. MCT1 and 4 overexpression is a hallmark of cancer progression and provides a promising target for chemotherapeutics and recent studies have shown that targeting these transporters effectively reduces the rate of tumor progression *in vivo*[18, 19, 20, 21, 22, 23, 24, 25].

The small molecule α-cyano-4-hydroxycinnamic acid (CHC, **1**) has been traditionally used as an MCT inhibitor for studying cellular and biochemical functions[26]. CHC and related α-cyanocinnamic acids have also been shown to inhibit the mitochondrial pyruvate carrier, an important molecular shuttle of pyruvate in the inner mitochondrial membrane to support TCA cycle and OxPhos[27]. However, the therapeutic potential of CHC is hindered by its lack of efficacy at low concentrations and high dose requirement for significant anticancer efficacy *in vivo*. Therefore, increasing the efficacy of CHC-based compounds to simultaneously target TCA cycle and OxPhos constitute novel chemotherapeutic strategy.

In this regard, we have replaced the 4-hydroxy group in CHC with N,N-dialkyl/aryl groups that has resulted in low nanomolar potency towards lactate uptake in both MCT1 and MCT4 expressing cell lines[18, 20]. Similarly, N,N-dialkyl carboxy coumarins were also found by us[19] and others[21] to be highly potent toward lactate uptake inhibition in MCT1 expressing cells. Although our first generation N,N-dialkyl/aryl CHC compounds are highly potent inhibitors, but *in vivo* efficacy studies required high doses (~50 mg/kg) for significant tumor growth inhibition in MCT1 expressing WiDr and MCT4 expressing MDA-MB-231 tumor models. *In vivo* pharmacokinetic analysis indicated that these compounds

are rapidly eliminated with biological half-lives of <1 hr[18]. We attribute this to unsubstituted N,N-diphenyl groups and N,N-dialkyl groups which are metabolically vulnerable to CYP450 enzymatic action and subsequent elimination.

Silyl structural units such as *tert*-butyldiphenylsilyl (TBDPS) and *tert*-butyldimethylsilyl (TBS) ethers have long been used as hydroxyl protecting groups in organic chemistry due to the flexibility and stability under different pH conditions[28, 29]. Recently, silyl ethers have been investigated as pharmacological tools due to their lipophilicity and high metabolic stability when administered *in vivo*[30]. Diverse functionality on the silicon atom results in varying metabolic and chemical stability, and the sterically hindered TBDPS group exhibits the highest stability[28, 29]. Hence, we envisioned that introduction of an acid stable TBDPS ether on CHC phenolic hydroxyl group would increase its lipophilicity, metabolic stability, and ability to influence mitochondrial function while also retaining MCT inhibitory characteristics. In this regard, we synthesized and evaluated novel silyl-CHC compounds for their *in vitro* MCT1 inhibitory properties, *in vitro* effects on cancer cell proliferation and metabolism, and *in vivo* safety and efficacy in a WiDr tumor xenograft model. The lead candidate compounds exhibited enhanced MCT1 and cancer cell proliferation inhibition properties, led to glycolysis and mitochondrial dysfunction, and showed significant *in vivo* tumor growth inhibitions.

Results

Synthesis of silylated CHCs **2a** and **2b** and un-silylated CHCs **2c** and **2d**

To understand the biological effects of silyl substitution on the CHC template, two representative derivatives **2a** and **2b** were synthesized (Supp. Info Fig. S1). The derivative **2a** is a silyl group containing TBDPS attached directly to CHC (TBDPS-CHC, Fig. 1). The derivative **2b** is also a silyl group containing TBDPS, which contains a 2-carbon spacer ethyl group (Ex-TBDPS-CHC, Fig. 1). The compounds **2c** (Ex-OH-CHC) and **2d** (Ex-Br-CHC) were synthesized as non-silylated analogs of extended derivative **2b** to demonstrate the importance of the silyl groups in providing biological activity (Fig. 1). The derivative **2c** contains polar hydroxy substitution whereas **2d** is a non-polar halogenated homolog of **2b**. The biological effects of parent compound CHC **1** and the four synthetic derivatives **2a–d** were then evaluated.

Figure 1

Structures of CHC **1**, silylated and non-silylated CHC derivatives **2a–d**

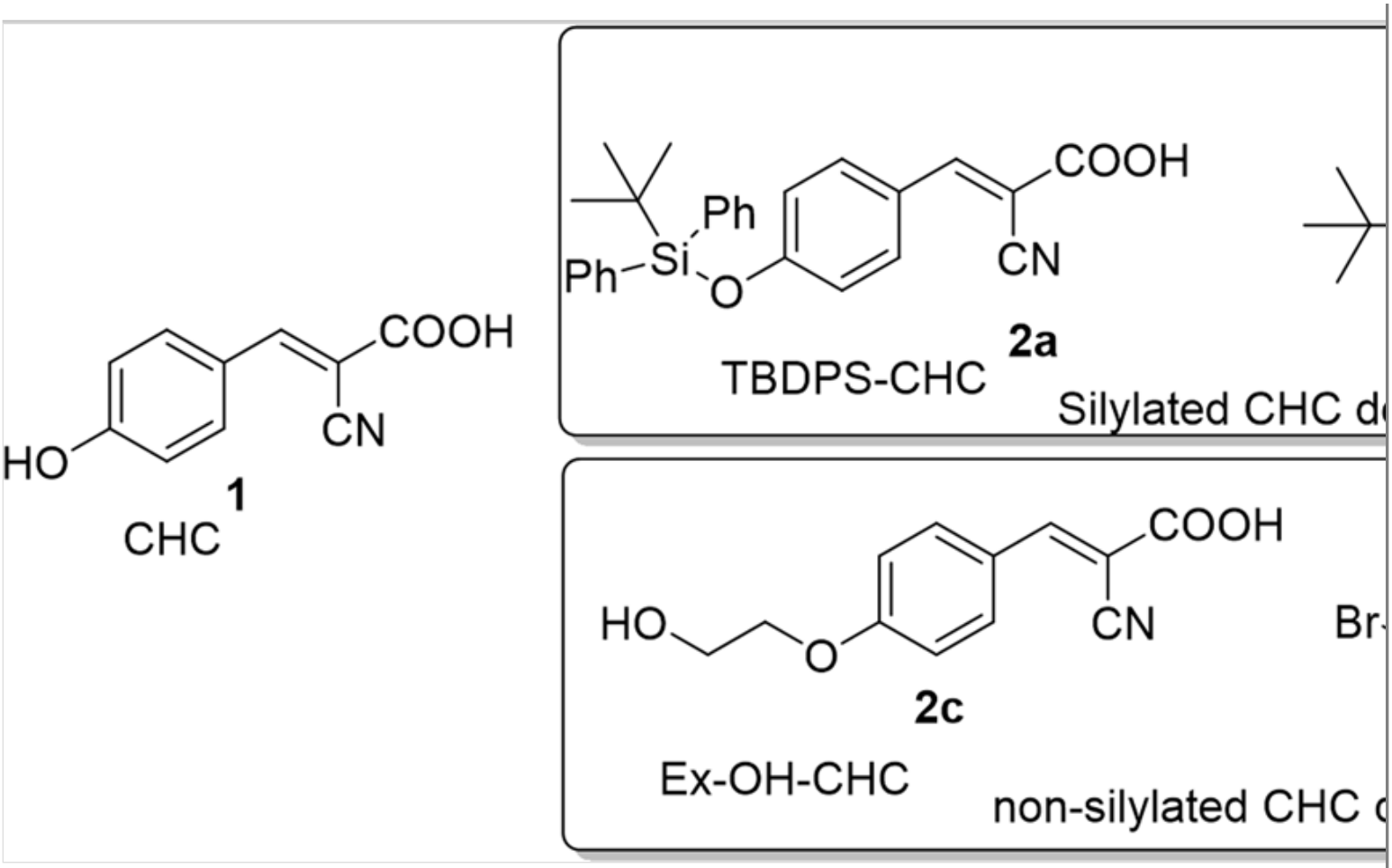

In vitro cell proliferation inhibition studies of **2a–2d**

Cell proliferation inhibition properties of candidate compounds **2a–2d** were evaluated using MTT assays on multiple cell lines. Compounds **2a** and **2b** showed highly improved cell proliferation inhibition properties with IC_{50} values of 6–93 μM compared to CHC's IC_{50} values of 1100–5300 μM in all the cell lines tested (Table 1 and Fig. 2A–D). The non-silicon CHC derivatives **2c** and **2d** did not show significant cell proliferation inhibition at concentrations up to 500 μM. Due to solubility limitations above this concentration (0.1% DMSO in growth media), the IC_{50} values of **2c** and **2d** were not determined.

Table 1

MTT IC_{50} (μM) values of CHC derivatives **2a–d** in MCF7, 4T1, WiDr, and MDA-MB-231 cell lines.

Compound	MDA-MB-231	4T1	MCF7	WiDr
CHC **1**	5300 ± 130	3600 ± 300	4000 ± 130	1100 ± 96
TBDPS-CHC **2a**	93 ± 0	56 ± 1	39 ± 3	41 ± 2
Ex-TBDPS-CHC **2b**	71 ± 1	22 ± 1	35 ± 3	6 ± 1
Ex-OH-CHC **2c**	>500	>500	>500	>500
Ex-Br-CHC **2d**	>500	>500	>500	>500
*Average ± SEM of three separate experiments.				

Figure 2

MTT cell proliferation and MCT1 inhibition IC_{50} values of candidate compounds: (**A**–**D**) represent MTT IC_{50} values in (**A**) MCF7, (**B**) 4T1, (**C**) WiDr, and (**D**) MDA-MB-231 cell lines. (**E**–**G**) represent L-[^{14}C]-lactate uptake study of (**E**) compound **2a** and (**F**) compound **2b**. (**G**) MCT1 IC_{50} of compounds **2a** and **2b** in MCT1 expressing RBE4 cell line. The average ± sem of minimum three independent experimental values were calculated. Repeated measures one-way ANOVA was used to calculate statistical significance (****P < 0.0001) between test compounds and CHC.

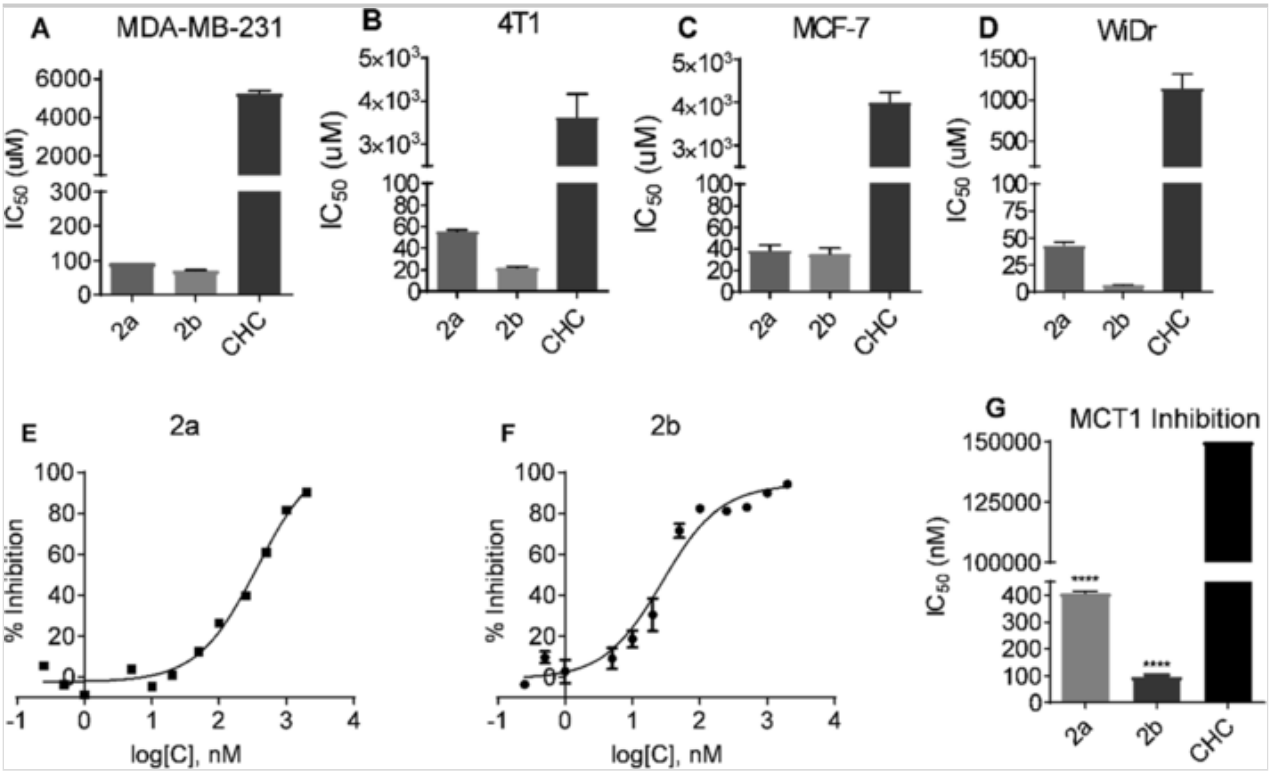

In vitro MCT1 Inhibition Assay with **2a–2d**

The silylated candidate compounds **2a** and **2b** were next evaluated for *in vitro* MCT1 transport inhibition properties using an L-[^{14}C]-lactate study on the MCT1 expressing RBE4 cell line as reported previously[18, 19, 20]. Both compounds **2a** and **2b** showed potent MCT1 inhibition with IC_{50} values 408 and 97 nM, respectively (Table 2, Fig. 2E–G). The parent CHC **1** exhibits weaker MCT1 inhibition properties with IC_{50} values > 150000 nM concentration. Non-silylated candidates **2c** and **2d** did not exhibit MCT1 inhibition properties at the concentrations tested (Table 2).

Table 2

MCT1 IC_{50} (nM) values of CHC derivatives **2a**–**d**.

Compound	MCT1
CHC **1**	>150000
TBDPS-CHC **2a**	408 ± 5

*Average ± SEM of three separate experiments.

Compound	MCT1
Ex-TBDPS-CHC **2b**	97 ± 7
Ex-OH-CHC **2c**	>5000
Ex-Br-CHC **2d**	>5000
*Average ± SEM of three separate experiments.	

Homology modeling of and computational inhibitor docking to human MCT1

To understand the potential molecular interactions of candidate inhibitors **2a** and **2b** with MCT1, homology modeling and computational docking studies were performed (Fig. 3). Five independent models of inward-open MCT1 were generated based on the human inward-open GLUT1 structure, PDB: 5eqi[31]. Due to the low sequence homology between human MCT1 and human GLUT1 (29%), consensus alignments were generated with the inclusion of additional major facilitator superfamily members and transmembrane regions were predicted by consensus topology prediction. This led to a final adjusted template and target sequence alignment for model generation. Although all models were minimized by the default optimization and molecular dynamics refinement, significant side chain rotamer variation was observed. One model was selected for further analysis based on an evaluation of the protein energy score within MODELLER and charged residue rotamer orientation in the transmembrane spans, avoiding exposure of charged residues to the putative lipid bilayer[32]. The resulting human MCT1 structure was compared to a previously reported rat MCT1 homology model also generated in an inward-open conformation but based on an *E. coli* glycerol-3-phosphate transporter (GlpT) template[33]. Overall, the registration of the transmembrane domains was remarkably similar with some residues showing a quarter to a half helical turn positioning difference and, of course, side chain rotamer differences were observed. We analyzed the residues involved in inhibitor binding between our inward-open human MCT1 structure and candidate inhibitors **2a** and **2b** (Fig. 3). These inhibitors showed much more robust inhibition of MCT1 *in vitro*, higher cell proliferation inhibition and increased ability to reduce tumor burden compared to the parent CHC or non-silylated-compounds.

Figure 3

Top docking pose of candidate compounds **2a** and **2b** to homology modelled human MCT1. (**A**) Relative binding pocket of compounds **2a** (yellow) and **2b** (green) docked to human MCT1, tan and light blue respectively. Electrostatic binding surface within 4.5 Å of the inhibitors is shown. (**B**) All MCT1 residues within 4.5 Å of docked compounds **2a** (yellow) and **2b** (green). (**C**) Electrostatic surface interactions of **2a** (yellow) and **2b** (green) with human MCT, orange to red represent increasing partial negative charge while green to blue represent increasing partial positive charge and yellow is a neutral protein surface. (**D**) Overlay of top binding poses of compound **2a** (yellow) and **2b** (green) in two orientations.

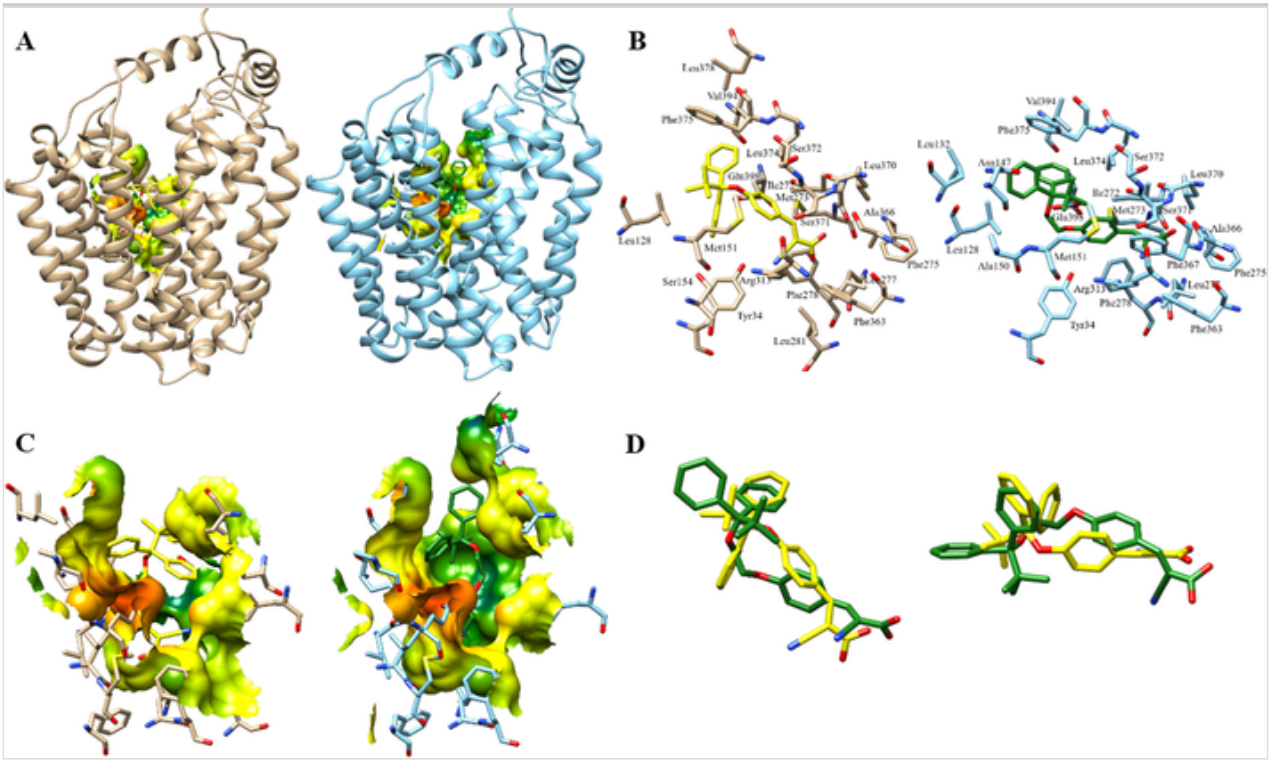

Inhibitor docking to the inward-open human MCT1 homology model was carried out in Autodock Vina[34]. In order to achieve an unbiased ligand/inhibitor binding pocket search our inspection area included the entire transmembrane spanning region and extended beyond the inward-open aqueous surface of the protein. The silicon atom in **2a** and **2b** was reverted to carbon *in silico* to enable docking, resulting in a bond length change of −0.32 Å from Si-C to C-C. The structural geometries experienced no change and the overall volume change was insignificant within the respective binding poses. The best ranked docking poses of inhibitors **2a** and **2b** to MCT1 were determined to be structurally similar (Fig. 3A–D). Both compounds were found to be surrounded by several aliphatic and aromatic side chains. Contact surfaces revealed subtle differences but some of the missing surfaces in **2a** bound MCT1 are attributed to the chosen 4.5 Å cutoff and are restored at 4.6 Å+ (Fig. 3C). All amino acids contacting (<4.5 Å away, including hydrogens) either **2a** or **2b** and their positioning in the putative MCT1 binding site can be seen in Fig. 3B. Some unique contacts appearing in either **2a** or **2b** are likely due to rotamer differences between the two structures, but the extended compound (Ex-TBDPS-CHC, **2b**) does uniquely reach residues Leu132, Asn147 and Ala150 in the extended binding pocket. Within the collection of poses of the two candidate compounds occupying this site there are better matched **2a** and **2b** overlays but at the expense of significant estimated binding free energy loss (Fig. 3D). The binding affinity of the top binding pose of **2a** was estimated to be −9.2 kcal/mol for inward-open MCT1 and −9.8 kcal/mol for **2b**. In contrast, the estimated binding affinity of parent compound CHC for MCT1 was −6.4 kcal/mol for the same binding site occupancy. This difference in estimated binding affinities of CHC and candidate compounds to MCT1 equates to an approximately 160-fold higher affinity of the candidate compounds for the inward-open MCT1 homology model, consistent with experimental observation. Further, of the top 20 binding poses determined for **2a** binding to MCT1, 11 of 20 occupied the same structural binding site with minimal RMSD changes (<2 Å) while 5 of 20 poses of **2b** occupied the same MCT1 site. Conversely, only 2 of 20 poses for parent compound CHC binding to MCT1 were structurally similar to the optimal candidate compound binding site. This observation can be thought of as a surrogate for binding specificity, again consistent with experimentally determined binding affinities.

ATP production by glycolysis and mitochondrial respiration pathways

We then carried out the effects of candidate compounds **2a** and **2b** on glycolysis and mitochondrial respiration pathways. To first characterize relative rates of ATP production from glycolysis and mitochondrial OxPhos in each cell line, an ATP rate assay was performed. Understanding basal levels of ATP production from each respective pathway is important in interpreting differential compound effects between WiDr and MDA-MB-231 cell lines. Here, it was observed that the MCT4 expressing MDA-MB-231 cell line was highly glycolytic in nature (75% glycolysis: 25% OxPhos) and the MCT1 expressing WiDr cell line equally shared ATP production between both pathways (51% glycolysis: 49% OxPhos) (Fig. 4A).

Figure 4

Glycolysis stress test of compounds **2a** and **2b** at 30 μM. (**A**) ATP rate assay of MDA-MB-231 and WiDr with respect to mitochondrial and glycolytic preference. Note higher percentage of mitochondrial respiration in WiDr when compared to MDA-MB-231 cell line. (**B,C**) represent glycolysis stress test profile of compounds **2a** and **2b** in (**B**) MCT1 expressing WiDr cell line, and (**C**) MCT4 expressing MDA-MB-231 cell line. Untreated cells were sequentially exposed first to test compound **2a** or **2b** (Inh) followed by glucose (Glu), oligomycin (Oli), and 2-deoxyglucose (2-DG). (**D**–**F**) represent the ECAR values of (**D**) glycolysis, (**E**) glycolytic capacity, and (**F**) glycolytic reserve in WiDr and MDA-MB-231 cell lines. The average + SEM values of three or more individual experiments were calculated. Repeated measures one-way ANOVA was used to calculate statistical significance (**P < 0.01, ****P < 0.0001) between test compounds and DMSO control (n = 3).

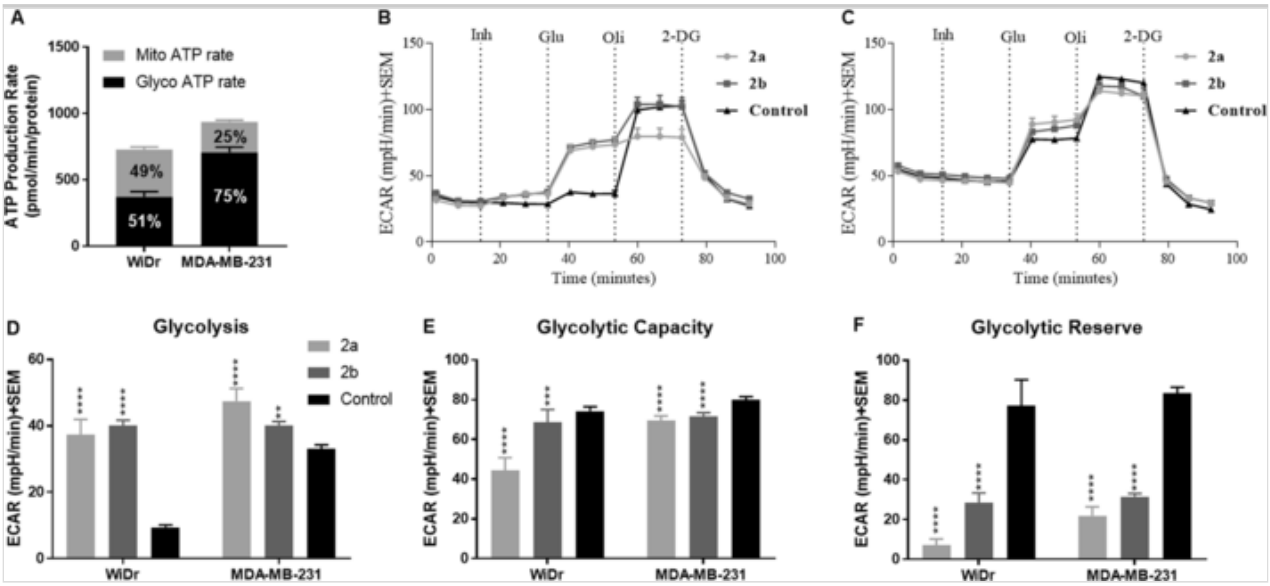

Evaluation of metabolic pathway profile of **2a** and **2b** using Seahorse XFe96® assays

Encouraged by significant cell proliferation inhibition and potent MCT1 inhibition properties of TBDPS-CHC **2a** and Ex-TBDPS-CHC **2b**, we evaluated these candidate compounds for their effect on metabolic profiles *in vitro* using a Seahorse XFe96® analyzer. Due to potential disruption in the flux of metabolically important lactate, both candidates were subjected to widely employed *Seahorse XFe96*® based glycolysis and mitochondrial stress tests in MCT1 expressing WiDr and MCT4 expressing MDA-MB-231 cell lines.

Glycolysis stress test

Candidate compounds **2a** and **2b** were evaluated for their effect on glycolysis, glycolytic capacity and glycolytic reserve. This assay measures extracellular acidification rate (ECAR) which is directly correlated with the rate of glycolysis. The ECAR for both cell lines in the presence of the test compounds can be seen above (Fig. 4B,C). In this assay, cells were initially starved of glucose to reduce their ECAR. Upon addition of glucose, a rise in ECAR was observed proportional to the rate of glycolysis in each cell line. An increase in basal levels of glycolysis in cells treated with test compounds compared to the controls represents a shift toward dependency on glycolysis for ATP production. Treatment with test compounds **2a** and **2b** in both WiDr and MDA-MB-231 cells significantly increased the basal glycolysis, with a more substantial increase in WiDr (Fig. 4D). It also was observed that WiDr control cultures exhibited a nearly three-fold decreased basal glycolysis when compared to MDA-MB-231 (Fig. 4D). Glycolytic capacity is the maximum rate of glycolysis the cell can attain in the absence of OxPhos as an ATP source. Both compounds **2a** and **2b** significantly reduced the glycolytic capacity in WiDr and MDA-MB-231 (Fig. 4E). The glycolytic reserve is the ability of cells to increase glycolysis when OxPhos ATP production is inhibited by oligomycin A. Here, we observed a significant decrease in the glycolytic reserve in both cell lines when treated with compound **2a** and **2b** (Fig. 4F).

Mitochondrial stress test

To assess mitochondrial stress, four parameters including maximal respiration, proton leak, ATP production, and spare respiratory capacity were measured. ATP production via OxPhos is dependent on mitochondrial integrity and can be measured directly via the oxygen consumption rate (OCR). Time-course OCR plots from WiDr and MDA-MB-231 cells were used to calculate **2a** and **2b** treatment-induced changes in specified parameters following the addition of various mitochondrial targeting agents (Fig. 5A,B). Compounds **2a** and **2b** induced significant mitochondrial stress in both WiDr and MDA-MB-231 cell lines. The FCCP induced maximal respiration was significantly decreased in both treated cell lines indicating that compounds **2a** and **2b** inhibit the cells ability to meet increased oxygen demands to retain a mitochondrial proton gradient (Fig. 5C). There was also a significant increase in proton leak, indicative of mitochondrial damage by **2a** and **2b** (Fig. 5D). Furthermore, oxygen consumption for mitochondrial ATP production was significantly decreased in both cell lines (Fig. 5E). Spare respiratory capacity is a value that is not directly linked to mitochondrial damage but represents the cells ability to respond to rapid ATP demands. WiDr and MDA-MB-231 cells exhibited a significant decrease in the spare respiratory capacity in the presence of test compounds (Fig. 5F).

Figure 5

Mitochondrial stress test of compounds **2a** and **2b** at 30 μM. (**A,B**) Represent mitochondrial stress test profile of compounds **2a** and **2b** in (**A**) MCT1 expressing WiDr cell line, and (**B**) MCT4 expressing MDA-MB-231 cell line. Untreated cells were sequentially exposed first to test compound **2a** or **2b** (Inh), followed by oligomycin (Oli), trifluoromethoxy carbonylcyanide phenylhydrazone (FCCP), and rotenone + antimycin a (R + AA). (**C**–**F**) Represent the OCR values of (**C**) maximal respiration, (**D**) proton leak, (**E**) ATP production and (**F**) spare respiratory capacity in WiDr and MDA-MB-231 cell lines. The average + SEM values of three or more individual experiments were calculated. Repeated measures one-way ANOVA was used to calculate statistical significance (*$P < 0.05$, **P < 0.01, ***P < 0.001, ****P < 0.0001) between test compounds and DMSO control (n = 3).

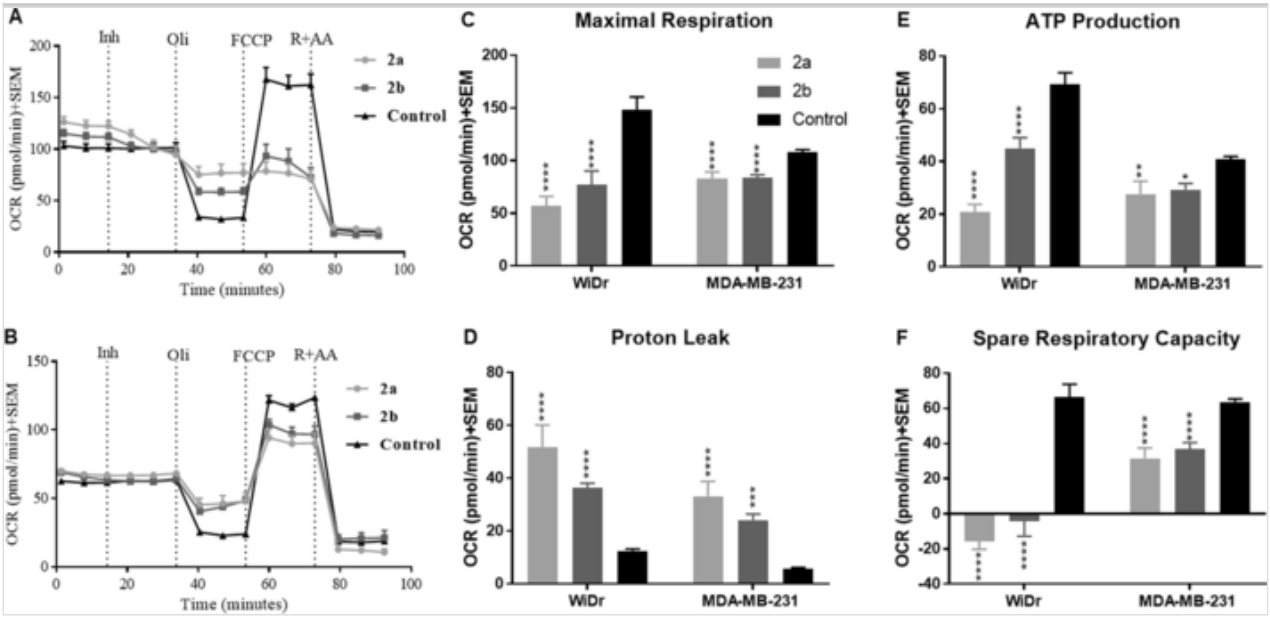

Fluorescent microscopy

To evaluate the effects on mitochondrial morphology and vitality, Mitotracker Red CMXROS (MTR) fluorescence imaging experiments were employed. Control WiDr and MDA-MB-231 cultures displayed well-defined MTR-positive mitochondria (Fig. 6). Cells treated with **2a**, however, exhibited a more diffuse and dim general cytoplasmic fluorescence, suggesting loss of MTR from mitochondria. Furthermore, differential interference contrast (DIC) microscope images illustrate substantial membrane blebbing and vesiculation in compound treated cultures (Fig. 6).

Figure 6

Fluorescent MTR microscopy of (**A**) MDA-MB-231 and (**B**) WiDr cells after 24-hour exposure to 30 µM compound **2a** and **2b**. All images were captured using the same magnification (see scale bar, 25 µm). Note compound **2a** resulted in substantial redistribution of MTR. Images were selected as representative of overall culture appearances.

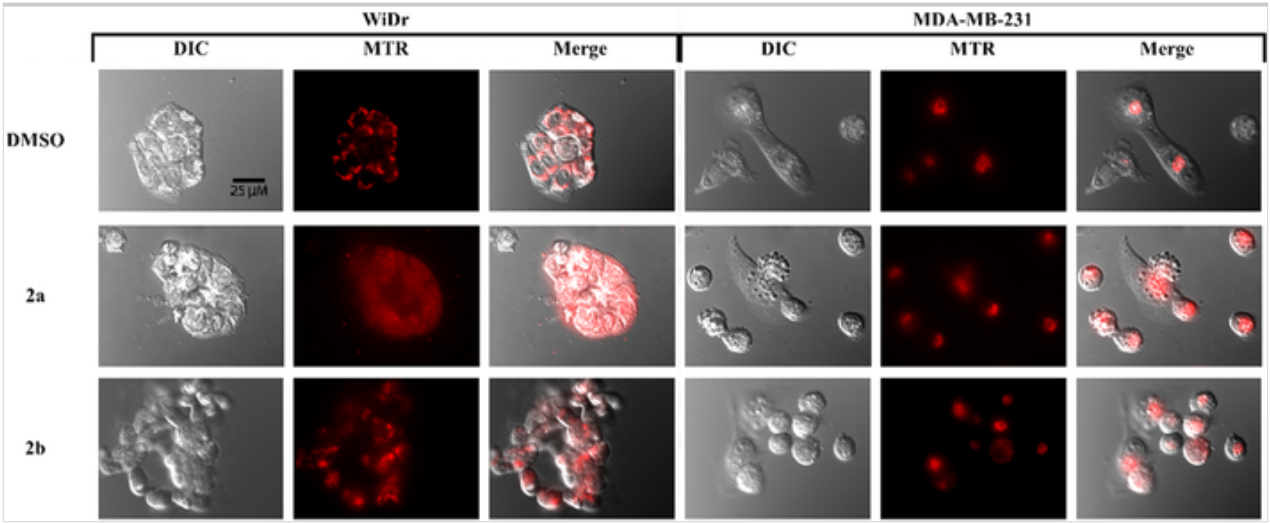

Western blot analysis

Owing to the enhanced antiproliferative effects induced by test compound **2a** when compared to CHC, western blot analysis of cell damage and death markers was performed. The master transcription factor p53 regulates the expression of numerous genes involved in cancer progression and is responsible for balancing proliferation and apoptosis[35]. In this regard, we evaluated the effects of compound treatment on p53 expression. Literature reports indicate that MDA-MB-231 and WiDr cells express distinct homozygous mutant forms of p53 that promote an aggressive malignant phenotype with resistance to apoptosis[36, 37]. In these studies, we observed that treatment with **2a** induced an increase in p53 expression in MDA-MB-231 cells but not in WiDr (Fig. 7A). Further, PARP1 is involved in the DNA repair pathway through sensing DNA-strand breaks and recruiting repair enzymes[38]. Importantly, PARP1 is a target of caspase cleavage under apoptotic conditions, and the appearance of the PARP1 cleavage product is a widely used indicator of cellular apoptosis. Here, we observed that 100 μM compound **2a** induced PARP1 cleavage in both WiDr and MDA-MB-231 cell lines, strongly suggesting the activation of apoptotic cell death pathways in treated cultures (Fig. 7A). Additionally, DNA damage may be a downstream effect of apoptotic nuclease activity or an increase in reactive oxygen species (ROS) from damaged mitochondria; as illustrated in microscopy and seahorse experiments. Histone 2AX phosphorylation (γH2AX) resulting from DNA single- and double-strand breaks is a widely employed marker for DNA damage[39]. In this regard, we investigated the effect of **2a** on DNA damage marker γH2AX (phosphorylated Ser139, histone H2AX) with a phospho-specific antibody. Treatment with **2a** (100 μM) led to substantial increases in the expression of γH2AX in both WiDr and MDA-MB-231 cell lines (Fig. 7A). Due to the potential of ROS leading to DNA damage and H2AX phosphorylation, we investigated the ability of antioxidant N-acetyl cysteine (NAC) to inhibit DNA damage of compound **2a** as evidenced by H2AX phosphorylation in the highly oxidative cell line WiDr (Fig. 4A). In these studies, we found that **2a-**induced H2AX activation was significantly reduced in cultures treated with NAC (Fig. 7B,C). However, NAC did not reverse PARP1 cleavage in treated cultures (Fig. 7B).

Figure 7

(**A**) Treatment with **2a** (DPS) for 24 hours induced PARP1 cleavage and histone H2AX phosphorylation in WiDr and MDA-MB-231 cells indicative of apoptosis and DNA damage. Further, treatment with **2a** lead to an increase in p53 expression in MDA-MB-231 cells in a dose dependent manner. (**B**) Treatment with the radical scavenger N-acetyl cysteine (NAC) reversed H2AX phosphorylation but not PARP1 cleavage in WiDr cells. (**C**) Densitometry analysis of γ-H2AX when compared to GAPDH as a loading control. Representative western blots of three independent experiments, and are cropped from the full-length images. Full-length blots can be found in the supplementary information, Figs. S2–S4. Repeated measures one-way ANOVA was used to calculate statistical significance (****$P < 0.0001$).

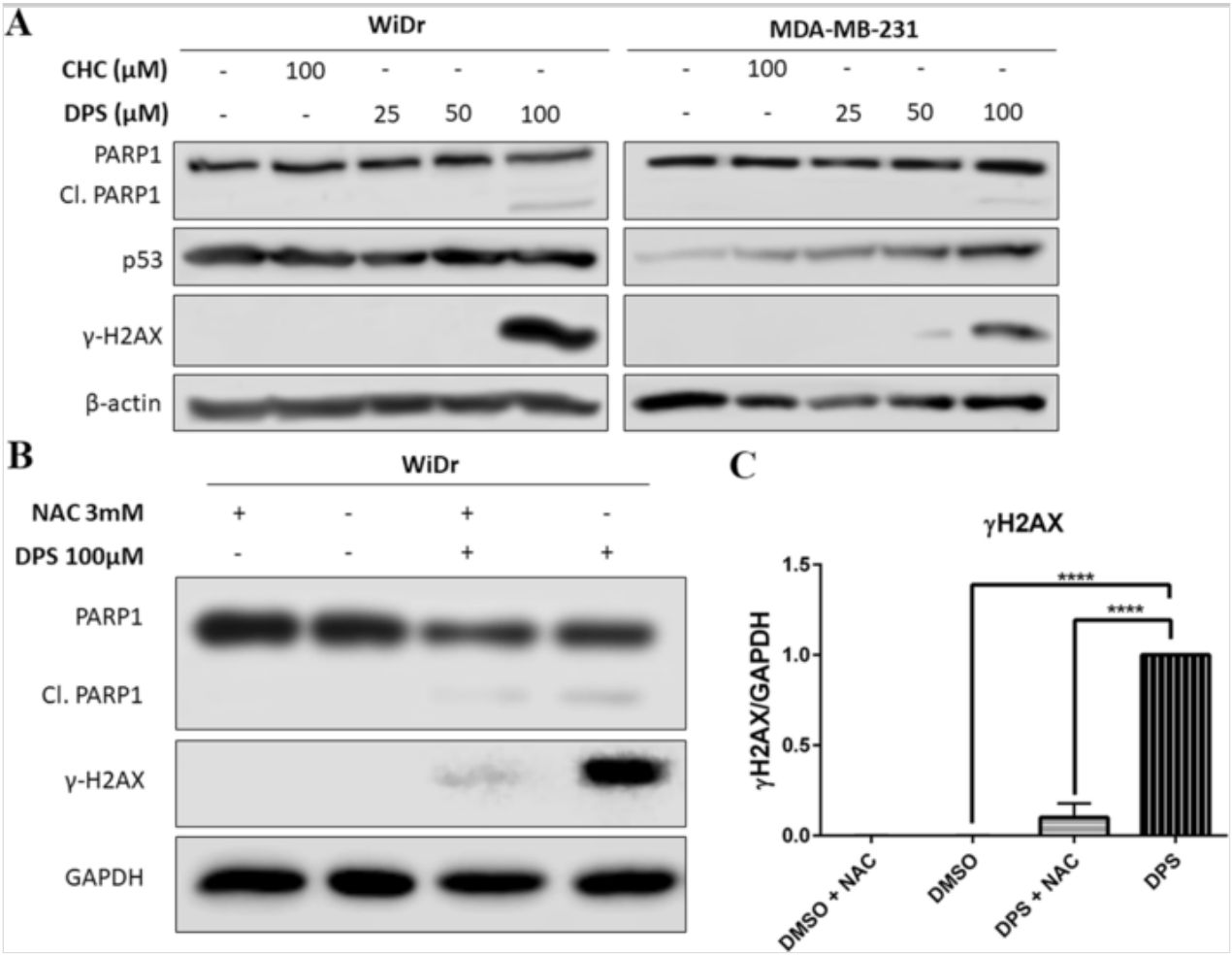

In vivo efficacy studies of MCT1 expressing WiDr tumor xenograft model

Based on *in vitro* cell proliferation inhibition, MCT1 inhibition, and effects on glycolysis/mitochondrial function, we advanced candidate compounds **2a** and **2b** for translational *in vivo* safety and efficacy studies. In this regard we first evaluated the systemic toxicity of candidate compounds in healthy CD-1 mice where it was found that once daily dosage (25 mg/kg) of both **2a** and **2b** were well tolerated over the course of a 16-day treatment period as evidenced by normal body weight gains (Fig. 6A,B) behavior, and grooming patterns. Next, an MCT1 expressing WiDr tumor xenograft model was chosen to evaluate the efficacy of **2a** and **2b**. After tumors were inoculated, they were allowed to reach ~150 mm^3 volume, and mice were randomly divided into three groups. Group-1 was administered 25 mg/kg (i.p.) of compound **2a**, group-2 was administered with 25 mg/kg (i.p.) of **2b**, and group-3 was designated as control group and given an injection of vehicle. Treatment was continued for 16 days, and tumor volumes were recorded. From this study, there was a significant suppression in tumor volume when treated with TBDPS-CHC derivative **2a (**Fig. 6C,D**)** compared to the control group. During the two-week treatment period, there was no significant loss of body weights in mice between treated and control groups. The Ex-TBDPS-CHC derivative **2b** also suppressed the tumor growth by 28%, but compound **2a** exhibited higher efficacy 36% compared to **2b**. At the end of the study, all the tumors were resected, and the tumor mass was weighed (Fig. 6D).

Discussion

Altered metabolism is an enabling characteristic of cancer cells that supports tumor growth and progression[2]. Diffusion of metabolites, oxygen, and nutrients throughout the tumor vary and hence, glycolysis and OxPhos machinery exhibit differential expression patterns depending on the microenvironment of the cells[9, 10, 12]. Interestingly, mitochondrial OxPhos has been linked to proliferation in cancer cells and lactate uptake via MCT1 provides these cells with necessary TCA cycle substrates in support of heightened OxPhos[9, 10, 12]. Mitochondrial OxPhos is a stable and efficient source of ATP production, but is vulnerable to damage in later stages of cancer progression. Under these conditions, cancer cells exhibit the capability to increase glycolysis to meet the energetic and biosynthetic demands. The evolution of various metabolic phenotypes helps to maintain tumor plasticity and resistance to therapeutic intervention. In this regard, we have evaluated the potential of silicon appended lipophilic CHC analogues **2a-b** to inhibit cancer cell proliferation, MCT1 based lactate uptake, disrupt glycolysis and mitochondrial metabolism, and suppress *in vivo* tumor growth.

Further, the α-cyanocinnamic template has also been shown to inhibit the mitochondrial pyruvate carrier[27] and hence, improving the lipophilicity of such molecules may lead to disruption of mitochondrial metabolism. Previously it has been shown that synthetic mitochondrial targeted silylated derivatives exhibit potent anti-cancer efficacy and hence gave a rationale to develop lipophilic silylates that may exhibit dual MCT1 and mitochondrial inhibitory properties[40, 41]. Silyl ethers **2a** and **2b** derived from CHC with their lipophilic characteristics present an attractive method to increase the cell proliferation. The *in vitro* cell proliferation studies of candidate compounds **2a-b** have shown that these molecules exhibit higher cell proliferation compared to CHC specifically in the MCT1 expressing 4T1 and WiDr cell lines. To evaluate the importance of the silyl group in providing anti-proliferative effects, parent molecules **2a** and **2b** were tested. The non-silylated CHC derivatives **2c** or **2d** did not exhibit any cell proliferation inhibition properties reinforcing the importance of the TBDPS group in providing the cytotoxic properties. To evaluate the MCT1 inhibitory properties of synthesized compounds **2a-d**, we performed a lactate uptake assay as previously described by us[18, 19, 20]. Again, both silylated derivatives **2a** and **2b** showed potent MCT 1 inhibition in low μM concentration compared to CHC which typically inhibits MCT1 function at or above 150 μM concentration. The non-silyl derivatives **2c** and **2d** were potent than CHC but much less potent than the silylated derivatives **2a** and **2b**.

The structure of inward-open human MCT1, generated based on our computational studies, appears to be of sufficient quality to identify the binding site of candidate MCT1 inhibitors TBDPS-CHC (**2a**) and Ex-TBDPS-CHC (**2b**). The binding site amino acids determined by the most favorable docking poses of the two compounds is shown to be very similar with the extended **2b** reaching a few additional residues. Surprisingly, many of the analogous amino acids were previously identified by Nancolas *et al*. for AstraZeneca AR-C155858 inhibitor binding to an independently generated rat MCT1 model, also initially modeled in the inward-open state[42]. The concordance of binding site residues, although not fully expected for such a structurally distinct inhibitor, lends confidence in the results obtained here and consistently define the inhibitor binding pocket. The lipophilic phenyl groups of **2a** and **2b** binding to MCT1 is characterized by several hydrophobic contacts, including aromatic stacking of one of the inhibitor phenyl groups to phenylalanine in the binding pocket. The extensive hydrophobic contact surface between the candidate compounds and MCT1 likely leads in large part to the dramatic increase in affinity of these inhibitors over the parent CHC compound. The favorable hydrophobic interactions are supplemented by several putative hydrogen bonds. In fact, it appears most polar atoms in compounds **2a** and **2b** are immediately adjacent to one or more polar side chains, including conserved Tyr34 and Arg313

in human MCT1 (Fig. 3B). The cyano group, or rotationally isosteric carboxyl group, of the derivative compounds specifically interact with the hydroxyl group of conserved Tyr34 and the guanidine group of Arg313 simultaneously, another likely strong contributor to specificity and high affinity of these compounds over parent compound CHC. CHC docking was predicted to be both lower affinity and much lower specificity (based on pose position occupancy). Nonetheless, swapping cyano and carboxyl positions, via bond rotation, maintains hydrogen bonding potential in each case. Some of the uniqueness of **2a** and **2b** inhibitor binding to inward-open MCT1 is likely due to rotational freedom in the inhibitors, exemplified by the imprecise overlay in Fig. 3D. Further, the three-atom insertion to **2b** (C-C-O) increases this rotational freedom and volume making the similarities even more remarkable. The similarity from end to end of the two compounds in the binding pocket may suggest that the three-atom extension is not particularly advantageous. Although, **2b** was estimated to have slightly higher binding affinity than **2a** (−9.8 kcal/mol vs. −9.2 kcal/mol) to MCT1, the number top of poses occupying this site out of 20 was much fewer (5 vs. 11, respectively). This suggests that the specificity of **2b** may be compromised by the three-atom extension, perhaps by the increase in rotational freedom and therefore the entropy of the extended structure. There appears to be some potential for optimization based on the **2a** and **2b** MCT1 docking poses. Of the residues within 4.5 Å of the compounds binding site, the most obvious unsatisfied interaction is that of conserved Glu398, also identified in the binding site of AstraZeneca inhibitor AR-C155858 in rat MCT[42]. Satisfaction of this negative charge with a polar or positively charged substituent might lead to much higher inhibitor affinity and/or specificity albeit with poorer lipid diffusive capacity. In addition, there appears to be an additional hydrophobic pocket near the cyano and carboxyl inhibitor substituents of the inhibitor binding site, currently occupied by the polar end of the candidate compounds. Of course, just outside the 4.5 Å area defining the contact surface for compound **2a** and **2b** there are other potential favorable interactions. The change of the sterically shielded silicon to carbon is not expected to change either the hydrophobic interaction or hydrogen bonding terms. The bond length change could potentially contribute to small differences in calculated binding energies, especially in highly constrained binding pockets - not true in this case (Fig. 3). Further, crystal structure comparison of silicon analogues of known protein agonists show nearly identical binding topologies[43]. Docking poses and calculated energies have also been shown to be very similar for silicon analogues[44]. For these reasons and more practically because Vina is not internally parameterized for Si, we chose to substitute carbon in its place in the current study. There are cases where this would not be advised, namely if the Si is not sterically shielded and/or the binding pocket itself is very conformationally constrained. In the current context, we believe that the computational substitution of carbon for silicon in compounds **2a** and **2b** does not influence the topological outcomes of the top binding poses and contributes minimally to the calculated binding energies. Nonetheless, the newly generated human open-inward MCT1 model may allow us to continue to improve small molecule inhibitor design.

It is interesting to note the possibility of mitochondrial pyruvate carrier (MPC) inhibition with compounds **2a** and **2b**, as inhibition of mitochondrial pyruvate uptake may result in feedback mediated inhibition of extracellular lactate uptake. These observations have been previously reported with similar cyanocinnamic acid compounds[27], along with aminocarboxy coumarin derivative 7ACC2[45] as inhibitors of mitochondrial pyruvate uptake and consequent non-binding feedback inhibition of MCT1 mediated lactate uptake. Similarly, effects of compounds **2a** and **2b** on mitochondrial respiration (Fig. 5) may be a result of direct MPC and feedback inhibition of MCT1.

Improved cell proliferation and MCT1 inhibition properties along with lipophilic characteristics prompted us to examine the effects of **2a** and **2b** on glycolysis and mitochondrial OxPhos. To study this, we

employed the standard Seahorse XFe96® based glycolysis and mitochondrial stress tests in MCT1 expressing WiDr and MCT4 expressing (MCT1 null) MDA-MB-231. In these experiments, real time measurements of extracellular acidification rate (ECAR) and oxygen consumption rates (OCR) give rise to glycolytic and mitochondrial respiration rates respectively. Changes in ECAR and OCR in cancer cells following the addition of specific metabolites and inhibitors generate a glycolysis and mitochondrial respiratory profile from which metabolic effects of synthesized derivatives can be observed.

In the glycolysis stress tests, the addition of oligomycin eliminates the cells ability to use the mitochondria (OxPhos) as a source of ATP production, and as a result cells reach a maximum theoretical glycolysis or referred to as glycolytic capacity. With exposure to the compounds, glycolytic capacity remained unchanged in WiDr, and there was a significant reduction in MDA-MB-231. This observation may offer evidence that the effectiveness of the compounds on glycolysis may depend on the intrinsic metabolic phenotype of the cell, as glycolysis is upregulated in the MDA-MB-231 cell line (Fig. 4). Further, it was interesting to note that both compounds resulted in a stimulated rate of glycolysis in the WiDr cell line. This data suggests that mitochondrial disruption caused by compound treatment may stimulate a heightened level of glycolysis to keep up with energy demands. This data further bolsters the claim that the metabolic effects of our compounds are a function of basal metabolic phenotype (Fig. 4). These results translate to glycolytic reserve which is the ability of the cell to switch its metabolic dependencies to glycolysis for ATP production. In both cell lines this parameter is significantly reduced especially with exposure to the directly attached silyl ether **2a**.

The mitochondrial stress test with test compounds has shown potent inhibition of numerous parameters of mitochondrial respiration. Exposure of cells to mitochondrial membrane proton uncoupler FCCP stimulates cells to increase oxidation of TCA cycle substrates and oxygen consumption to maximum capacity to replenish the proton gradient, and the difference between basal respiration and maximal respiration describes the spare respiratory capacity of a given cell line. Further, mitochondrial ATP production can be evaluated by observing the change in OCR after addition of ATP synthase inhibitor oligomycin. Mitochondrial proton leak due to compound induced damage to the mitochondrial membrane can also be evaluated from the mitochondrial respiratory profile. Here, the presence of test compounds potently inhibited maximal respiration, mitochondrial ATP production, and spare respiratory capacity, and lead to an increase in proton leak. Interestingly, there was a more significant effect on mitochondrial respiration in the more oxidative WiDr cell line (Fig. 5).

To visualize compound effects on mitochondrial morphology and vitality, mitotracker red CMXROS (MTR), a fluorescent mitochondrial probe that binds proportional to membrane potential, was used. In these studies, untreated cells exhibited a stable MTR intensity and structural organization of the mitochondria were easily distinguishable. After treatment with compound **2a**, cultures exhibited a diffuse mitochondrial localization when compared to control cultures. The diffusion of mitochondria is suggestive of mitochondrial damage caused by our compound as the compartmentalization of mitochondria is found in healthy cells with functioning mitochondria. Also, it is quite possible that mitochondrial damage induced by compound **2a** lead to MTR to leakage, resulting in an apparent diffused mitochondrial morphology. Regardless, mitochondria damage was apparent following compound treatment.

The connection between cellular metabolism and proliferation is a complex interaction that is strongly influenced by an elaborate relationship between the metabolic and cell cycle machinery[46, 47, 48]. In each phase of the cell cycle there are checkpoints on both biosynthetic and bio-energetic supply that are

required to maintain proliferation[46, 47, 48]. The inhibition of metabolic processes can interrupt cell proliferation and result in programmed cell death. In our study it was found that exposure to our compound caused PARP cleavage in both cell lines and an increase in the p53 marker. It is possible that an increase in mutant p53 cell lines and concomitant PARP1 cleavage at 100 μM **2a** may suggest regained pro-apoptotic functions of p53 as observed with other literature reported experimental anticancer drugs[49]. Further, N-acetyl cysteine was able to reverse compound induced DNA damage as indicated by reduced H2AX phosphorylation – indicating that increased ROS in treated cultures was likely responsible for DNA damage. This observation further supports mitochondrial targeting with compound **2a** as dysfunction of the mitochondria can result in release of ROS. However, we did not observe a noticeable decrease in PARP1 cleavage with the treatment of NAC, suggesting that apoptotic events caused by **2a** treatment may be triggered independently of ROS induced DNA damage. In this regard, it is likely that compounds **2a** and **2b** act through numerous mechanisms to illicit anticancer efficacy observed in WiDr xenograft study (Fig. 8B,C), which may qualify these candidates for combination studies with clinically used anticancer agents to realize their full potential.

Figure 8 Move fig 8 to PDF page 8 so that it is before the discussion section.

In vivo safety and efficacy study of lead compounds **2a** and **2b**. Systemic toxicity study of compounds (**A**) **2a** and (**B**) **2b** in CD-1 mice (n = 6). Note normal body weight changes in treated mice when compared to vehicle control group. (**C**) Tumor volumes and (**D**) tumor mass of WiDr tumor xenograft study of **2a** and **2b** in athymic nude mice (n = 6). Mann-Whitney's test was performed to calculate statistical significance for this study (*$P < 0.05$, **$P < 0.01$).

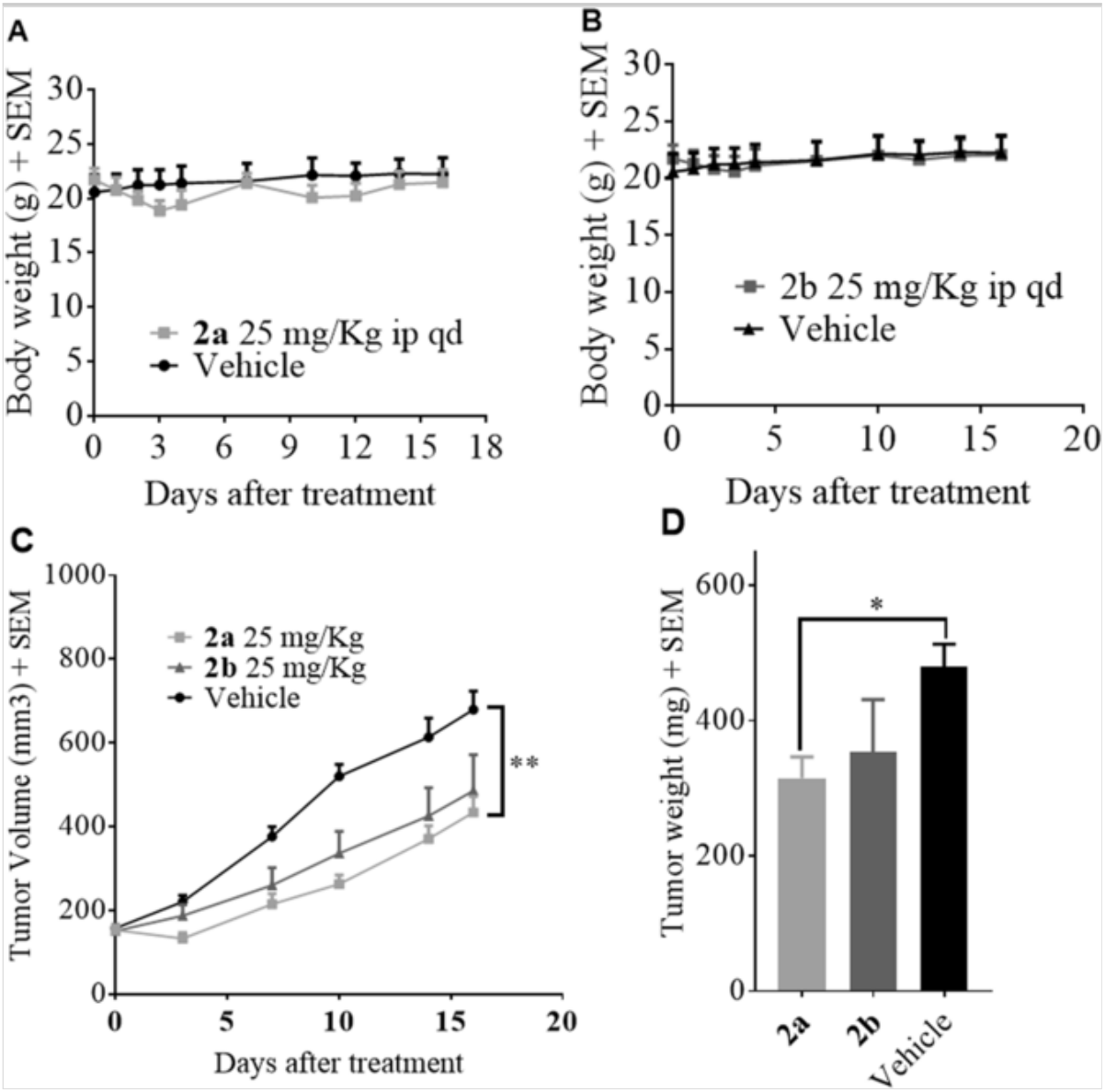

In conclusion, novel silyl cyanocinnamic acid derivatives have been synthesized and evaluated as potential anticancer agents. *In vitro* studies demonstrated that lead compounds **2a** and **2b** exhibited high cancer cell proliferation inhibition and potent MCT1 inhibition properties as determined by MTT assay and lactate-uptake studies, respectively. *In vitro* effects on glycolysis and mitochondrial metabolism illustrated that the **2a** and **2b** significantly perturbed both metabolic pathways. *In vivo* studies demonstrated that candidate compounds were well tolerated in healthy mice and exhibited good single agent tumor growth inhibition properties in a WiDr colorectal cancer xenograft model.

Materials and Methods

Cell lines and culture conditions

Human triple-negative breast cancer MDA-MB-231 cells (ATCC) were grown in DMEM supplemented with 10% FBS (Atlanta Biologicals) and penicillin-streptomycin (50U/ml, 50 µg/ml, Invitrogen). Human colorectal adenocarcinoma WiDr cells (ATCC) were cultured in MEM medium supplemented with 10% FBS and penicillin-streptomycin. Although WiDr was deposited with the ATCC as a colon adenocarcinoma line established from a 78-year-old female, DNA fingerprinting has shown this line to be

a derivative of HT-29[50]. Murine metastatic breast cancer 4T1 cells were grown in RPMI-1640 supplemented with 10% FBS and penicillin-streptomycin. Human estrogen receptor positive breast cancer MCF7 cells (Masonic Cancer Center, University of Minnesota) were grown in MEM supplemented with 6% FBS, EGF (0.01 µg/ml), NEAA, HDC (1 µg/ml), insulin (10 µg/ml), HEPES (12 mM) and sodium pyruvate (1 mM). Rat brain endothelial 4 (RBE4, a gift from F. Roux[18]) cells utilized in MCT1 inhibition assay were cultured in 1:1 α-MEM and F-10 HAM supplemented with 10% FBS (heat inactivated), 1 ng/ml basic fibroblast growth factor, 0.3 mg/ml geneticin, 1% antibiotic-antimycotic.

MCT1 inhibition assay via L-[^{14}C]-lactate uptake in RBE4 cells

MCT1 inhibition study was carried out using rat brain endothelial cells (RBE4) as reported previously[18].

MTT based cell proliferation inhibition assay

Cell proliferation inhibition was evaluated using 3-(4,5-dimethylthiazol-2-yl)-2,5-diphenyl tetrazolium bromide (MTT) assay as reported previously[19].

Homology modeling of human MCT1 protein structure

Human MCT1 membrane protein structure was generated by homology modeling with MODELLER 9.18 using the inward-open human glucose transporter 1 (hGLUT1) as a structural template, PDB file: 5eqi[31, 32]. Due to the minimal sequence similarity between the MCT1 and hGLUT1, we generated a final template alignment by consensus sequence alignment guided by consensus transmembrane spanning domain prediction. The alignments were generated using the following sequences: Human MCTs 1, 2, 3, 4, and 6; Human GLUTs 1 and 3; Bovine GLUT 5; Rat GLUT 3; and with and without *E. coli* major facilitator superfamily proteins LacY, EmrD and GlpT. Alignment programs PROMALS, MAFFT and MSAProbs were used to align the sequences followed by manual adjustment to eliminate gaps in the transmembrane spanning domains by alignment consensus and transmembrane domain consensus prediction[51, 52, 53]. Human MCT1 sequence similarity to human GLUT1 was 29% while similarity to *E. coli* LacY and GlpT were 24% and 23%, respectively. Transmembrane domain prediction software TMHMM, PloyPhobius, MEMSAT and CCTOP were used to generate a consensus membrane spanning topology[54, 55, 56, 57]. The adjusted sequence alignment was used as input into MODELLER 9.18 to build the MCT1 structure with the last 50 C-terminal amino acids removed. These amino acids are not represented in the template structure, are not considered to be important for inhibitor binding and are not part of a transmembrane spanning domain. Five independent models of MCT1 were built from the hGLUT1 structure template using default optimization and molecular dynamics refinement. An evaluation of structure fitness was based on the intrinsic discrete optimized protein energy score (DOPE) of MODELLER and an evaluation of charged residue rotamer orientation in the transmembrane spans, i.e. avoiding exposure of charged residues to the putative lipid bilayer. One model of human MCT1 was used for subsequent analysis. As with the homology model of rat MCT1 previously built by Manoharan, *et al*., we consider the models synthesized to be of intermediate quality but predictive in nature[33]. We briefly compare binding site residues identified here with those identified by Nancolas, et. al. for rat inhibitor binding[42].

Molecular docking studies

Human MCT1 homology model was used for computational docking studies of parent compound CHC and the TBDPS-CHC and Ex-TBDPS-CHC derivatives. Autodock Vina was used to dock the MCT inhibitors to the inward open homology model[34]. The intrinsic silicon atom of the two derivatives was changed *in-silico* to carbon for compatibility with the docking software. Partial charges were assigned to each atom of the inhibitors by the antechamber program built into UCSF Chimera using the AM1-BCC model[58]. The inhibitor docking search area was set intentionally broad, encompassing the entire membrane spanning domain and extending several angstroms toward the inward-open aqueous surface. Other variables such as adding hydrogens to the protein and removing non-polar hydrogens from the inhibitors were set to default values in Autodock Vina. Two independent docking calculations for each inhibitor were performed on human MCT1. Each docking run returned the top ten inhibitor poses determined by estimating an energy of interaction or binding affinity. Docked inhibitor poses were viewed with UCSF Chimera and the top poses were selected for further analysis. All MCT1 residues within 4.5 Å of the docked inhibitors were determined and compared for each compound. Autodock Vina estimated individual binding affinities were compared. Further, the number of poses nearly identical (< 2 Å RMSD) to the most favorable docked pose, estimated by position, orientation and MCT1 residues contacted for each inhibitor was used as a surrogate for binding specificity.

Seahorse XFe96® assessment of glycolysis and mitochondrial respiration

20,000 cells/well were plated in 96-well Seahorse plates (Agilent, part no. 101085-004) and incubated 16–24 hours at 37 °C at 5% CO_2. Flux pack sensors (Agilent, part no. 102416-100) were hydrated with XF calibrant solution (Agilent, part no. 100840-000) overnight at 37 °C in a non-CO_2 incubator. The serum free assay media was prepared from Seahorse base medium (Agilent, part no. 102353-100) enriched with glutamine (1 mM) and sodium pyruvate (1 mM). The pH of the media was adjusted to 7.4. For glycolysis stress test the serum free assay media was used. For the mitochondrial stress test glucose (10 mM) was added to make an enriched serum free assay media. For both stress tests an 8X stock concentration of test compounds in their respective media was prepared for microplate injections in port A. Stock solutions of glucose (90 mM), oligomycin (10 μM), and 2-deoxyglucose (Chem Impex, 550 mM) were prepared such that their final working concentrations are 10 mM, 1 μM and 50 mM, respectively, for glycolysis stress test. For mitochondrial stress test, stock solutions of oligomycin (9 μM), FCCP (2.5–10 μM, cell line dependent), rotenone + antimycin A (5.5 μM) were prepared such that their final concentrations were 1 μM, 0.25–1 μM, and 0.5 μM, respectively in the enriched test media. Under glycolytic stress test, the cells were treated with test compounds, followed by the addition of glucose, oligomycin and 2-deoxyglucose at 14.29, 33.8, 53.35, 72.87 minutes, respectively. Under mitochondrial stress test, cells were treated with test compounds, followed by the addition of oligomycin, FCCP, and rotenone + antimycin A, at 14.29, 33.8, 53.35, 72.87 minutes, respectively. Extracellular acidification rates (ECAR) and oxygen consumption rates (OCR) were recorded in real-time for glycolysis and mitochondrial stress tests, respectively, using a Seahorse XFe96® analyzer (Agilent). The parameters related to glycolytic and mitochondrial functions were calculated utilizing the Wave 2.4.0 software (Agilent). ATP rate assay experiment was performed using manufactures (Agilent) protocol, and respective mitochondrial and glycolytic ATP rates were normalized to protein (BCA assay) and calculated using Wave 2.4.0 software.

Fluorescent microscopy studies

MDA-MB-231 or WiDr cells (5×10^4 cells/mL) were seeded in glass-bottom dishes (MatTek Corp, part no. P35G010C) and incubated for 48 hours. Test compound (30 μM) was added and cells were again

incubated for 24 hours prior to fluorescent microscopic imaging. In some cultures, MitoTracker Red CMXROS (Invitrogen, M7512, 100 nM) was added 15 min prior to imaging. The growth media was removed and replaced with 5% FBS in 1X PBS for imaging. Cells were then examined and photographed using a Nikon TE2000 epifluorescent microscope and camera. The images shown are representative of at least 3 fields of view of three separate experiments.

Western blot analysis

50,000 WiDr or MDA-MB-231 cells were seeded in 100 mm dishes and were incubated for 48 hours. Cells were then treated with test compounds for 24 hours, washed twice with 1X PBS, solubilized in 200 µL SDS boiling buffer (5% w/v SDS, 10% v/v glycerol, and 60 mM Tris pH 6.8), and sonicated. The resulting cell lysate was then assayed for protein using the Pierce BCA protocol. A volume of test sample containing 10 µg protein was loaded on SDS PAGE gel for electrophoresis according to manufacturer's instructions. Proteins were transferred from the gel to nitrocellulose membrane according to the manufacturer's instructions. Membranes were blocked for 1 hr at 35 °C using 10% (w/v) non-fat milk in PBST and were exposed to primary antibody. PARP1 (rabbit polyclonal IgG, Origene, TA321555), p53 (rabbit polyclonal IgG, Santa Cruz, sc50329), and γ-H2AX (Upstate 05-636, 1:2500) were detected and visualized using HRP chemiluminescence. For relative quantitation, β-actin (mouse monoclonal IgG C4, Millipore, MAB1501, 1:10,000) and GAPDH (mouse monoclonal IgG, Santa Cruz, sc47724, 1:100) were detected and measured as a control protein.

In vivo systemic toxicity study

Five-week-old healthy CD-1 mice (Charles River) were obtained and acclimatized for one week prior to treatment. Mice (n = 6) were grouped randomly based on average body weight. Group-1 was administered with compound **2a** or **2b** (20 mg/kg, ip, qd) and group-2 was administered with vehicle (10% DMSO, 10% PEG, 40% HS-15 solution (18.8%w/v) ip, qd) intraperitoneally once daily, six days a week for a total of 16 days of treatment. Mice body weights were recorded daily as a proxy for animal health and were also examined for proper activity and grooming patterns. At the end of the study, mice were euthanized. A graph of days of treatment versus body weight ± SEM was generated using GraphPad software. All procedures performed using this method were approved by the University of Minnesota Institutional Animal Care and Use Committee (IACUC, protocol no. 1611-34326A) and are in accordance with all guidelines and regulations.

In vivo tumor growth inhibition study

WiDr cells (5×10^6 cells) were suspended in 1:1 mixture of matrigel (Corning, cat. no. 356237) and PBS and injected subcutaneously into the right flank of female athymic nude mice (Charles River). The mice were randomly assigned into 3 groups (n = 6 mice per group). Vertical and horizontal diameters of tumors were measured every two- or three-days using calipers. The tumor volumes were calculated assuming a perfect sphere using the formula $V = ab^2/2$ where 'a' is the longer diameter of the tumor and 'b' is the shorter diameter of the tumor. Treatment was initiated when the tumor volume reached 100 mm^3. The study was terminated after sixteen days and tumors were then resected and weighed. All procedures performed using this method were approved by the University of Minnesota Institutional Animal Care and Use Committee (IACUC, protocol no. 1612-34444A) and are in accordance with all guidelines and regulations.

Ethical statement

The animal studies were approved and conducted consistent with University of Minnesota IACUC protocols 1611-34326A (systemic toxicity study Fig. 8A,B) and 1612-34444A (*in vivo* efficacy study Fig. 8C,D).

Statistical analysis

Statistics were computed using GraphPad Prism version 7.0. Repeated measures one-way ANOVA was used for *in vitro* studies and Mann-Whitney test was used for *in vivo* studies. A *P*-value of <0.05 was considered significant where $*P < 0.05$; $**P < 0.01$; $***P < 0.001$; $****P < 0.0001$.

Supplementary information

is available for this paper at https://doi.org/10.1038/s41598-019-54709-7.

Publisher's note Springer Nature remains neutral with regard to jurisdictional claims in published maps and institutional affiliations.

Acknowledgements

This work was supported by University of Minnesota Duluth; Department of Defense Breast Cancer Research Proposal, Breakthrough Award (grant number W81XWH-15-1-0047, VRM); Department of Defense Breast Cancer Research Award (grant number W81XWH-15-1-0060, LRD), Whiteside Clinical Research Institute, Minnesota, and Randy Shaver Cancer Research and Community Fund, Minnesota.

Author contributions

V.R.M. performed the *in vitro* and *in vivo* study design and contributed to draft the manuscript; L.R.D. designed MCT1 inhibition assay and Seahorse XFe96 experiments; G.L.N. performed the synthesis and participated in the *in vitro* and *in vivo* studies; C.T.R. and J.H. designed and conducted florescence and western blotting studies, L.N.S., S.J. and S.K.J. cultured cells and carried out the cell proliferation studies and seahorse studies, J.R. designed and performed homology modeling of and molecular docking to human MCT1 structures. T.R.H. contributed to the animal studies and interpretation of the data. All authors read and approved the final manuscript.

Competing interests The authors declare no competing interests.

Supplementary information

Development of Novel Silyl Cyanocinnamic Acid Derivatives as Metabolic Plasticity Inhibitors for Cancer Treatment

References

1. Hanahan, D. & Weinberg, R. A. The hallmarks of cancer. *Cell.* **100**, 57–70 (2000).

2. Hanahan, D. & Weinberg, R. A. Hallmarks of cancer: the next generation. *Cell.* **144**, 646–74 (2011).

3. Cairns, R. A., Harris, I. S. & Mak, T. W. Regulation of cancer cell metabolism. *Nat. Rev. Cancer.* **11**, 85–95 (2011).

4. Dang, C. V. Links between metabolism and cancer. *Genes and Development.* **26**, 877–90 (2012).

5. Ganapathy, V., Thangaraju, M. & Prasad, P. D. Nutrient transporters in cancer: Relevance to Warburg hypothesis and beyond. *Pharmacol. Ther.* **121**, 29–40 (2009).

6. Ganapathy-Kanniappan, S. & Geschwind, J. F. H. Tumor glycolysis as a target for cancer therapy: Progress and prospects. *Mol. Cancer.* **12**, 152, https://doi.org/10.1186/1476-4598-12-152 (2013).

7. Pinheiro, C. *et al*. Role of monocarboxylate transporters in human cancers: state of the art. *J. Bioenerg. Biomembr.* **44**, 127–39 (2012).

8. Li, X., Yu, X., Dai, D., Song, X. & Xu, W. The altered glucose metabolism in tumor and a tumor acidic microenvironment associated with extracellular matrix metalloproteinase inducer and monocarboxylate transporters. *Oncotarget.* **7**, 23141–55 (2016).

9. Pavlides, S. *et al*. The reverse Warburg effect: Aerobic glycolysis in cancer associated fibroblasts and the tumor stroma. *Cell Cycle.* **8**, 3984–4001 (2009).

10. Martinez-Outschoorn, U. E. *et al*. Ketone bodies and two-compartment tumor metabolism: Stromal ketone production fuels mitochondrial biogenesis in epithelial cancer cells. *Cell Cycle.* **11**, 3956–3963 (2012).

11. Martinez-Outschoorn, U. E. *et al*. Stromal-epithelial metabolic coupling in cancer: Integrating autophagy and metabolism in the tumor microenvironment. *Int. J. Biochem. Cell Biol.* **43**, 1045–1051 (2011).

12. Martinez-Outschoorn, U. E., Peiris-Pagés, M., Pestell, R. G., Sotgia, F. & Lisanti, M. P. Cancer metabolism: a therapeutic perspective. *Nat. Rev. Clin. Oncol.* **14**, 11–31 (2017).

13. Lee, M. Metabolic interplay between glycolysis and mitochondrial oxidation: The reverse Warburg effect and its therapeutic implication. *World J. Biol. Chem.* **6**, 148–61 (2015).

14. Phan, L. M., Yeung, S. C. J. & Lee, M. H. Cancer metabolic reprogramming: importance, main features, and potentials for precise targeted anti-cancer therapies. *Cancer Biol. Med.* **11**, 1–19 (2014).

15. Halestrap, A. P. & Price, N. T. The proton-linked monocarboxylate transporter (MCT) family: structure, function and regulation. *Biochem J* **343**(Pt 2), 281–99 (1999).

16. Halestrap, A. P. & Meredith, D. The SLC16 gene family-from monocarboxylate transporters (MCTs) to aromatic amino acid transporters and beyond. *Pflugers Arch.* **447**, 619–28 (2004).

17. Dimmer, K. S., Friedrich, B., Lang, F., Deitmer, J. W. & Bröer, S. The low-affinity monocarboxylate transporter MCT4 is adapted to the export of lactate in highly glycolytic cells. *Biochem. J.* **350**, 219–27 (2000).

18. Gurrapu, S. *et al*. Monocarboxylate transporter 1 inhibitors as potential anticancer agents. *ACS Med. Chem. Lett.* **6**, 558–561 (2015).

19. Gurrapu, S. *et al*. Coumarin carboxylic acids as monocarboxylate transporter 1 inhibitors: *In vitro* and *in vivo* studies as potential anticancer agents. *Bioorg. Med. Chem. Lett.* **26**, 3282–86 (2016).

20. Jonnalagadda, S. *et al*. Novel N, N-dialkyl cyanocinnamic acids as monocarboxylate transporter 1 and 4 inhibitors. *Oncotarget.* **10**, 2355–68 (2019).

21. Draoui, N. *et al*. Antitumor activity of 7-aminocarboxycoumarin derivatives, a new class of potent inhibitors of lactate influx but not efflux. *Mol. Cancer Ther.* **13**, 1410–8 (2014).

22. Benjamin, D. *et al*. Dual Inhibition of the Lactate Transporters MCT1 and MCT4 Is Synthetic Lethal with Metformin due to NAD + Depletion in Cancer Cells Article Dual Inhibition of the Lactate Transporters MCT1 and MCT4 Is Synthetic Lethal with Metformin due to NAD + Depletion in Cancer Cells. *Cell. Rep.* **25**, 3047–58.e4 (2018).

23. Curtis, N. J. *et al*. Pre-clinical pharmacology of AZD3965, a selective inhibitor of MCT1: DLBCL, NHL and Burkitt's lymphoma anti-tumor activity. *Oncotarget.* **8**, 69219–36 (2017).

24. Noble, R. A. *et al*. Inhibition of monocarboxylate transporter 1 by AZD3965 as a novel therapeutic approach for diffuse large B-cell lymphoma and Burkitt lymphoma. *Haematologica.* **102**, 1247–57 (2017).

25. Wang, H. *et al*. Synthesis and Structure-Activity Relationships of Pteridine Dione and Trione Monocarboxylate Transporter 1 Inhibitors. *J. Med. Chem.* **57**, 7317–24 (2014).

26. Halestrap, A. P. The monocarboxylate transporter family-Structure and functional characterization. *IUBMB Life.* **64**, 1–9 (2012).

27. Halestrap, A. P. The Mitochondrial Pyruvate Carrier: Kinetics and Specificity for Substrates and Inhibitors. *Biochem J.* **148**, 85–96 (1975).

28. Lalonde, M. & Chan, T. Use of Organosilicon Reagents as Protective Groups in Organic Synthesis. *Synthesis (Stuttg).* **9**, 817–854 (1985).

29. Wuts, P. G. M. & Greene, T. W. Greene's Protective Groups in Organic Synthesis, 4th Edition. (Wiley-Interscience, 2006).

30. Franz, A. K. & Wilson, S. O. Organosilicon Molecules with Medicinal Applications. *J. Med. Chem.* **56**, 388–405 (2013).

31. Kapoor, K. *et al*. Mechanism of inhibition of human glucose transporter GLUT1 is conserved between cytochalasin B and phenylalanine amides. *PNAS* **113**, 4711–6 (2016).

32. Sali, A. & Blundell, T. Comparative Protein Modelling by Satisfaction of Spatial Restraints. *J. Mol. Biol.* **234**, 779–815 (1993).

33. Manoharan, C., Wilson, M. C., Sessions, R. B. & Halestrap, A. P. The role of charged residues in the transmembrane helices of monocarboxylate transporter 1 and its ancillary protein basigin in determining plasma membrane expression and catalytic activity. *Mol. Membr. Biol.* **23**, 486–498 (2006).

34. Trott, O. & Olson, A. AutoDock Vina: improving the speed and accuracy with a new scoring function, efficient optimization and multithreading. *J. Comput. Chem.* **31**, 455–461 (2010).

35. Yue, X. *et al*. Mutant p53 in cancer: accumulation, gain-of-function and therapy. *J. Mol. Biol.* **429**, 1595–1606 (2017).

36. Hui, L., Zheng, Y., Yan, Y., Bargonetti, J. & Foster, D. A. Mutant p53 in MDA-MB-231 breast cancer cells is stabilized by elevated phospholipase D activity and contributes to survival signals generated by phospholipase D. *Oncogene.* **25**, 7305–10 (2006).

37. ATCC. p53 Hotspot Mutation Cell Panels, https://www.atcc.org/en/Documents/Learning_Center/~/media/5F7B1CCACF724E3398BE56BFBEE3EFE4.

38. Chaudhuri, A. R. & Nussenzweig, A. The multifaceted roles of PARP1 in DNA repair and chromatin remodelling. *Nature.* **18**, 610–21 (2017).

39. Rogakou, E. P., Pilch, D. R., Orr, A. H., Ivanova, V. S. & Bonner, W. M. Double-stranded Breaks Induce Histone H2AX phosphorylation on Serine 139. *J. Biol. Chem.* **273**, 5858–68 (1998).

40. Kim, S. *et al*. Intra-mitochondrial biomineralization for inducing apoptosis of cancer cells. *Chem. Sci.* **9**, 2474–9 (2018).

41. Qu, Q. & Zhao, Y. Anticancer Effect of α-Tocopherol Succinate Delivered by Mitochondria-Targeted Mesoporous Silica Nanoparticles. *ACS Appl. Mater. Interfaces.* **8**, 34261–9 (2016).

42. Nancolas, B., Sessions, R. B. & Halestrap, A. Identification of key binding site residues of MCT1 for AR-C155858 reveals the molecular basis of its isoform selectivity. *Biochem J.* **466**, 177–88 (2015).

43. Buttner, M. *et al*. Silicon Analogues of the Retinoid Agonists TTNPB and 3-Methyl-TTNPB, Disila-TTNPB and Disila-3-methyl-TTNPB: Chemistry and Biology. *ChemBioChem.* **8**, 1688–99 (2007).

44. Wolf, S. *et al*. Evidence for a shape-based recognition of odorants *in vivo* in the human nose from an analysis of the molecular mechanism of lily-of- the-valley odorants detection in the Lilial and Bourgeonal family using the C / Si / Ge / Sn switch strategy. *PLoS One.* **12**, e0182147 (2017).

45. Corbet, C., *et al*. Interruption of lactate uptake by inhibiting mitochondrial pyruvate transport unravels direct antitumor and radiosensitizing effects. *Nat. Comm*. **9**, https://doi.org/10.1038/s41467-018-03525-0 (2018).

46. Buchakjian, M. R. & Kornbluth, S. The engine driving the ship: Metabolic steering of cell proliferation and death. *Nat. Rev. Mol. Cell Biol.* **11**, 715–27 (2010).

47. Kaplon, J. *et al*. Two-way communication between the metabolic and cell cycle machineries: the molecular basis. *Cell Cycle.* **14**, 2022–32 (2015).

48. Kalucka, J. *et al*. Metabolic control of the cell cycle. *Cell Cycle.* **14**, 3379–88 (2015).

49. Girardini, J. E., Marotta, C. & Del, G. Disarming mutant p53 oncogenic function. *Pharmacol. Res.* **79**, 75–87 (2014).

50. Chen, T. R., Drabkowski, D., Hay, R. J. & Macy, M. WiDr is a Derivative of Another Colon Adenocarcinoma Cell Line, HT-29. *Cancer Genet Cytogenet.* **27**, 125–34 (1987).

51. Pei, J. & Grishin, N. V. Sequence analysis PROMALS: towards accurate multiple sequence alignments of distantly related proteins. *Bioinformatics.* **23**, 802–8 (2007).

52. Katoh, K., Rozewicki, J. & Yamada, K. D. MAFFT online service: multiple sequence alignment, interactive sequence choice and visualization. *Brief Bioinform*., https://doi.org/10.1093/bib/bbx108 (2017).

53. Liu, Y., Schmidt, B. & Maskell, D. L. MSAProbs: multiple sequence alignment based on pair hidden Markov models and partition function posterior probabilities. *Bioinformatics.* **26**, 1958–64 (2010).

54. Sonnhammer, E. L. L., vonHeijne, G. & Krough, A. A hidden Markov model for predicting transmembrane helices in protein sequences. *Proc Int Conf Intell Syst Mol Biol.* **6**, 175–82 (1998).

55. Käll, L., Krogh, A. & Sonnhammer, E. L. L. An HMM posterior decoder for sequence feature prediction that includes homology information. *Bioinformatics.* **21**, 251–7 (2005).

56. Nugent, T. & Jones, D. T. Transmembrane protein topology prediction using support vector machines. *BMC Bioinformatics*. **10**, https://doi.org/10.1186/1471-2105-10-159 (2009).

57. Dobson, L., Remenyi, I., Tusnady, G. CCTOP: A Consensus Constrained TOPology prediction web server. *Nucleic Acids Res*. **43**, https://doi.org/10.1093/nar/gkv451 (2015).

58. Pettersen, E. F. *et al*. UCSF Chimera — A Visualization System for Exploratory Research and Analysis. *Wiley Intersci*., https://doi.org/10.1002/jcc.20084 (2004).